Numéro National de Thèse : 2020LYSEN061

THESE de DOCTORAT DE L'UNIVERSITE DE LYON

opérée par

l'Ecole Normale Supérieure de Lyon

Ecole Doctorale N° 206
École Doctorale de Chimie (Chimie, Procédés, Environnement)

Discipline : **Chimie**

Soutenue publiquement le 03/11/2020, par:

Tingting YU

Solid state luminescent molecules, macromolecules and materials, their response to stimuli and their applications in devices

Molécules luminescentes à l'état solide, macromolécules et matériaux , leurs réponses aux stimuli et leurs applications dans des dispositifs

---

Devant le jury composé de :

Achelle Sylvain	Maître de conférences	Institut de chimie de Rennes	Rapporteur
Romieu Anthony	Professeur	Université de Bourgogne	Rapporteur
Allain Clemence	Chargée de recherche	ENS Paris Saclay	Examinatrice
Ulrich Gilles	Directeur de recherche	Université de Strasbourg-ICPEES	Examinateur
MONNEREAU Cyrille	Maître de conférences	ENS de Lyon	Co-encadrant
ANDRAUD Chantal	Directrice de recherche	ENS de Lyon	Directrice de thèse

Acknowledgements

This dissertation was funded by the China Scholarship Council (CSC) and École Normale Supérieure de Lyon (ENS De Lyon). I would like first of all to extend my gratitude to CSC and ENS-Lyon for giving me the opportunity to work on this project and for funding the research.

This thesis was completed with the supervision of Dr. Chantal Andraud and Dr. Cyrille Monnereau. I would like to express my sincere thanks to Dr. Chantal Andraud, the director of Laboratoire de Chimie de l'Ecole Normale Supérieure de Lyon, providing me an opportunity to work in her lab under her guidance.Thanks for her care, support and help, both in my life and study during the last three years. I deeply want to show my great appreciate to Dr. Cyrille Monnereau, who taught me how to do the research, how to solve the problem, how to balance the study and life. In my PhD study, he always encouraged and motivated me to do what I interested in, during this process, he gave me a lot of professional ideas and suggestions. I benefit a lot from his scientific attitude and profound knowledge on his field of research.

I would like to take this opportunity to also thank the following people for their support and help: Prof. Hongping Zhou from Anhui University, for cellular bio-imaging. All our group members (current and former) and all staff members of Laboratoire de Chimie de l'ENS-Lyon.

All my friends. I cherished all the wonderful moments that we spent together.

Finally, I would like to thank my family. First, I want to thank you for making all your efforts to bring me up. Second, I want to thank you for your good education on me. The most important thing that I want to say "Thank you" is your great admiration on my own freedom. You never forced me to do anything I was not interested in, even you had already known that I would regret not doing it. You never forbade me to do anything I was truly interested in and supported me financially and mentally. You told me to look over the horizons and to pursuit my own dreams without hesitation. You also told me to consider everything carefully before getting start. Thanks for you, I love you!

Contents

Contents.....**I**

Abbreviations.....**IV**

General Introduction.....**VI**

Chapter 1 Introduction Two-photon Luminescent Responsive Probes with Aggregation Induced Emission Properties.....**1**

1 Aggregation-Induced Emission (AIE).....1

1.1 Background of AIE.....1

1.2 AIEgen working mechanisms.....3

1.3 AIEgen systems.....5

1.4 AIEgens applications.....10

2 Fluorescent Probes for Analytes Detection.....20

2.1 Components of a fluorescent probe for analyte detection.....20

2.2 Response mechanisms to analyte detection.....21

3 Two-photon Absorption (TPA).....28

3.1 Research background.....28

3.2 Effective two-photon absorption cross section.....30

3.3 Two photon fluorescence materials for biological systems.....31

4 Objectives.....32

Chapter 2 AIE-active Conjugated Polymer Nanoparticles as Platforms for Biological Applications.....**34**

1 Introduction.....34

1.1 Conjugated polymer.....35

1.2 Conjugated polymer nanoparticles (CPNs).....38

1.3 AIE conjugated polymer nanoparticles for biological applications.....41

1.4 Objectives.....42

2 Design, Synthesis and Optical Properties of Conjugated Polymers.....43

2.1 Design strategy.....43

2.2 AIE properties of three conjugated polymers.....49

3 Conjugated Polymer Nanoparticles.....53

3.1 Dynamic light scattering (DLS).....53

3.2 Scanning electron microscope (SEM).....54

4 Biological Applications of Conjugated Polymers.....55

4.1 MTT assays..... 56
4.2 Photobleaching assays..... 57
4.3 Cell imaging..... 59
5 Conclusion..... 61
Chapter 3 Benzothiazole Based AIE Active Fluorescent Probes for Acid and Vapors Detection 63
1 Introduction..... 63
1.1 Types of chemical fluorescent probes..... 63
1.2 Objectives..... 68
2 Design, Synthesis and Optical Properties of new chromophores..... 69
2.1 Design strategy..... 69
2.2 Synthesis and Characterization..... 69
2.3 Optical properties of the new family of compounds..... 72
3 Incorporation of molecules into devices..... 88
3.1 Reversible switching to acid vapor in solid state..... 88
3.2 Polymer thin films of DAD response to acid vapor..... 89
4 Cell Imaging..... 91
5 DAD-loaded Albumin in Bovine Serum (BSA)..... 92
6 Conclusion..... 96
Chapter 4 Tuning Spectral Properties of Benzobisthiazole based Compounds by Controlled Chemical Modification..... 98
1 Towards benzobisthiazolium containing probes with cyanine characteristics..... 98
1.1 Introduction and structural characteristics of cyanine probes..... 98
1.2 Different types of benzothiazole cyanine dyes..... 101
1.3 Objective..... 102
1.4 Synthesis and characterization of new benzothiazole cyanine dyes..... 103
1.5 Optical properties of new benzobisthiazolium cyanine..... 103
2 Other probes by functionalized new chromophore..... 107
2.1 Tuning the electronic properties of a chromophore by addition of peripheral substituents: chromophores of the A'-D-A-D-A' type..... 108
2.2 Design strategy, synthesis and characterization of morpholine appended compound **24** 114
3 Conclusion..... 122
Chapter 5 Towards A New Family of Compounds as Candidates for Super Resolution Imaging ? 124
1 Introduction..... 124
1.1 Abbe limit, and the super-resolution microscopy..... 124
1.2 Blinking molecules and the stochastic optical reconstruction..... 125

1.3 Objective..... 127

2 Characterization of the photoinduced “on/off” switching properties of benzobisthiazole derivatives..... 128

2.1 Qualitative assessment of the process..... 128

2.2 A first insight on the photoswitching mechanism..... 130

2.3 Reversibility of the switching process..... 131

3 Conclusion..... 132

Chapter 6 Conclusion..... 133

Chapter 7 Experimental Section..... 137

1 General information..... 137

2 Synthesis and characterization..... 139

3 Preparing film DAD@PMMA and DAD@PS..... 156

Bibliography..... 157

Abbreviations

AIE	Aggregation-induced emission
NIR	Near-infrared
ACQ	Aggregation caused quenching
VR	Vibrational relaxation
IC	Internal conversion
ISC	Intersystem crossing
RIM	Restriction of Intramolecular Motions
RIR	Restriction of Intramolecular Rotations
RIV	Restriction of Intramolecular Vibrations
TPE	Tetraphenylethene
AIEgen	Aggregation-induced emission luminogens
MeCN	Acetonitrile
IR	Intramolecular rotations
OLED	Organic Light-Emitting Diode
CPL	Circularly Polarized Luminescence
CD	Circular Dichroism
PET	Photo-induced Electron Transfer
ICT	Intramolecular charge transfer
FRET	Fluorescence Resonance Energy Transfer
TPA	Two-Photon Absorption
GM	Goeppert-Mayer 1 GM = 10^{-50} cm^4 s
SEM	Scanning electron microscopy
DLS	Dynamic light scattering
CPs	Conjugated Polymers
CPNs	Conjugated Polymer Nanoparticles
DP	Degree of Polymerization
GPC	Gel Permeation Chromatography
Mn	Number average molecular weight
Mw	Weight average molecular weight
Mz	Size average molecular weight

PDI	Polydispersity Index
|glum|	Dissymmetry Factor
ET	Electron transfer
eV	Electron volt
f_w	Water fraction
DFT	Density functional theory
HOMO	Highest occupied molecular orbital
LUMO	Lowest unoccupied molecular orbital
H	Hour
Hz	Hertz
TICT	Twisted intramolecular charge-transfer
NMR	Nuclear magnetic resonance
J	Coupling constant
TLC	Thin-layer chromatography
UV	Ultraviolet
ε	Molar absorption coefficient
λ_{em}	Maximum emission
λ_{max}	Maximum absorption
M	Molar per liter
μM	Micromolar per liter
ν_{abs}	Frequency of absorption maximum
ν_{em}	Frequency of emission maximum
σ	Two-photon absorption cross-section
Φ_f	Fluorescence quantum yield

General Introduction

Nowadays, luminescent materials are ubiquitous in the fields of optoelectronic devices, biological probes and bio-imaging, chemical sensing, display and other smart material applications. However, most luminescent materials are efficient emitters only in solution, in aggregates or solid state, the luminescence will decrease or vanish. This phenomenon severely restricts the accessible range of applications of luminescent materials, particularly their incorporation into functional devices. This has urged researchers to develop new luminescent materials exhibiting solid state and/or aggregation-induced emission (AIE) properties, a topic that has gained great attention in the last two decades.

In this thesis, we will focus on the synthesis and study of new luminescent conjugated chromophores presenting an alternation of electron donor and acceptor groups, with a specific focus on their emission properties in aggregates or solid states in the far-red or near infrared region, a range of wavelengths that is underrepresented in the current catalogue of AIEgens. We will study the influence of chain length and donor/acceptor substitution not only on the optical properties of the isolated compounds, but also especially on the material in its aggregated state. Finally, taking advantages of the specific properties of some of the as-designed candidates, we will explore their potential applications ranging from fluorochromic stimuli-responsive sensors (in film form) to red and NIR luminescent two-photon probes for biological imaging. In this context, two photon absorption (TPA) properties of our molecules were an important aspect of this work. Unfortunately, because of technical issues, measurement of the TPA cross sections could not be performed in the course

of this PhD, and will therefore not be reported in this manuscript.

Herein, Chapter **1** will be a general introduction about concepts that are central in this thesis such as aggregation-induced emission, fluorescent probe and two-photon absorption. Then, Chapter **2** to Chapter **5** will depict the main results achieved in this thesis, namely:

i) the synthesis of new alternating triarylamine or carbazole / tetraphenylethylene (TPE) polymers (**polymer-1, polymer-2, polymer-3**), the study of their luminescence properties in solution and aggregated states, and the characterization of typical J-aggregates emission features in solid state, unusual in TPE derivatives which we relate to the linear polymeric nature of the object.

ii) the development of a new family of diphenylamine / benzobisthiazole chromophores and controlled synthesis of oligomers belonging to this family (**DAD**, **$(DA)_2D$**, **$(DA)_5D$**). The investigation of their photophysical properties in solution and solid state, and more specifically their sensitivity to protonation. Their integration into acid-base responsive luminescent devices.

iii) The exploration of chemical transformations of the newly designed chromophore, in order to achieve solid state NIR emission, in particular by means of a change in the electronic character of the electronic transition from Intra-Molecular Charge Tranfer (ICT) to Cyanine transition. Their modification towards improvement of their biocompatibility, bioavailability and selectivity of their cellular compartments staining ability.

iv) The identification of a reversible photoinduced “on-off” switching of their luminescence properties, and our preliminary attempts to take advantage of this

phenomenon in the design of contrast-agents for super resolution imaging.

After concluding remarks, this thesis manuscript will end with an experimental section, and a listing of the bibliographic references used in this report.

Chapter 1 Introduction Two-photon Luminescent Responsive Probes with Aggregation Induced Emission Properties

1 Aggregation-Induced Emission (AIE)

1.1 Background of AIE

In the past time, research on luminescent molecules has generally acknowledged that aggregate formation will quench the emission of luminophores, a process often referred as aggregation-caused quenching (ACQ) (**Figure 1-1a**). This ACQ phenomenon is mainly due to π-π stacking which forms exciplexes that are not conducive to luminescence emission.[1] Luminescent materials are generally incorporated into functional devices as aggregates, thin films, or solid state, therefore ACQ phenomenon severely restricts the practical application of luminescent materials. Remediations to reduce the quenching and obtain materials with high luminescence efficiency in the aggregated state has therefore become an urgent issue.

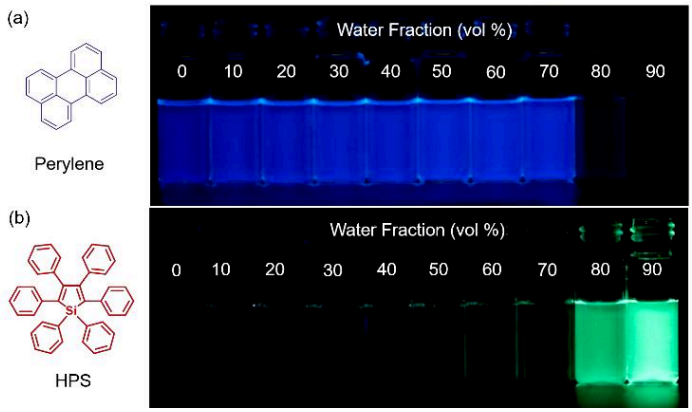

Figure 1-1. Molecular structures and picture of (a) perylene and (b) hexaphenylsilole (HPS) solutions with different poor solvent fractions taken under 365 nm lamp. Pictures taken from reference 8.

Scientists have tried to use various methods for obtaining materials with higher luminescence efficiency, such as controlling the chemical structure of organic molecules, introducing long alkyl chains as substituents, or synthesizing large branched molecules. These works have achieved some positive results, but cumbersome procedures, complex synthetic routes, and relatively low yields have limited the application of these materials. [2-4]

In the early 2000s, works of Tang's group reported a phenomenon where chromophore that did not luminesce in dilute solutions, started emitting efficiently in aggregates (**Figure 1b**).[5] In fact, similar observations had already been made in the past: as early as in 1852, Sir George Gabriel Stokes found that platinocyanides only became emissive in the solid state, their solutions look like mere water (**Figure 1-2**),[6] At the time, the limited knowledge of photophysics and the lack of appropriate spectrometric tools and techniques discouraged further research about this uncommon phenomenon. BenZhong Tang proposed a rationale theory for explaining this phenomenon, which was coined as the aggregation-induced emission (AIE) model. Since then, AIE has become an increasingly important topic in chromophore science.

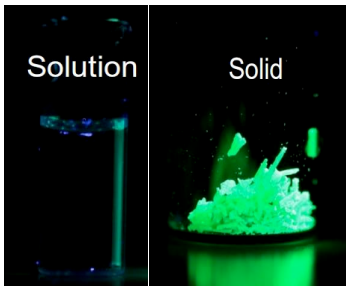

Figure 1-2. the luminescent picture of platinocyanide in solution and solid state. Pictures taken from reference 6

1.2 AIEgen working mechanisms

Understanding the mechanism of AIE phenomenon helps researcher know about compounds detailed photophysical processes which play an important role in the design and synthesis of new high-efficiency AIEgens materials. Therefore, exploring its working mechanism has become a very important topic in the last decade.

Jablonski Diagram, which was introduced in 1933, helped achieving molecular level understanding of luminescence phenomenon and rationalizing the fate of a molecule's excited state following light-irradiation, resulting from the interplay of various radiative (fluorescence, delayed fluorescence and phosphorescence) and non-radiative (internal conversion, intersystem crossing, vibrational relaxation) processes (**Figure 1-3**).[7]

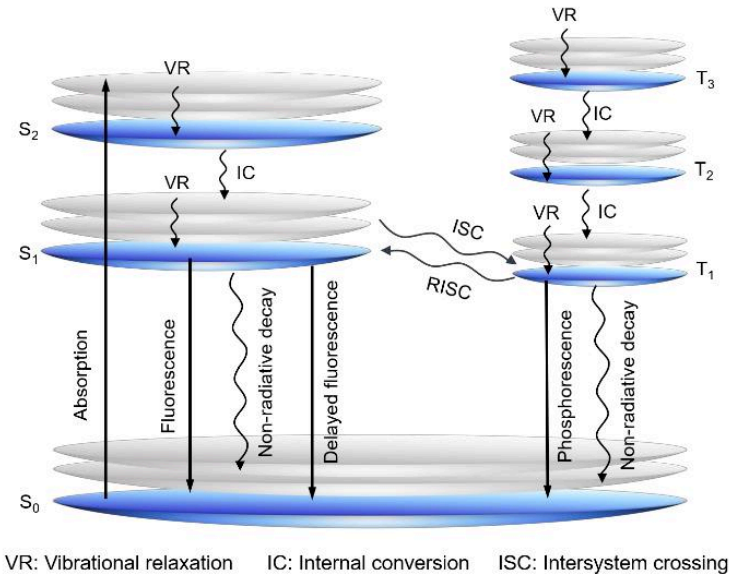

Figure 1-3. Jablonski Diagram.

Grounding on this model, Tang's group has proposed a mature theory about AIE mechanism — restriction of intramolecular rotation (RIR) (**Figure 1-4a**) and restriction of intramolecular vibration (RIV) (**Figure 1-4b**): both RIR and RIV can be summed-up into a more generic

term named restriction of intramolecular motion (RIM) (**Figure 1-4**). According to this model, in solution or in the mono-dispersed state, intramolecular motions including rotations and vibrations boost the non-radiative decay channels ultimately resulting in complete quenching of the emission (sometimes qualified as a "dark state"). In the aggregated state, the restriction of intramolecular motion responsible for non-radiative decay channels are blocked, bringing about the enhanced emission. For example, TPE is an archetypical group with AIE properties (**Figure 1-4a**). Four benzene rings are connected to the vinyl group through a single bond : in dilute solution, the benzene ring freely rotates / vibrates around the single bond to dissipate excitation energy through non-radiative pathways, while in aggregated state its rotation is blocked providing a strong fluorescence.[8] Theoretically, any chemical modification resulting in restriction of intramolecular motion can potentially generate AIE. Therefore, based on this principles, scientists have developed various new AIEgens like we mentioned before.

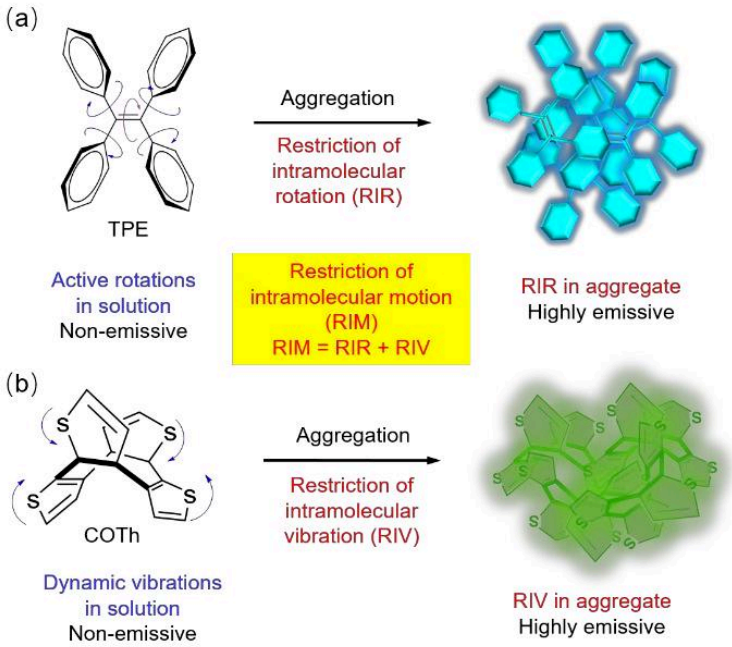

Figure 1-4. (a) Tetraphenylethene (TPE) becomes emissive when aggregated due to the restriction of intramolecular rotations (RIR). (b) Cyclooctatetrathiophene (COTh) shows AIE activity due to the restriction of intramolecular vibration (RIV) in the aggregated state. Pictures taken from reference 7.

1.3 AIEgen systems

Nowadays researchers have developed numerous AIE-compounds. Depending on their molecular structural features, they can be divided into the following categories:

1.3.1 Pure hydrocarbon based AIEgens

AIE compounds only containing hydrocarbon system have played an important role in initial research works aiming at refining mechanistic understanding of the AIE phenomenon. Tetraphenylethylene (TPE) have been the most widely studied model for mechanistic research and have served as the core for construction of many new AIEgens. Also there are other hydrocarbon AIEgens comprise notably 9,10-Distyrylanthracene[9] and 1,4-di[(E)-2-phenyl-1-propenyl]benzene derivatives[10].

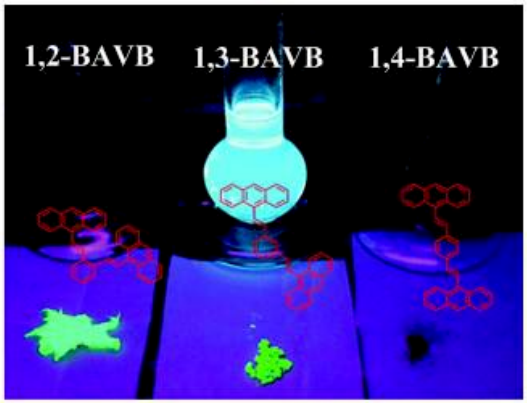

Figure 1-5. Fluorescence image of the solutions and solid of compounds 1,2-BAVB, 1,3-BAVB and 1,4-BAVB. Picture taken from reference 11

For example, Li's group synthesized three anthracene derivatives 1,2-BAVB, 1,3-BAVB and 1,4-BAVB by combining two anthracenyl groups anchored onto different position of the benzene ring[11]. In ethanol solution, 1,2 and 1,4-BAVB hardly emit light (fluorescence quantum yield ca 0.1%) and only 1,3-BAVB shows strong fluorescence. After adding water into system, the compound aggregated and precipitated. In that case, only the fluorescence of

1,2-BAVB powder was enhanced, and the fluorescence quantum yield reached 12% (**Figure 1-5**), underlying the crucial importance of molecular isomerisms and spatial arrangements on the properties of a given AIEgen.

1.3.2 Heteroatom-containing AIEgens

Pure hydrocarbons have simple structure and are easy to synthesize, but these compounds usually emit blue fluorescence, which cannot fulfill the requirements of a majority of practical applications. Changing the molecular structure and increasing molecular conjugation degree can make the compound emit red fluorescence, however, planar configuration is prone to form π-π stacking, resulting most often in the ACQ phenomenon. The introduction of heteroatoms such as oxygen, nitrogen, and sulfur into the molecule can be used to tune the molecular electron distribution owing to the heteroatom electronegativity, causing strong intramolecular charge transfer (ICT) polarized state with far red emission in polar solvents. Based on this theory, a large number of heteroatom-containing AIEgens have been synthesized.

Taking advantage of the excellent electron withdrawing properties of isophorone, Zhou's group introduced aromatic heterocycles and aza crown ether groups to construct a series of new isophorone derivatives with large Stokes shifts (> 140 nm). Among them, some compounds showed good AIE properties (**Figure 1-6**).[12a] while others, although closely related, experienced more classical ACQ. A similar approach had previously been used in our group, with similar outcome.[12b]

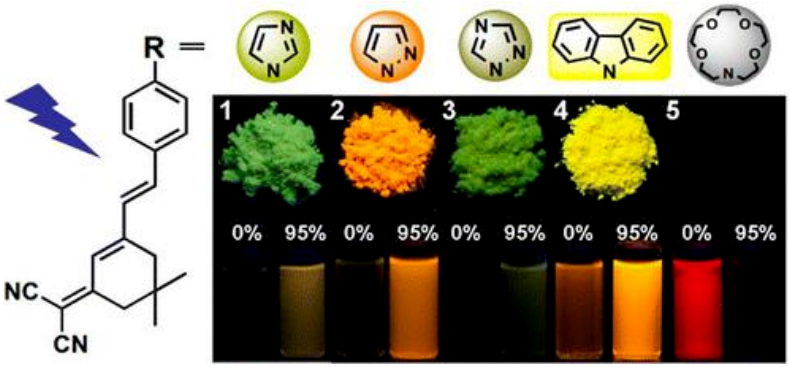

Figure 1-6. Fluorescent images of **8**-**12** in ethanol, ethanol/water and in the form of powder. Picture taken from reference 12.

Xiang's group using salicylaldehyde and 1,2-diamine to prepare two small organic compounds. Among them, SB2 displays AIE properities.[13] Crystal structure results showed that all atoms of SB2 molecule are almost located in one plane of π-conjugated system of SB2. In dilute solution of MeCN, there are still N-N single bond intramolecular rotations (IRs) which results in a quenched fluorescence; in aggregates, the short interplanar distance results in tight packing of the molecules which eliminates the N-N single bond IRs and triggres the AIE phenomenon (**Figure 1-7**).

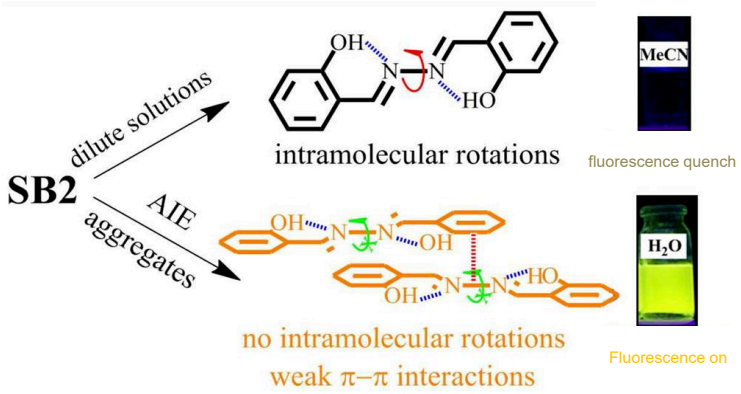

Figure 1-7. Structures and fluorescence images of the solutions and solids of compounds. Picture taken from reference 13.

1.3.3 Macromolecular AIEgens

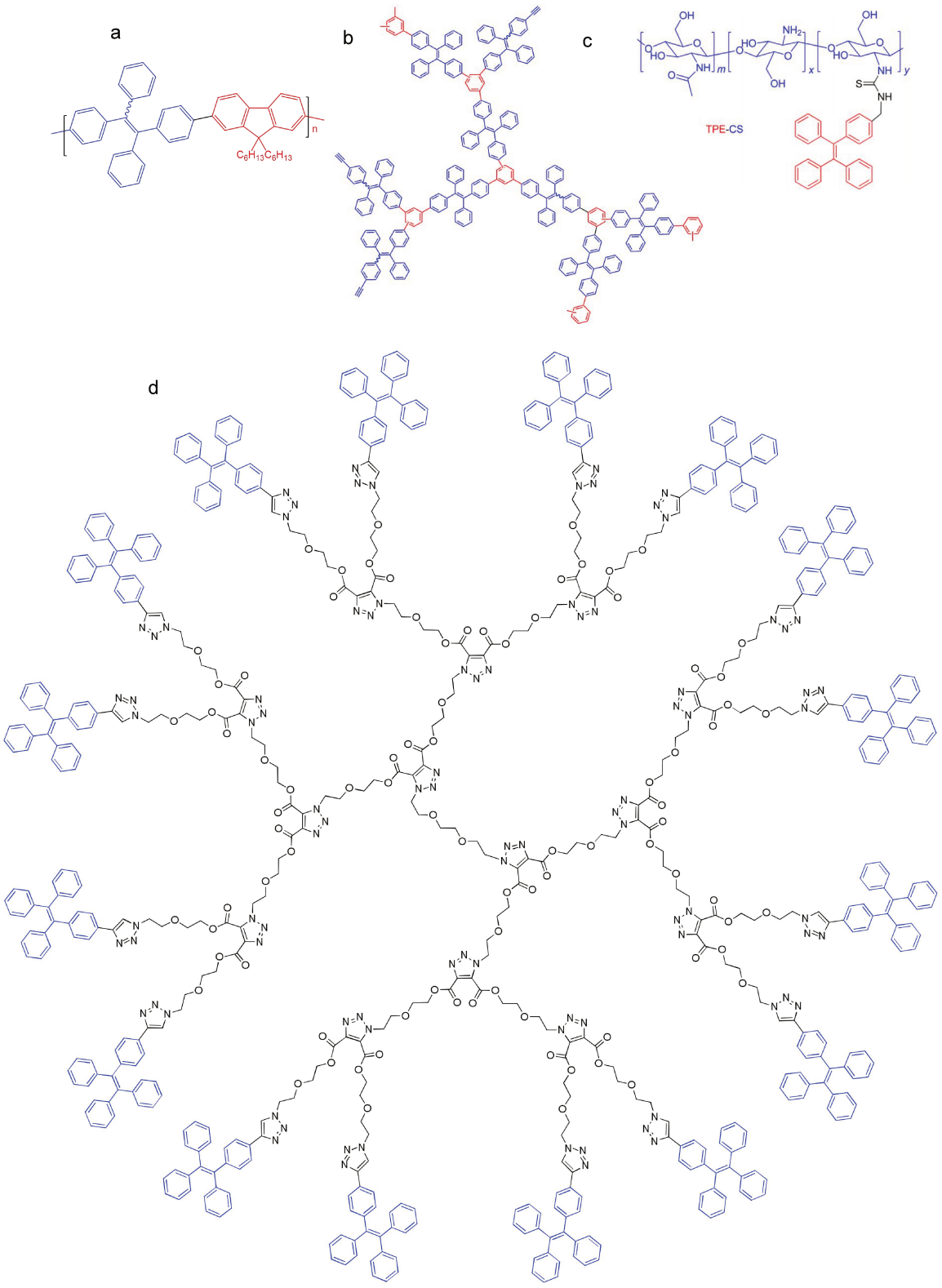

Figure 1-8. Chemical structures of representative AIE-active polymers.

Since 2001, the AIE phenomenon has rapidly developed and led to the conception of a large diversity of small molecular AIEgens. Yet, considerable progress has also been achieved

regarding the exploration of macromolecular AIE systems. Compared with traditional small molecule system, macromolecular AIE materials create optimal conditions for their self-assembly (reduced solubility in organic solvents and long distance organizations) and ultimately for the preparation of efficient light-emitting devices.[14] Schematically, there are mainly four kinds of macromolecular AIEgens:

— main-chain polymers[15] (**Figure 1-8a**);

— hyperbranched polymers[16] (**Figure 1-8b**);

— side-chain polymers[17] (**Figure 1-8c**);

— dendrimer systems[18] (**Figure 1-8d**).

1.3.4 Metal-complex AIEgens

Metal complexes have found practical uses in stoichiometric and catalytic processes as well as optoelectronics. However, just like in organic system, ACQ phenomenon remains an issue. Fortunately, taking advantage of the principle used in the conception of organic AIEgens, researcher have developed some metal complexes which show AIE properties.[19-20]

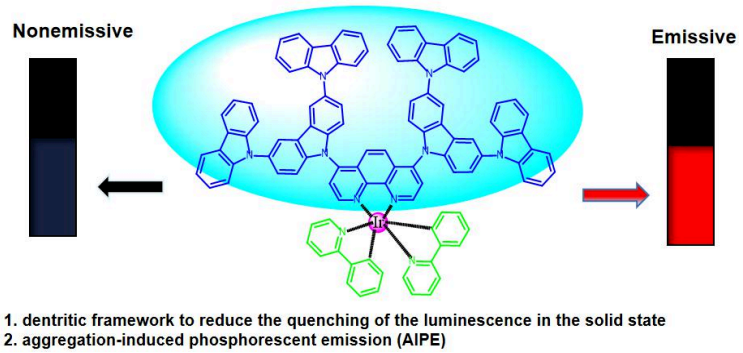

Figure 1-9. Molecular structure of Iridium (Ⅲ) complex with AIPE property. Picture taken from reference 21

Phosphorescent Ir complexes present many advantages compared to organic molecules or first period transition metal complexes, such as high phosphorescence quantum yield, longer phosphorescent lifetime, large pseudo Stokes-shifts and easily adjustable emission wavelengths. They have therefore been widely used as emitters in OLEDs devices, or as phosphorescent contrast agents in photoluminescence bio-imaging, or chemical sensors. Su *et al.* synthesized a carbazole group-substituted phenylpyridine Ir complex,[21] which hardly emits light in acetonitrile solvent (phosphorescence quantum yield *ca* 0.1%) ; after adding water, the phosphorescence is significantly enhanced, as a result of aggregation-induced phosphorescence emission (AIPE) (**Figure 1-9**).

1.4 AIEgens applications

As a result of the unique and excellent photophysical properties of AIE compounds, more and more researchers have focused on this field, and the prospect of AIE materials gradually emerged. To date, AIE materials display a wide range of potential applications in the fields of stimuli responsive materials, biological detection, DNA imaging, protein detection, cell membrane imaging, mitochondrial imaging, bacterial imaging, tissue imaging, photodynamic therapy, ion detection, explosive detection, fingerprint recognition, light emitting diodes, optical waveguides, circular polarized light, liquid crystal and other fields.[22-30] Representative examples are listed in the following section:

1.4.1 Organic light emitting diode (OLED)

An organic light-emitting diode is a solid-state device that can convert electrical energy into light. Its light-emitting layer requires organic substances that display light emission in

their solid or aggregated state, and stable chemical properties. Compared with traditional ACQ compounds, AIE materials have received extensive research attention and obviously appear more suitable for the preparation of OLED devices.

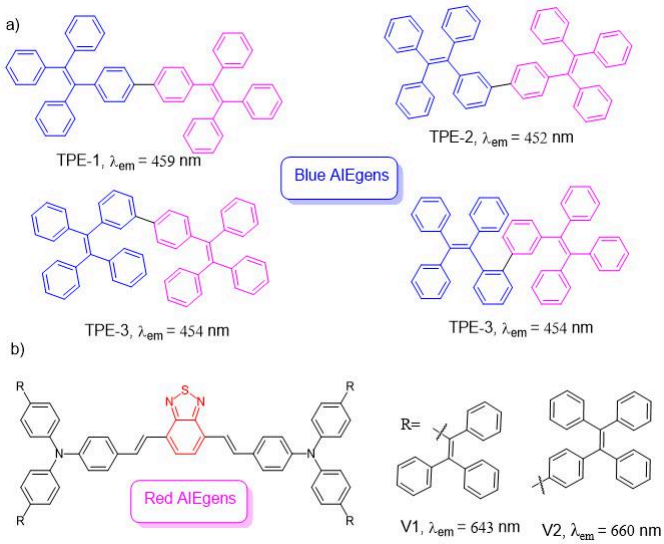

Figure 1-10. AIEgens in OLED devices: (a) Blue AIEgens; (b) Red AIEgen.Picture taken from reference 31, 32.

For example, Li's group and others simply connected two TPE units to obtain a series of blue light emitting AIE compounds (shown in **Figure 1-10a**). These AIEgens which show rigidity, excellent thermal stability and good chemical stability, can be used to prepare OLED devices. The emission wavelengths of the undoped devices prepared by the researchers are located at 435-459 nm, resulting in deep blue light emitting materials.[31] Chi' teams also prepared two AIE compounds (V1 and V2) incorporating a central heteroaromatic benzothiadiazole group (shown in **Figure 1-10b**). The emission wavelengths of OLED devices based on these two compounds were 643 nm and 660 nm, respectively, and red light emission was thus achieved. More importantly, the maximum brightness of undoped devices based on compound V2 can reach 13535 cd-m^{-2} which compares very favourably to the best light emitting systems.[32] Through the efforts of scientists, at present, OLED devices based on

AIE compounds have basically realized full-color light emission, and are constantly moving towards the direction of high efficiency and low energy consumption.

1.4.2 Stimuli response

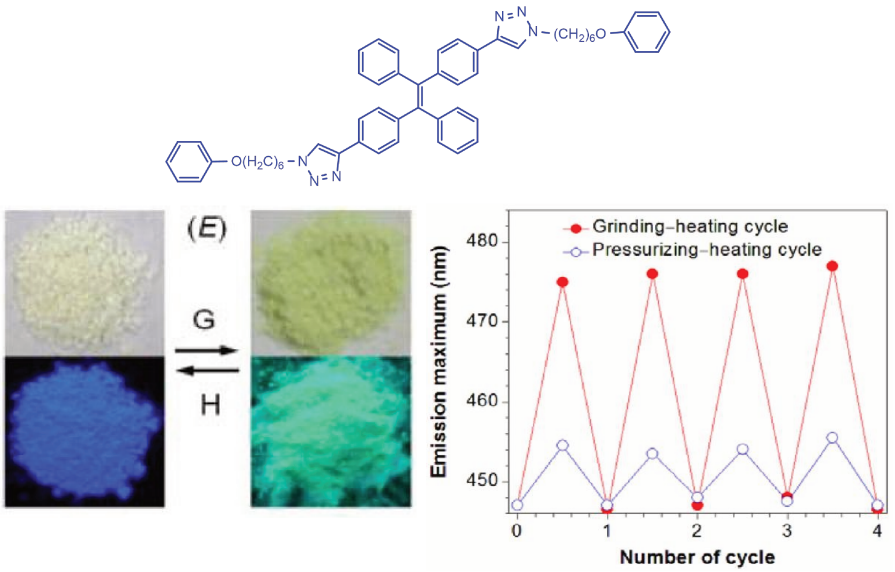

Figure 1-11. The mechanochromic effect (left) and reversible switching of emission of (E)-BPHTATPE by repeated grinding−heating (red line) or pressurization−heating (blue line) cycle (right). Pictures taken from reference 33.

A stimulus-responsive material is a "smart" material that can change its physical or chemical properties under external stimuli. Among those, chromotropic material can be stimulated by external force, and photoluminescence performance of the compound can be affected by changing the stacking form. Qin's group prepared a TPE derivative (*E*)-BPHTATPE with AIE properties, which fluorescence quantum efficiency is close to 100%. After grinding (*E*)-BPHTATPE crystals, the fluorescence emission peak was red-shifted from 447 nm to 477 nm, demonstrating obvious mechanoluminescence properties; The effect is attributed to a modification of molecular packing upon scratching from a crystalline to an amorphous form. After 4 cycles of reversible switching of emission by repeated

grinding-heating (red line) or pressurization-heating (blue line), they still display the same emission behavior.[33]

1.4.3 Circularly polarized luminescence (CPL)

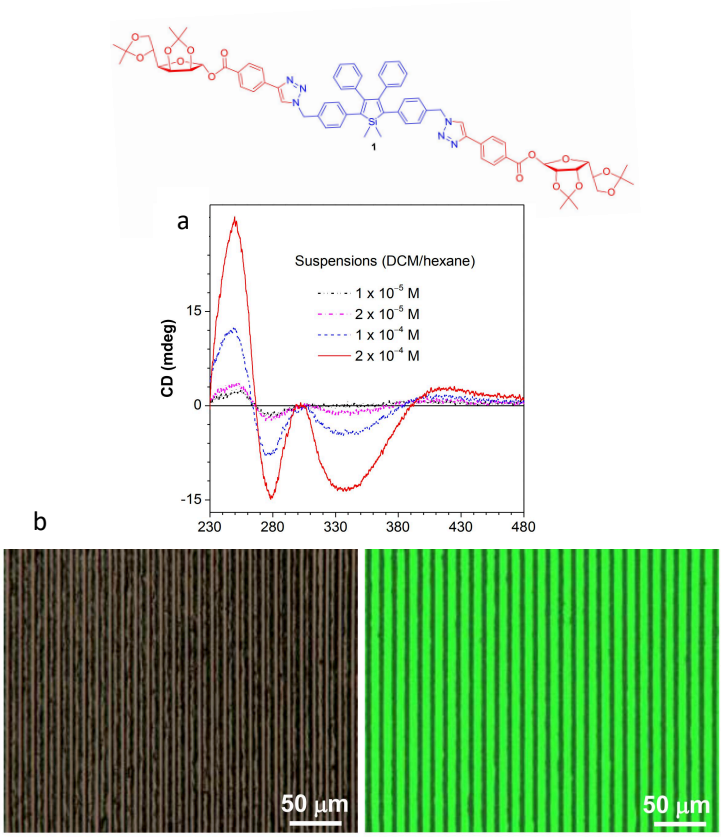

Figure 1-12. (a) CD spectra of compound 1; (b) Fluorescence microscope images under sunlight (left) and UV lamp (right) of compound 1 in microfluidic channels on quartz substrates. Pictures taken from reference 34.

In order to maintain good CPL properties at the device scale, chiral molecules need to avoid fluorescence quenching caused by molecular aggregation. Therefore, introducing chiral groups into AIE materials is an effective means to construct efficient CPL material molecules. As shown in **Figure 1-12**, based on the classic dimethyl tetraphenyl thiazole, chiral sugar units are attached to both ends of the benzene ring, yielding compound 1.[34] It does not display significant fluorescence and circular dichroism (CD) signals in dilute solutions, yet

when the molecules aggregate, it exhibits aggregation-induced CD and CPL properties. The reason for this phenomenon is the tendency of molecules to self-assemble to form right-handed helical nanostructures when aggregated, which translates into right-handed CPL properties of the assembly. The |glum| of the CPL of compound 1 in aggregated state is in the range of 0.08 — 0.32, which is two orders of magnitude higher than most common chiral organic small molecule luminescent materials. It provides a new basis for the construction of CPL organic small molecules with high fluorescence quantum yield and high asymmetry factor.

1.4.4 Ion detection

The detection of trivalent metal cations has fundamental importance for biology and environmental importance. For example, Cr^{3+} is an essential trace element for the human body, but excessive Cr^{3+} will lead to disorders of glucose and lipid metabolism and induce diabetes and cardiovascular diseases. In addition, Al^{3+} is also one of the most common trivalent metal ions. It is suspected to play a role in the aetiology or pathogenesis of Alzheimer's disease[35a]. Similarly, Fe^{3+} is an important component of molecules that undergoe redox reactions or transport oxygen [35b].

Based on this background, Sun and his collaborators prepared a pyridine-containing tetraphenylethylene derivative Py-TPE as a specific probe for such trivalent metal cations.[35c] This low emissive compound turns into a bright red emitter upon protonation of the pyridine moieties: complexation of water molecules to Cr^{3+}, Al^{3+} and Fe^{3+} (M) form $M(OH)_3$ complexes which results in the release of large amount of protons (3 per metal ion), then promoting the protonation and red light emission of Py-TP. As a result, the latter can be used

to detect and distinguish the above three ions specifically from other metal cations as shown in **Figure 1-13**.

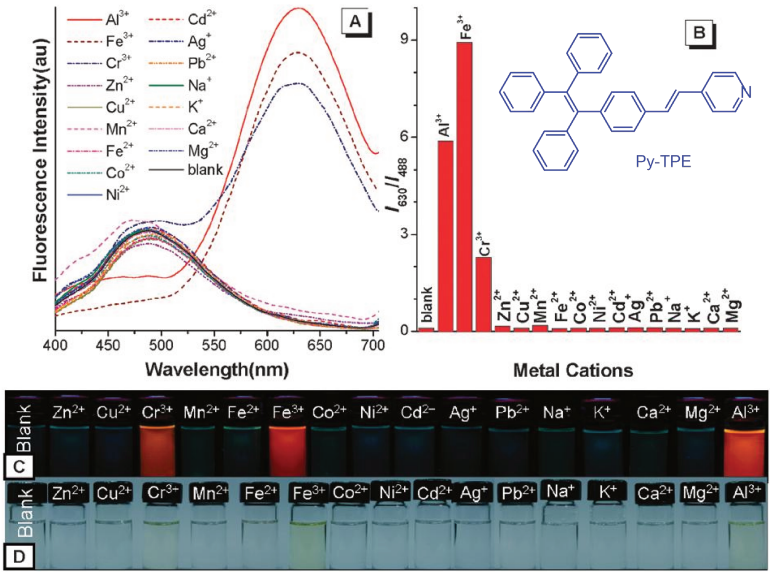

Figure 1-13. (A) Fluorescence spectra of detecting different ions; (B) Diagram of I_{630}/I_{488}; (C) Images of Py-TPE in different ions. Pictures taken from reference 35.

1.4.5 Biological applications

1) Tissue imaging

The team of Liu applied AIE molecules to near-infrared biological tissue imaging technology. In general, the absorption of biological substrates is negligible in the near-infrared region (700-1000 nm), and near-infrared light can therefore more efficiently penetrate deep tissues, with minimal interference and phototoxicity. Therefore, AIE molecules for *in vivo* imaging should ideally combine efficient red or NIR fluorescence with NIR excitation. Here, the researchers prepared a molecule containing TPE and benzothiadiazole (BTPEBT),[36] which can be excited by near-infrared light and emit green fluorescence in the aggregated state. Upon assembly with DSPE-PEG2000, the compound precipitates into light-emitting nanoparticles with AIE properties: diameter is about 33 nm and the molecule was used to

image the brain, spinal cord and subcutaneous vascular tissues of mice as shown in **Figure 1-14**.

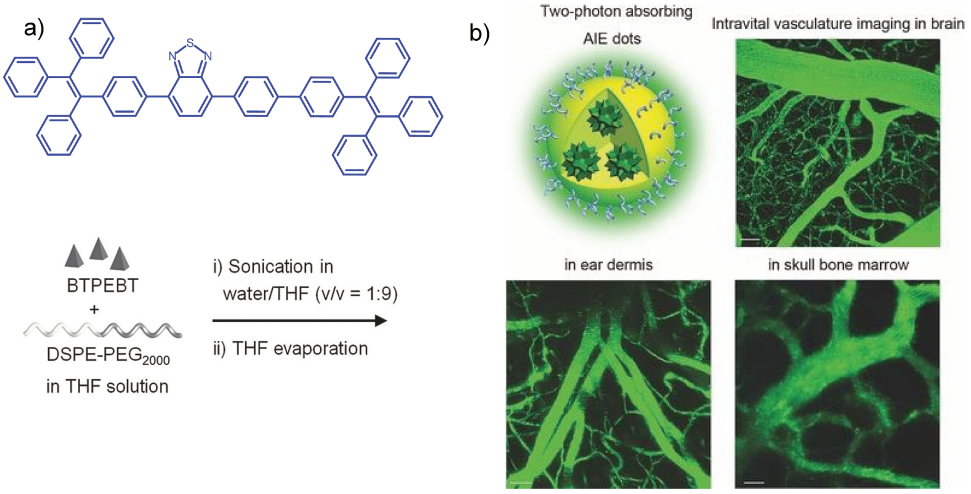

Figure 1-14. (a) The chemical structure of BTPEBT and preparation of quantum dots; (b) Mouse tissue imaging: in brain, in skull bone marrow; in ear dermis. Pictures taken from reference 36.

2) Cell membrane imaging

Apart from the basic function of the cell barrier, the plasma membrane (PM) plays an important role in many cell behaviors, such as cell spreading, cell migration, cell trafficking etc. Additionally, abnormality of PM is an important biomarker for cell status and many diseases. Therefore, visualization of PM is important in early medical diagnosis and basic research in biology. Professor Jong has designed a fluorescent probe featuring characteristics of aggregation-induced luminescence for rapid and sensitive imaging of cell membranes in vivo.[37] The probe based on an extended purine core, combines a hydrophobic alkyl chain and a positively charged quaternary ammonium salt, which helps maintaining a good solubility in water while displaying no luminescence characteristics; once embedded into the cell membrane through hydrophobic interaction and electrostatic interaction, restriction of molecular motions by the phospholipid bilayer activates the RIR process, resulting in bright

fluorescence upon photoexcitation (**Figure 1-15**).

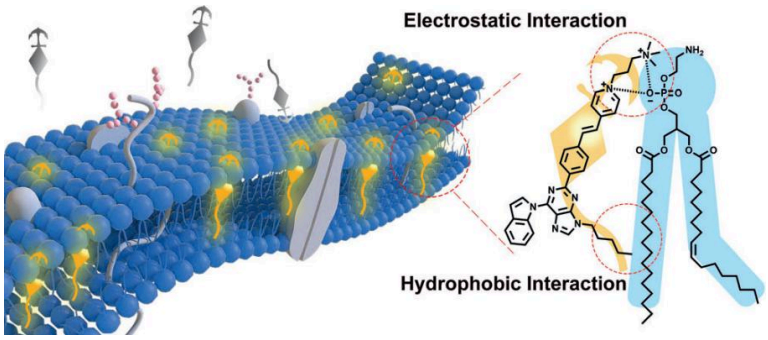

Figure 1-15. Schematic of probes and plasma membrane (left). A single probe and phospholipid molecule to illustrate of the proposed labeling strategy (right). Pictures taken from reference 37.

3) Cellular organelle imaging

Organelles in eukaryotic cells such as lysosomes, mitochondria, lipid droplets, nucleus, and endoplasmic reticulum play crucial roles in cellular function and activities. It's important to visualize and monitor the organelles to provide valuable information for diagnosis and medical intervention and study in details the cell machinery. AIE light-up molecular probes display great potential for organelle imaging. By conjugating AIEgens with functional units that can target cellular organelles through physical interactions (for instance cationic moieties such as pyridinium or phosphonium derivatives, hydrogen bond acceptors like morpholine), lots of AIE molecular probes have been developed for mitochondria,[38-44] lysosome,[45-47] lipid droplets,[48-50] and nucleus[51-53] imaging. For example, a series of AIEgens based on positively charged pyridinium and quinolinium moieties with different donor–acceptor (D-A) strength were developed by Zheng and his co-workers (**Figure 1-16A**).[54] Among those, DCQu not only can selectively target cancer cells over normal cells but also specifically stains mitochondria with good photostability (**Figure 1-16B**, **B1** and **1-16C**).

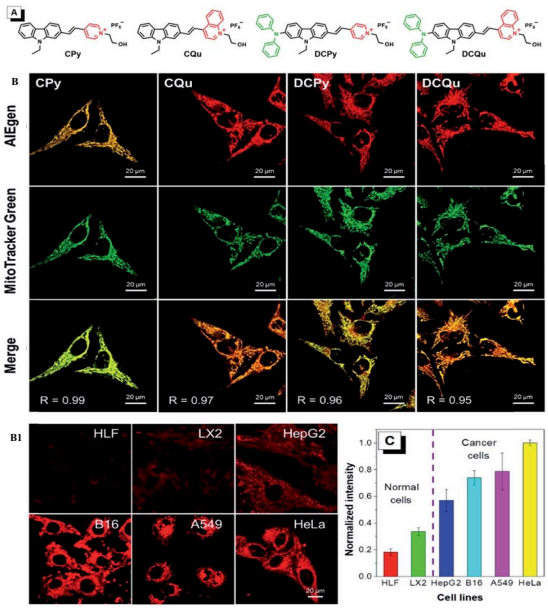

Figure 1-16. (A) Molecular structures of AIEgens; (B) Co-localization images of HeLa cells; (B1) Images of normal cells (HLF and LX2) and cancer cells (HepG2, B16, A549 and HeLa) stained with DCQu; (C) Fluorescence intensity of different cells incubated with DCQu. Pictures taken from reference 54.

4) Bacteria imaging and Photodynamic therapy

Bacterial infection has become a worldwide public health issue, especially in clinical practice. In recent years, photodynamic antimicrobial therapy and bacterial imaging using AIE materials has become a potential opportunity to tackle this problem. One of the initial examples of AIE light-up molecular probes for bacterial imaging was reported by Tang *et al.* through decorating tetraphenylethene (TPE) with two boronic acids to yield a blue-emitting probe.[55] Recently they further constructed fourteen AIE probes based on TPE derivatives with one cationic ammonium group and different hydrophobic groups to fine-tune their hydrophobic and electrostatic interactions with bacteria, which provided a more comprehensive understanding of the mechanism and amplified the differences in fluorescent response of bacteria (**Figure 1-17a**).[56] After incubating the probes with seven different bacterias, each probe can generate unique fluorescence pattern that can be used for bacterial

discrimination (**Figure 1-17b**). This platform realizes the identification of bacteria type with nearly 100% accuracy and rapid detection time (< 0.5 h) in a complex environment containing mixture of different bacteria. This approach has greatly boosted the potential clinical application of AIE molecular probe for rapid bacterial imaging and identification.

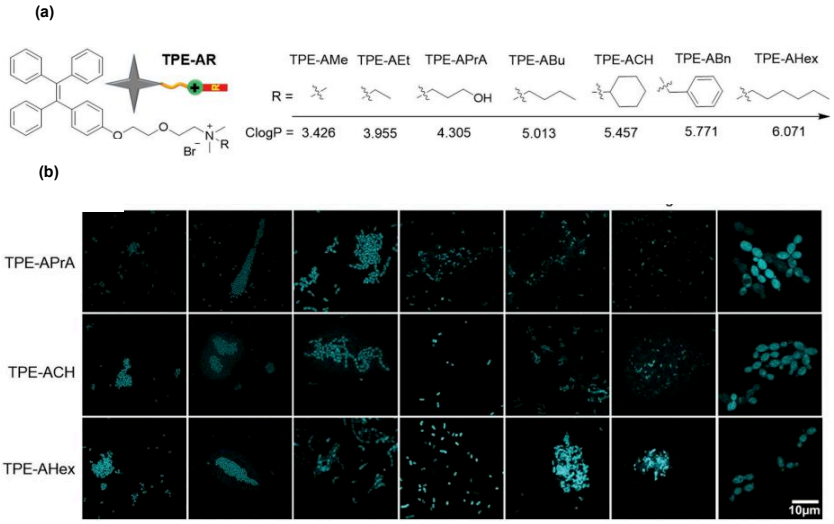

Figure 1-17. (a) Structure of TPE-ARs. (b) CLSM images of seven pathogens after incubation of TPE-APrA, TPE-ACH, and TPE-AHex for 15 min. Pictures taken from reference 56.

In order to improve therapeutic effect of tumors, various treatment methods such as chemotherapy, radiation therapy and photodynamic therapy are used daily in clinical research. Photodynamic therapy is a very promising approach using photosensitization of molecular oxygen (to generate singlet oxygen) by energy transfer from a photoactive compound, but it is likely to produce tumor drug resistance and has low therapeutic effect on hypoxic tumors and deep tumors. In view of these limitations, the team of Liu recently designed and prepared a multifunctional modified molecular drug based on AIEgens and cisplatin (**Figure 1-18**).[57] The drug can not only selectively target tumor cells, but also has the same curative effect as cisplatin. More importantly, the combined effect of the drug and photodynamic therapy is higher than that of cisplatin. The mechanism at the origin of singlet oxygen production, often

observed with TPE derivatives in their aggregated state, is not well understood yet.

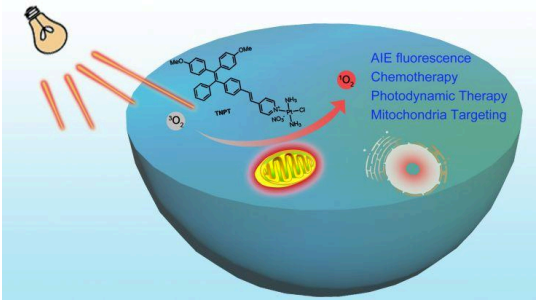

Figure 1-18. A schematic diagram of theranostic agent (TNPT). Pictures taken from reference 57.

2 Fluorescent Probes for Analytes Detection

As briefly mentioned in the first part of this chapter, the high sensitivity of fluorescence to environmental variations and the fact that luminescence signal can be observed even at very low concentrations of the probe and analyte makes it particularly well suited for the detection of chemical traces especially in aqueous or physiological environment.

Chemical fluorescent probe detect analytes mainly depending on fluorescence signal's change (enhancement, decrease or emission wavelength shift, *etc*.) that occurs upon probe/analyte interaction. It has the advantages of low cost, simple operation, low detection limit, high sensitivity and selectivity. Therefore, chemical fluorescence probe has played an important role in detection, imaging and diagnosis and many other fields related to environment security and defense.[58-60]

2.1 Components of a fluorescent probe for analyte detection

Fluorescent probes used in the detection of chemicals usually consist of three parts: receptor, fluorophore and spacer (**Figure 1-19**). The receptor group determines the selectivity and specificity. If the interactions between the receptor and analyte is noncovalent, the probe

is referred to as a chemosensor. If the binding interaction between the receptor and analyte results in chemical reaction, the indicator is described as a chemodosimeter.[61] The fluorophore group determines the sensitivity of recognition, and the linking part plays a molecular recognition hub role and will also influence the extent of interaction between the fluorophore end receptor, thus possibly the nature and intensity of the response.

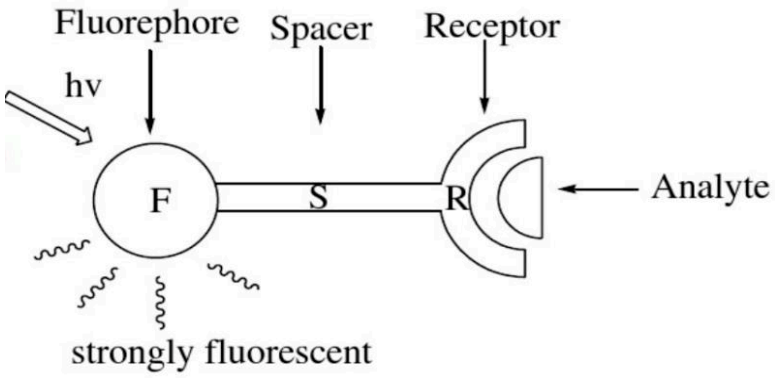

Figure 1-19. Schematic diagram of chemical fluorescence probe recognition analyte.[62]

2.2 Response mechanisms to analyte detection

So far, the response mechanisms of chemical fluorescent probes mainly involve such processes as photoinduced electron transfer (PET), perturbation of intramolecular charge transfer (ICT), fluorescence resonance energy transfer (FRET), formation of excimer, aggregation-induced luminescence, C = N isomerization, although this list is non-exhaustive

2.2.1 Photo-induced electron transfer (PET)

Since Roger Y. Tsien[63] for the first time designed Ca^{2+} fluorescent probe based on PET mechanism, it has gradually become the most common recognition mechanism. In most PET probes, before guest molecule binds to the receptor unit, an intramolecular electron transfer between the receptor and fluorophore results in fluorescence quenching. Depending on the

relative energy levels of the frontiers orbitals of the fluorophore and receptor, the former can either behave as an excited state electron donor (oxydative PET, as in **Figure 1-20**) or acceptor (reductive PET, as in **Figure 1-21**). Once the guest molecule is combined with recognition group, the photo-induced electron transfer will be inhibited or blocked, thus restoring fluorescence (**Figure 1-20a**). This process can be better understood in the figure below (**Figure 1-20b**).[64-65]

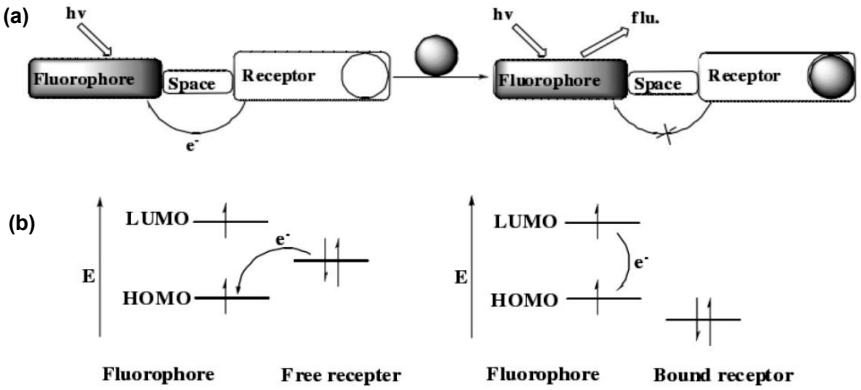

Figure 1-20. (a). Schematic diagram of the reductive PET mechanism in a chemosensor; (b). Frontier orbital energy diagram of the reductive PET mechanism. Pictures taken from reference 62.

Lin and his co-workers[66] select dinitrophenyl ether coumarin as fluorophore and 2,4-dinitrobenzenesulfonyl group as receptor to design H_2S probe in **Figure 1-21**. Here PET process is reversed compared to above, as the 2,4-dinitrobenzenesulfonyl units can accept the electrons of coumarin and restrain the blue fluorescence of CMDN *via* the oxydative PET mechanism. When reacting with H_2S, leading to the separation of the sulfonic and hydroxyl group, the fluorescence of the probe CMDN is enhanced because of the suppression of the PET process.

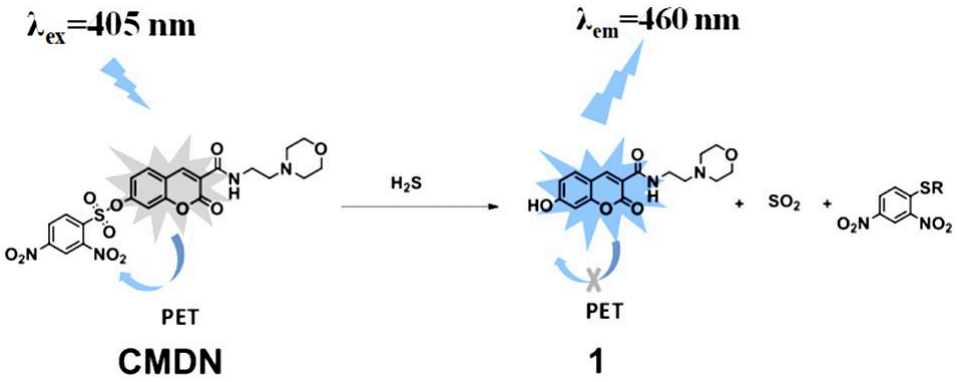

Figure 1-21. The chemical structures of the probe CMDN and compound 1 as well as the proposed sensing mechanism for the detection of H_2S through a chemodensimetric oxydative PET mechanism. Pictures taken from reference 66.

2.2.2 Intramolecular charge transfer (ICT)

Fluorescent probe relying on ICT mechanism usually connect a strong electron withdrawing group (Acceptor) and electron donor group (Donor) via a π-conjugated bridge to form a D-A system. When the probe is excited, ICT process occurs through delocalization of the electron density from the donor to the acceptor, and the maximum emission wavelength will be red-shifted or blue-shifted. In general, if the recognition group is an electron-donating group, the combination with analyte will reduce donor's electron-donating ability, electron delocalization at the excited state will decrease, and the emission spectrum will be blue-shifted; in the case where interaction of the analyte takes place with the electron acceptor, its electron withdrawing character will be reinforced and emission will be red-shifted.

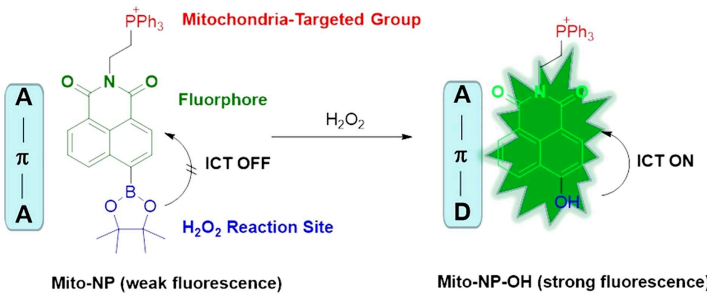

Figure 1-22. The structure and fluorescence response mechanism of the mitochondria-targetable H_2O_2 probe Mito-NP. Pictures taken from reference 67.

Liang[67] *et al.*, reported the synthesis and biological application of the chemodosimetric fluorescent probe Mito-NP for the detection of mitochondrial H_2O_2. In this work, a triphenylphosphonium (TPP) moiety acts as a mitochondria-targeted carrier, 1,8-naphthalimide as the fluorophore provides a suitable fluorescent platform, and a protected boronate group was used as the reaction site because of its good selectivity and sensitivity toward H_2O_2. Moreover, the boronate group could be removed by H_2O_2 to produce the hydroxyl product and generate an electron donor-electron acceptor dipolar conformation (D–π–A). It exhibited a large turn-on fluorescence signal and increased Stokes shift (93 nm) owing to the ICT process (**Figure 1-22**).

2.2.3 Fluorescence resonance energy transfer (FRET)

Different from the first two types of fluorescent probes, fluorescence resonance energy transfer process means that when a pair of suitable energy donor molecules and acceptor molecules are separated by a certain distance which is shorter than the so called Forster Radius (R0), with a relative orientation (non-orthogonal) enabling coupling of their respective transition dipole moment and emission spectrum of the donor and absorption spectrum of the acceptor effectively overlap, the donor in excited state will transfer part or all energy to the receptor which will be excited (**Figure 1-23**). The receptor can be a fluorescent substance or a quencher that only absorbs but does not emit (“black hole”).

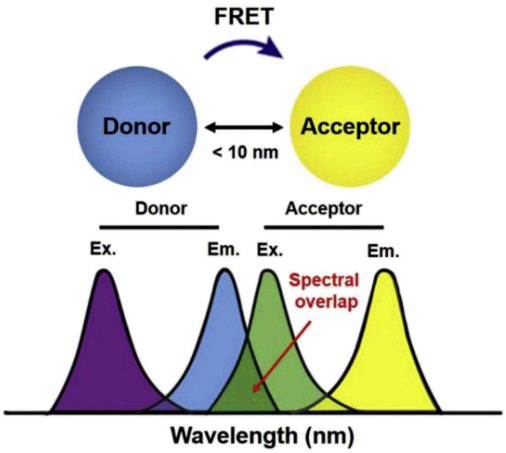

Figure 1-23. Schematic illustration of FRET. Pictures taken from reference 68

Inspired by bioinorganic TPA model compounds that exhibit Cu(I)-dependent oxidative cleavage chemistry[69a-69b], Chung *et al.*,[70] design FCP-1 which connects a fluorescein FRET donor and rhodamine FRET acceptor with copper-responsive TPA linker. Changes in labile Cu(I) levels would modulate intramolecular FRET efficiency and lead to different fluorescence intensities of the donor and acceptor at two different wavelengths that can be self-calibrated in a ratiometric manner (**Figure 1-24**). Under lower Cu(I) levels, the probe stays intact and displays large FRET and rhodamine-dominant emission regardless of the excitation wavelength. With higher Cu(I) levels copper-dependent oxidative cleavage of the TPA linker occurs and lowers FRET and therefore fluorescein-dominant emission upon exciting the absorption band of the latter are then obtained.

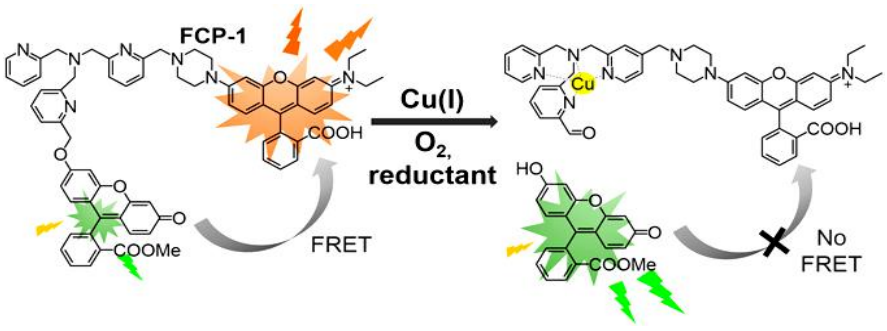

Figure 1-24. Design of FRET copper probe FCP-1. Pictures taken from reference 70.

2.2.4 Formation of excimers

The mechanism uses two identical fluorophores (usually it is polycyclic aromatic hydrocarbons such as naphthalene, anthracene, pyrene) which should have suitable distance (around 35 nm) to connect with recognition group for constructing a fluorescent probe. Excitation of the compound leads to the formation of an intramolecular excimer, a dimeric fluorophore pair which is only stable at the excited state. Generally, when excimer structure of the probe is formed, its original monomer fluorescence emission gradually weakens and disappears, and at the same time it will show a strong and broad excimer emission peaks at a longer wavelength, with no fine vibration structure.

Based on their previous results, Kriangsak[71] *et al.,* developed a new excimer sensor BPTG (**Figure 1-25**). BPTG is a turn-on probe for lipopolysaccharide（LPS) detection and displays monomer and excimer emissions in aqueous solution with a detection limit at 5 nM. BPTG is highly selective for LPS over heparin and other anionic biological species. The unique molecular architecture of BPTG provides a better understanding for the rational design of fluorescence sensors.

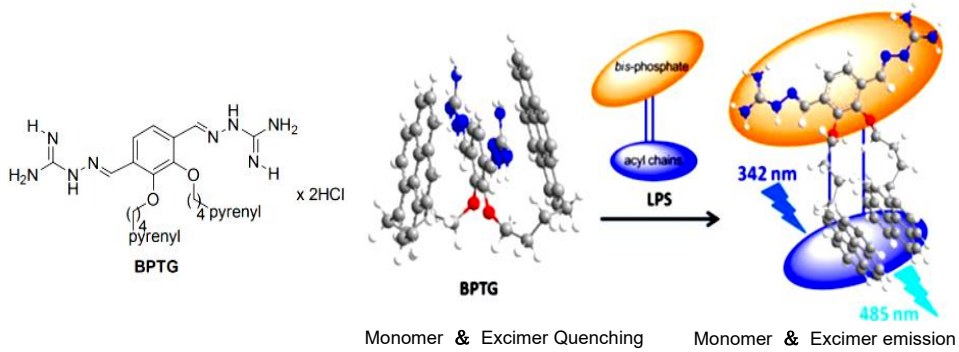

Figure 1-25. The chemical structures of the probe BPTG and the proposed sensing mechanism for detection of LPS. Pictures taken from reference 71.

2.2.5 C = N Isomerization

In 2007, Wang's group[72] first proposed the C = N isomerization based recognition mechanism. They connected the signaling group coumarin and the recognition group antipyrine derivative through C = N to construct a Zn^{2+} fluorescent probe 33. When no metal ions are added, the fluorescence is quenched due to the C = N isomerization dissipating excited state energy through non-radiative process.

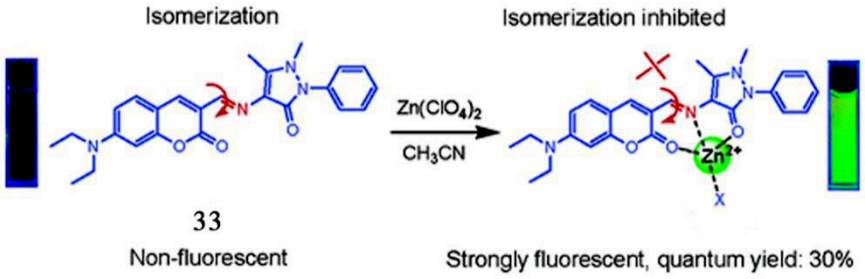

Figure 1-26. Recognition mechanism of 33. Pictures taken from reference 72.

After the addition of Zn^{2+}, the empty orbital of Zn^{2+} interacts with the lone pair electron provided by the O atom of the two carbonyl groups in the probe molecule and the N atom of the C = N. The C = N isomerization process is suppressed, so the fluorescence emission is enhanced (**Figure 1-26**).

Based on this mechanism, some research groups have successively designed a series of chemical fluorescent probes for other ions. For example, Zhou's group[73] based on the C = N isomerization mechanism designed fluorescent probe 34 which has a high selectivity for magnesium and no interference from calcium. Moreover, it can be utilized to detect magnesium ion in lysosome of living cells and as a magnesium ion indicator in living plant tissues (**Figure 1-27**).

This mechanism constitutes an interesting illustration of the use of similar concepts as the restriction of intramolecular motions (here restriction of isomerization around the C = N bound) as previously described in the conception of AIEgens in making of chemical responsive probes.

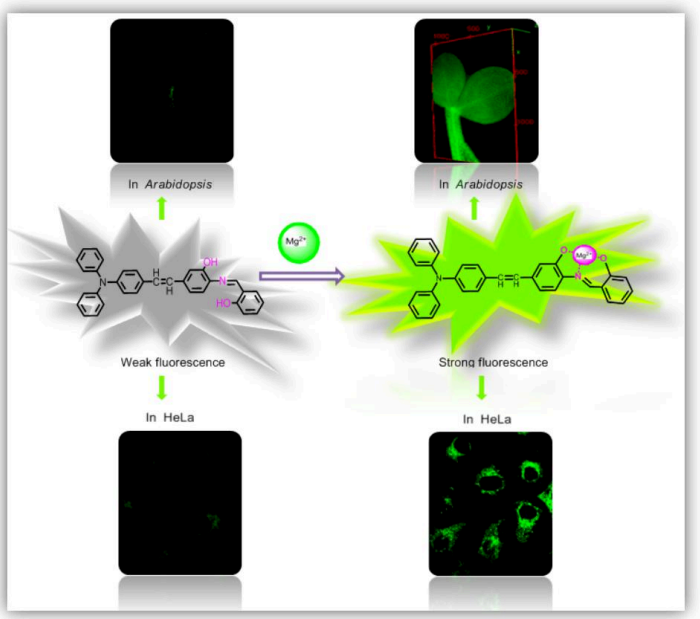

Figure 1-27. Schematic of probe detecting Mg^{2+} in HeLa cells and plant tissues. Picture taken from reference 73.

3 Two-photon Absorption (TPA)

3.1 Research background

Two-photon absorption is a third-order nonlinear optical phenomenon, related to the hyperpolarisability of the electron cloud which can be polarized depending on the intensity of the incident electromagnetic wave following the nonlinear equation (**1**).

$$P = P_0 + X^{(1)}E + (1/2)X^{(2)}E^2 + (1/6)X^{(3)}E^3 \quad (1)$$

where: P_0 is the polarization in the absence of a field (some materials, such as polyvinylene difluoride when poled, can have a finite bulk polarization in the absence of an applied field);

$X^{(1)}$ is the susceptibility of the material (which is related to the dielectric constant); $X^{(2)}$ and $X^{(3)}$ are the second- and third-order susceptibilities, respectively; E is the applied electric field.

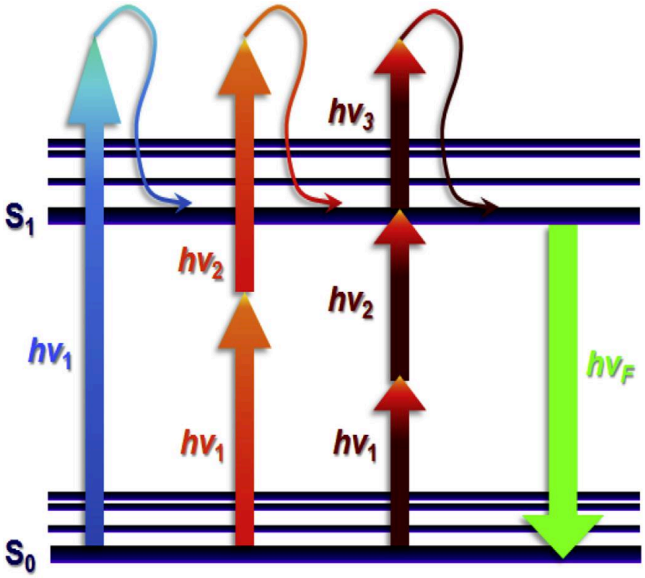

Figure 1-28. Energy diagram illustrating one-photon absorption (OPA, blue), two-photon absorption (TPA, orange), and fluorescence (green). Picture taken from reference 74.

Nonlinear absorption takes place exclusively in optical materials exposed to strong pulsed laser irradiations. In these conditions, incident light intensity exceeds a threshold value allowing molecules at their ground state to absorb two (or more) photons at the same time, as summarized in **Figure 1-28**.

As early as 1931, Maria Göppert-Mayer established the basis of quantum mechanical theory of two-photon absorption, long before adequate intense light sources became available for its experimental observation.[75a] It is only in the early 1960s when the laser appeared that W.Kasier and C.G.B.Garret experimentally characterized an upconverted emission of a CaF_2:Eu crystal consecutive of an electronic transition occurring at twice the incident laser frequency, which confirmed the existence of two-photon absorption phenomenon.[75b]

As a third-order nonlinear optical process, TPA intensity is proportional to the square of incident light intensity. The excitation energy of TPA being equal to half of the actual

absorption energy levels of the chromophore, it operates in a range of wavalength (usually between 700-1300 nm), where scattering is reduced and transparency of many materials (including living tissues) is high, making it a hotspot research in high-technology field where light transmission over long distances is requested.

3.2 Effective two-photon absorption cross section

The two-photon absorption cross section is a physical quantity used to describe the two-photon absorption capacity of a molecule. It is usually represented by the symbol σ and its unit is the Göppert-Mayer GM (1GM = 10^{-50} $cm^4 \cdot s \cdot photon^{-1}$) to commemorate one of the theory founders Maria Göppert-Mayer. According to Göppert-Mayer's theory, two-photon absorption cross section is proportional to the imaginary part of the third-order nonlinear coefficient (χ^3) [76]

$$\sigma = \frac{8\pi^2 h\nu^2}{n^2 c^2 \mathrm{N}} \mathrm{I_m}(\chi^3)$$

where σ represents the two-photon absorption cross section, I_m (χ^3) represents the imaginary part of third-order nonlinear coefficient, h is Planck constant, ν is the frequency of the incident light, n is the refractive index of the medium, and c is the speed of light. According to the consensus that has been established so far, two-photon absorption cross section is strongly related to intramolecular charge transfer (ICT)[77-78], that is the greater the degree of intramolecular charge transfer, the larger the two-photon absorption cross section. Therefore, it has become a common strategy to increase the intramolecular charge transfer by controlling polar molecules' electron donating and accepting abilities.

In the field of bioimaging, effective two-photon absorption cross-section is also known as two-photon brightness can be simply expressed as $\delta = \sigma \times \Phi$, where δ represents the effective two-photon absorption cross section of molecule, σ is the experimentally measured two-photon absorption cross section, and Φ is the experimentally measured two-photon fluorescence quantum yield (since the measurement technique of two-photon fluorescence quantum yield is technically challenging, it is usually approximated with single-photon fluorescence quantum yield, following Kasha's rule). Therefore, TPA materials used in biological field not only need to possess large two-photon absorption cross-section, they also require a large fluorescence quantum yield to ensure detection of a significant fluorescence signal even at the low local concentration typically encountered in living media.

3.3 Two photon fluorescence materials for biological systems

Due to the features of long wavelength excitation and short emission, two-photon fluorescence combines high spatial resolution and deep tissue penetration, which makes two-photon technology particularly relevant in biological imaging and detection. An efficient two-photon fluorescence material should have the following characteristics[79-81]: 1) high biocompatibility, it is mainly reflected in appropriate solubility, biocompatibility and low cytotoxicity towards cells. According to the recent literature report[82], the best water solubility of two-photon fluorescence materials suitable for biological development application should be several micromolar. If the water solubility is too good, it may be difficult to penetrate the cell membrane because it is more stable in aqueous solution than in cells, so it can not stain cells or tissues efficiently; if the water solubility is too poor, it will slow down the staining rate or lead the compound to precipitate before actual cell internalization. 2) effective

two-photon absorption cross-section, because the two-photon material molecules entering into cells or tissues are usually in the micromolar level, large two-photon absorption cross-section, as well as a high fluorescence quantum yield are required to ensure that the molecules entering into cells or tissues can emit as much light as possible.

Therefore, it is very important to design and synthesize two-photon fluorescence molecules with appropriate solubility and significant two-photon absorption cross section. Solubility can be realized by reducing the molecular size[83] and introducing solubilizing groups (various hydrophilic or lipophilic groups)[84]. Alternatively, stable colloidal suspension of fluorophores (in the form of fluorescent organic nanoparticles, FON, for instance) can be beneficial as they combine physiological stability and sufficient lipophilicity of the individual chromophore to ease cell membrane internalization. On the other hand, increasing the effective absorption cross section can be realized by tuning strength of push-pull electron group in polar molecules, increasing conjugation length which can increase molecular ICT process,[85] or increasing the number of branches, which can result in synergistic enhancement effect[86]. In addition, the effective two-photon absorption cross section can be increased by optimizing the luminescent moities[87] *ie* to increase its fluorescence quantum yield, for instance by rigidification of the core structure (incorporation of fuse aromatic cycles or heterocyles) that will limit nonradiative dissipation of the excitation energy.

4 Objectives

In summary, AIEgens based molecules undergone considerable developments regarding the understanding of their photophysical mechanisms, the tuning of their spectral properties and the expansion of the range of applications they cover. However, conventional AIE

molecules usually emit blue (at best green) light and exhibit low biocompatibility which indeed limits the AIE molecules biological applications. Thus, in this thesis, we will modulate molecular structures to adjust the luminescence properties then develop some two-photon AIE fluorescent probes which not only present a high luminescence efficiency in aggregated state but also combine a red-shifted emission, and large TPA cross sections (potentially, as this point could not be investigated in details) as superior candidates for bio-imaging.

First, we will develop three new conjugated luminescence polymers, evaluate their photophysical properties and study the influence of chain length on the optical properties both in isolated compounds and in aggregated state, then explore their use as luminescent two-photon probes for applications in bio-imaging; second, we will introduce a series of benzobisthiazole-based quadrupolar dyes that display efficient and reversible switching of their spectroscopic properties upon protonation. Their excellent fluorescence properties, that combine large Stokes shift, high luminescence quantum yield and very marked changes depending on protonation state, make them particularly interesting candidates as fluorochromic stimuli-responsive sensors. On the other hand, based on this new benzobisthiazole based molecules, we will adjust this molecular structure to develop new two-photon NIR fluorophores.

Finally, we will introduce our current efforts to explore the potential of these molecules as contrast agents for dSTORM super-resolution microscopy, owing to an unreported on-off switching mechanism of their luminescence.

Chapter 2 AIE-active Conjugated Polymer Nanoparticles as Platforms for Biological Applications

In this chapter, three new polymers incorporating tetraphenylethene (TPE) as electron accepting (A) and di- or tri-phenylamine derivatives as electron donating (D) iterative units will be designed and synthesized through Sonogashira coupling. First we will investigate their spectroscopic and AIE performances. Then, dynamic light scattering (DLS) and scanning electron microscope (SEM) measurements will be carried out in order to characterize nanoparticles' size and morphology following their nanoprecipitation and self-assembly in aqueous solution. Finally, we will evaluate their potential as nanoprobes for intravital fluorescence imaging contrast agents.

1 Introduction

In recent years, fluorescent materials had played an important role in the fields of biomedicine, molecular detection, optical imaging, and disease diagnosis and treatment due to their unique optical properties[88-89]. As presented in Chapter I, current fluorescent materials mainly include: fluorescent proteins, organic fluorescent molecules (organic small molecule dyes and carbon quantum dots) and inorganic nanoparticles (upconversion nanoparticles and inorganic semiconductor quantum dots). Fluorescent protein, as a genetically encoded molecule in living body, has the advantages of good biocompatibility and high sensitivity, and can be used to monitor in situ the complex physiological processes in cells and living bodies. However, serious photobleaching, and other shortcomings limit its widespread

applicability[90-91]. Traditional organic fluorescent molecules have a wide variety of properties including in particular finely tunable emission wavelengths, and have been widely used in biological fluorescence imaging and molecular detection. However, shortcomings such as luminescence quenching in physiological media, small stokes shift and poor photostability have reduced its application prospects[92]. Finally, metallic nanoparticles have sometimes outstanding spectroscopic properties, yet are often associated with long term accumulation within organs such as liver, spleen and kidney, which results in long term toxicity and limits their clinical use. It can be seen that the development of fluorescent materials that combine the advantages of small organic molecules and of nanoparticles, without their associated drawbacks, is a particularly interesting approach. For this reason, conjugated polymers and organic nanoparticles have achieved rapid development in the cross fields of chemistry, materials science, biomedicine, *etc*.

1.1 Conjugated polymer

Since the late 1970s, and the discovery of the properties of iodine-doped polyacetylene[93-94] by the American physicist Heeger, New-Zealander chemist MacDiarmid and Japanese chemist Shirakawa, conjugated polymers (CPs) has gradually become a hot topic in basic research and practical applications, and continuously made breakthroughs in above mentioned fields[95-96]. Conjugated polymer are formed by the alternation of C-C and C=C or C≡C bonds, and thus can include multiple light-emitting units that are electronically conjugated to each other through delocalized π bonds in the main chain. Due to these large π-conjugated backbones and delocalized electronic structures, they show excellent photoelectric properties.

For example, **Figure 2-1** shows the absorption and emission spectra as well as the pictures under white and ultraviolet light of a variety of polymers incorporating different D and A iterative units[97] . It is obvious that the emission wavelength of the conjugated polymer can cover the entire visible light band, showing excellent spectral tunability, excellent photostability and good biocompatibility[98-99]. Moreover, when conjugated polymer is excited, the generated exciton can be quickly transferred to the energy acceptor along the long-range π electron skeleton, thereby it can transform small fluctuations in the environment that would affect this long range organization into changes in fluorescence signals, which can realize high sensitive detection of analytes.[100] Generally, chemical synthesis is the main method for preparing conjugated polymers. Many C-C coupling strategies, such as Wittig reaction, Heck reaction, Wessling Reaction, Stille reaction, Suzuki reaction, Glaser reaction, Sonogashira reaction, Click reaction, etc. have been used in this regard [101-104]. **Table 1** summarizes the most typical CPs polymerization methods.[105]

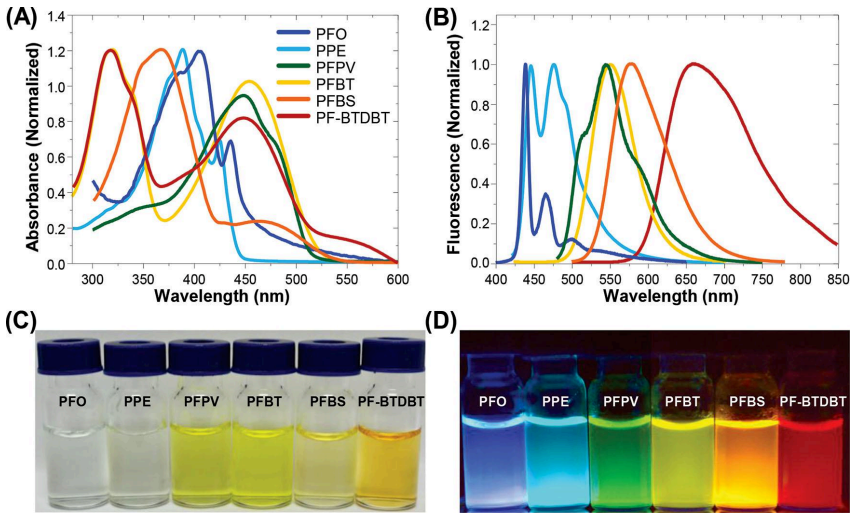

Figure 2-1. Optical properties of different conjugated polymer solutions; Picture taken from reference 97.

Polymerization methods	Schematic structures and reaction examples
Suzuki coupling	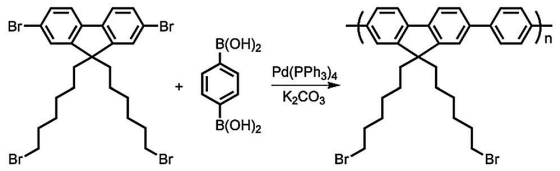
Heck coupling	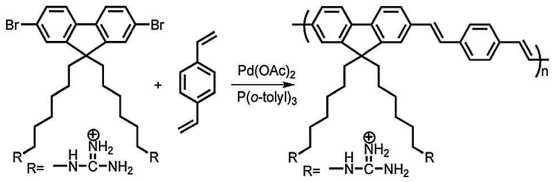
Sonogashira ..	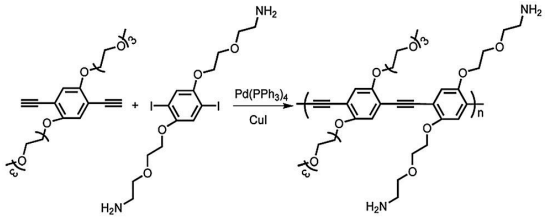
Oxidative polymerization	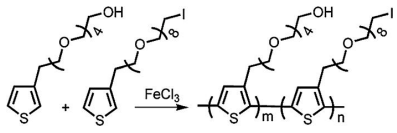

Table 1. Typical polymerization methods[105]

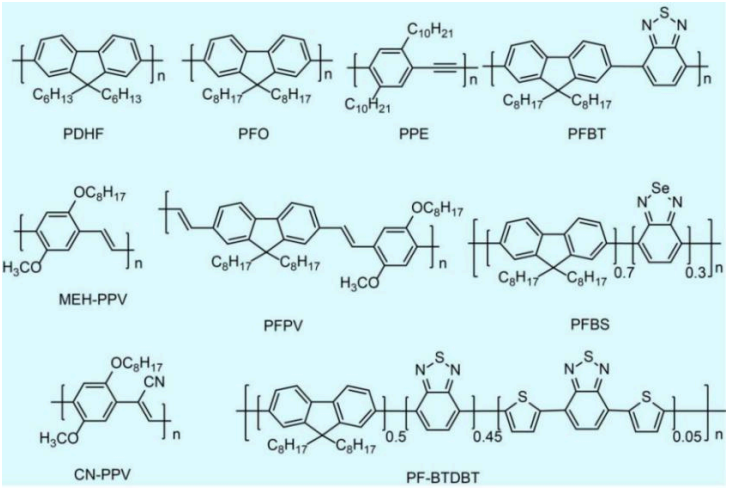

Figure 2-2. The structures of some conjugated polymers and co-polymers.

With the continuous research on the topic, more and more conjugated polymers have been synthesized. Depending on the nature of their skeletons, they can be classified as:

polyacetylene (PA), polyfluorene (PF), polyphenylenethynylene (PPE), polyphenylene (PPP), polyaniline (PANi), polythiophene (PT), polypyrrole (PPy). In recent years, conjugated co-polymers have emerged, such as fluorene-benzothiadiazole conjugated copolymer (PFBT), fluorene-phenylene conjugated copolymer (PFPV), fluorene-benzothiadiazole-thiophene conjugated copolymer (PF-BTDBT) *etc.*[106-110], **Figure 2-2** lists some examples of such copolymer architectures with, their synthetic methodology of preparation.

1.2 Conjugated polymer nanoparticles (CPNs)

Nanosized structures have been shown to display enhanced affinity towards several biological compartments of interest such as tumor tissues owing to the so-called EPR effect (Enhanced Permeation and Retention). EPR effect results from the fact that while the microvascular endothelial space in normal tissues is dense and structurally complete, making it difficult to cross the blood vessel walls for macromolecules and nanosized structures, tumor tissue are characterized with a rich blood vessels network, with poor structural integrity, wide gaps in the endothelial walls, and lack of lymphatic reflux which causes macromolecules substances and particles to easily escape the blood stream and accumulate within the tumoral tissues. Therefore, EPR effect promotes the selective distribution of macromolecules in tumor tissues, which can be taken advantage of for tumor therapy. In this context, using conjugated polymers (CPs) as active components it is possible to prepare conjugated polymer nanoparticles (CPNs)[111] that will exploit this effect. CPNs have for this reason been widely applied for in vivo fluorescence imaging[112]. Table 2 lists the properties and possible applications of CPNs in this field.[113]

Conjugated polymer nanoparticles (CPNs)			
Properties	Large absorption coefficient	Good photostability	Tunable spectra property
	High brightness	Favorable compatibility	Facile functionalization
Applications	Imaging	Cell activity regulation	Therapy
	Fluorescence imaging	Gene expression	Photodynamic therapy
	Luminescence imaging	Thermosensitive ion channels	Photothermal therapy
	Photoacoustic imaging	Enzyme activity	Combination therapy
	Raman imaging	Photosynthesis	

Table 2. Summary of properties and applications of CPNs.

As materials for biological applications, CPNs are mainly prepared by miniemulsion, self-assembly and reprecipitation.

1) Reprecipitation method

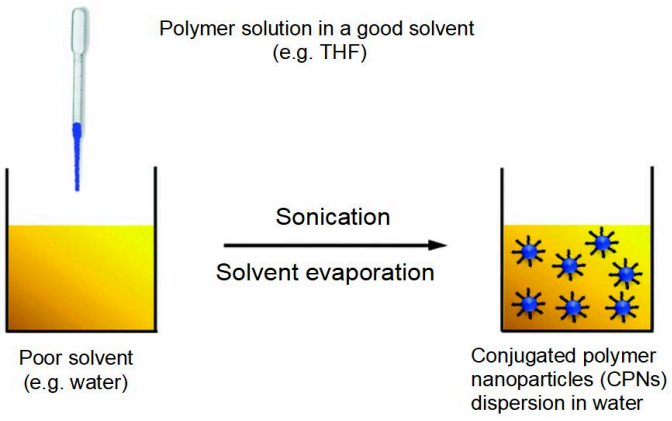

Figure 2-3. The schematic diagram of nanoprecipitation.

Nanoparticles formation by reprecipitation (also called nanoprecipitation method) consists in injecting a small amount of organic compounds dissolved in good solvent into vigorously stirred water. As shown in the **Figure 2-3**, the exclusive solubility of most organic polymers in organic solvents allows molecules to aggregate and grow to obtain organic

nanoparticles when dispersed in water. This method is easy to operate and has become one of the preferred methods for preparing organic nanomaterials in general and CPN in particular. The mechanism responsible for long term colloidal stability of CPNs in aqueous media is not fully understood to date. Polymer chains are generally spherical because spherical shape has a low surface energy which will form more stable particles.

McNeill et al[114-115] prepared three different polymers PDHF, MEH-PPV and PFPV **(Figure 2-4)** and used reprecipitation method to prepare nanoparticle aqueous solution with fluorescent properties. The three resulting polymer nanoparticles were characterized by transmission electron microscope and scanning fluorescence microscopy. The data showed that polymer nanoparticles prepared by nanoprecipitation method combined good colloidal stability in water with large brightness and photostability.

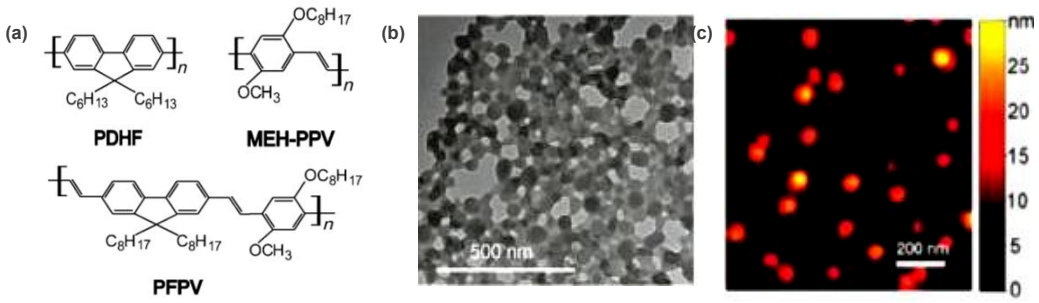

Figure 2-4. (a) The structures of polymer PDHF, MEH-PPV, and PFPV[115]; (b) TEM picture of PNPs[114]; (c) AFM picture of PNPs[115].

2) Mini-emulsion method

Unlike nanoprecipitation method, the mini-emulsion method[116] uses organic solvents that are not miscible with water. Therefore, the mini-emulsion method must involve surfactants as stabilizers to prevent the formed emulsion from phase segregation. First, conjugated polymers are dissolved in an organic solvent and then are injected into aqueous

solution containing surfactant. Under ultrasonic conditions, the organic phase containing the polymer is dispersed into the aqueous phase to form an emulsion. Removal of the organic solvent in the solution by rotary evaporation yields the surfactant stabilized polymer nanoparticles in the aqueous phase.

3) Self-assembly method

For this preparation method[117], the charged CPs and the co-assembly reagent bearing opposite charge are independently dissolved or dispersed in the water, sequentially. The obtained solutions or dispersions are blended together in a certain ratio under stirring. Then though centrifuging in high speed, the resulting self-assembled functionalized CPNs can be easily separated.

1.3 AIE conjugated polymer nanoparticles for biological applications

According to chapter 1, we know that the use of traditional fluorogens in the preparation of luminescent NPs is highly restricted in sensitivity and effectiveness because of the ACQ phenomenon. The discovery of AIE has therefore strongly fueled the development of luminescent probes and nanoparticles (NPs) for various imaging applications.[118] Besides luminescence imaging, conjugated polymers made of AIEgens, and the resulting AIE conjugated polymer nanoparticles have greatly expanded their potential to encompass photoacoustic (PA) imaging, photodynamic therapy (PDT), photothermal therapy (PTT) and other biomedical fields.[119-120] For example, recently, through rational engineering of the CP backbone and side chain substituents, Qin's group[121] successfully designed and prepared an AIE conjugated polymer with an excellent biocompatibility and super strong reactive oxygen species (ROS) generation ability, which was used in vitro and in vivo for antibacterial purpose

(**Figure 2-5**).

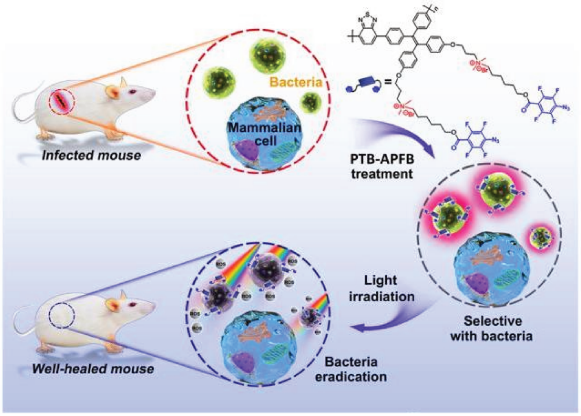

Figure 2-5. Chemical structure of PTB-APFB and its selective antibacterial application. Picture taken from references 121.

There are many typical AIE molecules (**Figure 2-6**) which can be envisioned as the core moieties in conjugated polymer

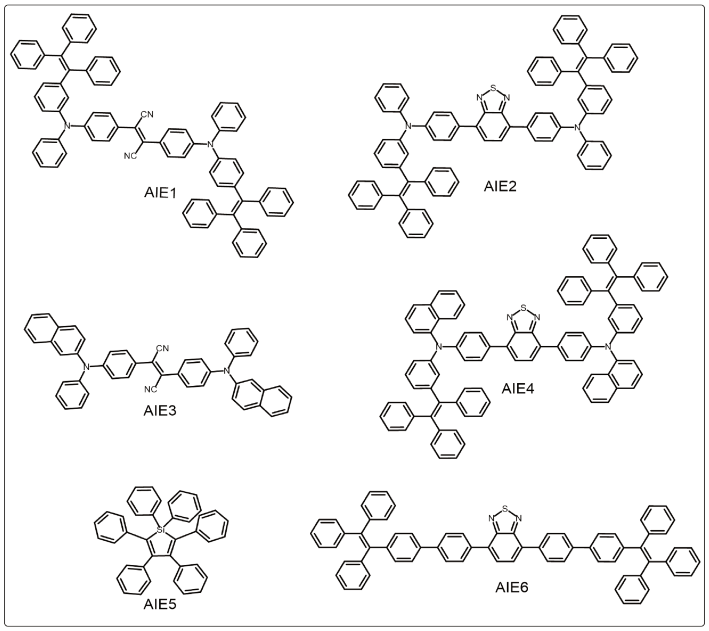

Figure 2-6. AIE dyes used for encapsulation into different types of polymer NPs.

1.4 Objectives

Inspired by these interesting results about AIE nanoparticles based on conjugated polymers, we envisioned the development of organic nanoparticles as platforms for intravital

fluorescence imaging and theranostic applications with optimized structural features for improved two-photon absorption properties, based on the general structure depicted in **Figure 2-7**.

In this chapter, we will focus on the synthesis of such main chain conjugated polymers, in which different organic fluorophores with structures aiming at maximizing two-photon absorption properties will be incorporated as repeating units into oligomeric and polymeric assemblies. Then taking the nanoprecipitation approach to get fluorescent organic nanoparticles we will study their linear and non-linear spectroscopies, evaluate their AIE properties and utilize them for fluorescence imaging in cells.

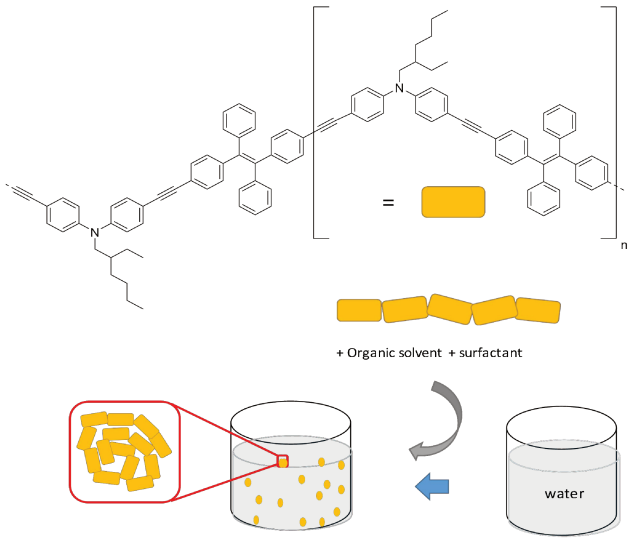

Figure 2-7. Fluorescent organic nanoparticle synthesis using conjugated polymer nano-precipitation approach.

2 Design, Synthesis and Optical Properties of Conjugated Polymers

2.1 Design strategy

Donor-Acceptor (D-A) type molecular structures in which electron donating unit and

electron withdrawing unit are alternately connected in the molecular main chain afford charge transfer interaction between donor and acceptor, which can be tuned by changing their donating/withdrawing electron ability. This features can be used 1/ to adjust the polymer's optical band gap and thereby tune its absorption and emission wavelength 2/ to enhance the oscillator strength associated to the electronic transition, and thereby maximize its one- and two-photon absorption properties and brightness (see Chapter I).

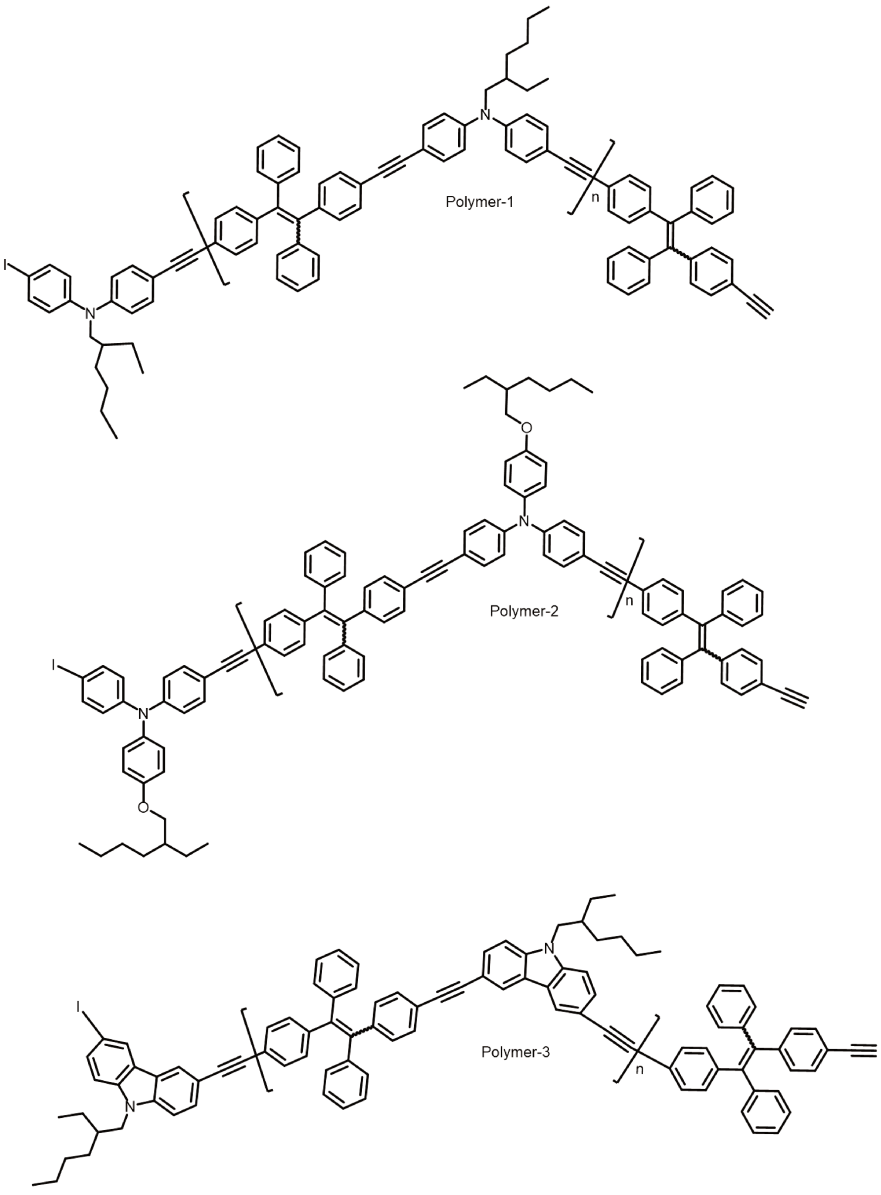

Figure 2-8. The structures of three new conjugated polymers.

According to this principle, we designed D-A polymers structure as displayed in **Figure 2-8**, where tetraphenylethylene (TPE)-fluorogen, which is a typical molecule with aggregation induced emission (AIE) characteristics, is used as the core units which plays the role of electron acceptor (A), and di- or tri- phenylamine or carbazole derivatives are used as the electron donors(D). The structure of the latter is not only aimed at improving the TPA properties but also owing to the alkyl chain functionalization which can improve molecular solubility.. Sonogashira coupling is a high yielding, convenient procedure to afford C-C coupling between aryl and ethynyl groups in mild conditions. Thus, according to reported method[122a], Sonogashira coupling "polymerization" step was used to connect the difunctional units to get a $(D\text{-}A)_n$ structure polymer.

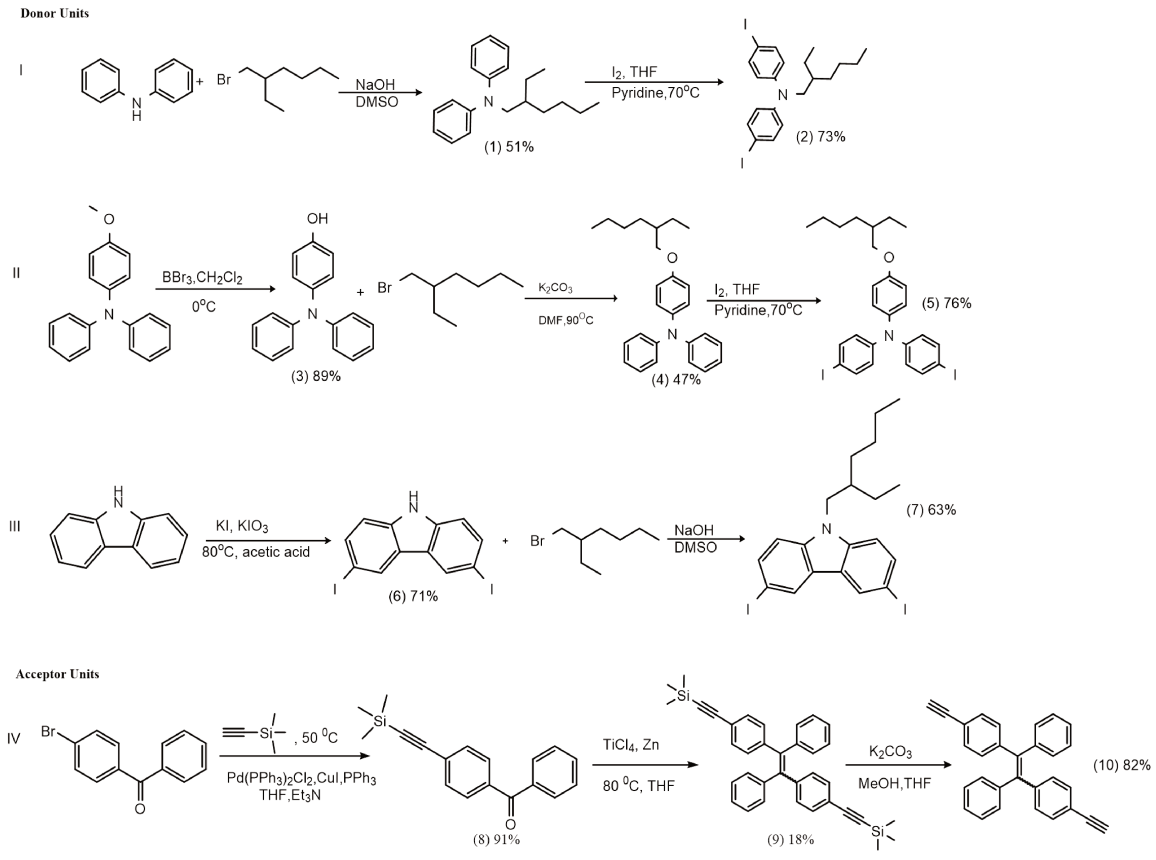

Figure 2-9. Synthesis of Donor and Acceptor molecules.

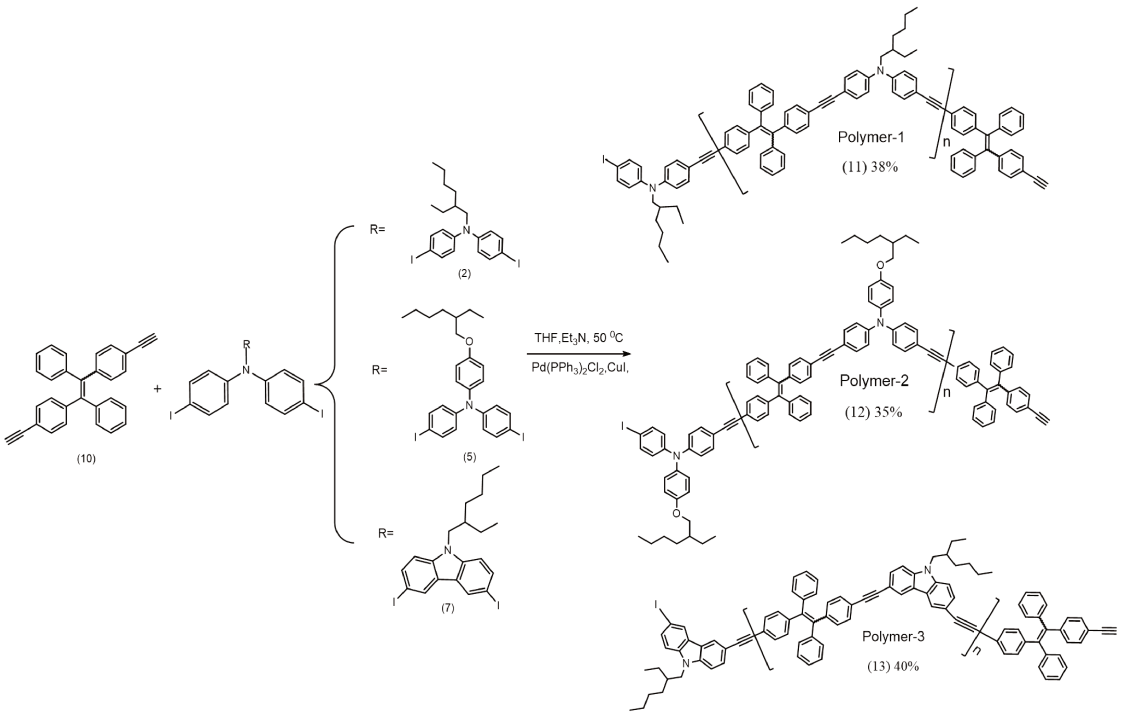

Figure 2-10. Synthesis of **polymer-1**, **polymer-2**, **polymer-3**.

Following this approach p**olymer-1, polymer-2 and polymer-3** were obtained through Sonogashira coupling between acceptor **10** and Donor **2**, **5** or **7**, with $Pd(PPh_3)_2Cl_2$ and CuI as catalysts, at 50 °C in dry THF/ Et_3N mixtures (**Figure 2-9**, **2-10**). Compound **10** was prepared in three steps, from the starting material 4-bromobenzophenone which was first involved in a Sonogashira reaction to get compound **8**, then in a McMurry coupling under catalyst zinc and titanium tetrachloride condition. Finally, cleavage of the trimethylsilane part was achieved in a weak base environment to get our target compound **10**.

Figure 2-11 displays the ^1H NMR of all synthesized polymers. Characteristic peaks can be identified, by comparison with the ^1H NMR of the starting D and A monomers: the peak around 3.80 ppm belongs to Ha of the donor-appended alkane chain; Hb, Hc, He, Hn, Hj, Hl also can be found in the spectrum in the form of broad multiplets around 1.00 ppm. Finally, low field broaden peaks around 7.00 ppm can be attributed to the main chain aromatic protons,

which consist in a superimposition of TPE and diphenylamine, triphenylamine and carbazole peaks for **polymers-1**, **2 and 3** respectively.

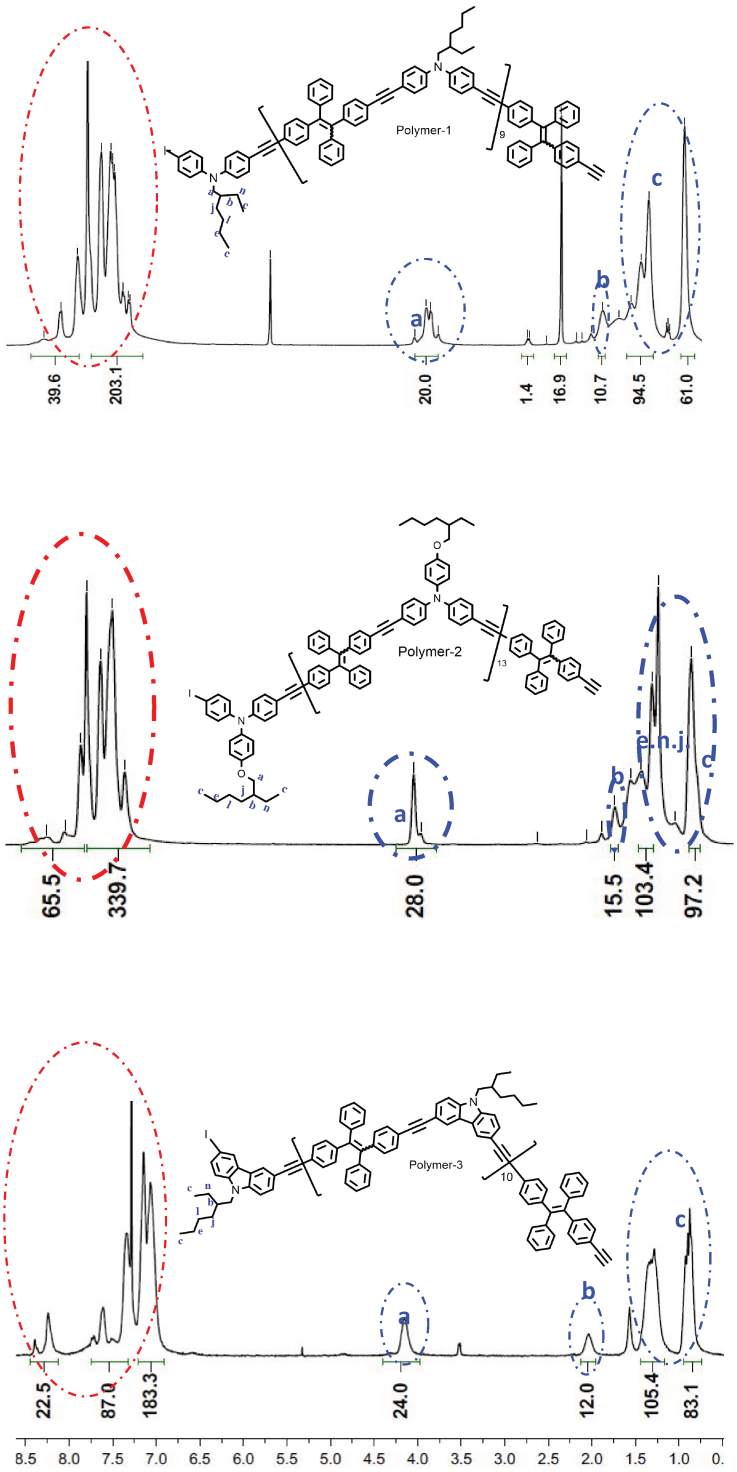

Figure 2-11. ^{1}H NMR of three polymers in $CDCl_3$. Blue circles highlight the alkyl substituents, red circle correspond to the main chain's aromatics

Moreover, a qualitative prediction of the degree of polymerization (DP) (or repeating units number) could be determined by comparing the relative proton peak intensity of a known moiety (typically an end-groups with a known number of protons) to that of the repeating chain unit, following a previously published approach.[122b] Based on this method it was possible to to estimate DP values n of 10, 14, 11 for **polymer-1**, **polymer-2** and **polymer-3**, respectively (in **Figure 2-12** we selected **polymer-1** as a representative example for the process of calculating DP value).

Gel Permeation Chromatography (GPC) was also carried out to refine this estimation and also calculate the dispersity (M_w/M_n) of three polymers. GPC data are listed in **table 3**. DP were calculated considering the average molecular mass in weight (M_w), resulting in values on good agreement with ^{1}H NMR data. Polydispersity index (PdI) was found between 1.7 and 2.7, indicating a relatively uniform molecular weight distribution for the three polymers, although significantly less controlled in the case of **polymer 2**.

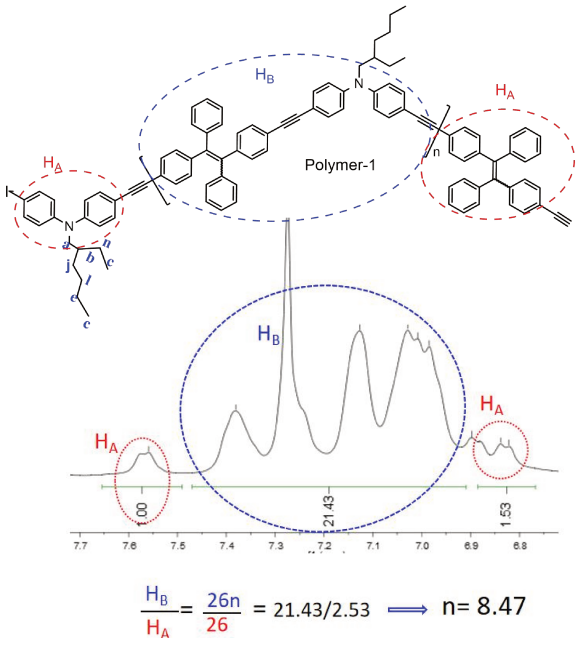

Figure 2-12. By ^{1}HNMR spectrum to calculate the value of DP.

Compound	M_n	M_w	M_z	$M_{(D-A)}$	$M_w/M_{(D-A)}$	Dispersity	Degree of polymerization
polymer-1	4165	7181	11306	687	10.4 ≈ 10	1.72	10
polymer-2	3959	10748	19772	764	14.1 ≈ 14	2.71	14
polymer-3	4359	7547	11972	685	11.2 ≈ 11	1.73	11

Table 3. GPC data and dispersity, degree of polymerization of three polymers.

2.2 AIE properties of three conjugated polymers

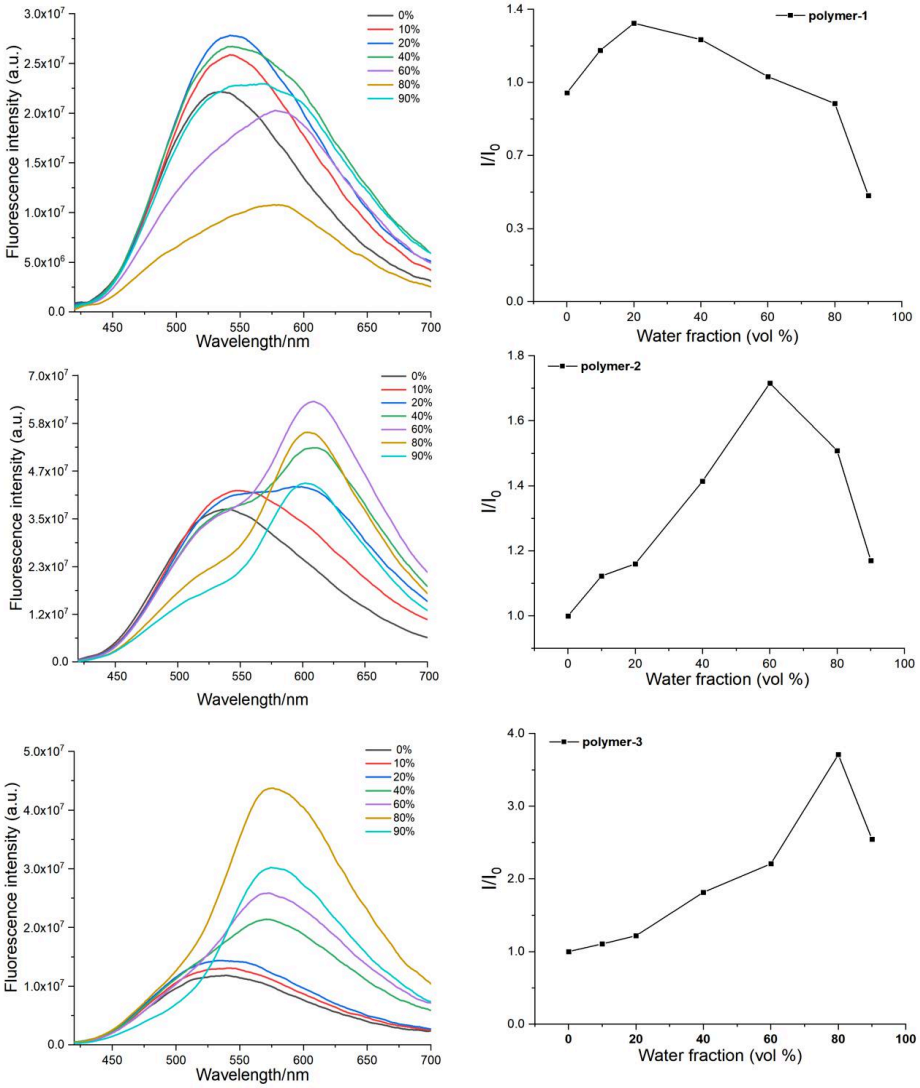

Figure 2-13. Emission spectra (left) of three polymers in THF/water mixtures with different water fraction. Excitation wavelength is 370 nm, 390 nm, 360 nm respectively. I/I_0 values versus water fractions in THF/water mixtures (right). I_0 is the luminescence intensity of THF solution. The concentration of all solutions and suspensions are 1×10^{-5} mol/L.

Samples	Conditions	λ_{max}[a]	λ_{max}[b]	$\Delta\nu$[c]	Φ_f[d]
Polymer-1	solution	372	533	8119	0.021
	f_w 90%	375	580	9425	0.017
polymer-2	solution	389	537	7084	0.013
	f_w 90%	395	605	8787	0.018
Polymer-3	solution	364	534	8745	0.016
	f_w 90%	365	576	10036	0.043
[a] Absorption peak position in nm (1.0×10^{-5} mol L^{-1}). [b] Peak position of emission in nm (1.0×10^{-5} mol L^{-1}), excited at 370 nm (**polymer-1**), 390 nm (**polymer-2**) and 360 nm (**polymer-3**). [c] Stokes shift in cm^{-1}. [d] Absoluted quantum yields determined by using integrating sphere.					

Table 4. Photophysical properties of **polymer-1**, **polymer-2**, **polymer-3**.

First we investigated the AIE properties of all synthesized polymers in different water fractions. Results are featured in **Figure 2-13**. For **polymer-3** (excitation at 360 nm), weak AIE properties are observed: the fluorescence intensity is enhanced upon increasing the water fraction (*f*w), to reach a maximum 4 times enhancement (compared with THF solution) when *f*w is 80%, with a quantum yield increased from 1.6% to 4.3%. **Polymer-2** also shows this AIE phenomenon, although to an even more modest extent: when *f*w increases from 0 to 60%, the fluorescence intensity is increased by a factor 1.8 times. At last, no obvious AIE behavior is observed in the case of **polymer-1**: with increasing *f*w, its fluorescence intensity is first increased (*f*w < 20%) and then slowly decreased (*f*w > 20%). In the three cases, aggregation is accompanied with the same red-shift of the emission maxima. Further experiments were conducted to study the red-shift phenomena (**Figure 2-14a**). The related optical properties of three polymers were recorded in solution and suspension (THF/water=1:9) state, main data are reported in **Table 4**. The corresponding absorption and emission spectra were displayed in

Figure 2-14a. In THF solution, maximum absorption wavelength at 372 nm, 389 nm, 364 nm were found for polymer **1**, **2** and **3** respectively. In suspension, the absorption spectrum showed broaden transitions, with a slight red-shift of the absorption maxima, indicating the transition from the isolated molecules to the nano-aggregates. Moreover, a tail is seen at the red-edge of the main electronic transition: this can be explained by the scattering phenomena resulting from the formation of nanoparticles, which is typically observed in the absorption spectra of NPs[123a-123b]. Emission spectrum of three polymers in suspension showed a narrow band emission and an obvious red-shift (53 nm, 68 nm and 42 nm respectively), as compared to the organic solution.The maximum emission wavelength reached 580 nm, 605 nm, 576 nm for polymer **1**, **2** and **3** respectively. This phenomenon seemingly indicates that nano-aggregates result in the formation of J-type exciton,[123c] which is highly unusal for TPE based AIEgens, for which aggregation usually comes with a slight blue shift[123d-123e]. For example, the compound TPE-TPA which had been recently obtained in our group in the framework of Jean Rouillon's thesis (unpublished) shows a clear blue shift of its emission in aggregated state, resulting from restriction of intramolecular motion (**Figure 2-14b**). We postulate that this uncommon property results from the aggregation induced alignment of successive D-A subunits, which behave as individual chromophore within the polymer chain. Restriction of subunits mobility in the solid state may reinforce this alignment, and enhance the excitonic coupling at the origin of the observed J-aggregate emission. This phenomenon should however be further confirmed by future studies.

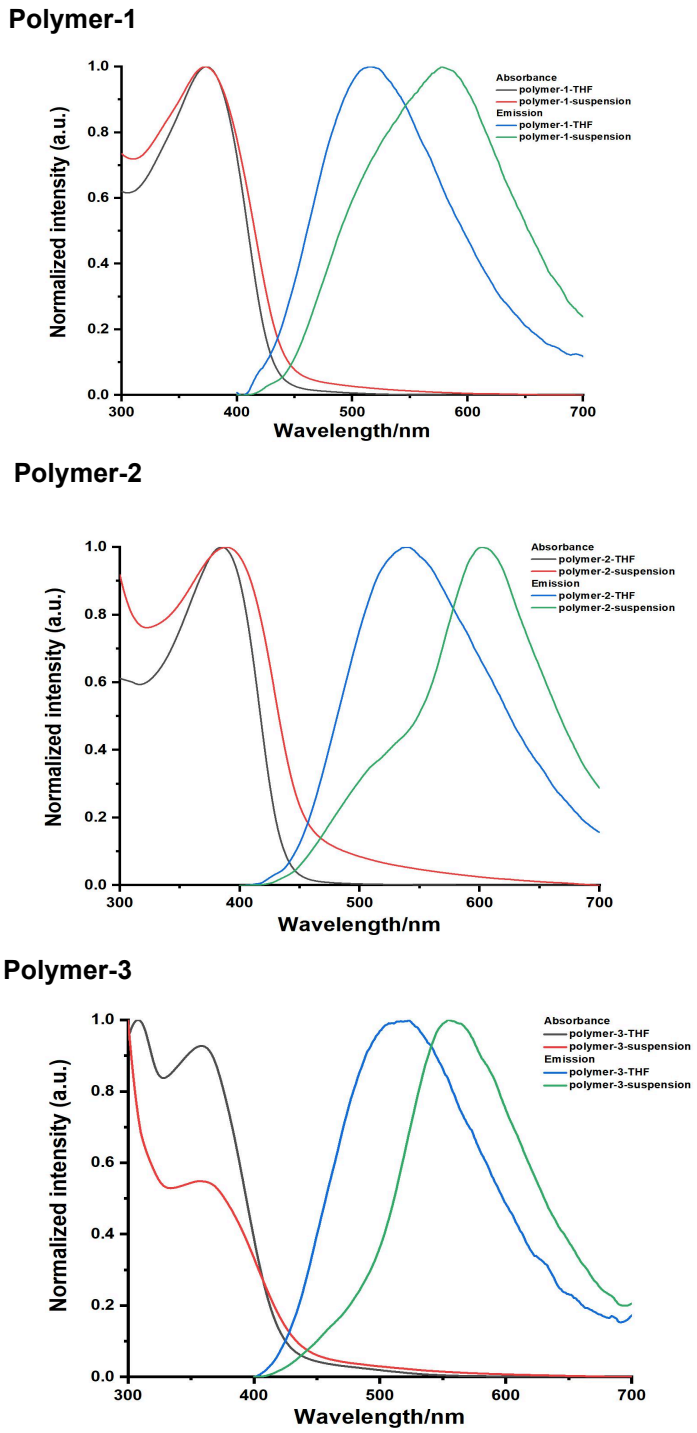

Figure 2-14a. Absorption and emission spectra of **polymer-1**, **polymer-2** and **polymer-3** in THF and THF/water (1:9) mixtures. Excitation wavelength is 370 nm, 390 nm, 360 nm respectively. The concentration of all solutions and suspensions are 1×10^{-5} mol/L.

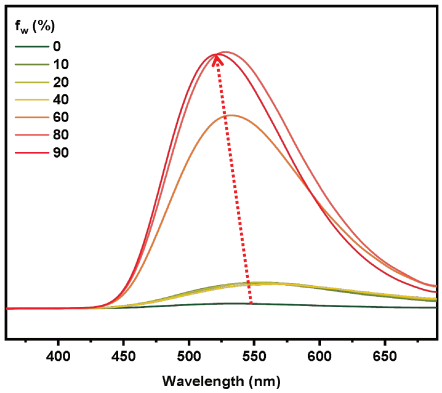

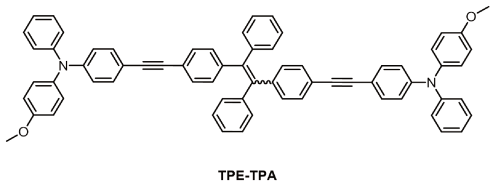

Figure 2-14b. Emission spectra of compound TPE-TPA in THF/water mixtures with different water fraction. Excitation wavelength is 375 nm.

3 Conjugated Polymer Nanoparticles

Preparation of the conjugated polymers nanoparticles was achieved using the nanoprecipitation methodology depicted in paragraph **1.2** of the present chapter. 4.5 ml H_2O was added dropwise onto 0.5 ml THF solution of conjugated polymer (1×10^{-3} mol L^{-1}) under sonication condition, then the remaining THF was evaporated to get the NPs suspension.

3.1 Dynamic light scattering (DLS)

Dynamic light scattering (DLS) was first carried out, in order to confirm the formation of luminogen nanoparticles in THF-water mixtures and to measure the particles size and distribution. In **Figure 2-15** the results show that the average NPs' diameters of **polymer-1**, **polymer-2** and **polymer-3** are 86.4 nm, 90.6 nm, 119.0 nm respectively: all the values are around or below 100 nm which is a suitable size for applicationS in biological fields. Polydispersity index (PdI) is the standard tool to evaluate the size distribution of NPs: the smaller the value, the more uniform the distribution of NPs. As a matter of fact, PdI of three polymers are 0.28, 0.21 and 0.23 respectively (**Figure 2-15**), consistent with the formation of relatively monodisperse nanoparticles.

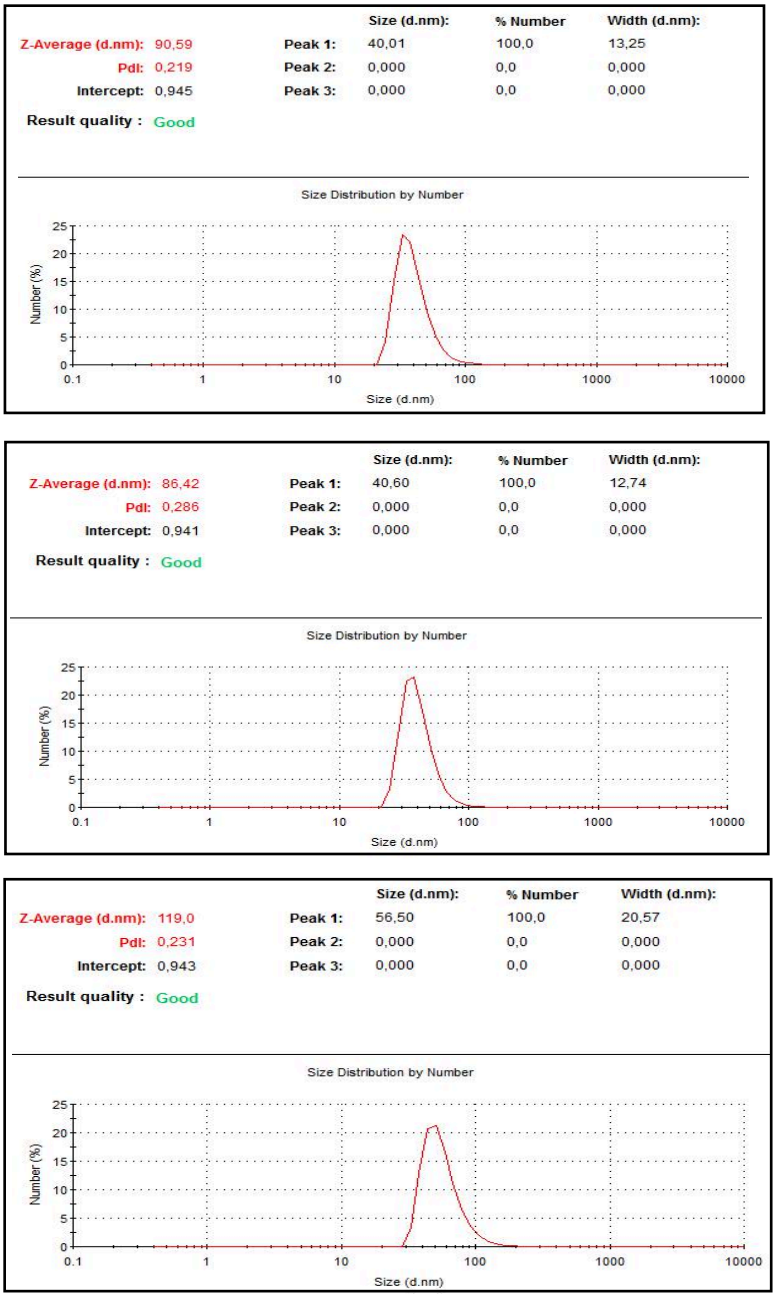

Figure 2-15. Dynamic light scattering (from top to bottom) of polymer-1, polymer-2, polymer-3 nanoparticles.

3.2 Scanning electron microscope (SEM)

Subsequently, scanning electron microscope (SEM) images were recorded to gain insight on the morphology of NPs. First, for preparing samples, the polymer solution (THF/H_2O = 1/9) was dropped onto the surface of a silicon wafer with conductive adhesive. As the SEM photos show in **Figure 2-16**, suspensions of all three polymers consist in small spherical and relatively uniform particles which are nicely dispersed at the surface of the silicon wafer,

consistent with the results of DLS experiments, although average diameter does not seem to exceed 50 nm in the SEM images.

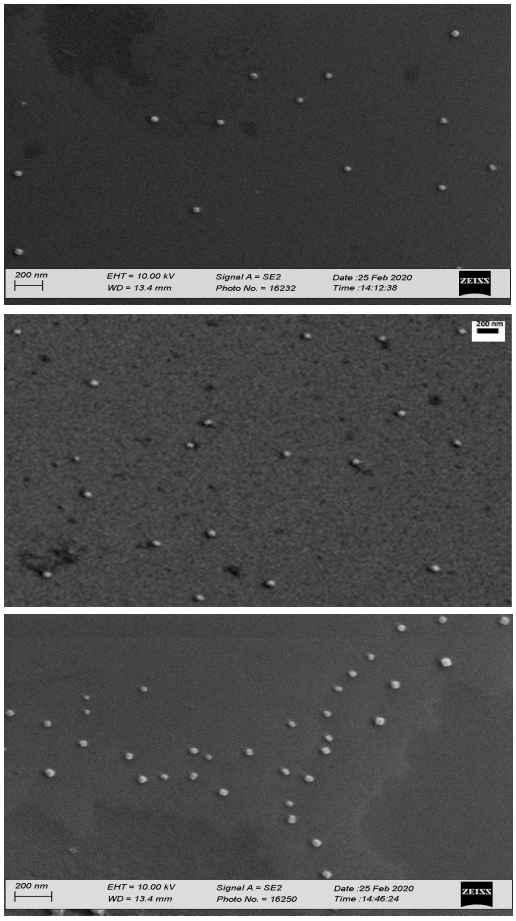

Figure 2-16. SEM of **polymer-1**, **polymer-2** and **polymer-3** (from top to bottom).

In conclusion, based on the results of DLS and SEM, we confirm that at high water content, homogeneous and relatively monodisperse nanoparticles are formed which possess spherical shape and suitable size for applications in a biomedical context. In a final stage, we thus explored the potential of the three polymer for biological applications.

4 Biological Applications of Conjugated Polymers

All experiments were performed at the Anhui university, in Key Laboratory of Chemistry for Inorganic/Organic Hybrid Functionalized Materials of Anhui Province.

4.1 MTT assays

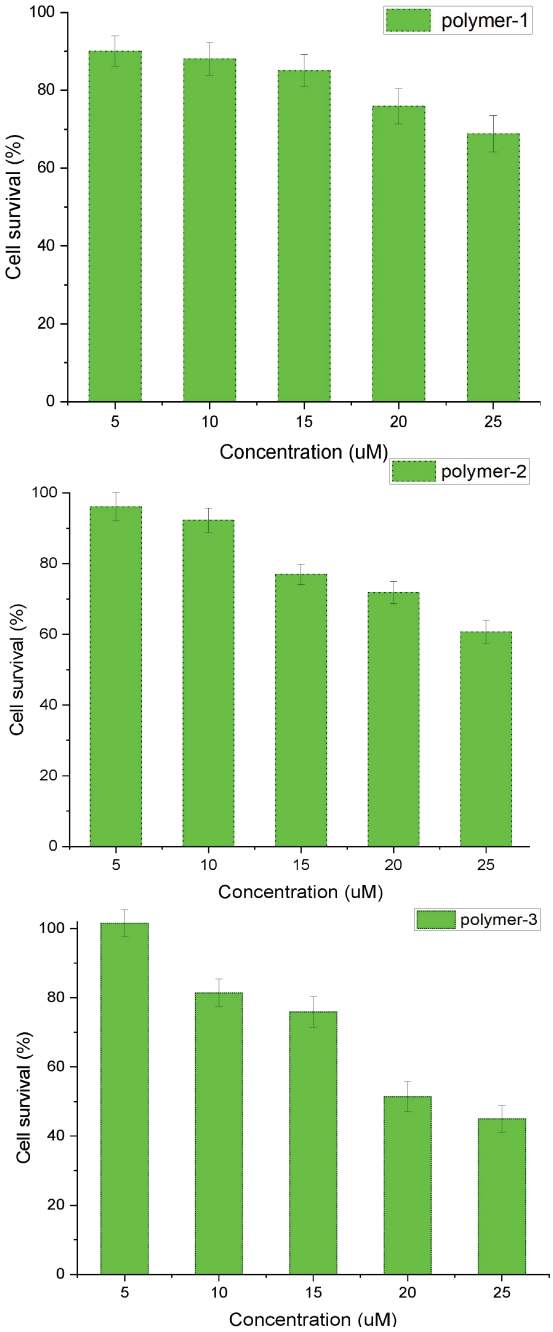

Figure 2-17. MTT assay of HeLa cells treated with three polymers at different concentrations for 24 h.

Low toxicity is essential for biological applications, so we first evaluated the toxicity of three polymers by MTT (methylthiazolyldiphenyl-tetrazolium bromide) assays[124] MTT assays were carried out by utilizing three polymers at different concentrations of 5, 10, 15, 20 ,25 μM to incubate HeLa cells for 24 h, then recording the cells viability to assess their

toxicity. The successive steps took place as follows: HeLa cells were predigested with trypsin and incubated in 96-well plates for 24 h. Before adding samples, incubation medium was carefully removed and fresh medium was added, then different volumes of DMSO solution of **polymer-1**, **polymer-2**, **polymer-3** were added. Volumes were adjusted so that the final concentration of polymers in the medium is 5, 10, 15, 20 and 25 μM, cell culture were incubated at 37 ºC and 5% CO_2 for 24 h. Then the cells were treated with MTT of 5 mg/mL (40 mL/well) and continuously cultured 4 h under the above conditions. Then the optical density value at 570 nm was recorder for each sample and the cell survival rate could be obtained according to the following formula:

$$\text{Cell viability \%} = OD_{570}\,(\text{sample})/OD_{570}\,(\text{control})\times 100$$

OD_{570} (sample) represents the optical density of medium added with different concentrations of compounds, and OD_{570} (control) represents the optical density of cells and culture medium without samples. Each individual cytotoxic experiment was repeated three times. In **Figure 2-17**, when the concentration of three polymers are below 15 μM, the cell viability remained above 80%, which ensures good compliance with the cell imaging condition. It demonstrates that three polymers show low toxicity, although the latter is increased between **polymer-1** and **3**.

4.2 Photobleaching assays

In addition, photostability was also evaluated to assess the applicability of each polymer towards cell imaging. Photobleaching rates of three polymers incubated with HeLa cells in a PBS buffer solution at 37 °C for 0-10 minutes (final concentration of three polymers are 10 μM) were investigated by monitoring changes in their fluorescence intensity under continuous

laser scanning upon excitation at 405 nm. Quantification of the fluorescence intensity of the confocal image was conducted *via* an Image J plug-in ROI (region of interesting) manager.

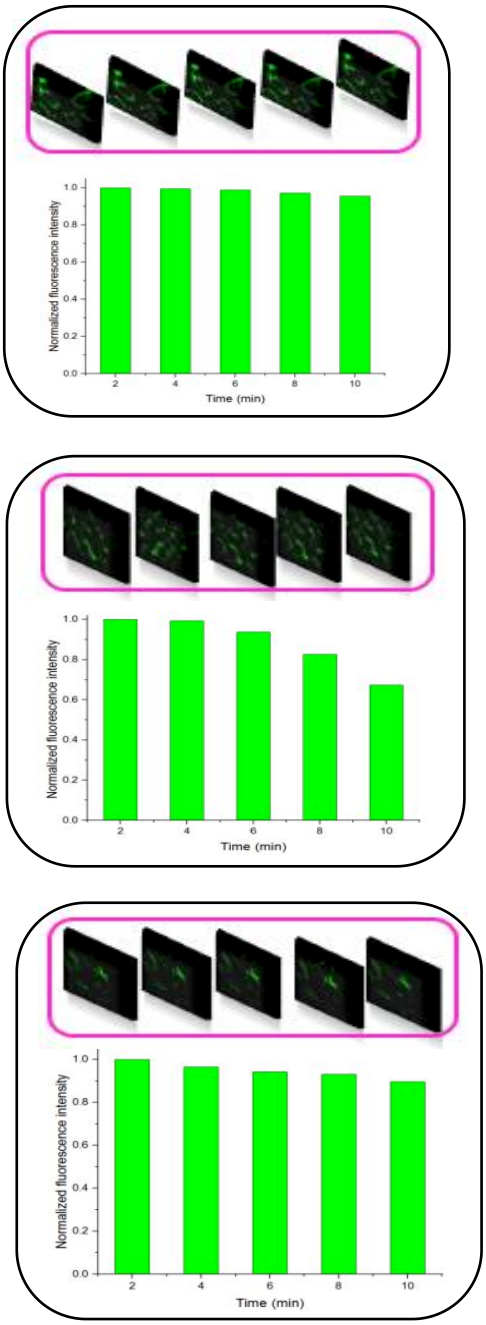

Figure 2-18. Photo-bleaching experiment of HeLa cells over continued laser scanning (top to bottom is **polymer-1**, **polymer-2** and **polymer-3** respectively).

As shown in **Figure 2-18**, after 10 minutes continuous laser scanning, fluorescence intensity of **polymer-1**, **polymer-2**, **polymer-3** remained almost unchanged: only **polymer-2**

showed a slight decrease from 8 minutes. This indicated that these three polymers display good photostability, which is an often observed benefit of CPNs compared to their molecular analog. Combined with the results of MTT assays this results clearly demonstrate that three conjugated polymers are relevant materials in fluorescence cells imaging.

4.3 Cell imaging

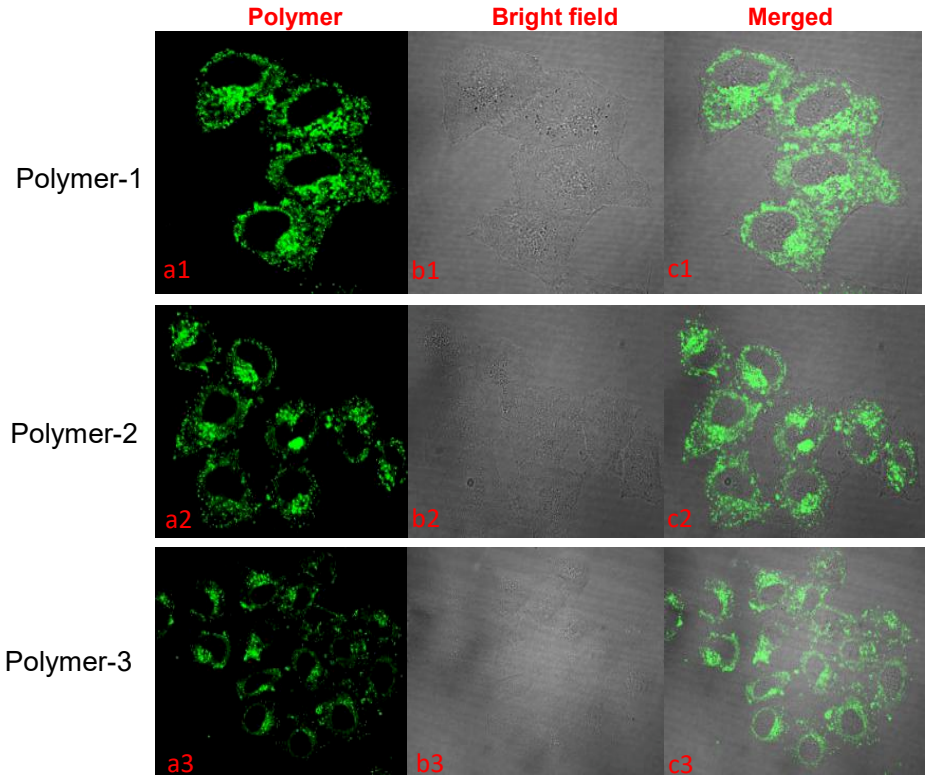

Figure 2-19. Fluorescence images of HeLa cells incubated with with **polymer-1**, **polymer-2**, **polymer-3**. (a1-a3) **polymer-1**, **2**, **3**; (b1-b3) bright-field; (c1-c3) merged field; (λ_{ex} = 400 nm, λ_{em} = 500-600 nm).

We utilized confocal fluorescence microscopy to investigate the capability of the three polymers in cell staining. Confocal fluorescence imaging **(Figure 2-19)** showed that all polymers could readily penetrate cell membrane and produce granular luminescent spots in the cytoplasm. Such granular character is often associated with lysosomal accumulation of the fluorescent probes: in order to test this possibility, we undertook co-localization imaging

experiment between the three polymers and Lyso-Tracker Deep Red (a commercial dye that specifically light up lysosome).

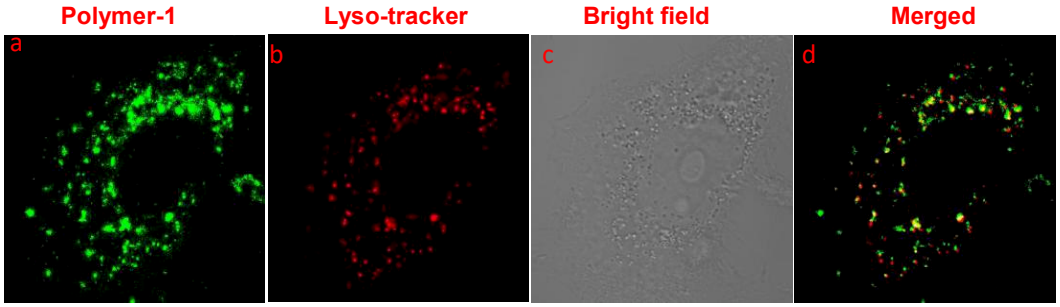

Figure 2-20. Fluorescence confocal images of HeLa cells treated with **polymer-1** (10uM) (λ_{ex} = 400 nm, λ_{em} = 500 - 600 nm) and Lyso-Tracker deep Red (1uM) (λ_{ex} = 647 nm, λ_{em} = 660 - 680 nm); (a) **polymer-1**; (b) Lyso-Tracker deep Red; (c) bright-field; (d) merged-field.

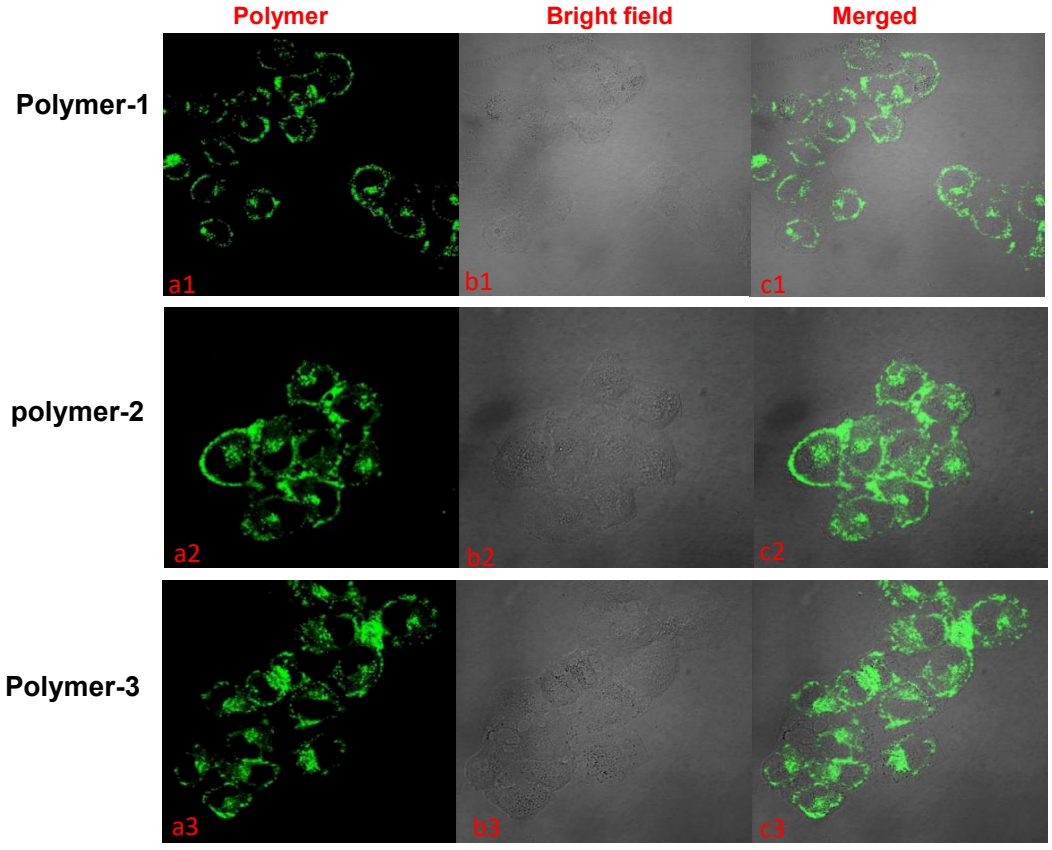

Figure 2-21. Two photon fluorescence images of HeLa cells with **polymer-1**, **polymer-2**, **polymer-3**. (a1-a3) **polymer-1**, **2**, **3**; (b1-b3) bright-field; (c1-c3) merged field; (λ_{ex} = 800 nm, λ_{em} = 500-600 nm).

Figure 2-20 shows the images of co-localization experiments performed with **polymer-1**.

From this data the value of Pearson's colocalization coefficients[125] between **polymer-1** and lysotracker (describing the correlation of the intensity distribution between the probe and commerical dyes signal) was 0.11, which indicates an absence of co-localization of both markers. In conclusions, there is no specific accumulation of the newly designed polymers into lysosomes after entering cell, the granular character of the picture probably results from the nanoparticular nature of the probe.

Finally, two-photon confocal microscopy imaging was also performed with those three polymers in **Figure 2-21**, confirming their suitability for two-photon fluorescence microscopy cellular imaging.

5 Conclusion

In this chapter, three TPE-based polymers relying on similar A-(D-A)$_n$-D structures were synthesized *via* Sonogashira cross-coupling. First, these as-synthesized polymers were characterized by ^{1}H NMR, ^{13}C NMR and GPC techniques, indicating a degree of polymerization of three polymer is 10, 14 and 11 respectively along with a decent PdI (1.7 to 2.7, depending on the considered polymer).

Then we investigated their self-assembly behavior in aqueous solution and spectroscopic performances. Among those three polymers, only **polymer-2** and **polymer-3** exhibit (weak) AIE properties in suspension, characterized by an increase of their fluorescence intensity by 1.8 and 4 times respectively. In contrast with most reported TPE based AIEgens, emission properties seem here to result from the formation of J-aggregates, accounting for the observed large red shifted and characteristically narrow emission band observed for the three conjugated polymers. For **polymer-2,** this results in a maximum emission peak position at

605 nm, in the red region, which constitutes a very positive feature in view of fluorescence microscopy imaging. Unfortunately, as mentioned above this red-shift goes with at best only a weak aggregation induced enhancement in luminescence quantum yield.

Dynamic light scattering (DLS) and scanning electron microscopy (SEM) results show that the three polymers form spherical nanoparticles in suspension, with an uniform diameter size around 50 (SEM) to 100 (DLS) nm. We also demonstrated that all three polymers display low toxicity and good photostability in suitable concentration for bioimaging. The one and two-photon confocal fluorescence imaging show that three polymers can penetrate cell membrane and stain HeLa cells.

Chapter 3 Benzothiazole Based AIE Active Fluorescent Probes for Acid and Vapors Detection

1 Introduction

1.1 Types of chemical fluorescent probes

Nowadays, fluorescence probes have been widely developed and used in different fields. In early 2020, the new coronavirus (Covid-19) has turned into a major worldwide outbreak. It has caused a variety of respiratory and intestinal diseases, among a variety of other symptoms and unknown pathologies, and has been associated to a significant lethality causing a huge threat to global public health security. In response to the demand for reliable virus detection and diagnosis, global companies and research institutes have developed many virus detection kits and methodologies. Based on the advantages of strong specificity, high sensitivity, good repeatability, etc., fluorogenic real-time quantitative polymerase chain reaction (RT-PCR) technology is currently the most widely used method, which fully demonstrates the superiority of fluorescence probe.

More generally, detection and recognition of analytes based on fluorescent changes has become a very active field of research. Depending on the various kinds of detected substances, analyte responsive fluorophores can be subdivided into heavy metal ion fluorescent probes,[126] anion fluorescent probes,[127-128] pH fluorescent probes,[129-130] amino acid fluorescent probes,[131-132] *etc*.

1) Heavy metal ion fluorescent probes

Heavy metal ions mainly include three types which can be considered either useful (such as copper, iron, zinc, cobalt, nickel, manganese), harmful (such as lead, cadmium, mercury,

arsenic, thallium) or have neutral or unclear effects (such as titanium, zirconium) to human body. But no matter what kind of metal ion, excess is harm to human body. Therefore, it's a great significance to detect heavy metal ions in the environment, for instance in waste waters or industrial and domestic residues.

In 2016, Yu *et al.*[133] designed and synthesized a pycolyamine-triphenylamine derivative as a nickel probe (**Figure 3-1**). In acetonitrile, upon complexation of nickel ion to the pycolyamine end group of the fluorophore, the intramolecular charge transfer is tuned which causes obvious fluorescence intensity decrease. When competitive chelating agent TPEN (N,N,N',N'-tetrakis(2-pyridylmethyl)ethylenediamine) is added, the maximum emission intensity will increase again, in a reversible fluorescence "on-off-on" process, with a detection limit of nickel ion that reaches 1.83 μM. Finally, the probe was successfully utilized in cell imaging though reversible on-off-on fluorescence changes for quick detection of Ni^{2+} in mitochondria.

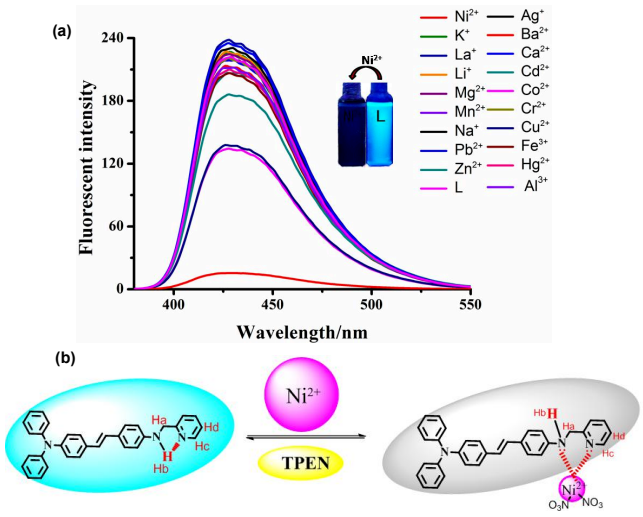

Figure 3-1. Fluorescence spectra of probe L in CH_3CN upon addition of 1equiv. of different nitrate salts. Inset: L and L+Ni^{2+} under UV lamp at 365 nm. (b) A proposed binding mode between probe and Ni^{2+}.

2) Amino acid fluorescent probes

Amino acids (AA) are the basic constituent units of macromolecular proteins. According to the different side chain groups, they can be divided into more than 20 naturally occurring AA, such as glycine (Gly), tryptophan (Trp), aspartic acid (Asn). As AA play an important role in physiological processes, such as protein expression, their overexpression and regulation can be associated with diagnosis and treatment of a variety of diseases. Detecting various AA is also one of the important functions that has been successfully realized with fluorescent probes.

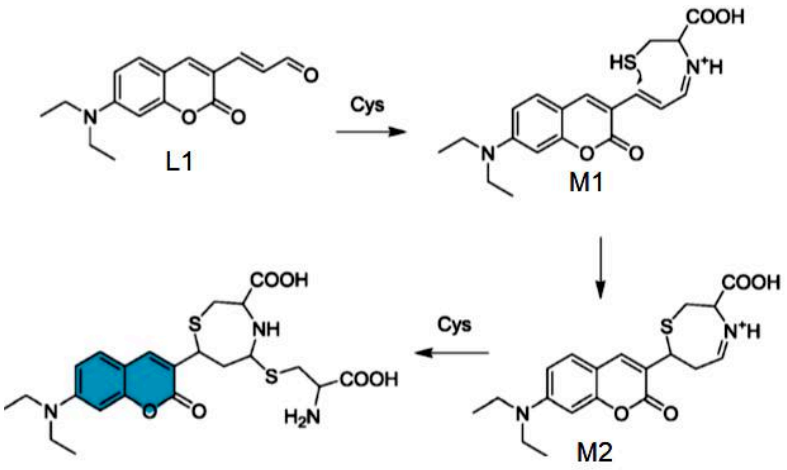

Figure 3-2. The reaction of probe L1 with Cys.

In 2011, Lin *et al*.[134] reported a ratiometric fluorescent probe L1 (**Figure 3-2**), which belongs to coumarin class and could selectively recognize cysteine (Cys). The maximum fluorescence emission peak of probe is at 557 nm, and fluorescence quantum yield is low. After adding Cys, the peak at 560 nm decreases, new peak at 487 nm dramatic appears and gradually increases. The response mechanism could be elucidated that the amino group of Cys initially reacted with aldehyde to afford the imine intermediate M1, which then underwent a ring closure to generate an intermediate M2 that further reacted with one more Cys to form L1-Cys. The process involves a shortening of the conjugation pathway from L1 to L1-Cys,

accounting for the observed spectroscopic evolution.

3) Anion fluorescent probes

Fluorescent probes that recognize anions also have great significance in environmental and biological research. For example, as a physiological by-product of normal aerobic metabolism, reactive oxygen species (ROS) play important roles in redox system, cell growth and proliferation. 1,2 superoxide anion ($O_2^{\bullet-}$) is the most commonly encountered ROS, and the concentration of $O_2^{\bullet-}$ can reflect the degree of overall oxidative stress in organisms. In 2020, Zhang *et al.*[135] have developed a ratiometric fluorescent probe TP-Tfs for $O_2^{\bullet-}$ detection, based on oxidative cleavage of a trifluoromethylsulfonyl (Tfs) cap in **Figure 3-3**. TP-Tfs exhibited good sensitivity and selectivity towards $O_2^{\bullet-}$ with a low detection limit. They have applied TP-Tfs for $O_2^{\bullet-}$ detection in living cells and in vivo during the process of tumor treatment.

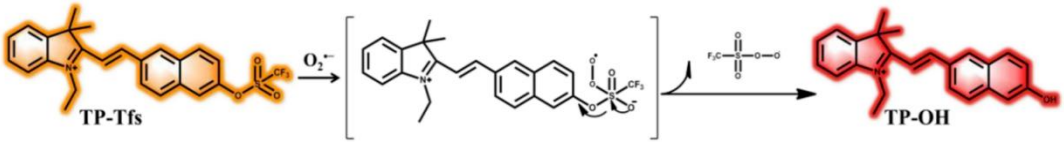

Figure 3-3. The structure of TP-Tfs and its proposed reaction mechanism towards $O_2^{\bullet-}$.

4) pH Fluorescent probes

Acidity and alkalinity also play an important role in biological, physiological and chemical processes. Therefore, the detection of pH is also one of the applications of fluorescent probes. pH fluorescent probes usually have three design strategies:

a. acid-base reaction based on nitrogen-containing heterocycle and amino group;[136-138]

b. acid-base reaction based on phenolic hydroxyl group;[139-140]

c. acid/base mediated rhodamine ring opening and ring closing.[141-142]

Among them, probes with nitrogen-containing heterocycles as recognition groups are more specifically responsive to acid; probes with phenolic hydroxyl groups as recognition sites are more susceptible to alkalis; both are based on a similar principle, *i.e.* the perturbation of the charge transfer processes at the molecular scales. Probes with rhodamine ring opening and closing mechanism work according to a different mechanism but are not highly stable: sometimes metal ions also can cause the ring to open which will bring interference. Thence, it is necessary to design pH fluorescent probes with wide range of pH response and high selectivity and stability.

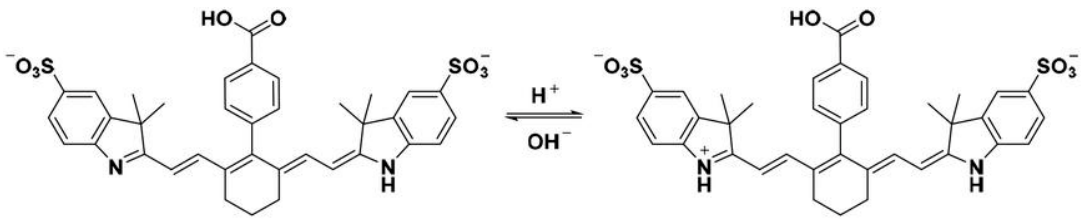

Figure 3-4. The structure of probe and its response mechanism towards H^+.

In 2015, Gilson et al.[143] used an unsubstituted Cy7 dye molecule to obtain NIR fluorescent pH activatable probe for tumor specific imaging (**Figure 3-5**). When pH is decrease, it will induce fluorescence increasing with a pKa at 5.2.

All above depicted fluorescent probes are suitable for solution environment. In actual life or industrial production, thin film or solid-state stimulus responsive fluorescent probes are more and more investigated by researchers because of their advantages such as convenient portability, simple use, easy storage and eligibility to the detection of atmospheric contaminants. It also opens up multiple potential application in such diverse fields as counterfeiting, display, security and defense, *etc*.[144] For all these applications design of an

ideal stimulus responsive probe requires addressing various challenging features such as a high luminescence quantum yield, low detection threshold (sensitivity) and large associated changes in the luminescence in response to the stimulus (specificity).

Solid state occurring photophysical phenomenon such as luminescence caused quenching constitute major hurdles towards the conception of such operative luminescent devices, and severely hampers the performances (in terms of efficiency and sensitivity of the response to the external stimuli) of the resulting component. For that reason, recent progresses in the understanding of the mechanisms associated to the optimization of aggregation induced / solid state emission, and the development of the underlying molecular engineering principles, have been a major breakthrough in the last decade. Among the many chemical entities that have been identified as potential solid state emitters, benzothiazole meet many criterions that, in our opinion, make it as a candidate of choice for the elaboration of acid responsive luminescent materials and devices.

1.2 Objectives

Stimuli responsive probes that undergo reversible switching upon protonation, with large changes in their spectroscopic signatures, and can operate both in solution and in the solid state are of primary importance for the design of advanced sensors and actuators. Inspired by this idea, in this chapter we will design and introduce a series of quadrupolar dyes that display efficient and reversible switching of their spectroscopic properties upon protonation. Their fluorescence properties, that combine large Stokes shift, high luminescence quantum yield and very marked changes depending on protonation state, will make them particularly interesting candidates for sensing devices, as illustrated upon integration of the molecule into

optically transparent polymer film.

2 Design, Synthesis and Optical Properties of new chromophores

2.1 Design strategy

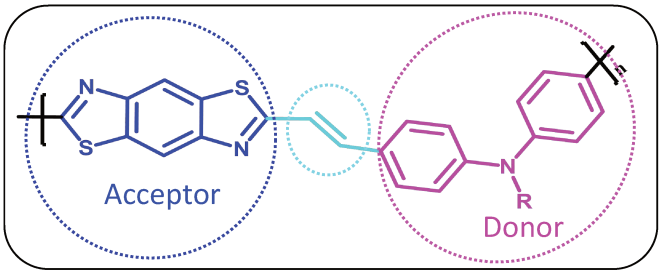

Scheme 1. Structure of aiming compound.

As we know, benzothiazole, containing two heteroatoms sulfur and nitrogen, show a strong electron-withdrawing ability, that make them eligible as electron acceptors in extended dipolar or quadrupolar-conjugated structures.[145] Rigid planar, large conjugated structure and associated electronic transition of benzothiazole-based system usually bring about high luminescence quantum yield and large Stokes shift.[145] Thus, in this chapter, we choose to work on oligomeric derivatives of a quadrupolar structure (DAD type) and design the structure depicted in **Scheme 1**. It consists in a benzobisthiazole moieties here used as acceptor part and diphenylamine as donor part. Introducing a straightforward condensation procedure, we were able to link them together by double bond (C=C) and control the length of the formed oligomers.

2.2 Synthesis and Characterization

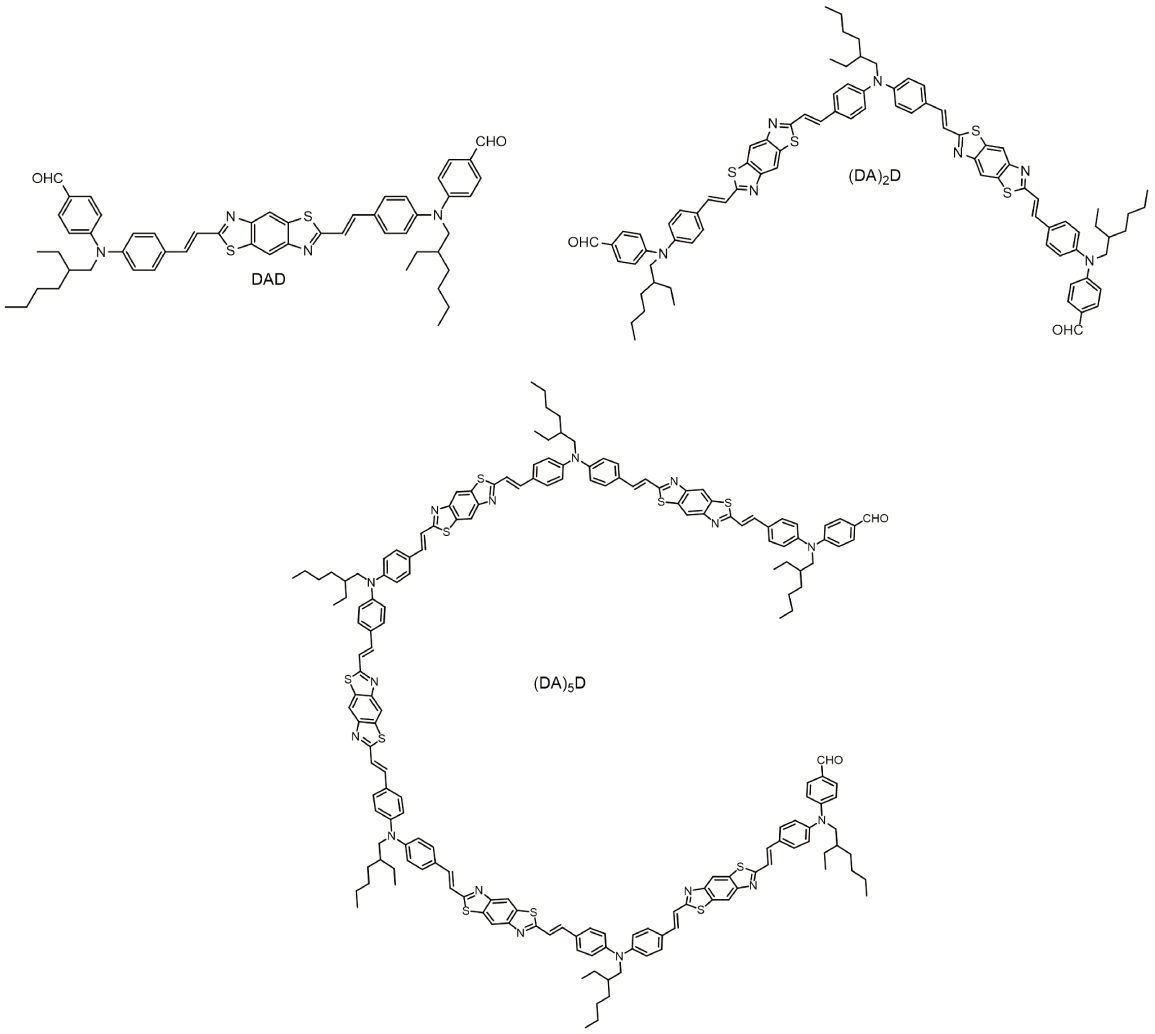

Figure 3-5. The structures of three new chromophores.

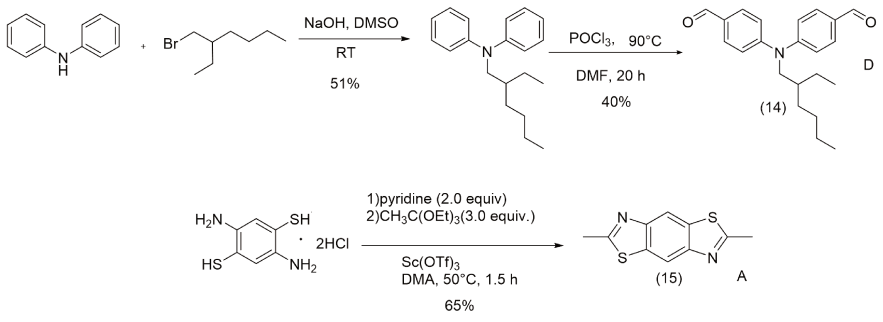

Scheme 2. Synthetic procedure for A and D.

According to the reported method[146], synthesis of all compounds derives from the key synthons A and D. Both molecules can be synthesized in a limited number of high yielding chemical steps from commercially available materials as depicted in **Scheme 2**.

Then, as depicted in **Scheme 3** when involved in a Knoevenagel condensation in a 3:1 (diarylamine (D)/benzobisthiazole (A)) ratio, **DAD** is formed almost exclusively, and only minor amounts of larger oligomers are formed. Interestingly, by playing on the ratio of the individual A and D components, formation of extended version of the target chromophore can be achieved: it is in particular possible to isolate exploitable amounts of **$(DA)_2D$** but also an oligomeric compounds with an average of 5 repeating units **$(DA)_5D$** (**Figure 3-5**), in the presence of equimolar amounts of A and D.

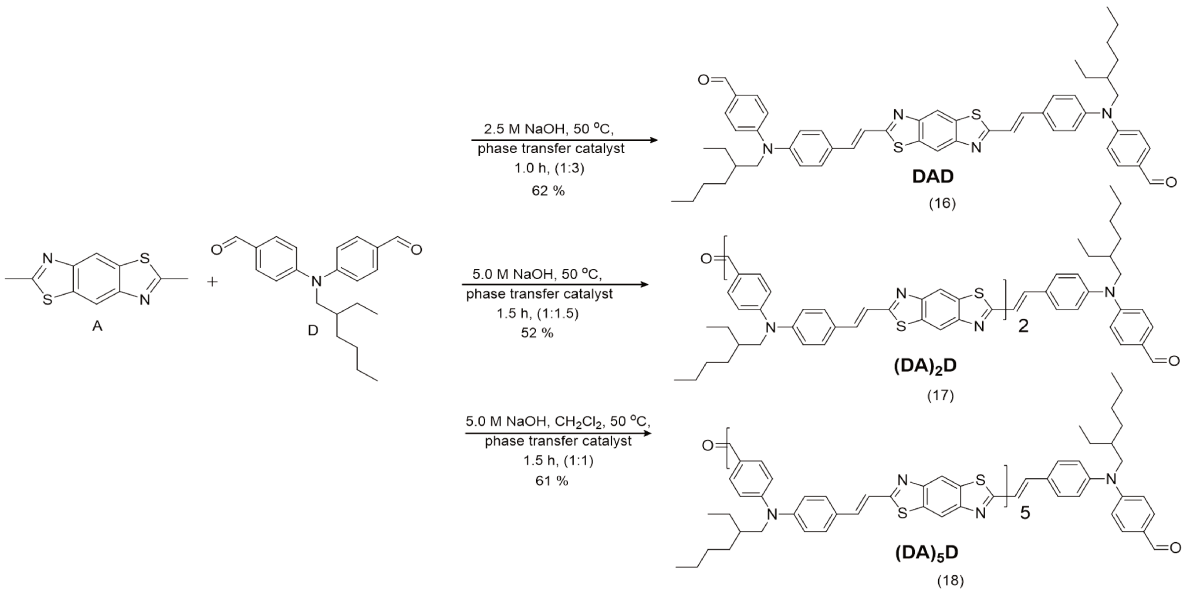

Scheme 3. Synthetic procedure for **DAD**, **$(DA)_2D$** and **$(DA)_5D$**.

Furthermore, as a consequence of the symmetrical nature of the reactants involved in this synthetic procedure, it is worth noting that only D terminated products are obtained, as if the first Knoevenagel step was exacerbating the reactivity of the benzobisthiazole unit in regard with the second one. Molecules were fully characterized, and their purity was assessed by ^{1}H NMR (**Figure 3-6**) and ^{13}C NMR, COSY, HMQC, HMBC and HR-MS. **DAD** and **$(DA)_2D$** are obtained as pure compounds, yet HR-MS shows that **$(DA)_5D$** is obtained a mixture including

shorter and longer oligomeric derivatives.

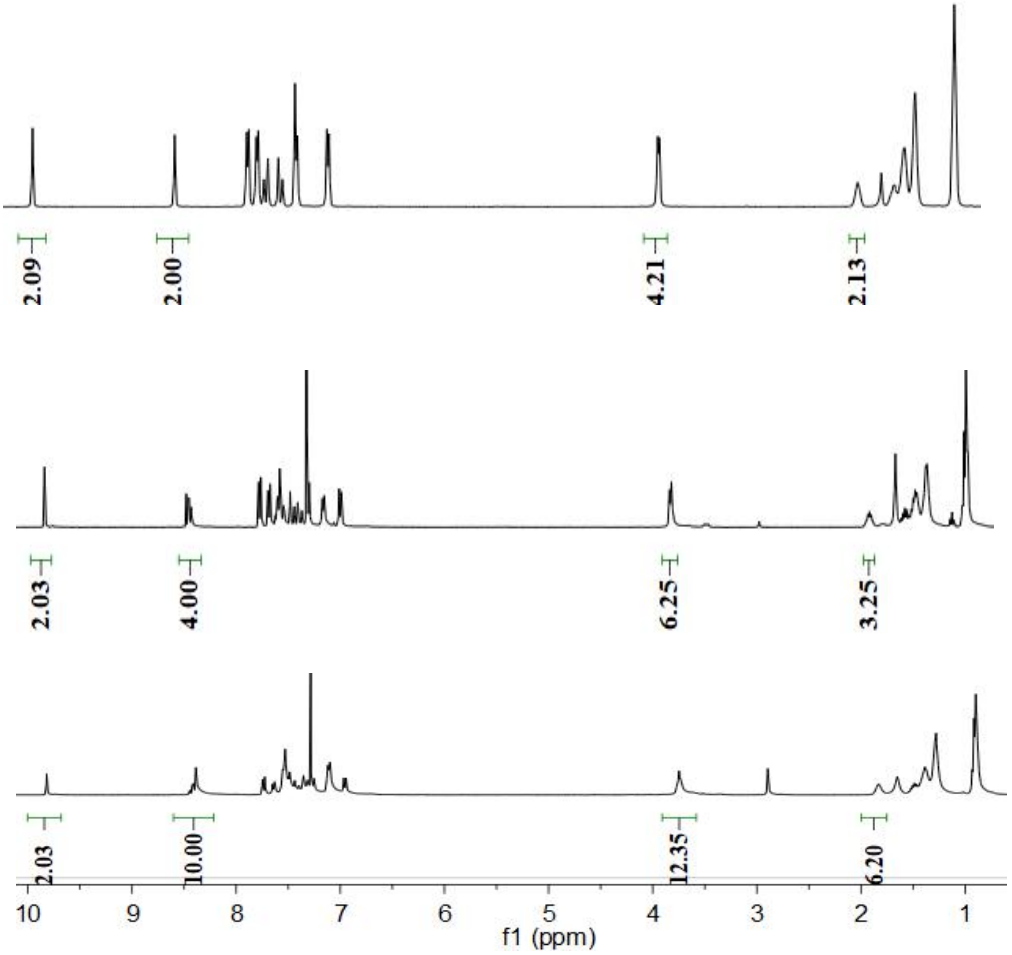

Figure 3-6. **^{1}H NMR** of three chromophores in $CDCl_3$; top **DAD**, middle **$(DA)_2D$**, bottom **$(DA)_5D$**.

2.3 Optical properties of the new family of compounds

It has been established in the past that benzothiazole withdrawing molecules are prone to protonation in highly acidic environment, with a reported pKa *ca* 2 in water[147-148]. Interestingly, protonation of the as-designed benzobisthiazole based architectures will result in a marked increase of the electron withdrawing character of the resulting benzobisthiazolium moieties, further reducing the optical gap and shifting both the absorption and emission spectrum towards the red. As a consequence, protonation translates into a drastic change in the spectral features of the probe, as illustrated in the following.

2.3.1 Main spectroscopic data of the new family of compounds

First, molecules synthesized accordingly were evaluated regarding their photophysical and spectroscopic properties. We list the relevant data of three new compounds **DAD**, **(DA)$_2$D**, **(DA)$_5$D** in **table 1**.

Compound		λ_{max}[a]	λ_{max}[b]	$\Delta\nu$[c]	Φ_f
In solution	**DAD**	430	508	3570	0.32
	(DA)$_2$D	455	531	3145	0.30
	(DA)$_5$D	464	532	2825	0.14
In solid state	**DAD**	440	550	4545	0.44
	(DA)$_2$D	545	604	1792	0.18
	(DA)$_5$D	546	605	1786	0.013

[a] Maximum absorption peak position in nm (1.0×10^{-5} mol L^{-1}). [b] Peak position of maximum emissiom in nm (1.0×10^{-5} mol L^{-1}), excited at the absorption maximum. [c] Stokes shift in cm^{-1}. Φ Absolute quantum yield.

Table 1. Main spectroscopic data of the studied compounds.

In spite of the relatively large structural differences among the series, both absorption and emission (**Figure 3-7**) maximal wavelength turned out to depend little on the length of the π-conjugated skeleton. Only a slight red-shift in the maximal absorption wavelength is observed upon extending the structure from **DAD** to **(DA)$_2$D** to **(DA)$_5$D**. However, comparison in the shape of the UV-Vis absorption spectra of the extended chromophore **(DA)$_2$D** and mostly **(DA)$_5$D** to that of **DAD** clearly reveals the occurrence of conformational disorder in the formers (**Figure 3-7**): as the conjugation pathway is increased absorption band is broadened and a characteristic shoulder is seen at long wavelength. It most likely relates to the presence of different conformations of the molecule, a consequence of Peierl's distorsion,

as often observed in extended oligophenylenethynylene derivatives[149-150].

Influence of the extension of the conjugated skeleton is even weaker regarding the emission signature, which is virtually unchanged in terms of band position and solvatochromism in spite of the suspected Peierls distortion: emission spectra looks very similar among the series (**Figure 3-7**), which either indicates a localization of the exciton on a single **DAD** subunit of the molecule or alternatively relates to inefficient emission of twisted conformations of the molecule.

In agreement with the latter hypothesis, while luminescence quantum yield in chloroform solution is similar in **DAD** and **$(DA)_2D$** (quantum yield *ca* 0.3) extension of the conjugation length in **$(DA)_5D$** results in a significant lowering of luminescence quantum yield of the molecule in solution (quantum yield *ca* 0.14). Interestingly, the effect of this extension is even more detrimental on the solid state emission: while **DAD** experiences a small increase of its luminescence quantum yield in the solid state (0.44) as compared with the solution, that of **$(DA)_2D$** is reduced to 0.18, and solid state luminescence is fully quenched for **$(DA)_5D$**. This suggests that increase in conformational disorder resulting from the extension of the π-conjugated backbone may unfavorably impact the solid state packing of the molecule, which may in turn affect the solid state photophysical properties of the molecule.

As a summary, while extension of the π-conjugated backbone results in a slight red shift and mostly a broadening of the absorption band of the oligomers **$(DA)_2D$** and **$(DA)_5D$** with respect to the reference **DAD**, no relevant evolution is observed in the emission profile. However, luminescence efficiency is significantly reduced in solution and even more at the solid state.

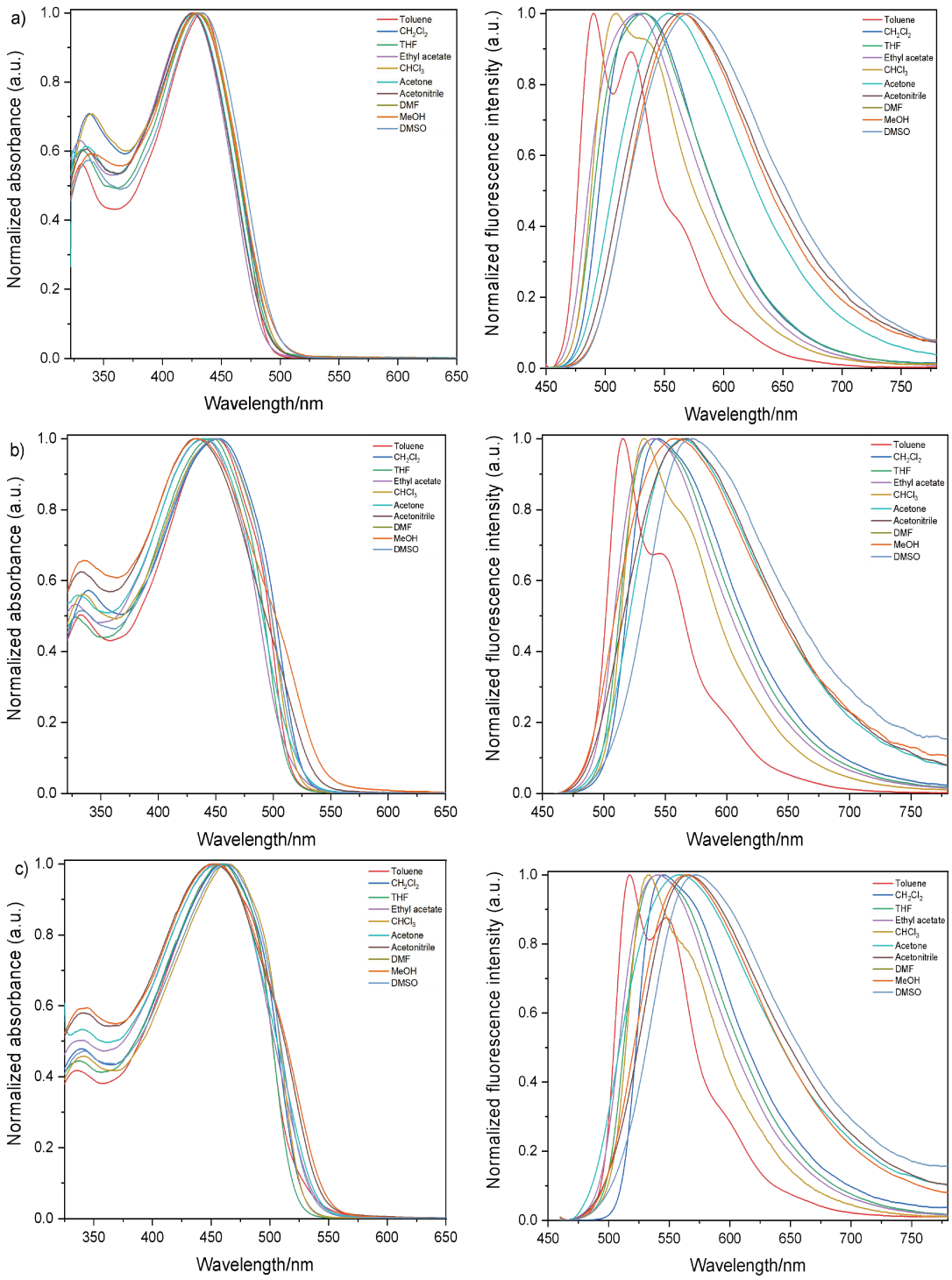

Figure 3-7. Normalized absorption (left) and emission spectra (right) of (a) **DAD**, (b) **(DA)$_2$D** and (c) **(DA)$_5$D** in different solvents. The excitation wavelength is 430 nm, 450 nm, 450 nm, respectively. The concentration is 1.0×10^{-5} mol L^{-1}.

2.3.2 Response to acid of the new family compounds

Because of the presence of a nitrogen atom with an available electron lone pair, benzothiazole ring display basic properties which have recently been taken advantage of in the making of pH probes [151-152]. We decided to further investigate this phenomenon in the following

2.3.2.1 Preliminary screening of the response to acid in solution environment

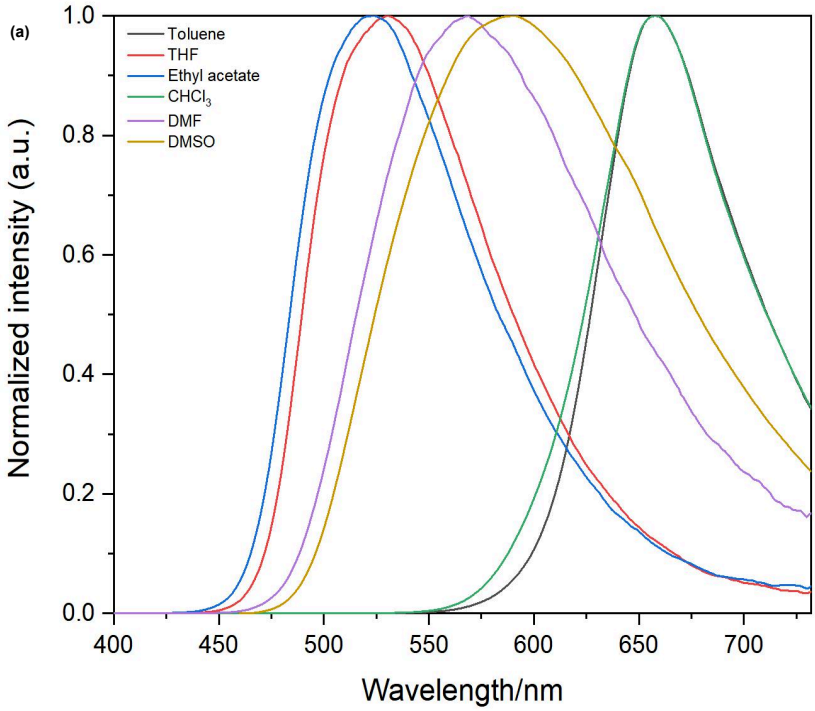

Figure 3-8a. Normalized emission spectra of TFA (50 μL, 0.13 M) added into **DAD** in different solvents. The excitation wavelength is 430 nm. The concentration is 1.0×10^{-5} mol L^{-1}.

First, we carried out a preliminary screening experiment in **Figure 3-8**, adding a similar volume of TFA (50 μL, 0.13 M) into solution of the three compounds in different solvent. Emission spectra reveals that acidification of the medium result in a very marked red-shift in emission for all compounds dissolved in either chloroform or toluene (**Figure 3-8**), indicating that all of them have an obvious response to H^+ in both solvents.

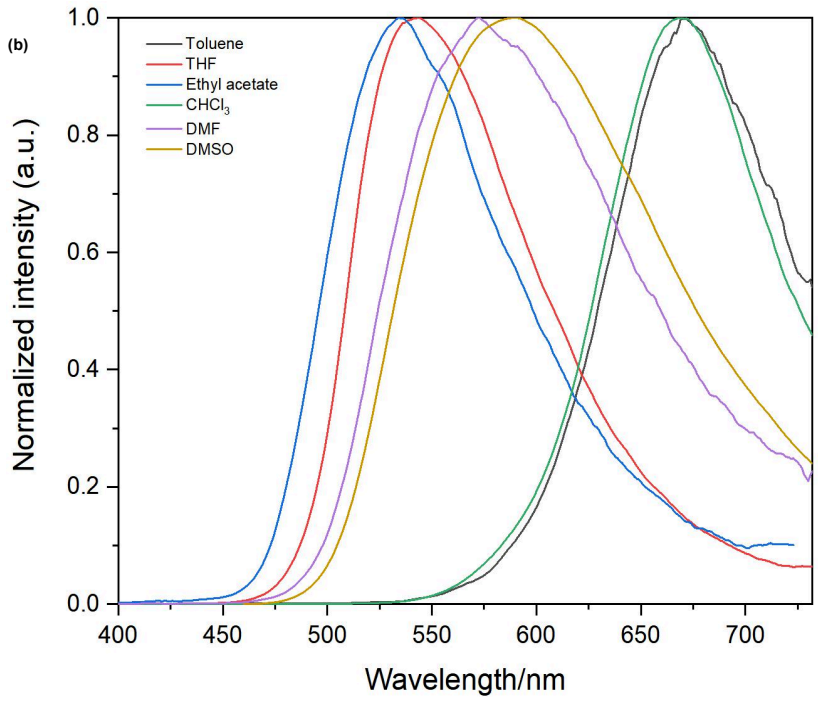

Figure 3-8b. Normalized emission spectra of TFA (50 μL, 0.13 M) added into **$(DA)_2D$** in different solvents. The excitation wavelength is 450 nm. The concentration is 1.0×10^{-5} mol L^{-1}.

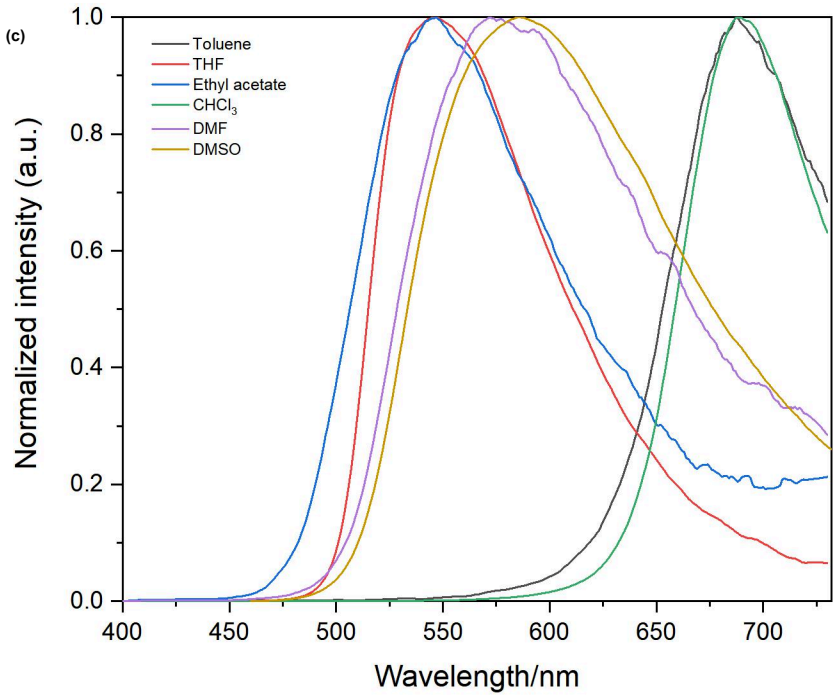

Figure 3-8c. Normalized emission spectra of TFA (50 μL, 0.13 M) added into **$(DA)_5D$** in different solvents. The excitation wavelength is 450 nm. The concentration is 1.0×10^{-5} mol L^{-1}.

In all other solvents no significant changes are observed upon addition of TFA, indicating that no protonation occurs at this acid concentration in these solvents. In the

following, we decided to focus our investigation on chloroform, which seemed like the best suited solvent.

To more precisely assess the dependence on the response on molecular structure, we compared evolution of the luminescence of **DAD**, **$(DA)_2D$**, **$(DA)_5D$** upon addition of TFA in chloroform (**Figure 3-9**).

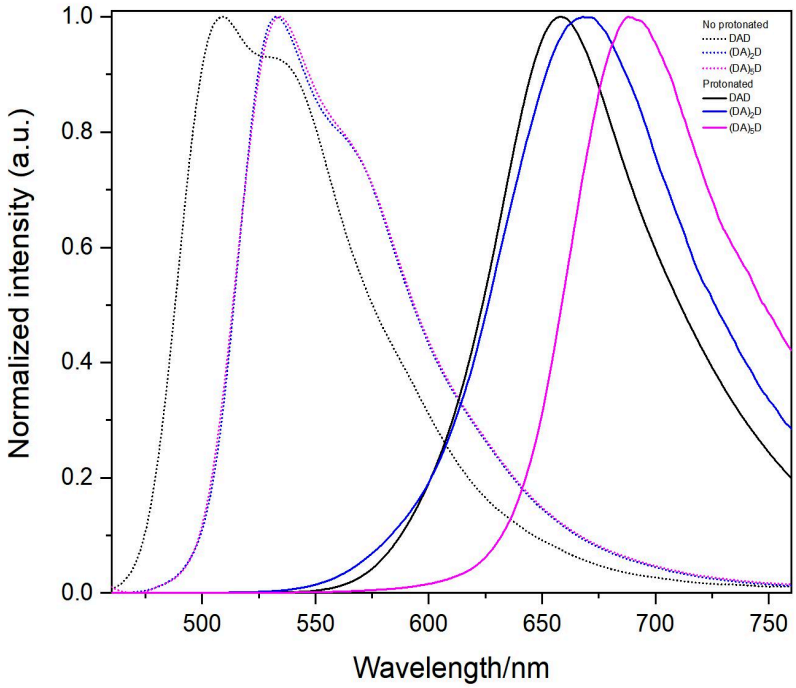

Figure 3-9. Normalized emission spectra of **DAD**, **$(DA)_2D$** and **$(DA)_5D$** in $CHCl_3$ at no protonated and protonated (added TFA (50 μL, 0.13 M)) condition. The excitation wavelength is 430 nm, 450 nm, 450 nm, respectively. The concentration is 1.0×10^{-5} mol L^{-1}.

As the emission spectra in **Figure 3-9** shows, after adding TFA (50 μL, 0.13 M), **DAD** (quantum yield *ca* 0.06), **$(DA)_2D$** (quantum yield *ca* 0.03) and **$(DA)_5D$** (quantum yield *ca* 0.01) display around 4464 cm^{-1}, 3826 cm^{-1}, 4191 cm^{-1} red shift respectively. It is seen that, while the resulting emission appears a little more red shifted for longer oligomeric molecules, the emission efficiency is, here again, significantly decreased.

2.3.2.2 Response to acid in solid environment

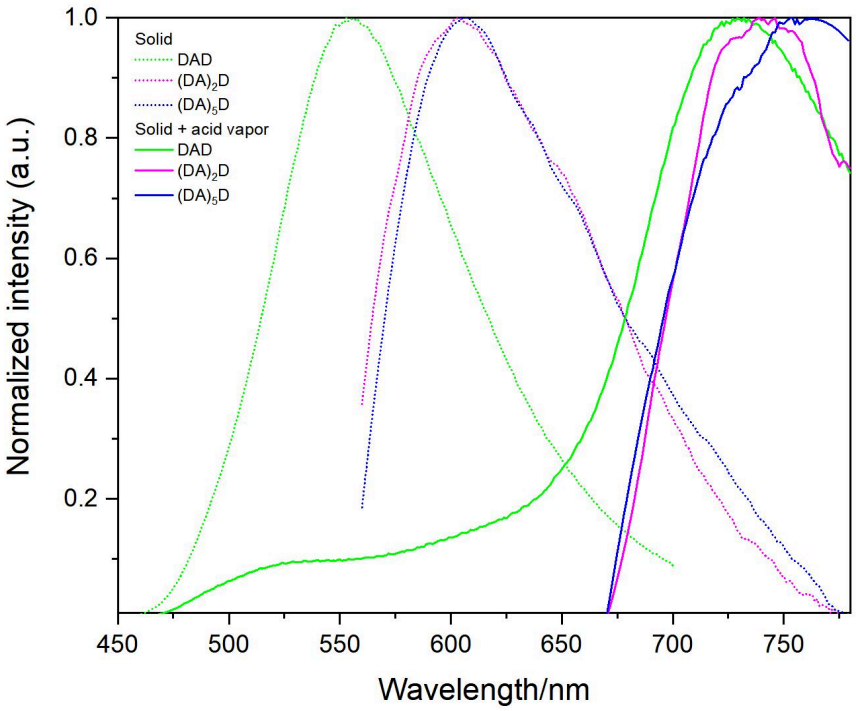

Figure 3-10. Emission spectrum in solid state of **DAD**, **$(DA)_2D$**, **$(DA)_5D$**, excitation wavelength at 440 nm, 545 nm, 545 nm respectively; with acid vapor in solid state of **DAD**, **$(DA)_2D$**, **$(DA)_5D$**, excitation wavelength at 565 nm, 658 nm, 658 nm respectively.

Then we looked at the solid state response of the chromophores: solutions of each compound in chloroform was casted onto a glass plate and left overnight, until the solvent is completely evaporated. A solid layer was thus obtained on the glass surface. The prepared film was attached on the top of a small glass vial (5 mL) and put into a bigger glass becher containing TFA solution. The becher was capped, leading to acidic vapor accumulation: meanwhile, the emission of the film changed quickly from yellow to dark red when irradiated under 365 nm UV light. **Figure 3-10** show the spectral changes in luminescence upon vapor exposition, which is characterized by an even more red shifted emission maximum (beyond 700 nm) compared to solution. While **DAD** still remains more intensively emissive (quantum yield *ca* 0.07), the others show an almost fully quenched emission.

While all three compounds display compelling responsiveness of their emission properties towards protonation, **DAD** looks as the most promising, because of a much more intense emission efficiency. In the rest of the studies we focused on **DAD** for further investigations.

2.3.3 Sensitivity of DAD's response to acid

2.3.3.1 Dependence of the response to acid concentration

Solvent	Condition	$\lambda_{max}{}^{a}$	$\lambda_{max}{}^{b}$	$\Delta\nu^{c}$	Φ_f
Toluene	Nonprotonated	433	479	2217	0.35
	TFA	472	619	5031	0.21
	Excess TFA	554	648	2618	0.12
Chloroform	Nonprotonated	430	508	3570	0.32
	TFA	470	640	5651	0.10
	Excess TFA	552	656	2872	0.06

[a] Maximum absorption peak position in nm (1.0×10^{-5} mol L^{-1}). [b] Peak position of maximum emission in nm (1.0×10^{-5} mol L^{-1}), excited at the absorption maximum. [c] Stokes shift in cm^{-1}. Φ Absolute quantum yield. In toluene, the concentration of TFA is 0 (no protonated), 25 mM (slight excess TFA) and 75 mM (larger excessTFA) respectively; In chloroform, the concentration of TFA is 0 (no protonated), 75 mM (slight excess TFA) and 125 mM (larger excessTFA) respectively.

Table 2. Main spectroscopic data of the **DAD** in toluene and chloroform in different acid concentration conditions.

First, we carried out the following experiment: adding mild excess TFA (10 μL, 25 mM) and large excess (30 μL, 75 mM) TFA into toluene solution of **DAD** (quantum yield *ca* 0.21 and 0.12 respectively, in **Figure 3-11b**); or adding mild or large excess TFA (30 μL, 75 mM and 50 μL, 125 mM; quantum yield *ca* 0.10 and 0.06 respectively, in **Figure 3-11a**) into chloroform solution of **DAD** (in chloroform solution more TFA should be added in order to

reach a similar protonation as with in toluene), we studied the evolution in absorption and emission characteristics of the compound. **table 2** list the basic spectroscopic data of **DAD** in these two solvents.

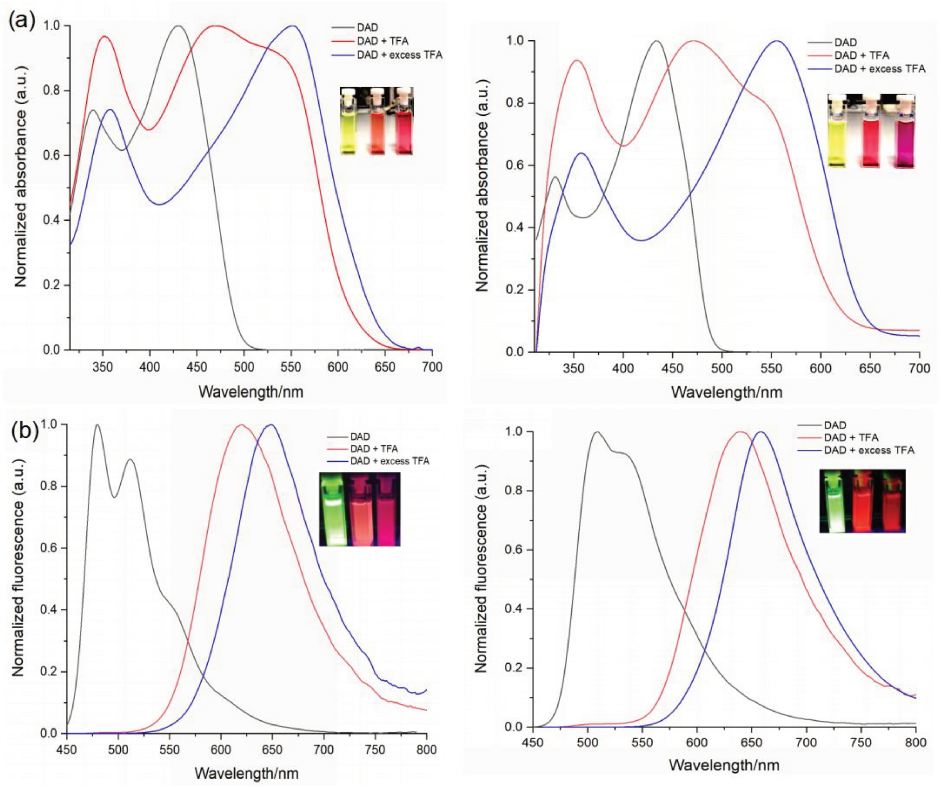

Figure 3-11. absorption (a) and emission (b) spectra of a solution of **DAD** in chloroform (right) and toluene (left), before (black) and after (red and blue) addition of TFA.

The absorption and emission spectra obtained in both solvents illustrate the same evolution: three distinct signatures, highlighted in black, red and blue in **Figure 3-11** can be attributed to the three different protonation state (unprotonated: black; monoprotonated on one of the thiazole units: red; deprotonated on both thiazole units: blue) which are successively attained upon incremental addition of TFA. This interpretation is confirmed by time dependent density functional theory (TD-DFT) calculations, which were conducted by Tangui le Bahers, at the LCENS, at the B3LYP/6-31G(d) level: theoretical position of the absorption

maxima calculated for the three protonation state are in good agreement with experimental data (**table 3**).

DAD	$\lambda_{max,\ exp1}$(nm)	$\lambda_{max,\ cal}$ (nm)
nonprotonation	430	415
monprotonation	470	478
bisprotonation	552	517

Table 3. Absorption of experimental (λ_{exp}) and calculated wavelength (λ_{cal}) for **DAD** different protonation states.

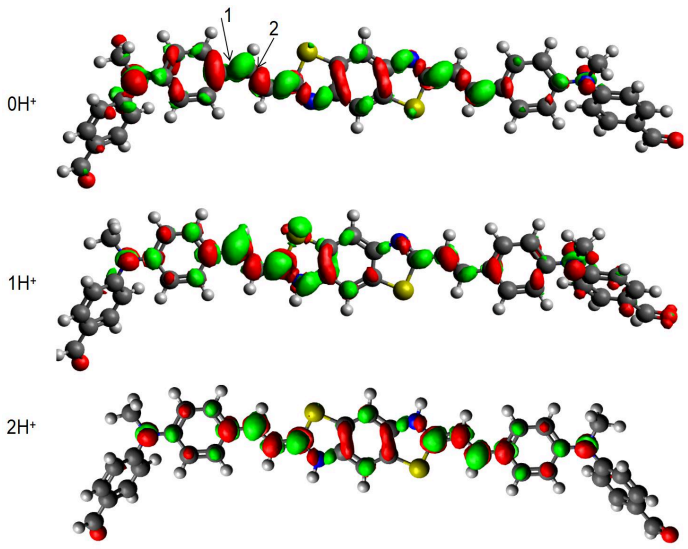

Figure 3-11c. Computed evolution of the electronic distribution between ground and lowest lying excited state for non protonated ($0H^+$), monoprotonated ($1H^+$), bisprotonated ($2H^+$) **DAD.** Red lobes correspond to a depletion in electron density, green lobes to an enrichment.

The optimized structures for the three protonation states, and the associated variations in electron density distributions between the ground and lowest excited state (**Figure 3-11c)** show (i) a lowering of the charge transfer character between the electron donating and withdrawing moieties of the molecule, towards a more evenly distributed electron density, with alternation of electron enriched and electron spoiled carbons, typical of a cyanine transition; (ii) a lowering of the bond length alternation from 0.1 Å for the nonprotonated

DAD ($0H^+$) to 0.05 Å for the bis protonated (between adjacent bonds 1 and 2 as featured in **Figure 3-11c**) with the degree of protonation.

As a consequence, protonation of the molecule is easily perceived by the naked eye, both in absorption (color of the solution changing from yellowish to purple) and emission under UV light (from greenish to deep-reddish) in **Figure 3-12**.



Figure 3-12. Photo of **DAD** solution with TFA concentration is increasing 0, 10 μL (25 mM), 20 μL (50 mM), 30 μL (75 mM), 40 μL (100 mM), 60 μL (150 mM), 80 μL (200 mM), 200 μL (500 mM), 400 μL (1 M), the color is gradually change from yellow to purple/ red, a) Observing undersunlight; b) Observing under 365 nm lamp. The concentration of **DAD** solution is 1.0×10^{-5} mol L^{-1} in chloroform.

2.3.3.2 Quantitative assessment on the response to acid

Attempts to quantify the sensitivity of the **DAD** as an acid responsive probe, and evaluate its detection limit, were performed by incremental addition of TFA into a 1.0×10^{-5} mol L^{-1} solution of **DAD** in chloroform: protonation could be easily monitored by plotting the ratio of the emission intensity at the respective maxima of the protonated form and the native neutral form of **DAD** (I_{625} / I_{535}) *vs* added concentration of TFA.

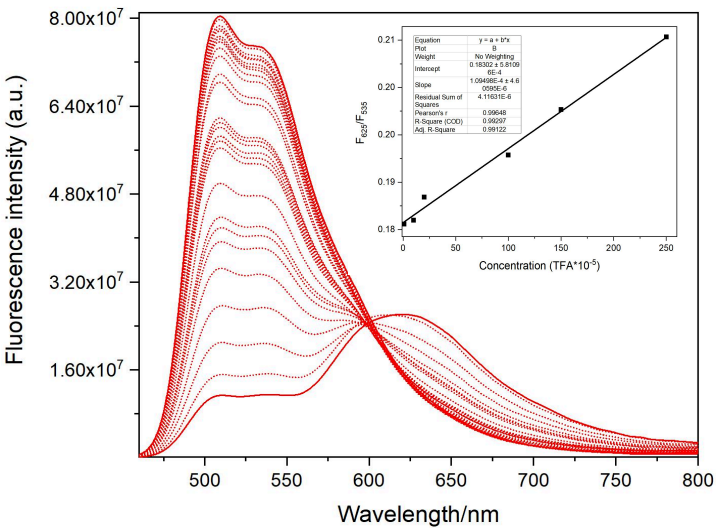

Figure 3-13a. Titration of **DAD** solution (1.0×10^{-5} mol L^{-1}) in chloroform with different concentrations of TFA (from 0 - 10 mM). (Inset) linear fitting of the ration of the emission intensity at 625 nm and 535 nm (I_{625}/I_{535})

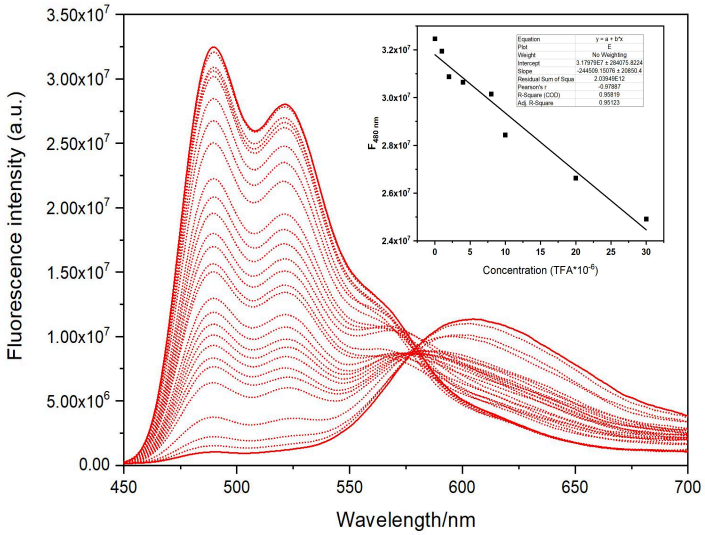

Figure 3-13b. Titration of **DAD** solution (1.0×10^{-6} mol L^{-1}) in toluene with different concentrations' TFA (from 0 - 5 mM). (Inset) linear fitting of the ration of the emission intensity at 480 nm.

A characteristic evolution is achieved, which could be fitted to a linear trend in agreement with existing literature.[154a] From the slope of the obtained line and the associated mean standard deviation, a detection limit (3Sb/m, where m is the slope of the calibration curve and Sb is the blank standard deviation) of 30 μM in chloroform could be extrapolated (**Figure 3-13a**). The same titration experiment in toluene was also conducted by addition of different concentration TFA into a 1.0×10^{-6} mol L^{-1} solution of **DAD**: a similar result was observed in

Figure 3-13b, the detection limit was calculated in 4 μM.

In both of these two figures **3-13a** and **3-13b**, position of the emission band associated the newly formed species (ca 600nm and 625 nm in toluene and chloroform, respectively) confirm that in the investigated range of concentration, only monoprotonation occurs (consistant with the qualitative experiments depicted above); moreover, the presence of an isosbestic point throughout the titration (in chloroform, toluene data shoud be re-recorded) suggest that the two consecutive protonation events take place sequentially, with a large difference in associated equilibrium constant: in other words the second protonation event is thermodynamically much less favored that the first one, most probably because of the high enthalpic cost associated to the formation of a biscationic species.

2.3.3.3 Mechanism study by NMR titration and reversibility experiment

In order to further study the phenomenon and confirm localization of the protonation on the thiazole rings of the molecule, NMR titration was performed by incremental addition of TFA onto the **DAD** molecule dissolved in $CDCl_3$ (4.0×10^{-2} $mol\cdot L^{-1}$; in **Figure 3-13**). Distinctive shifts of the proton signals could be pointed out, which affect mainly the aromatic singlet proton of the benzobisthiazole unit (shifted downfield), and the protons of the neighbouring ethylene bridge (downfield shift and additional "splitting" of the chemical shifts. Interestingly, changes in the chemical shifts are progressive; moreover no breaking of the molecule's centrosymmetry could be evidenced at the NMR timescale, and the peaks remained narrow and well resolved: this seemingly indicates that protonation equilibrium is fast at the NMR timescale, and that, at NMR concentrations (about two order of magnitude higher than those used for fluorescence), double protonation of the basic sites is

simultaneously rather than sequentially achieved.

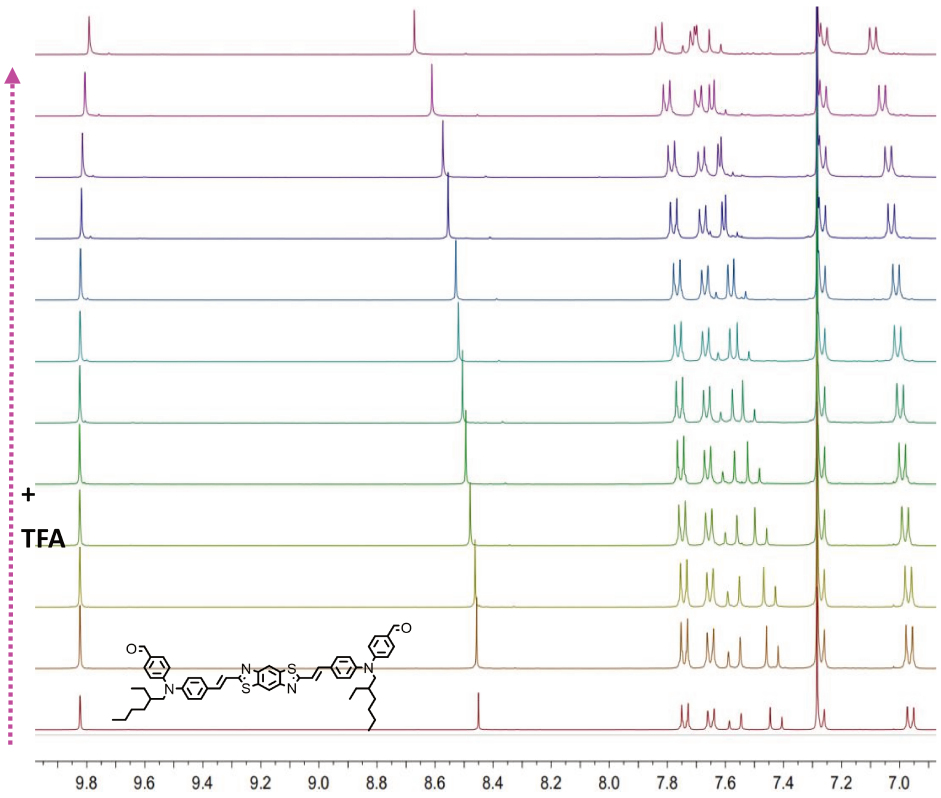

Figure 3-13. NMR (400 Hz, $CDCl_3$ solvent) titration of **DAD** with adding different concentrations of TFA (0, 0.02 eq., 0.06 eq., 0.10 eq., 0.2 eq., 0.6 eq., 1.00 eq., 2.00 eq., 4.00 eq., 8.00eq., 12.00 eq., 20.00 eq.)

Addition of excess trimethylamine (TEA) into the NMR tube containing protonated **DAD**$^{2+}$ fully restored the initial greenish luminescence characteristic of the nonprotonated form. Reversibility of the protonation process was also confirmed by concomitant evolution of the NMR spectrum (**Figure 3-14**), where chemical shifts following TEA addition closely resemble that obtained prior to TFA titration.

Reversibility and recyclability of the process was also assessed by spectrofluorimetric measurements. Characteristic switching of the luminescence between the typical signature of the **DAD** and **DAD**$^{+}$ forms could be achieved by successive addition of TFA (**DAD** → **DAD**$^{+}$) and TEA (**DAD**$^{+}$ → **DAD**) into a chloroform solution of **DAD** (1.0×10^{-5} mol L^{-1}). Luminescence measurements did not show significant lowering of the luminescence response

after 5 cycles of TFA/TEA addition in **Figure 3-15**, illustrating the good reversibility of the process, and thus the potential of the molecule as a reversible proton sensor.

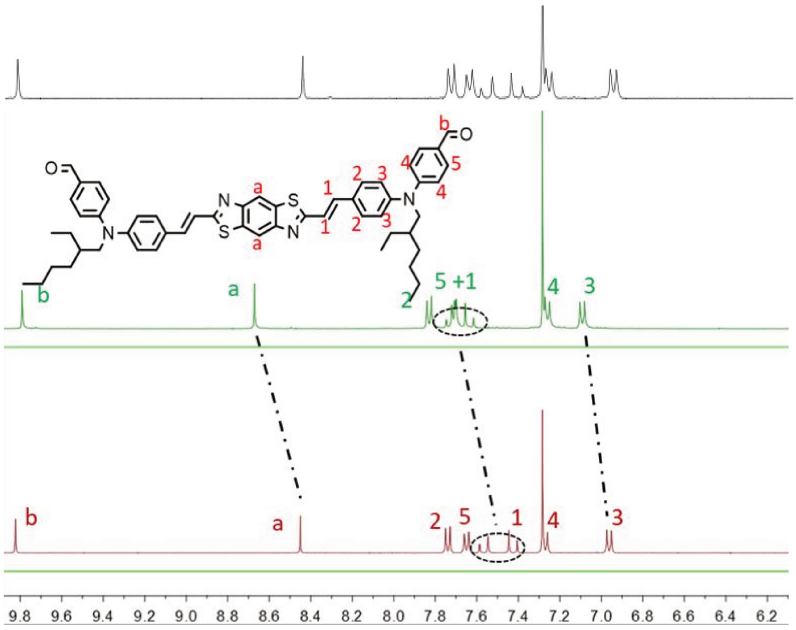

Figure 3-14. Close-up on the aromatic region of the NMR spectra of **DAD** in $CDCl_3$, after dissolution (bottom) addition of TFA (middle) addition of excess triethymaine (top) with proton attribution, main changes in chemical shifts are highlighted as dotted lines.

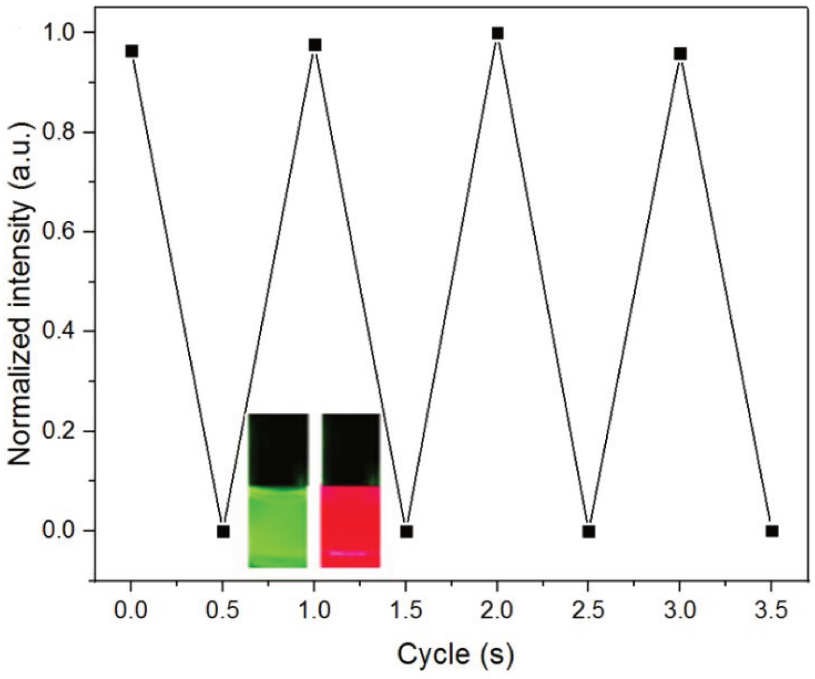

Figure 3-15. Reversibility of luminescence switching upon successive additions of TFA and TEA, based on the intensity of the 508 nm luminescence; each cycle corresponds to a consecutive addition of TFA (half integers

values) and TEA (integer values); Inset: appearance of the fluorescence cuvette in neutral/basic (green) and acidic (red) medium.

3 Incorporation of molecules into devices

In the former section we show that the solution performance of **DAD** based chromophore could be translated at the solid state (powder), this is an important feature in view of the making of device, so we addressed the process ability of our compound into functional thin films or materials

3.1 Reversible switching to acid vapor in solid state

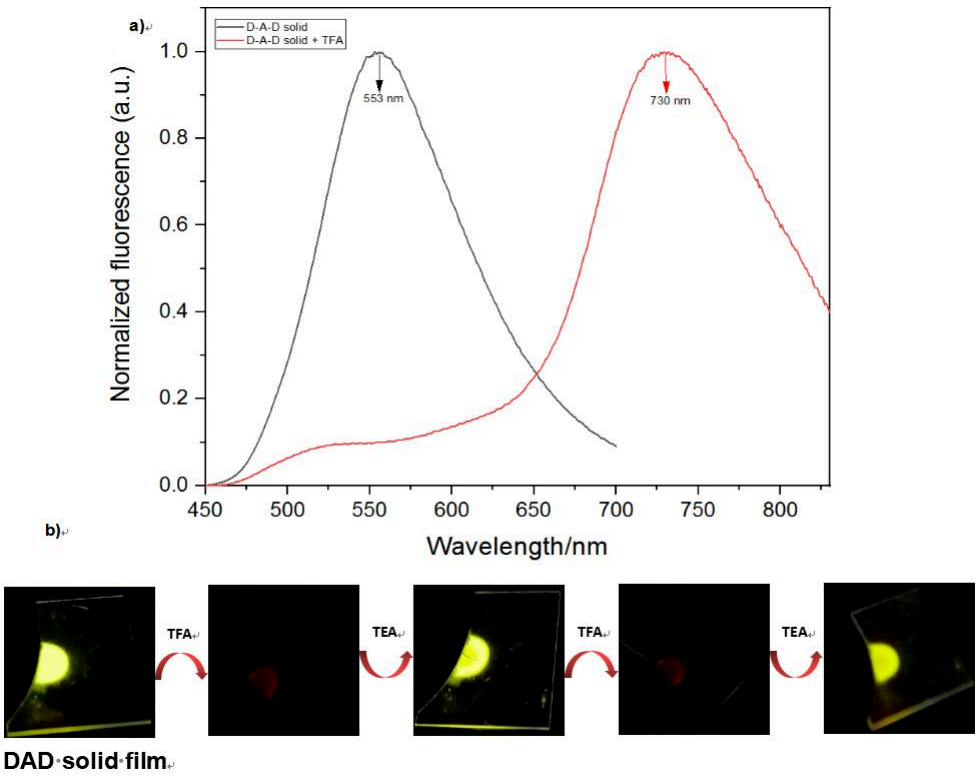

Figure 3-16. a) Emission spectrum of (**DAD**) and (**DAD** + acid vapor) in solid state; b) Luminescence switching of solid **DAD** upon exposure TFA vapors and trimethylamine.

Even more interestingly the reversible switching properties translated well to the solid state: deposition of a thin film of **DAD** powder on a glass plate (by simple evaporation of a

concentrated THF solution) followed by exposure to TFA vapors (following the previously described protocol) resulted in almost instantaneous change in the powder color and luminescence under UV light (from greenish to reddish). Conversely, exposure of the resulting protonated reddish material to TEA vapors fully restored the initial luminescence of the native material in **Figure 3-16b**. The cycle could be repeated several times. **Figure 3-16a** shows the associated evolution of the emission spectra of solid **DAD** and **DAD** upon exposure to acid vapor.

3.2 Polymer thin films of DAD response to acid vapor

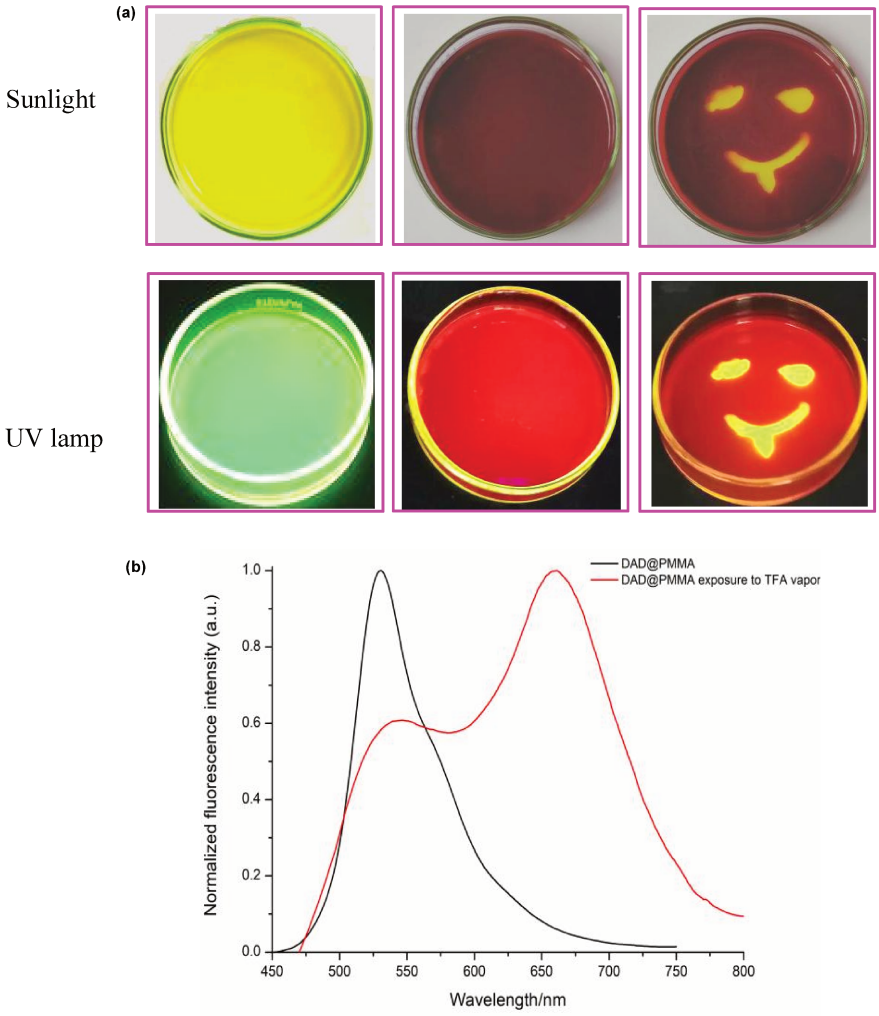

Figure 3-17. a) Pictures of **DAD@PMMA** (left); **DAD@PMMA**+TFA vapors (middle); **DAD@PMMA**+TFA **vapors**+ammonia solution (right); b) Emission spectrum of **DAD@PMMA** and **DAD@PMMA**+TFA vapor.

With the aim to further establish the potential of the newly designed molecules regarding their integration into functional devices, polymeric films were prepared and drop casted onto glass substrate. Incorporation into **PMMA** (**DAD@PMMA**) coated the glass surface with a thin, brittle and optically transparent film. We first evaluated the luminescence efficiency of the film obtained with this procedure: a quantum yield as high as 0.5 was obtained, in good agreement with the data obtained for the powdered compound (0.44) underlining its potential interest for its application in fluorescent functional devices.

Subsequently, exposure to TFA vapors resulted in a rapid change of the film's color, from bright yellowish to dark reddish. This process also came with a concomitant change in the associated fluorescence as visualized under 365 nm UV lamp, from greenish to orange-reddish, as a clear evidence of the protonation event (quantum yield *ca* 0.13). Fluorescence spectra was monitored (**Figure 3-17b**), revealing that only partial protonation was achieved, yet this extent of protonation largely afforded easy visual detection of the acid exposure. Upon exposing this protonated film to ammonia solution vapors, full recovery of the initial state was achieved. As an illustration of the sensitivity of the process, deposition of a drop of ammonia at the surface of the film lead to selective recovery exclusively on the exposed spot, as illustrated in **Figure 3-17a**.

Similarly, a thin, flexible membrane could be obtained by applying a similar protocol, substituting **PMMA** for **polystyrene** (**DAD@PS**) in **Figure 3-18** bottom. In this case, luminescence quantum yield was 0.49 and a color change from yellowish to orange was also observed when exposed to the acid vapor. This flexible membrane is convenient as a fluorescent functional device in practical applications.



DAD@PS **DAD@PS**+TFA vapor

Figure 3-18. The photo of **DAD@PS** (left and middle), **DAD@PS+TFA** vapors under sunlight.

4 Cell Imaging

Based on the excellent luminescence efficiency of **DAD**, in wavelength relevant for biological systems, we tried to explore another possible application in cell imaging. Although attempt to observe protonation in acidic physiological medium did not succeed, we envision that its dual solid state/solution emission properties could result in interesting properties as contrast agents.

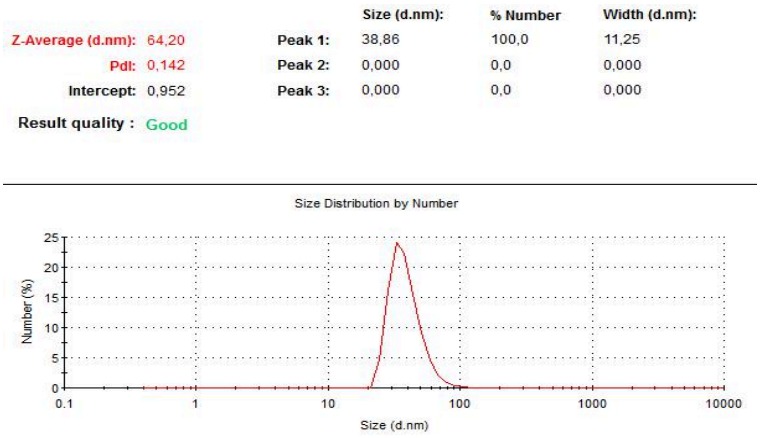

Figure 3-19. Dynamic light scattering of **DAD** suspension; The concentration is 1.0×10^{-5} mol L^{-1}.

First, suspension of **DAD** was prepared by dropwise addition of concentrated **DAD** solution in DMSO into pure water to obtain the suspension, with a final concentration of **DAD** = 1.0×10^{-5} mol L^{-1}. DLS measurements (**Figure 3-19**) showed the formation of small particles with an average diameter *ca* 65 nm and a PDI value of 0.142 which indicate that

DAD forms uniform nanoparticles of suitable size for cell imaging.

We thus investigated the capability of **DAD** in cell staining. HeLa cells were incubated with 10 μM DMSO solution of **DAD** at 37 °C for 30 min and washed three times with phosphate-buffered saline (PBS, pH = 7.4). Then we performed fluorescence imaging using the confocal fluorescence microscopy mode on an Olympus FV 1000 confocal laser-scanning microscope. These images (**Figure 3-20**)clearly revealed that the fluorophores within the suspension can penetrate cell membrane and stain the cytoplasm. These preliminary measurements illustrated that **DAD** could successfully stain HeLa cells.

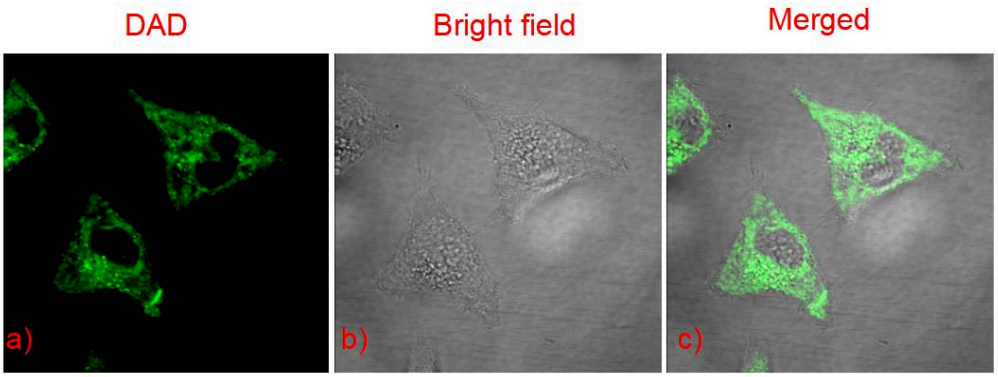

Figure 3-20. Fluorescence confocal images of HeLa cells with a)**DAD**; b) bright field; c) merged.

5 DAD-loaded Albumin in Bovine Serum (BSA)

Bovine serum albumin (BSA) **(Figure 3-21**) is a globular protein in bovine serum. It contains 583 amino acid residues, has a molecular weight of 66.430 kDa, and an isoelectric point of 4.7. The surface charge (Zeta potential) of BSA in solution is affected by the pH of the solution [153-155].

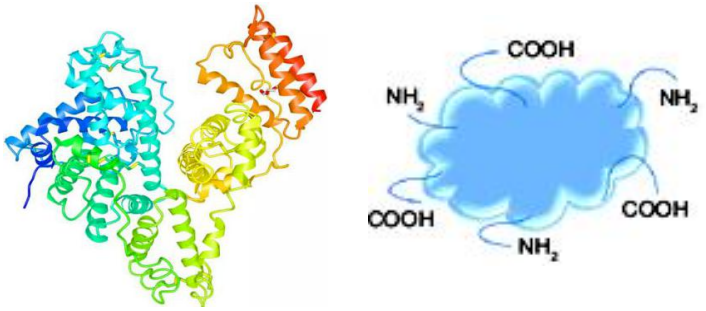

Figure 3-21. Spatial structure (left) and graphical structure (right).

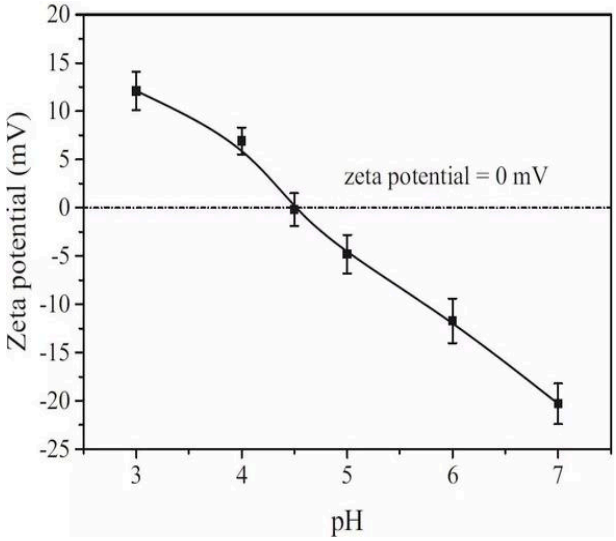

Figure 3-22. Relationship between BSA surface charge and pH (BSA concentration is 15 mg mL^{-1}).

When pH is higher than its isoelectric point, the BSA is negatively charged; conversely, when it is lower than the isoelectric point, it is positively charged (**Figure 3-22**). The surface of BSA contains a large number of carboxyl and amino groups which can be used for the binding of activated groups on the surface (such as the free carbonyl moieties present in **DAD**). Meanwhile, when poorly water-soluble substances are loaded to BSA, they will be transported more easily into biological environment.

Therefore, in order to improve the bioavailability of **DAD**, we encapsulated it within bovine serum albumin to obtain nanoparticles (NPs). 13 mg of BSA were dissolved in 5 ml H_2O, 4 ml of THF containing a predetermined amount of **DAD** (5%, weight ratio) were added

dropwisely into the aqueous solution of BSA under sonication at room temperature. The residual THF was removed by rotary evaporation under vacuum.

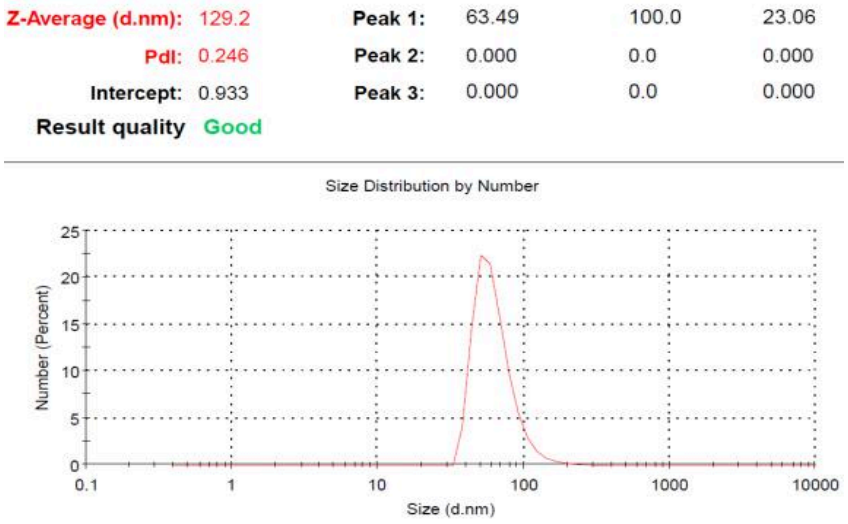

Figure 3-23. The dynamic light scattering experiment of **BSA loaded DAD**.

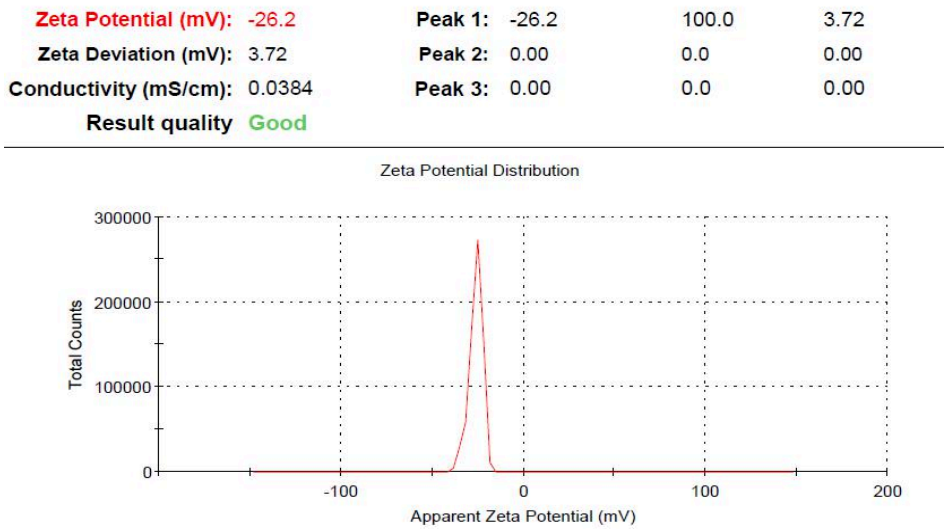

Figure 3-24. Zeta potential of **BSA loaded-DAD**.

The size of loaded-NPs and its PDI was measured by DLS (**Figure 3-23**). Compared with unloaded-NPs, size of **BSA loaded-NPs** is 129.2 nm and PDI value is 0.246 which show that after loading BSA, the NPs look larger and less uniform than the pristine "pure" **DAD** suspensions depicted above. In this case, quantum yield of 0.036 was measured

We also measured the Zeta potential of **BSA loaded-NPs** (**Figure 3-24**), the negative

value of -26.2 mV indicates the NPs are surrounded by outer layers of ionized carboxylic groups.[156]

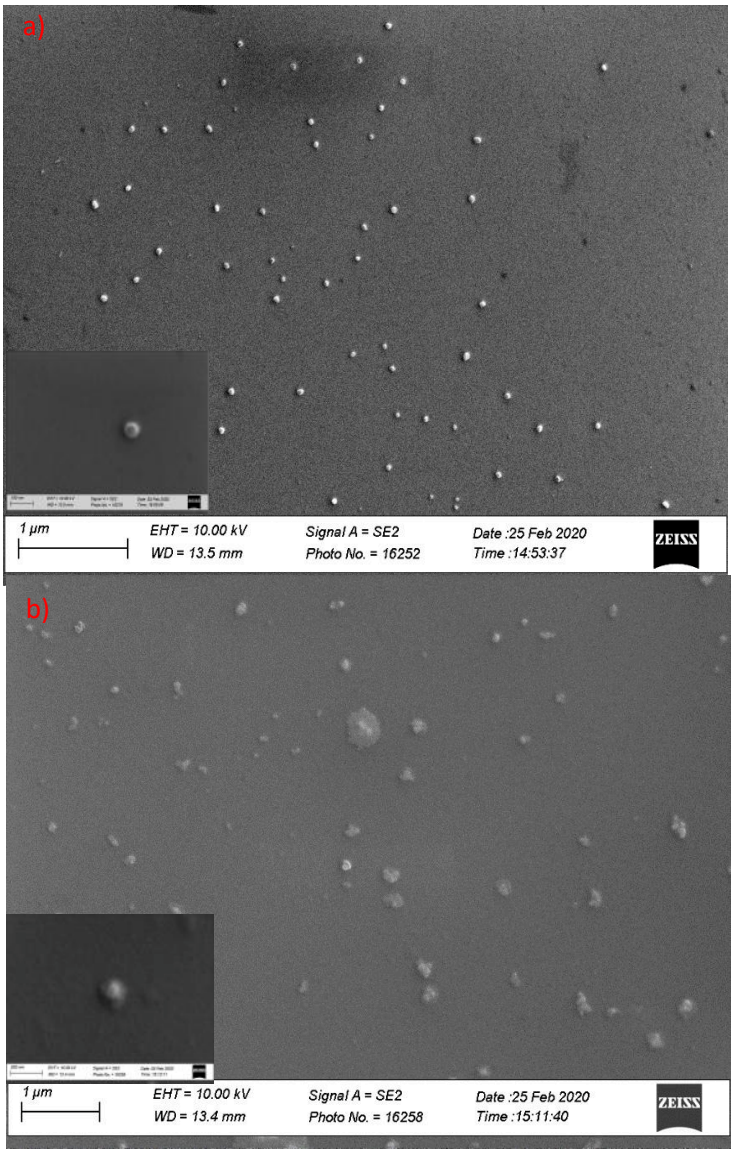

Figure 3-25. SEM images of **DAD** (a) and **BSA loaded DAD** (b).

In order to confirm the formation and clearly see the morphology of the nanoparticles, we performed scanning electron microscope experiment (**Figure 3-25**) and compared the size and morphology of particles obtained upon suspension of pure **DAD** with those observed in the presence of BSA. These images confirmed the information derived from DLS:

1) **DAD**, on the one hand, forms uniform size, spherical shape particles (**Figure 3-25a**);

2) Coprecipitation with BSA results in less uniform, more dispersed bigger nanoparticle, shaped as irregular sphere. More specifically, an irregular layer of BSA is clearly seen around **DAD** spherical particles (**Figure 3-25b**, inset images are magnified representative examples single particles of **DAD** and **BSA loaded DAD** respectively).

Thus, all the results demonstrate that BSA has successfully loaded on the surface of **DAD**. A schematic diagram is proposed in **Figure 3-26** on the basis of SEM results, which shows DAD molecule assembled as a regular spherical NP surrounded with a Corona of BSA molecules. We envision to study the potential of these molecules for intravital microscopy imaging in a near future

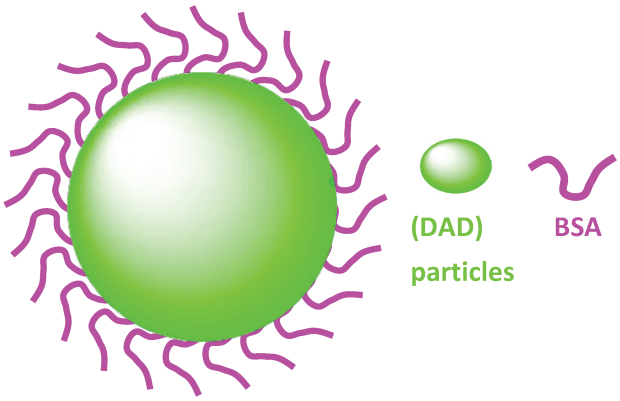

Figure 3-26. The schematic digaram of **BSA loaded DAD**.

6 Conclusion

In this chapter, we successfully synthesized a family of new chromophores (**DAD**, **$(DA)_2D$**, **$(DA)_5D$**) by a straightforward Knoevenagel condensation reaction procedure. They combine different interesting spectroscopic features such as large molar extinction coefficients, large Stokes shifts, high luminescence quantum yields both in solution and in the solid state, and very large sensitivity of the absorption and emission to protonation (red shift of more than 3000 cm^{-1} and allowing easy naked eye detection of the protonation event) that

make them excellent candidates for future pH based actuators. The protonation mechanism, responsible for the pH response, was elucidated for one of the compounds by a combination of spectroscopic experiments (spectrofluorimetry and NMR) and theoretical computation: from the NMR titration results, we confirmed that the protonation process is happening at the core of benzobisthiazole. Fluorescence titration and theoretical calculation results indicate that the associated spectral changes result from two successive protonation equilibria, with a change in the nature of the electronic transition from a typical ICT to a cyanine-like transition.

Reversibility of the process was assessed by successive exposure to acid and base vapors, illustrating that the new chromphore can realize a recyclable response to strong acid. Moreover, these reversible switching properties also translated well to the solid state. Even more interesting, with the aim to further establish the potential of the newly designed molecules regarding their integration into functional devices, it can be successfully incorporated into polymeric films which present high luminescence and have a strong reversible response to acid vapor.

On the other hand, the potential of **DAD** as a biological probe was also investigated in a series of preliminary experiments. We showed that it can penetrate through cell membrane and stain HeLa cells upon simple incubation of the latter with a nanosuspension of the chromophore. In order to improve biocompatibility of the object, in view of future use as an intravital contrast agent for instance, we tried to load chromophore **DAD** into BSA nanoparticles. According to the DLS, SEM and Zeta potential results, formation of hybrids nanoparticles involving BSA and **DAD** was achieved, with a BSA layer coating the surface of our particles.

Chapter 4 Tuning Spectral Properties of Benzobisthiazole based Compounds by Controlled Chemical Modification

For the new class of compounds included in chapter 3, the presence of terminal aldehyde moieties at each end of the molecules on the one hand, and the presence of nucleophilic nitrogen atoms in the benzobisthiazole ring at the center of DAD molecules on the other allows envisioning different chemical modifications. We can take advantage of the later for further tuning the spectroscopic or solid state packing properties of the molecule by playing on the nature of additional substituents which can be introduced by i) various condensation reaction (Koevenagel, amine or hydrazine/carbonyl condensation *etc*.) on the aldehyde or ii) quaternarization of the benzobisthiazole system. In this chapter, we will focus on exploring the possibility to use these chemical modifications to further improve the photophysical properties and expand the range of applications of this new class of compounds.

1 Towards benzobisthiazolium containing probes with cyanine characteristics

1.1 Introduction and structural characteristics of cyanine probes

With the development of fluorescent probes and optical imaging technology, in recent years, near-infrared (NIR) imaging methods have been widely used in cell labeling, tissue and in vivo imaging.[157-159] NIR microscopy presents unique advantages: first, many intrinsic biomolecules can release autofluorescence in biological tissues when excited by visible light, while their autofluorescence is strongly reduced when using a NIR source; secondly, due to

the long wavelength emission of near infrared light (usually in 650-900 nm region, the "biological transparency window"), scattering as well as reabsorption of the emitted light by the surrounding tissue are strongly reduced. Both aspects are highly beneficial to penetrate deeper tissue, making NIR more suitable for biological imaging; finally, as the low frequency of near infrared light carries low energy and interacts weakly with biological tissues, NIR excitation can reduce light-induced damage to living tissues, making it more conducive to intravital imaging, in particular.[160-161]

Fluorescent agents with good stability and high fluorescence efficiency in the near infrared region are an essential component of near-infrared imaging, yet developing probes with large absorption coefficient and high emission efficiency in this range of wavelengths is highly challenging.[162] In this framework, cyanine dyes have often been considered as particularly well suited structures to be used as near-infrared contrast optic agents. A typical structure of cyanine dye contains two nitrogen-containing heterocycles, which are connected by a conjugated oligomethine framework containing an odd number of carbon atoms. Owing to this structure, a formal positive charge carried by one of the nitrogen atom of the nitrogen-containing heterocycles is fully delocalized over the whole conjugated backbone, forming a resonant structure between two limit forms (charge being localized on the other nitrogen atom in the second one) (**Figure 4-1**).[163]

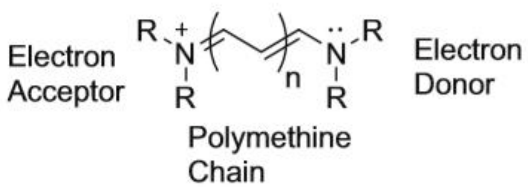

Figure 4-1. General structure of polymethine dyes.

Because of the so called solitonic nature of the associated transition, cyanine dyes usually have a narrow absorption band and a large molar extinction coefficient.[164] Studies have shown that by expanding the conjugated framework of the polymethine bridge the absorption and emission spectra of cyanine dye can be red-shifted: addition of one conjugated vinyl group in the polymethine chain can produce up to a 100 nm red shift, and addition of one conjugated ring on the nitrogen-containing heterocycle can produce additional 20 nm red shift.[165] Therefore, the absorption and emission of trimethine cyanine (Cy3) (maximum excitation is 554 nm and emission is 568 nm) are in the visible light region , while the maximum emission wavelengths of pentamethine cyanine (Cy5) (maximum excitation is 649 nm and emission is 666 nm) and hepatic cyanine (Cy7) (maximum excitation is 743 nm and emission is 767 nm) are in the near infrared region (**Figure 4-2**).

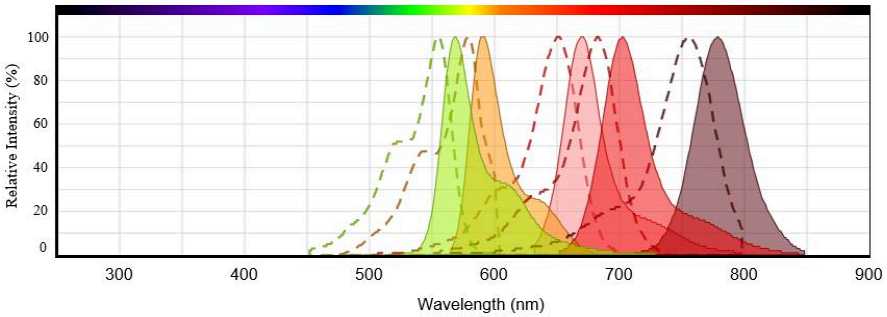

Figure 4-2. The spectra of Cyanine (from left to right: Cy3, Cy3.5, Cy5, Cy5.5, Cy7 respectively).

However, such chemical transformations on the cyanine dyes are also accompanied by some disadvantages, such as lowered fluorescence quantum yield and solubility in aqueous solution, related to an increased tendency towards aggregation, or reduced photostability. Additional chemical modifications can therefore be needed to circumvent those issues. For example, W. Pham *et al*.[166] modified a C7 cyanine by introducing four sulfonate group in the molecule, which greatly improves the water solubility of the dye (**Figure 4-3a**); YT Chang *et*

al.[167a] found that a aminocyanine dye presents higher photostability after acetylation (**Figure 4-3b**). We also used similar strategies, and other functionalizations with hydrosolubilizing polymers, to water-solubilize cyanine derivatives for use as intravital contrast agents[167b]

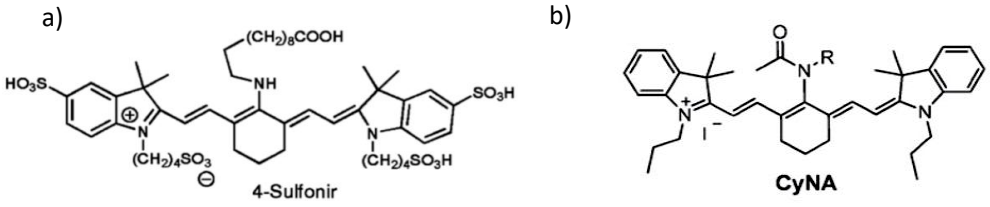

Figure 4-3. The structure of cyanine dyes.

At present, researchers have synthesized lots of cyanine dyes by using different N-containing heterocycles such as indolenine, quinolone, benzoxazole or benzothiazole.

1.2 Different types of benzothiazole cyanine dyes

From the first occurrence in literature of benzothiazole-based cyanine molecule in the late 18th century[168], until now, a large variety of symmetric and asymmetric benzothiazole cyanine dyes have been synthesized.[169-170] Depending on the length of their conjugated backbone and resulting spectroscopic features, they can be divided into four categories: 1) monomethine cyanine dyes[171], which have a narrow absorption peak and high fluorescence intensity, the typical absorbance is around 450-470 nm depending on the substituents of benzothiazole core; 2) trimethine cyanine dyes[172], which absorb in 550-570 nm; 3) pentamethine cyanine dyes[173], which absorb in 650-670 nm and have emission in the near-infrared region around 690-710 nm. 4) heptamethine cyanine dyes[174], both of the absorption and emission are in the region of 750-1100 nm. Some representatives examples of these different categories of benzothiazole cyanine dyes are featured in **Figure 4-5**.

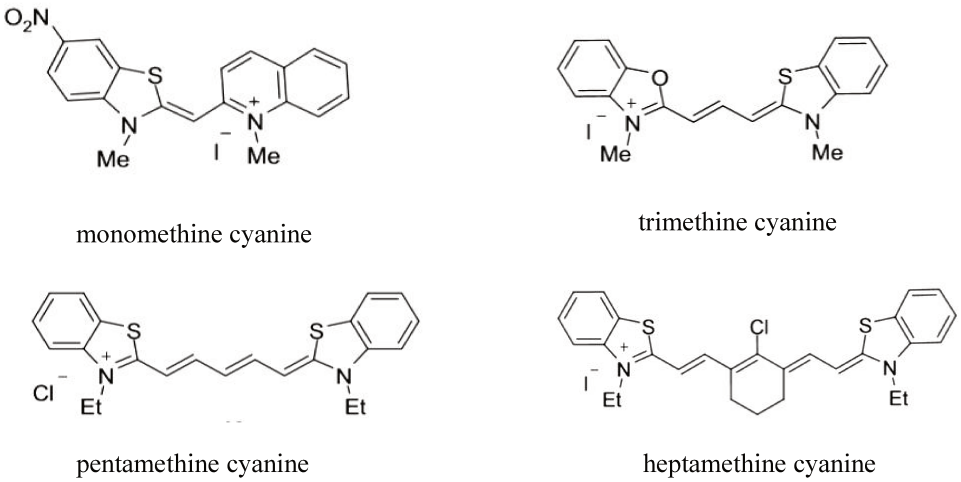

Figure 4-5. Structure of benzothiazole cyanine dyes.

1.3 Objective

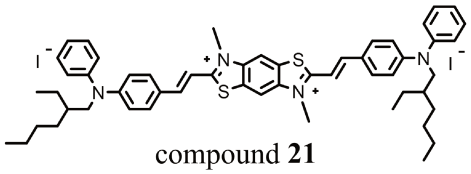

Figure 4-6. The structure of new benzobisthiazole cyanine dyes.

Chromophores depicted in the previous chapter were constructed around a benzobisthiazole core structure. We showed that protonation of the later resulted in a drastic change in the spectroscopic features, with a cyanine like spectroscopic signature for the resulting benzobisthiazolium compound, and we took advantage of the properties in the making of acid-based controlled reversible luminescent switches. In the work depicted in the present Chapter, we considered that the introduction of permanent charges on the nitrogen atom using alkylating agents, could afford new NIR emitting fluorescent dyes with potentially interesting properties such as enhanced TPA properties (owing to their quadrupolar structure, that contrasts with most depicted cyanines).[175]

In the following, we will describe how a simple reaction procedure, involving a commercially available methylating agent can be used to generate new benzobisthiazolium containing quadrupolar fluorophores (**Figure 4-6**). Then, we will focus on elucidating its main spectroscopic features. Considering the similarity in its absorption and emission properties with reported cyanine dyes, we will finally explore its potential as a near infrared probe.

1.4 Synthesis and characterization of new benzothiazole cyanine dyes

The synthetic route depicted in **Scheme 1** was used to synthesize our target molecule. First, in order to alleviate reactivity issues related to the presence of terminal aldehyde moieties, a non-formylated analog of **DAD** (compound **16**) was synthesized. It was then reacted with dimethyl sulfate under microwave activation, affording the new benzobisthiazolium containing compound **21**. Both of the final compound **20** and **21** were fully characterized by ^{1}H and ^{13}C NMR, COSY, HMQC, HMBC and HR-MS

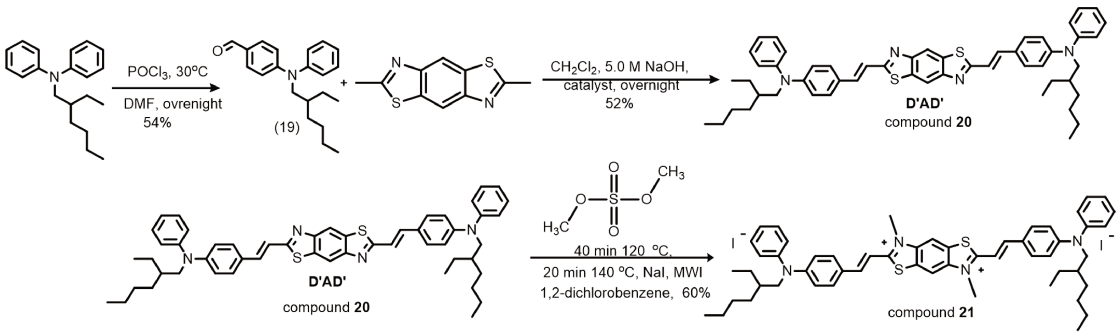

Scheme 1 synthesis route towards benzobisthiazolium containing compound **21**.

1.5 Optical properties of new benzobisthiazolium cyanine

The absorption and emission properties of compound **21** were then investigated in different solvent, results are gathered in **table 1**. Solvent dependent evolution of the spectral

absorption signature is manly characterized by a remarkable negative solvatochromism, ie an hypsochromic shift of the emission maxima with increasing solvent polarity. This effect goes with a significant decrease of the absorption coefficient upon increasing solvent polarity from dichloromethane to DMSO (Toluene set asides, for reasons that will be further detailed in the following). Both properties are classically encountered in asymmetric cyanine and merocyanines, and are ascribed to a solvent dependent partial ground state transfer of the electronic density of the molecule from the electron donating to the electron withdrawing group (from structure A1 to structure A2, according to the equilibrium sequence proposed by Dähne)[176] in **Figure 4-7**.

Solvents	λ_{max}[a]	ε_{max}[b]	λ_{max}[c]	Φ_f[d]
Toluene	666	7.4	757	1804
Dichloromethane	653	15	709	1209
Chloroform	641	14	695	1212
Acetonitrile	620	11	696	1761
Dimethyl sulfoxide	614	9.8	697	1939
[a] Maximun absorption position (nm). [b] Maximum molar absorbance in 10^4 mol^{-1} L cm^{-1}. [c] Maximum emission position (nm), excited at 600 nm. [d] Stokes shift in cm^{-1}. The concentration is 1.0×10^{-5} $mol\cdot L^{-1}$				

Table 1. The absorption and emission spectral characteristics of compound **21** in different solvents.

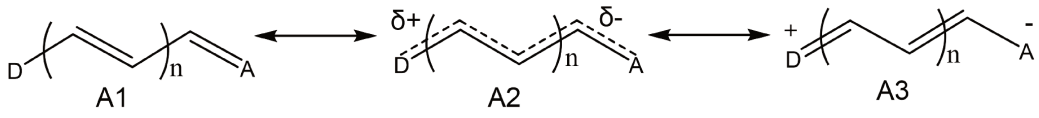

Figure 4-7. Schematic diagram of the equilibrium sequence. Taken from reference [176]

As **Figure 4-8** shows, band shape in the absorption spectrum in lower polarity solvents are typical of that generally associated to cyanines with a very intense narrow main transition accompanied with a lower intensity vibronic shoulder at the blue edge of the band (typical

Cy5 signature is featured as **Figure 4-9**). Similarly, a typical cyanine looking alike emission with low Stokes shift (in the 1200-1900 cm^{-1} range depending on the considered solvent) is observed in dichloromethane and chloroform (quantum yield *ca* 0.03); in spite of a similar band-shape, luminescence quantum yield is strongly reduced in acetonitrile and DMSO.

In all aforementioned solvents, maximum emission peak position is found around in 695-710 nm, which constitutes a relevant range of wavelengths for future imaging experiments in biological media. Situation strongly differs in toluene, which is characterized by a significant redshift of the absorption (666 nm) and of the very weak emission (757 nm) an ill-defined band structure, which could result from partial chromophore aggregation in the investigated range of concentrations, which could be a consistent hypothesis in line with the noticed low solubility of compound **21** in this solvent.

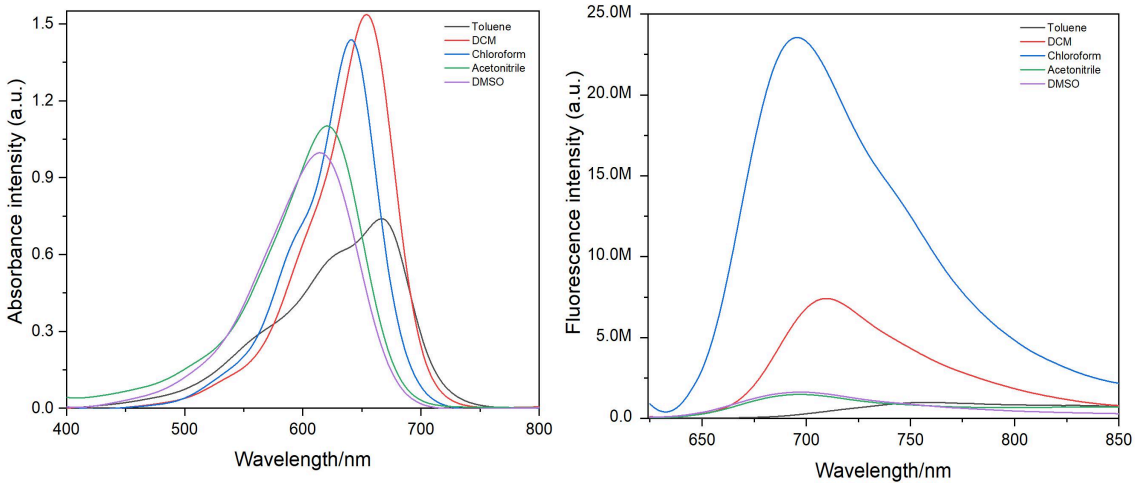

Figure 4-8. Absorption (left) and emission (right) spectrum of compound **21** in different solvents. Exciation wavelength is 600 nm. The concentration is 1.0×10^{-5} mol·L^{-1}.

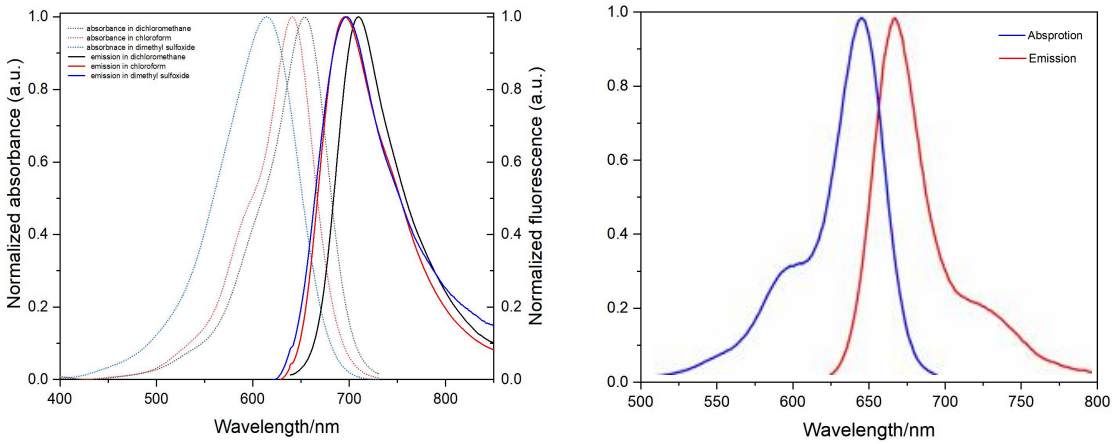

Figure 4-9. The normalized absorption and emission spectrum of compound **21** (left) in dichloromethane, chloroform, dimethyl sulfoxide. Excitation wavelength is 600 nm; the normalized absorption and emission spectrum of a commercial fluorophore, Cyanine 5 maleimide (right).

While the shape of the narrow absorption band, large molar extinction coefficient and the maximum absorption and emission peak position of compound **21** are extremely similar with the spectrum features of Cyanine 5 (**Figure 4-9**), the former is characterized by a much increased Stokes shift compared to the commercial dye Cy5 (<500 cm^{-1} in most solvents). This indicates that compound **21** as an archetype of benzobisthiazolium based cyanine derivative presents advantageous characteristics in view of bio-imaging applications. Exploration of its potential in this context is underway.

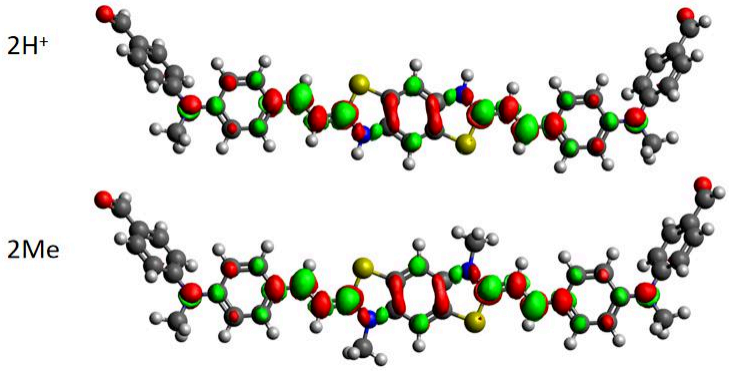

Figure 4-10. Computed evolution of the electronic distribution between ground and lowest lying excited state for bisprotonated **DAD** ($2H^+$), and compound **21** (2Me)**.** Red lobes correspond to a depletion in electron density, green lobes to an enrichment

Similar to what was done in chapter 3 to theoretically investigate the protonation process, time dependent density functional theory was conducted at the B3LYP/6-31G(d) levels using Gaussian 09. In good agreement to the results obtained with the deprotonated analogue of DAD ($2H^+$), in **Figure 4-10** methylated compound **21** experiences a similar reduced Bond Length Alternation (BLA) between single and double bond, and a similar evolution of the electron density between its ground and excited state, which constitute two typical features of cyanine chromophores. This confirms that either upon bisprotonation of the thiazole's nitrogen or through irreversible methylation of the latter, **DAD** derivatives can acquire a partial but marked cyanine character, characterized by an intense and narrow emission in the far-red or NIR range, and a decreased (yet superior to "regular" cyanine chromophores) Stokes shift. In addition, one can anticipate larger two-photon absorption properties compared to regular cyanines, although this point could not be studied in the course of this thesis because of technical issues with the optical bench.

2 Other probes by functionalized new chromophore

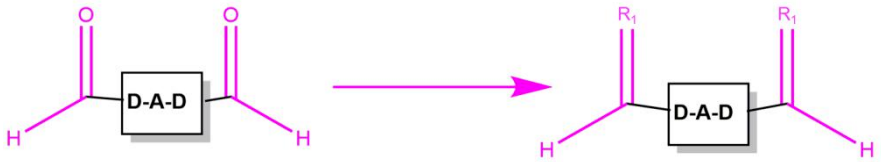

Figure 4-11. Schematic diagram of the second strategy.

As mentioned in the introductive lines of this chapter, the terminal aldehyde group of **DAD** is another reactive moiety then can be exploited for chemical modification of the benzobisthizazole starting compound (**Figure 4-11**) in order to improve bioavailability and compatibility of the molecule and tune its solution and/or solid state spectral properties.

As a proof of concept we synthesized the following molecules (**Scheme 2**) through different (Knoevenagel or Schiff's) condensation reactions:

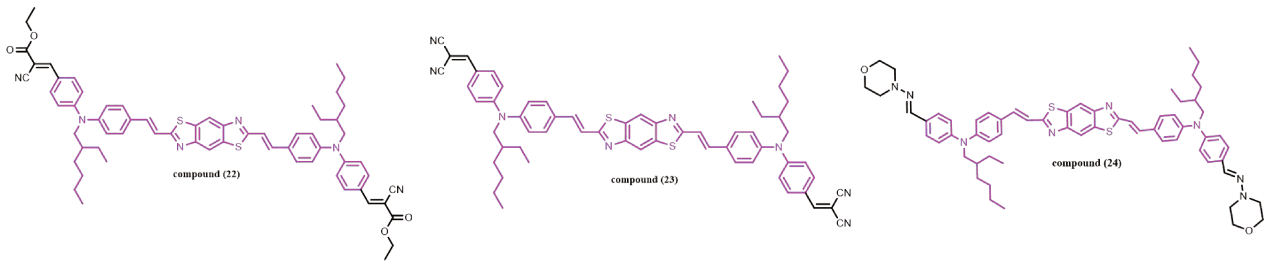

Scheme 2. The structures of new molecules.

2.1 Tuning the electronic properties of a chromophore by addition of peripheral substituents: chromophores of the A'-D-A-D-A' type

2.1.1 Design strategy, synthesis and characterization of compound 22 and 23

We tried to take advantage of the possible peripheral functionalization strategy using condensation reaction to introduce targeting moieties onto our as-designed benzobisthiazole based probes. As we know, narrowed energy-gap could induce red-shifted emission, a property that we already explored in the previous section. Besides the particular case of cyanine chromophores, there are two methods to achieve this goal in chromophores featuring ICT type of electronic transitions: i) extending the π-conjugation system; ii) introducing donor and acceptor groups into a π -conjugated luminogen to tune the HOMO/LUMO energy either by raising the HOMO or dropping the LUMO. In this framework, cyano substituted vinyl groups and other derivatives such as isophorone or tricyanofurane are a class of extremely potent acceptor moieties which have been often selected to tune molecular emission wavelength towards the NIR region..[177] Therefore, we tried to introduce different types of

cyano substituted vinyl groups into our **DAD** molecule with the objective to study their effect on the molecular optical properties.

Herein, we choose ethyl cyanoacetate and malononitrile as precursor electron deficient reagent to undergo condensation with the active carbonyl of **DAD** for synthesizing new compound **22** and **23** (**Scheme 3**). In both cases, reaction can be achieved using the conditions depicted in **Scheme 5**, and the two new compounds are unambiguously characterized by ^{1}H, ^{13}C NMR and HR-MS.

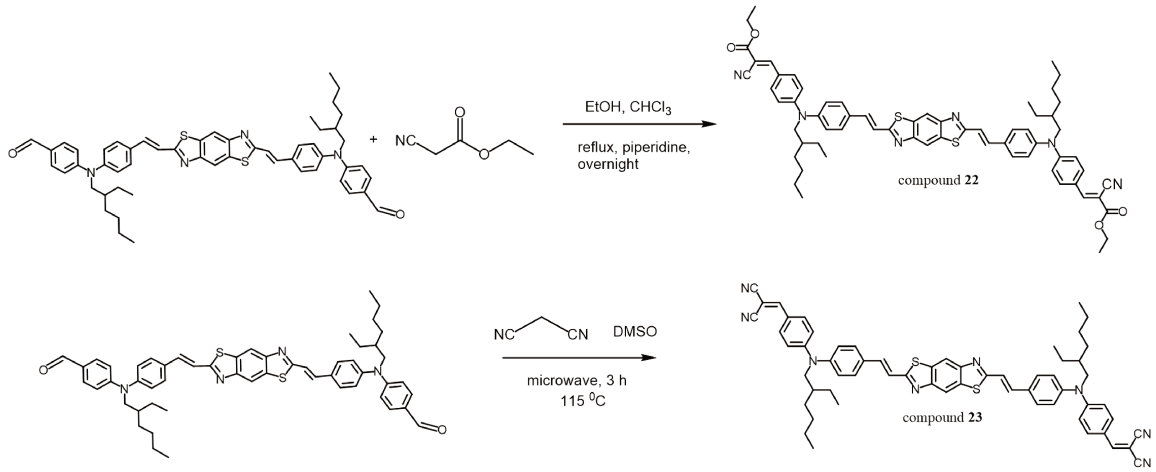

Scheme 3. Synthesis routes of compound **22** and compound **23**.

With these new molecules in hand, we initiated a comparative study of their basic optical properties in pure solvent and aggregated state with their unsubstituted precursor **DAD**, and then evaluated their potential in bio-imaging.

2.1.2 Optical properties of compound 22 and 23 in pure solvent

First, we compared the absorption and emission spectrum of these two compounds with those of their **DAD** precursor (**Figure 4-12**). Absorption spectra are located in the same range of wavelengths for both compounds and show only little dependence on the nature of the

solvent, characteristic of a little polarized ground state, as generally observed in quadrupolar molecules[178]: depending on the solvent maximum absorption peak position of compound **22** varies from 448 nm to 454 nm and compound **23** is from 441 to 453 nm, which lies in the exact same range as their **DAD** precursor. A stronger solvent dependence of the emission wavelength is seen, with the maximum emission peak shifting from 535 nm to 570 nm for compound **22** and from 543 nm to 578 nm for compound **23** when solvent goes from ethyl acetate to DMSO range. Again, lower polarity solvent (toluene) stands apart, as it does not seem to fit within the general trend of solvatochromism. In particular, in this solvent, compound **23** exhibit a seemingly much larger red shift than in other solvents.

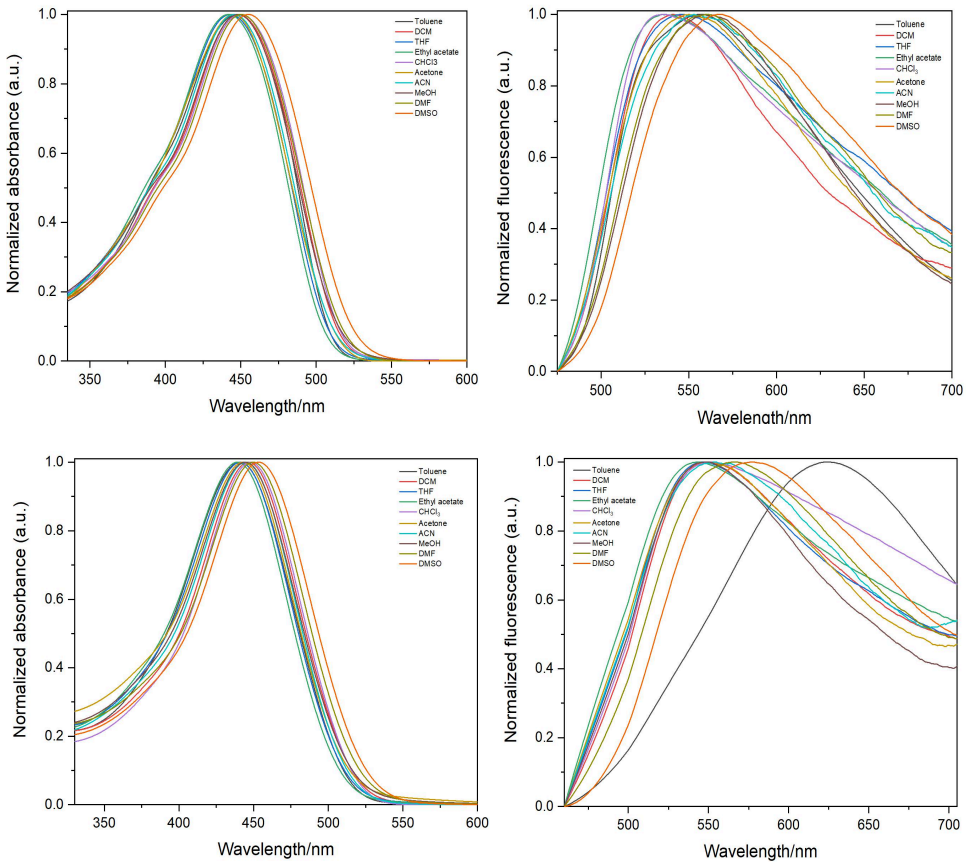

Figure 4-12. Normalized absorption and emission spectra of compound **22** (above) and **23** (below) in different solvents. Excitation wavelength is 450 nm; The concentration is 1.0×10^{-5} mol·L^{-1}.

Again, comparison with **DAD** reveals that the properties of the molecules in solution are

only marginally affected by the addition of peripheral electron withdrawing substituents.

In contrary, while compound **22** does not exhibit any luminescence in suspension, compound **23** shows AIE properties, which go with a large redshift (2298 cm^{-1}) of the emission. **Table 2** list the spectroscopic properties of compound **23** and **DAD** in solution and suspension. It clearly appears that, while luminescence quantum yield of **DAD** is higher in both cases (solution and suspension) compared to **23**, luminescence characteristics of the solubilized and aggregated form of the molecule are virtually undiscernible. By comparison, not only **23** display significant AIE properties, but the associated suspension emission takes place in the far-red/NIR which might find useful prospects in bioimaging

Compound 23	λ_{max}[a]	ε_{max}[b]	λ_{max}[c]	$\Delta\nu$[d]	Φ^1	Φ^2
Acetone	442	11.5	548	4376	<0.01	<0.01
Suspension	443	7.7	648	7141	0.015	
DAD	λ_{max}[a]	ε_{max}[b]	λ_{max}[c]	$\Delta\nu$[d]	Φ^1	Φ^2
Acetone	427	7.7	562	5625	0.1	0.44
Suspension	430	5.6	564	5525	0.02	

[a] Maximum absorption peak position in nm (1×10^{-5} mol L^{-1}). [b] Maximum molar absorbance in 10^4 mol^{-1} L cm^{-1}. [c] Peak position of maximum emission in nm (1×10^{-5} mol L^{-1}), excited at the absorption maximum. [d] Stokes shift in cm^{-1}. Φ^1 Absolute quantum yield in solution. Φ^2Absolute quantum yield in solid. Suspension **23**: **23** in acetone/water (1 / 9) mixture. Suspension **DAD**: 50 µL **DAD** (dissolved in DMSO) drop into 5 mL H_2O.

Table 2. Spectroscopic properties of compound **23** and **DAD** in solution and suspension.

2.1.3 AIE properties of compound 22 and 23

After our preliminary screening experiments of compound **22** and **23**, it was noticed only compound **23** in acetone/water mixture exhibits an obvious AIE phenomenon. As **Figure 4-13** show, when *f*w (in acetone/water mixture) increases, compound **23** presented a broadeding in

absorption spectra, which is an alike result of abovementioned AIEgen indicating that the nano-aggregates are formed; for emission spectrum, with *f*w increasing, there is a clear luminescence enhancement, the intensity reaches its maximum when *f*w is 90% , with a value that is around 5.5 times that obtained in pure acetone. Remarkable redshifts (*ca* 2300 cm^{-1}) accompanied this process. These results illustrate that the J type nanoaggregates of compound **23** are formed here. This infrared emission characteristic makes compound **23** possess a potential in bio-imaging. Exploration of its potential in this context is underway..

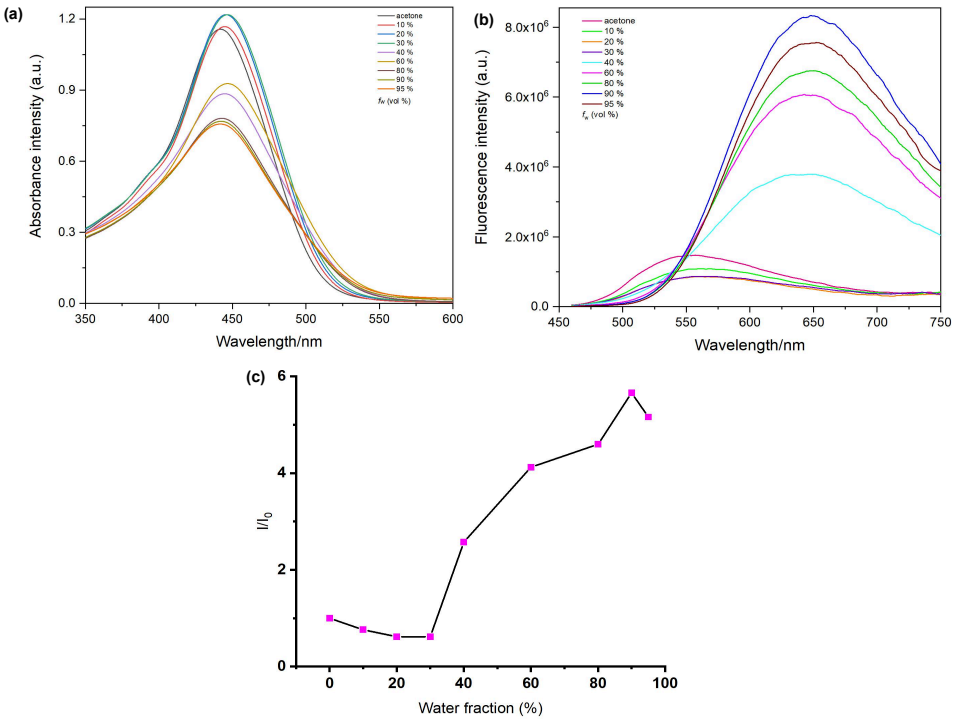

Figure 4-13. Absorption (a) and emission spectra (b) of compound **23** in acetone/water mixtures with different water fraction; Excitation at 443 nm; (c) plots of I/I_0 values versus water fractions in acetone/water mixtures. I_0 is the luminescence intensity in pure acetone solution. The concentration is 1.0×10^{-5} mol·L^{-1}.

2.1.4 Nanoparticles of compound 23

Nanoparticles of compound **23** were obtained by the nanoprecipitation method depicted earlier. Here again 4.5 mL H_2O was added into a 0.50 mL acetone solution of compound **23** to

prepare nanoparticles, which characteristics were studied by DLS and SEM imaging. The DLS experiment show that average diameter of the nanoparticles is *ca* 111.7 nm and PdI value is 0.2 (**Figure 4-14**), showing that compound **23** in aggregates forms uniform nanoparticles with a diameter compatible with it use in living media.

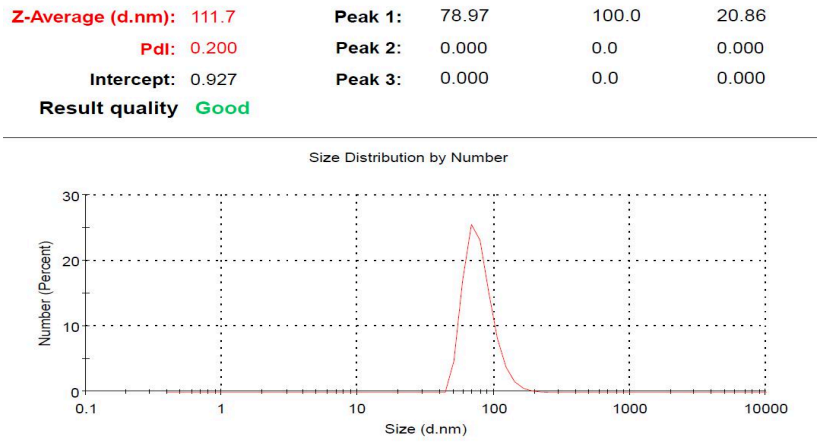

Figure 4-14. Dynamic light scattering of compound **23**.

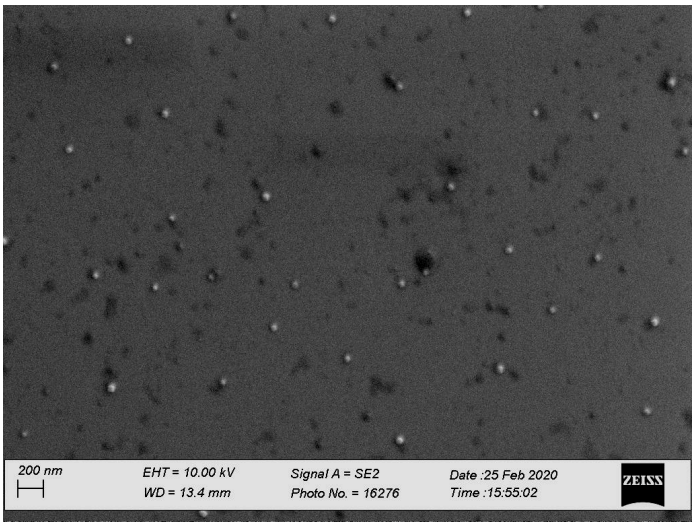

Figure 4-15. SEM photo of compound **23**. The concentration is 5.0×10^{-5} mol L^{-1}.

Same method as chapter 2 was used to prepare the SEM sample: the mixed dilute suspension (*f*w 90%, H_2O/acetone) of compound **23** was dropped on the surface of silicon wafer with conductive adhesive, then dried upon airing for one night. **Figure 4-15** shows the SEM image: nano-sized and uniform spherical particles are formed and aggregated on the

surface of silicon wafer, in line with the result of DLS experiment. In this case also, the average diameter of the nanoparticles as observed in SEM look significantly smaller (below 50 nm) than that obtained through DLS measurement. These experiments illustrate the potential of the compound for applications in bioimaging, which will be illustrated latter in this chapter

2.2 Design strategy, synthesis and characterization of morpholine appended compound 24

As we know, lysosomes are the main catabolic organelle existing in lots of animal cells (except erythrocytes).[179] There are large amount of hydrolytic enzymes in their spherical vesicles and it can decompose the materials that enters into cell from outside or digest the local cytoplasm or organelle of the cell itself,[180] which plays an important role in life activities. Thus, visualization of lysosomes is of high biological and medical value. Lysosomes are in a weak acid environment (pH 4.5-5.5), and many alkaline substances with biofilm permeability can accumulate in lysosomes. Therefore, it is possible to design and synthesize lysosome fluorescent probes by connecting weakly alkaline groups (morpholine, dimethylamino, and tertiary alkyl amino groups, *etc*.) that have specific localization in lysosomes.[181-183] Herein, we use morpholine-4-amine as a reagent to undergo Schiff's type of condensation with the active carbonyl of **DAD,** yielding to the synthesis of new morpholine appended compound **24** (**Scheme 4**)

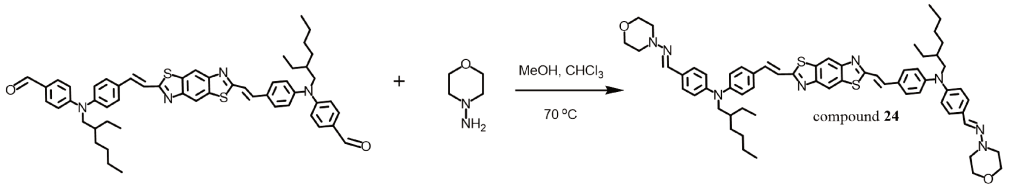

Scheme 4. synthesis route of compound **24**.

Compound **24** was characterized by ^{1}H and ^{13}C NMR and HR-MS. Next, we will investigate its basic optical properties in pure solvent and aggregated state, and then evaluate their potential in bio-imaging.

2.2.1 Optical properties of compound 24 in aggregated state

Samples	**solvents**	$\lambda_{max}{}^{a}$	$\varepsilon_{max}{}^{b}$	$\lambda_{max}{}^{c}$	$\Delta\nu^{d}$	Φ^{1}	Φ^{2}
Compound 24	DMSO	465	10.6	572	4022	0.017	0.1
	Suspension	467	5.4	647	5957	0.14	
DAD	DMSO	432	7.9	569	5573	0.08	0.44
	Suspension	430	5.6	564	5525	0.02	

[a] Maximum absorption peak position in nm (1×10^{-5} mol L^{-1}). [b] Maximum molar absorbance in 10^{4} mol^{-1} L cm^{-1}. [c] Peak position of maximum emission in nm (1×10^{-5} mol L^{-1}), excited at the absorption maximum. [d] Stokes shift in cm^{-1}. Φ^{1} Absolute quantum yield in solution. Φ^{2}Absolute quantum yield in solid. Suspension **24**: **24** in DMSO/water (1 / 9) mixture. Suspension **DAD**: 50 μL **DAD** (dissolved in DMSO) drop into 5 mL H_2O.

Table 3 Spectroscopic properties of compound **24** and **DAD** in solution and suspension.

In **table 3** we list the spectroscopic properties of compound **24** and **DAD** in solution and suspension. As the result show, when introducing morpholine substituent into **DAD** molecule, first, the quantum yield of compound **24** drops compared to that of than **DAD** compound in solution and solid state. Quantum yield is 0.017 (DMSO solution), yet it is markedly increased in the solid state to 0.1, indicating that a restriction of intramolecular motion (quite classicaly observed with imine containing fluorophores) might be at the origin of the solid

state emission**.** In suspension (here prepared from DMSO solution, for solubility reasons) compound **24** exhibits stronger luminescence with AIE characteristic (quantum yield is *ca* 7 times that of **DAD**) and exhibit a similar 2274 cm^{-1} redshifts as already pointed out for compound **23**. This might indicate that formation of similar J-aggregates are responsible for the characteristic emission of **24** in the aggregated state.

In order to confirm this point, we studied in details the optical properties of compound **24** in the aggregated state; the nanoprecipitation method detailed in chapter 2 was used to prepare suspensions of compound **24** in different aqueous suspensions. In **Figure 4-16**, with the *f*w (water fraction) increasing, absorption spectra show clearly broadened absorption band and long tails, which as already mentioned in chapter 2 is characteristic of the formation of nano-aggregates, the long tail in particular being caused by scattering effects due to the presence of the nanoparticles. Meanwhile, a significant splitting and red-shifting (for the lowest-in-energy component of the band) of the ICT absorption band is characterized, indicating probable Davydov splitting characteristic of the formation of J aggregates. This tendency is confirmed upon examination of the evolution of luminescence characteristics. Compound **24** exhibits weak emission with low fluorescence quantum yield (0.017) in DMSO; however, when *f*w is increasing, the fluorescence intensity rapidly increases to the maximum value (quantum yield is *ca* 0.14, reached at *f*w 40%) corresponding to a *ca* to 7 times enhancement compared to the initial solution; it then decreases slightly, to reach a value around 5 times higher pure DMSO for *f*w 100%. These changes in intensity can be explained by the restriction of intramolecular rotations (RIR) mechanism of the imine bond which isomerization constitutes a powerful non-radiative dissipation pathway that generally

quenches luminescence in solution[184]. Meanwhile, the large red shift observed for the emission maximum (*ca* 2300 cm^{-1}) constitute another clear indication that J aggregates have formed upon aggregation of compound **24**.

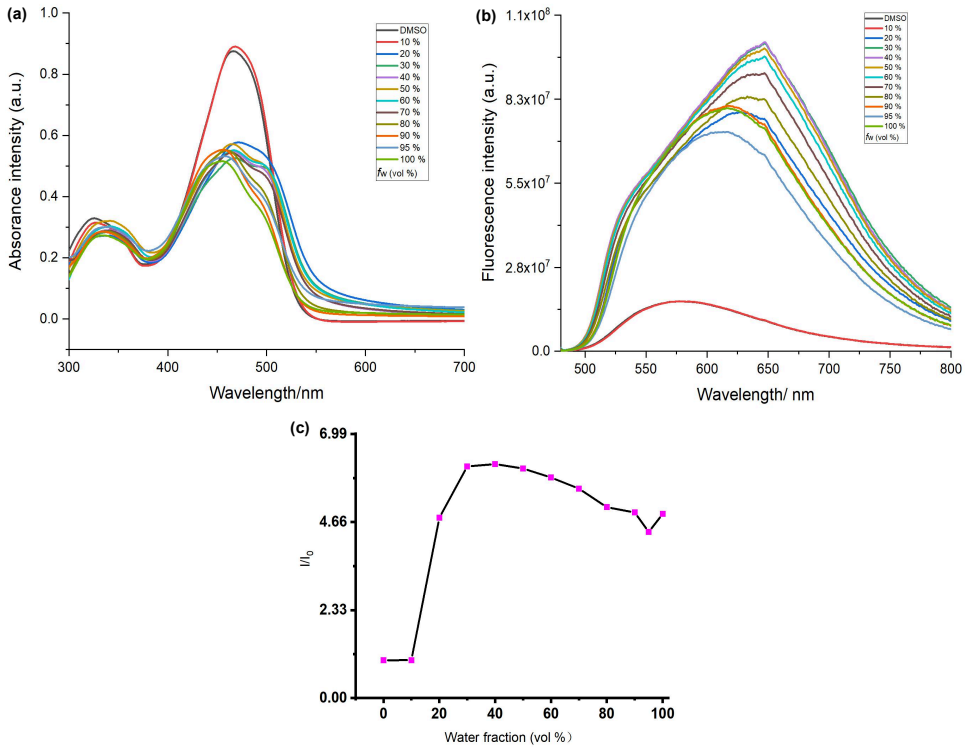

Figure 4-16. Absorption (a) and emission spectra (b) of compound **24** in DMSO/water mixtures with different water fraction; Excitation wavelength is 465 nm; c) plots of I/I_0 values versus water fractions in DMSO/water mixtures. I_0 is the luminescence intensity of DMSO solution. The concentration is 1.0×10^{-5} mol·L^{-1}.

Similar qualitative results are observed when the nanoprecipitations are performed in THF/water mixtures, confirming the AIE properties of compound **24** (**Figure 4-17**). The onset of luminescence enhancement is delayed, with a maximal value obtained for *f*w of 80%; in the initial stage of nanoprecipitation, up to *f*w of 50%, the fluorescence intensity is slightly decreased, which has been previously ascribed to the occurrence of a dark twisted intramolecular charge transfer (TICT) phenomenon in the presence of more polar dielectric surrounding environment.[185] All these results confirm the potential of compound **24** to

behave as a good AIEgen.

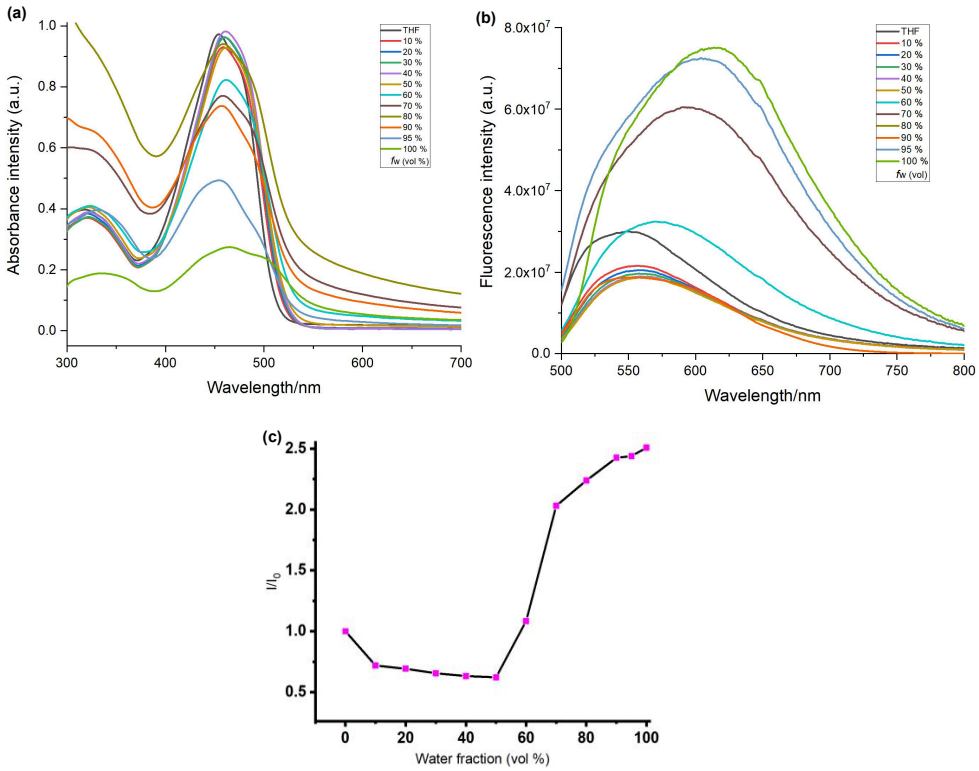

Figure 4-17. Absorption (a) and emission spectra (b) of compound **24** in THF/water mixtures with different water fraction; Excitation wavelength is 454 nm; c) plots of I/I_0 values versus water fractions in THF/water mixtures. I_0 is the luminescence intensity of THF solution. The concentration is 1.0×10^{-5} mol·L^{-1}.

2.2.2 Nanoparticles of compound 24

After preparation of nanoparticles by nano-precipitation of 50 μL DMSO solution of compound **24** by addition of 5 mL H_2O, DLS experiment was conducted on the resulting nanoparticles of **24**. Similar to what was obtained for CPNPs in chapter 2, data reveals the presence of relatively small sized nanoparticles with moderate dispersity (PdI = 0.24), in **Figure 4-18**, compound **24** shows that the average diameter of the formed nanoparticles is *ca* 97 nm and PdI value is 0.239, which indicates that **24** forms uniform and relatively monodisperse nanoparticles of suitable size for cell imaging.

		Size (d.nm):	% Number	Width (d.nm):
Z-Average (d.nm): 96,77	Peak 1:	48,26	100,0	15,28
PdI: 0,239	Peak 2:	0,000	0,0	0,000
Intercept: 0,957	Peak 3:	0,000	0,0	0,000
Result quality : Good				

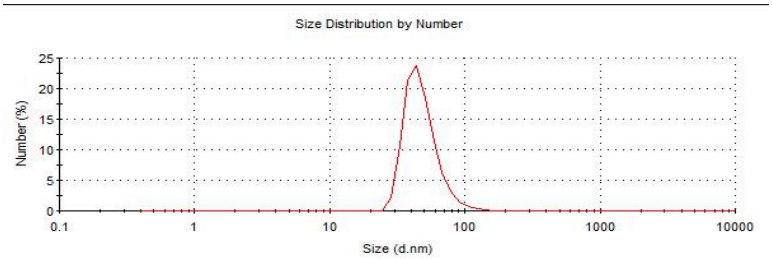

Figure 4-18. Dynamic light scattering of compound **24** nanoparticles.

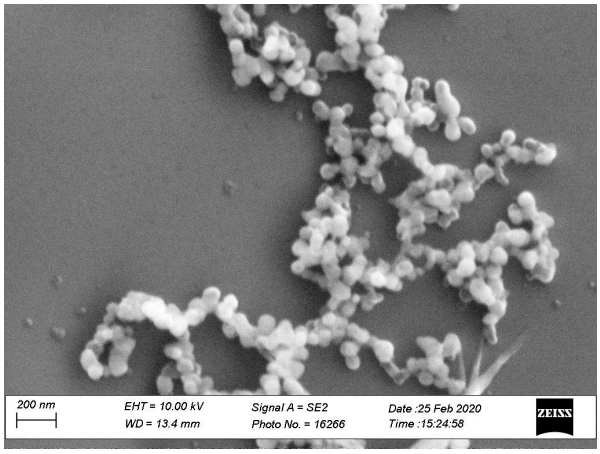

Figure 4-19. SEM photo of compound **24**. The concentration is 5.0×10^{-5} mol·L^{-1}.

SEM experiment was performed to confirm the information derived from DLS and directly visualize the morphology of the nanoparticles. Again, samples were prepared by dropping the mixed dilute solution (*f*w 90%, H_2O/THF) of compound **24** on the surface of silicon wafer with conductive adhesive then dried upon airing for one night. **Figure 4-19** shows an illustrative SEM picture: in agreement with DLS data, it confirms that nano-sized and uniform spherical particles are formed, which aggregate on the surface of silicon wafer. Both SEM and DLS results confirm that the morphology of particles obtained with **24** closely resembles that of compound **23**.

2.2.3 Cell imaging

With the far-red fluorescent nanoparticles of compound **24** in hands, we explored their capability in cell imaging. HeLa cells were incubated with 10 μM DMSO solution of compound **24** at 37 °C for 30 min and washed three times with PBS (PH=7.4). Intracellular fluorescence distribution was then observed on a confocal microscope, revealing that compound **24** successfully penetrates cell membrane and provides staining of the perinuclear region (**Figure 4-20**).

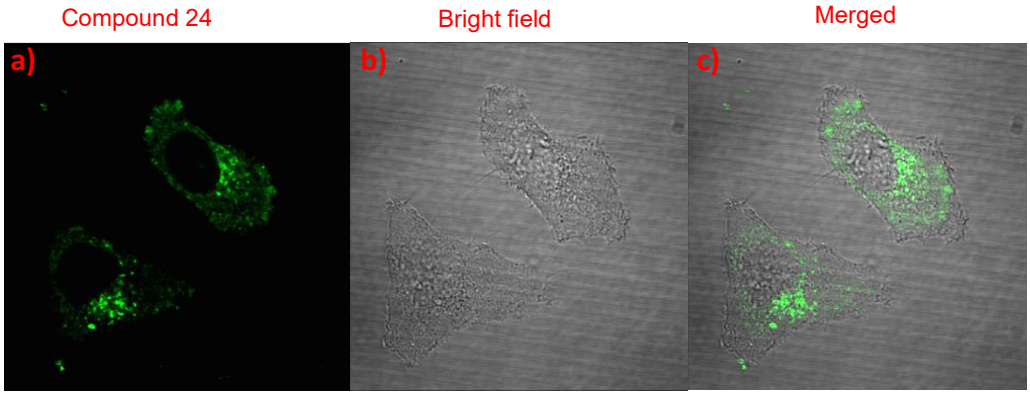

Figure 4-20. Confocal fluorescent images of HeLa cells stained with compound **24**: a) compound **24**; b) bright-field; c) merged-field.

Finally, we tried to evaluate the potential of our morpholine substituted analogue of **DAD** (compound **24**) for specific lysosome staining. Comparing the fluorescent staining pattern obtained by compound **24** with commercial dye Lyso-Tracker Red (which specifically light up in lysosome) in **Figure 4-21**, a Pearson's colocalization coefficients around 0.78 is found, indicating that compound **24** mainly (although probably not exclusively) stains lysosomes in cell.

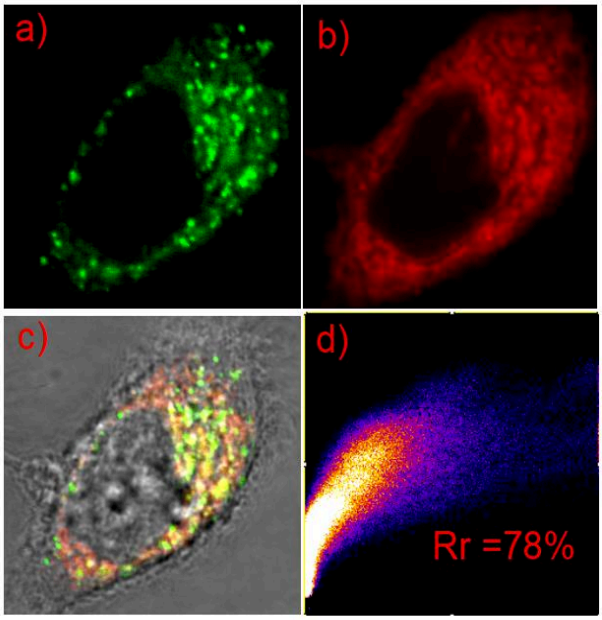

Figure 4-21. Confocal fluorescent images of HeLa cells: a) compound **24**; b) Lyso-Tracker Deep Red; c) merged-field; d) co-localization profile between compound **24** and Lyso-Tracker Deep Red.

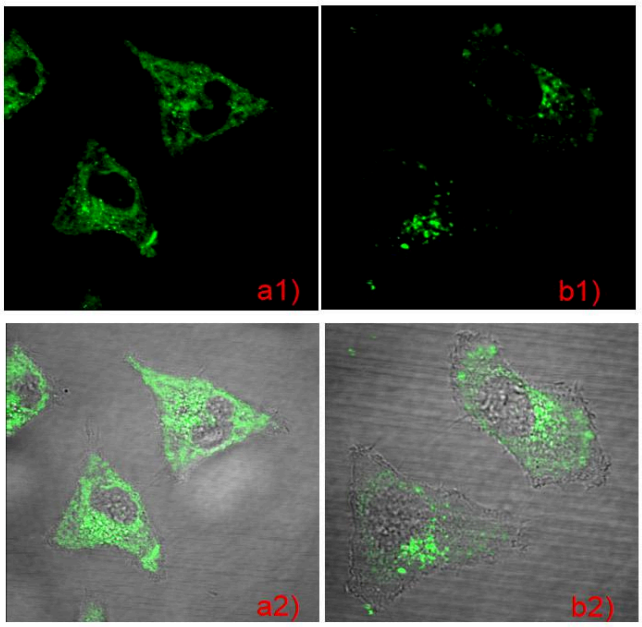

Figure 4-22. Confocal fluorescent images of HeLa cells: a1)-c1): **DAD**, compound **24**; a2-c2): merged-field of **DAD**, compound **24**.

In order to confirm that morpholine modification is responsible for the observed selectivity, we compared the imaging results obtained with compound **24** and our benchmark compound **DAD** (**Figure 4-22**) Incubation of HeLa cells with **DAD** resulted in homogeneous

staining of the cytosol area, with no apparent specificity to any organelle. This result constitute preliminary evidence that morpholine functionalization in compound **24** is the key moiety in lysosomial targeting, although these conclusions should be confirmed by similar co-staining experiments with lysotracker as performed with compound **23**.

3 Conclusion

In conclusion, **DAD** constitutes a powerful platform toward further chemical modifications that we used to expand the range of spectroscopic behavior and/or bioavailability features, using two distinct strategies.

First, a benzobisthiazolium based cyanine derivative (compound **21**) was obtained by a simple quaternarization procedure of the thiazole ring. The resulting benzobisthiazolium compound **21** exhibits a narrow absorption band with large molar extinction coefficient, and an intense emission in the NIR, which illustrates the possibility to tune the nature of the electronic transition by quaternarization of the central substituent, from an ICT to a transition with a marked cyanine character. Compared to regular commercially available cyanines (like Cy5), compound **21** displays larger Stokes shift and the asymmetric nature of the cyanine transition leads us anticipate larger two-photon absorption properties, a point that we hope to be able to confirm soon. All these features give compound **21** advantageous characteristics in view of bioimaging applications.

Second, ethyl cyanoacetate and malononitrile were introduced into **DAD** molecule to get compound **22** and **23** with the objective to generate a new type of **A'DADA'** quadrupolar structure and study its effect on the molecular optical properties. Comparison of the absorption and emission spectrum with **DAD**, reveal that the spectroscopic properties of the

molecules are only marginally affected by the addition of peripheral electron withdrawing substituents in solution. However, in the aggregate state compound **23** show a largely red shifted emission in suspension comparing with **DAD**, which we attribute to the formation of J aggregates. Finally, a new morpholine appended compound **24** was synthesized by Schiff's type of condensation. First, its self-assembly behavior in aqueous solution exhibit apparently AIE property with similar features as for compound **23.** In suspension (DMSO/water mixtures), compound **24** shows 5-6 times fluorescence intensity increase. Meanwhile, the large red shift observed for the emission maximum (*ca* 2300 cm^{-1}) constitute again a strong indication that J-aggregates may have formed upon aggregation of compound **24**. DLS and SEM results present in suspension the formation of spherical nanoparticles with an uniform diameter size around 97 nm. Because of these advantageous spectroscopic features and morpholine functionalization (known as a passive lysosome targeting unit), **24** was successfully involved in bio-imaging experiments and co-localization results illustrate that it specially stains lysosomes.

Chapter 5 Towards A New Family of Compounds as Candidates for Super Resolution Imaging ?

1 Introduction

As we often say: seeing is believing. However, the resolution of the human eye is too limited when it comes to the micrometric world. We are powerless to observe bacteria, viruses, and the details of cells including cell structure, molecular interactions and dynamic processes. Optical microscopy can help gaining access to the surface of this world, yet the nature of light itself constitutes a seemingly uncrossable boundary.

1.1 Abbe limit, and the super-resolution microscopy

In 1873, German physicist Abbe proposed the concept of optical diffraction limit d as a ratio between the probing light wavelength and the objective diameter, or "numerical aperture", NA ($d = \lambda/2NA$, about 200 nanometers in modern microscopes).[186] In order to surpass the optical limit, scientists tried to develop new tools and tricks based on numerical treatment of the image. Super-resolution microscopy (SRM) is a new technology that has emerged in recent years and was awarded the Nobel Prize in Chemistry in 2014.[187] Compared to other strategies aiming at artificially overcoming optical resolution such as X-ray microscopes, various electron microscopes and atomic force microscopes, super-resolution fluorescence imaging can be performed under standard temperature and pressure condition and operates with limited damage to the activity of biological samples to obtain samples' nano-scale image information.

1.2 Blinking molecules and the stochastic optical reconstruction

One strategy of SRM overcoming the diffraction barrier uses photoswitchable molecules to resolve dense populations of molecules with super-resolution. The principle is to switch fluorophores between on and off state: using this strategy the exact center position of each individual fluorescent molecule can be precisely identified and plotted on each individual image. The repetition of this process multiple times builds up, upon superimposition of the frames, a highly detailed super-resolution image with all of the locations from each repetition appearing at individual nanometric spots.[188-190] This probe-based superresolution imaging is generally referred to as single-molecule localization microscopy (SMLM), or more precisely dSTORM (direct Stochastic Optical Reconstruction Microscopy) when organic fluorophores such as cyanines are used or PALM (Photo Activation Localization Microscopy) when using photoactivatable fluorescent proteins (**Figure 5-1**).[191-193] Due to the fast development of SMLM, a very important challenge for chemists consists in identifying and exploit photo-switchable fluorophores. As early as in 1997, Dickson *et al*.[194] had identified reversible photoswitching within an individual fluorescent protein molecule. To date four classes of fluorophores have been shown to display photo-switchable luminescent properties 1) small-molecule organic dyes, mostly including cyanines[195-196]; 2) photoactivatable/switchable fluorescent proteins[197-198]; 3) inorganic quantum dots (QDs)[199-200] and carbon dots (CDs)[201-202].

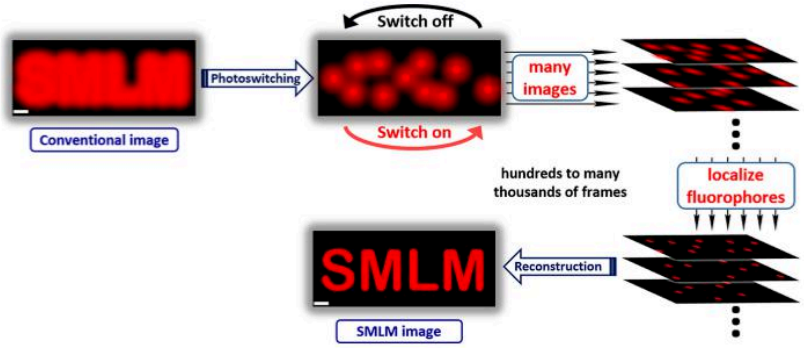

Figure 5-1. Basic principle of SMLM. Picture taken from reference 193.

Among those, small organic molecule fluorescent dyes being easy to modify the targeting group, they have been the most commonly used labeling dyes. For example, in 2008, Heilemann *et al*.[203] found that upon irradiation of a commercial cyanine fluorescent dye (Alexa 647) by a laser with the wavelength of 647 nm , each dye molecule emits photons for a thousands of excitation cycles, then enters a dark state. The dye molecules can return to the fluorescent state under a second laser irradiation with a wavelength of 514 nm (**Figure 5-2**).

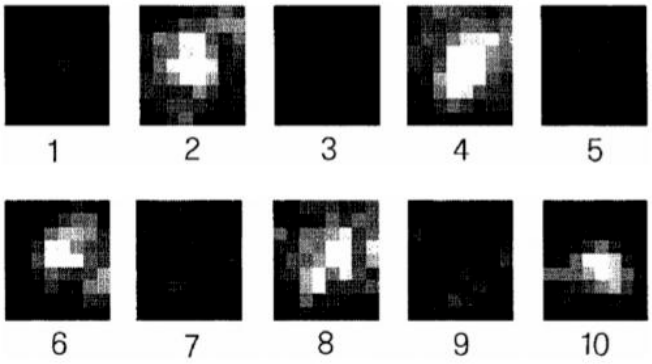

Figure 5-2. On-off photoswitching of yellow fluorescent protein (YFP). Picture taken from reference 194.

In 2012, Zhuang's research group[204] reported that commercial membrane dyes such as cell membranes, mitochondria, lysosomes, endoplasmic reticulum, etc. performing at 562 nm in standard fluorescence microscopy conditions, could be turned into a dark state (or seemingly "photobleached") using stronger excitation light intensity; conversely, similarly to what we

depicted above for Alexa 647 irradiation with a 405 nm wavelength laser can restore the initial fluorescence emission. These dyes enabled observation of subtle phenomena such as the intermediate state of mitochondrial division and fusion, and the extension of endoplasmic reticulum microtubules, with a spatial resolution of 30-60 nm and a temporal resolution of 1-2s.

In a word, design of a new type of super-resolution fluorescent probe not only should consider the photoswitching property but also the long term photostability of the fluorescent probe, its stable localization within the cell and low background fluorescence interference, to afford high contrast. These features are conducive to super-resolution localization imaging of living cells.

1.3 Objective

During our characterization of the different benzobisthiazole derivatives studied in chapter 4, we noticed a peculiar evolution of their fluorescence properties upon long term photoirradiation at the maximum of their absorption wavelength: after an initial rapid bleaching of their luminescence signal, a plateau (*ca* 70% of the initial luminescence intensity) is attained; then, irradiation at a higher energy (lower wavelength, in the UV), almost fully (> 97%) restores the initial luminescence intensity.

Inspired by these preliminary results, we explored the photoswitching properties of compounds synthesized in previous chapters, and the results of these works are reported herein. First we measured the reversible switching in a dark and fluorescent state of three fluorophores (**Figure 5-3**). Then preliminary imaging experiments will conduct to evaluate

their potential in super resolution imaging.

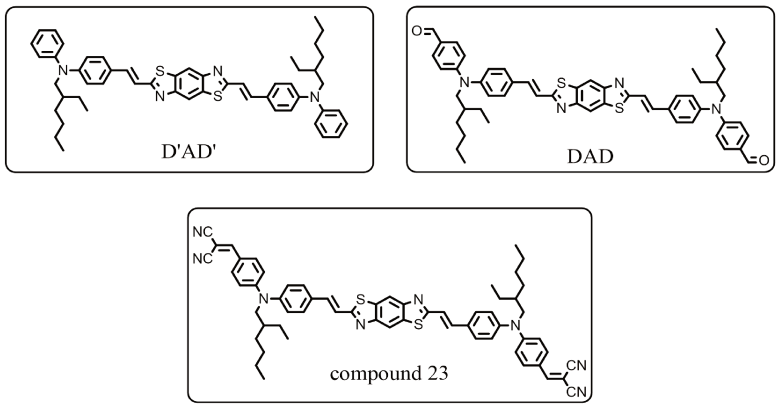

Figure 5-3. Structures of three fluorophores.

2 Characterization of the photoinduced "on/off" switching properties of benzobisthiazole derivatives

2.1 Qualitative assessment of the process

The reversible "photobleaching" or "on/off" switching of the three studied compounds is illustrated in **Figure 5-4**, which features one bleaching/recovery cycle of the three compounds upon successive irradiation in the visible (bleaching) and Near-UV (recovery): In details, the "bleaching" step consists in an irradiation under continuous visible light (480 nm), near the absorption maxium of the chromophore, leading to a gradual decrease of the luminescence intensity, down to a plateau value *ca* 70% of the initial intensity. After this first irradiation step, recovery is achieved by changing the wavelength of the irradiation to UV light (350 nm): luminescence intensity increases with a reverse but otherwise similar kinetic profile and reaches a new plateau value, similar to that obtained before initial visible light irradiation (as verified by measurement of luminescence intensity with a 443 nm excitation between each cycle).

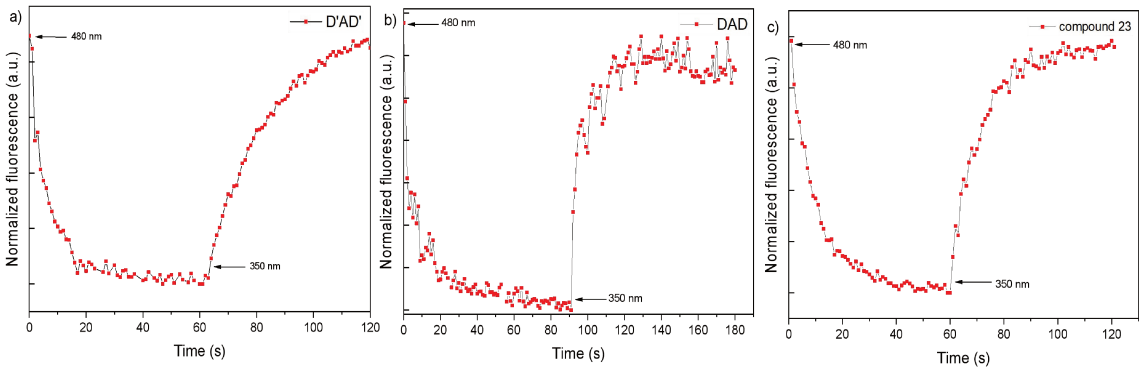

Figure 5-4. Kinetic luminescence of a) D'AD'; b) DAD; c) compound 23.

To study the extent of variations induced by the different irradiations cycles, we examined the fluorescence spectrum of the three compounds (excitation at 443 nm) after each irradiation cycle under visible light (480 nm) or UV (350 nm) (**Figure 5-5**).

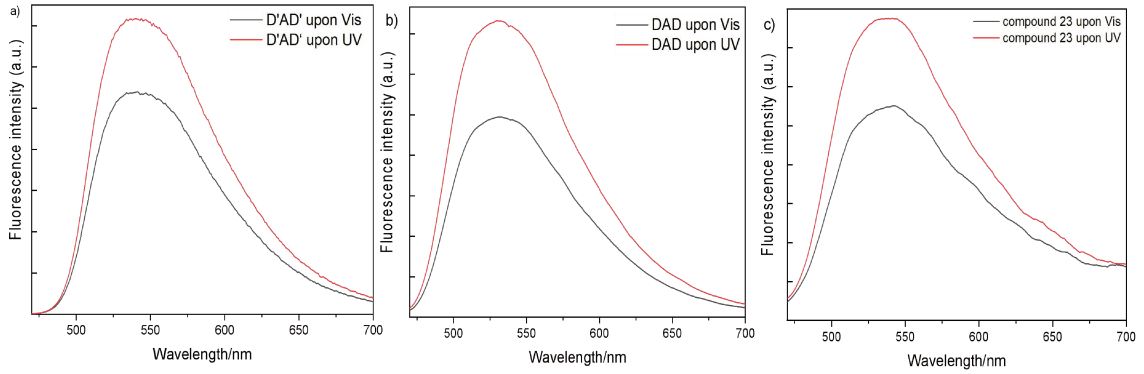

Figure 5-5. Fluorescence spectrum of a) D'AD'; b) DAD; c) compound 23 modulated with visible light (480 nm) or UV light (350 nm) irradiation; λ_{ex}= 443 nm.

Compound	D'AD'	DAD	compound 23
Efficiency (%)	0.26	0.32	0.32

Table 1 Photoconversion efficiency of three compounds.

Using these data, the photoconversion efficiency of three compounds were calculated (**table 1**). All compounds show a similar conversion efficiency around 30%.

2.2 A first insight on the photoswitching mechanism

The experiments detailed above suggest that the process responsible for the observed spectroscopic evolution might correspond to an equilibrium process between a luminescent and non-luminescent form of each benzobisdithiazole derivative, which equilibrium can be reversibly shifted depending on the incident wavelength to which the compound is exposed.

In order to verify this hypothesis, bleaching and recovery data were fitted according to a kinetic model corresponding to the monomolecular reversible transformation equilibrium of A into B (A↔B). Fitting could be achieved with a correlation coefficient R^2 (0.99) **(Figure5-6)**, in good agreement with the above mentioned hypothesis.

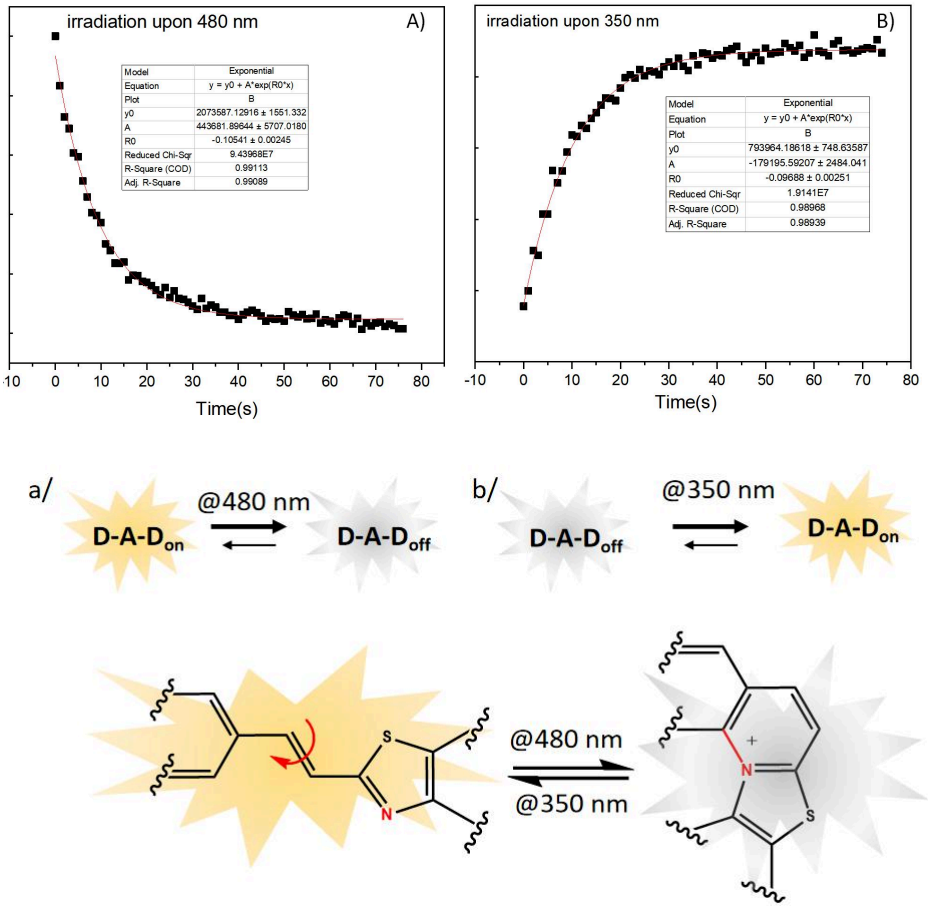

Figure 5-6 Putative mechanism of the luminescent "on" and dark "off".

By analogy with existing literature, we postulate that the mechanism responsible for the observed response is the following: all studied molecules are prone to undergo a reversible photoinduced transition between a luminescent "on" and a dark "off" form, following a cycloaddition process involving the nitrogen atom of each thiazole ring and the neighboring benzyl unit, consecutive to an isomerization of the double bond.[205] Equilibrium of the process can be shifted by *ca* 30% depending on the incident wavelength used in the photoirradiation process, following the mechanism schematically depicted in **Figure 5-6**.

This postulated mechanism should of course be confirmed by future theoretical and experimental works, beyond the timeline of the present thesis work.

2.3 Reversibility of the switching process

An important prerequisite for the probe to be used as a SRM contrast agent is its ability to undergo reversible on-off switching on multiple consecutive cycles, to enable acquisition of multiple individual images that will then be recombined.

Figure 5-7 presents the change in fluorescence intensity (measured at 545 nm, upon excitation of the sample at 443 nm) after each step of the bleaching/recovery cycles, recorded on 10 consecutive cycles.

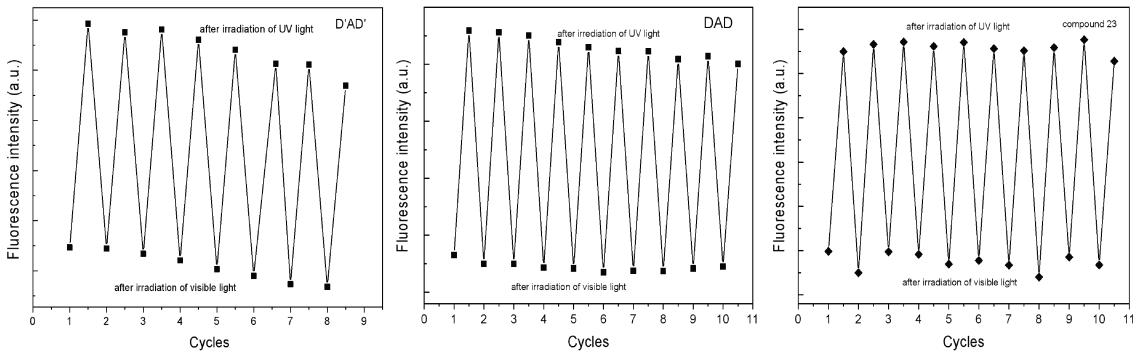

Figure 5-7 Reversible fluorescence photoswitching cycles of a) D'AD'; b) DAD; c) compound 23 (λ_{ex} =

443 nm, λ_{em} = 545 nm).

The three compounds display a good reversibility of the process with a luminescence intensity after 10 cycles which is 93%, 95%, and 98% that of the initial value. DAD and compound 23 displayed the best cycling ability, while D'AD' shows signs of fatigue with a progressive and steady decrease of its luminescence intensity upon cycling.

Encouraged by the above results regarding the exploration of photo-conversion properties of the new family compounds, we envisioned to continue their future investigation as contrast agents in super resolution imaging. Preliminary experiments are currently underway

3 Conclusion

Herein, through the kinetic and photoswitching experiment results, we could illustrate that our new family compounds present the ability to undergo reversible on/off photoswitching of their luminescence, with a simple UV-vis activation. Based on the kinetic results and observed thermodynamic equilibrium, we postulated a mechanism to account for the proccess. This mechanism is based on a key photocylisation step between the nitrogen of the thiazole ring and the adjacent phenyl.

We hope that this mechanism could be exploited in a near future to expand the scope of the properties of the new benzobisthiazole compounds introduced in this thesis work towards their use as contrast agents in super resolution imaging.

Chapter 6 Conclusion

This thesis has introduced several conjugated chromophores presenting the characteristic of an alternation of electron donor and acceptor groups, specifically engineered for dual optimization of their AIE characteristics and TPA properties. The content mainly focused on studying the properties of solution or aggregated states (including suspension and solid state) which exhibit advantages of applications ranging from fluorochromic stimuli-responsive sensors (in film form) to luminescent two-photon probes for the bio-imaging.

In a first part, three tetraphenylethene based A-(D-A)$_n$-D conjugated polymers were synthesized by Sonogashira cross-coupling. Their degree of polymerization is 10, 14 and 11 respectively. As a result of different donor groups and various chain length, three polymers present different spectroscopic properties. **Polymer-2** and **polymer-3** show an AIE phenomenon, accompanied with an uncommon large red shifted in their emission spectrum. Especially the maximum emission wavelength of **polymer-2** in suspension is shifted to 605 nm, in the red region. **Polymer-1** doesn't have a fluorescence increase but it still displays a red shift in emission spectra. We explained this phenomenon by the appearance of luminescence typical of J-aggregates in the solid state. DLS and SEM measurements of the conjugated polymers show that in suspension they form spherical nanoparticles and the particles have a uniform diameter size around 100 nm. Finally, all of them display low toxicity and good photostability in suitable concentration and also can penetrate cell membrane and stain the cytoplasm of HeLa cells, which can be verified by one and two-photon confocal fluorescence imaging.

In a second part, we successfully synthesized a new family of extended benzobisthiazole based chromophores (**DAD**, **$(DA)_2D$**, **$(DA)_5D$**) by Knoevenagel condensation reactions. These compounds combine large molar extinction coefficient, large Stokes shift, and high luminescence quantum yield in both solution and solid state. Especially, they show a stimulus response to acid by a protonation process in both solution and solid state : this process allows easy, concentration dependent naked eye detection of the protonation event that make them excellent candidates for future pH based actuators. Spectrofluorimetry, NMR experiments and theoretical computation are combined together to explain the mechanism of this stimulus response which consists in a bis-protonation process occuring at the core of benzobisthiazole moiety, which switches the electronic transition type from ICT to cyanine-like.

Successive additions of acid and base in the medium show that chromophore display a reversible response to strong acid over more than 10 cycles, which indicate that protonation does not induce chemical degradation of the compound. Introduction of the new chromophores into solid state and polymeric films was achieved, and we proved that the reversible switching properties not only take place in solution but also translate well to the solid and polymeric films, opening-up the possibility to incorporate these compounds into functional devices.

On the other hand, preliminary experiments involving **DAD** as a biological probe (either alone or with a BSA layer coating for improving biocompatibility) show that the nanosuspension of **DAD** can stain Hela cells.

In a third part, we use chemical modifications, namely i) alkylation of the nitrogen or ii) various condensation (Koevenagel/amine condensation) reaction on the aldehyde to expand

the spectroscopic properties of this new class of benzobisthiazole based chromophores. Using these two strategies, a benzobisthiazolium based cyanine derivative (compound **21**), ethyl cyanoacetate terminated derivative (compound **22**), malononitrile terminated derivative (compound **23**) and morpholine terminated derivative (compound **24**) were successfully obtained. Of all, compound **21** exhibits the most interesting evolution of its spectroscopic properties, that combine similar NIR emission features as commercial NIR cyanine dye (Cyanine 5), with a much increased Stokes shifts compared to Cy5 (< 500 cm^{-1} in most solvents). These results of compound **21** constitute advantageous characteristics in view of bioimaging applications.

By comparison, the absorption and emission spectrum of compound **22** and **23** are only marginally affected comparison with **DAD** molecule in solution. Yet compound **23** displays marked AIE properties, and its J-aggregate emission is characterized by a much red shifted maximum compared to **DAD**. Morpholine terminated compound **24** also exhibit similar AIE characteristics The restriction of intramolecular rotations (RIR) of the imine bond induces 7 times fluorescence intensity increase and a large red shift of the emission maximum (over 2000 cm^{-1}) which constitutes again a clear indication that J aggregates have formed upon aggregation of compound **24**. Compared with **DAD**, in suspension, compound **24** presents a much stronger luminescence efficiency and infrared emission characteristics. At last, it has been successfully involved in fluorescence microscopy experiments in cells, and co-localization results illustrate that it specially stains in lysosomes.

In a word, in this thesis we had successfully developed new types of conjugated chromophores presenting suspension or solid emitting properties; by chemical modifications,

new two-photon NIR fluorophores are also successfully developed. Interestingly, we recently found out that our new chromophores show a reversibly photoswitchable phenomenon of their emission spectrum, which is a prerequisite to be used as a probe for dSTORM type of super resolution imaging . Preliminary imaging experiments will be undertaken shortly to evaluate their potential in this framework.

Chapter 7 Experimental Section

1 General information

All of the chemicals and solvents were purchased from commercially available sources and used without further purification. All solvents for spectral measurment were of spectrophotometric grade. Anhydrous solvents were purchased over activated molecular sieves and used as received. Mass spectra [high-resolution mass spectrometry (HRMS)] were performed with a hybrid quadrupole time-off light mass spectrometer, microToF-Q II at the Centre de Spectrométrie de Masse of University of Lyon. Gel Permeation Chromatography (GPC) measurements of **polymer-1**, **polymer-2** and **polymer-3** were perfomed at the INSA lab in university of Lyon on PSS GRAM column setup, solvent is THF, universal calibration is used for molecular mass determination. Bruker Advance NMR operating at 400 MHz for ^{1}H and 101 MHz for ^{13}C or 300 MHz and 75 MHz respectively were used to record proton and carbon spectra, chemical shifts are referenced to Me_4Si (^{1}H, ^{13}C). singlet (s), doublet (d), triplet (t), or multiple (m) were used to describe the splitting patterns. Column chromatographic separations were conducted on Merck silica gel 60 (0.040-0.063 μm) and analytical thin-layer chromatography (TLC) was performed on Merck silica gel TLC plates F-254.

UV-Visible spectra were recorded with the Jasco 670 UV-Visible spectrophotometer. Luminescence spectra were measured on a Horiba-Jobin Yvon Fluorolog-3® spectrofluorimeter. Spectra were reference corrected for both the excitation source light intensity variation (lamp and grating) and the emission spectral response (detector and

grating). According to Porres *et al.*[1] and Mello *et al.*[2], the absolute fluorescence quantum yield (Φ) were performed by an integrating sphere collecting all the emission (2π steradians covered with spectralon®). The sphere was corrected for both excitation and emission with standard correction factors. Microwave syntheses were conducted in a 20 or 5 mL sealed tube on a Biotage Initiator 2.5 single-mode reactor using external IR temperature control. Dynamic Light Scattering (DLS) and Zeta Potential measurements were employed under Zetasizer Nano ZS. The scanning electron microscopy (SEM) were conducted on Zeiss SUPRA 55VP with the assistance of Frédéric CHAPUT (LC ENS, Lyon).

Computational methodology: All Calculations were performed by Tangui Le Bahers (LCENS) The absorption energies were investigated by time-dependent density functional theory (TD-DFT). All calculations were performed by the use of B3LYP/6-31G(d) levels using Gaussian 09.

Cell culture and Co-localization: Biological tests wereperformed in the Key Laboratory of Chemistry for Inorganic/Organic Hybrid Functionalized Materials of Anhui Province, China. HeLa cells were grown in the culture medium which was Dulbecco's modified Eagle's medium (DMEM) supplemented with 10% fetal calf serum (FCS, GIBCO), fungizone and L-glutamine, streptomycin and penicillin. For live cell confocal laser scanning microscopy experiment, HeLa cells were firstly seeded in 24-well glass dish at a density of 10,000 cells per well, and then incubated for 72-96 hours at 37 °C in 95% air 5% CO_2 allow the cells to reach ~ 90% confluence, the culture medium changed every two days. Compounds (1 mM) were prepared in DMSO solution, and precipitated into in culture medium of Hela cells at required concentration for 30 min at 37 °C in 95% air 5% CO_2 and then imaged with confocal

microscopy. Lyso-Tracker Deep Red (647/668 nm) were dissolved in DMSO at a concentration of 1 mM. For colocalization experiments, compounds (10 μM) were incubated with HeLa cells in culture medium for 25 min. Then the medium were replaced with fresh medium in the presence of Lyso-Tracker Deep Red (1 μM) for 20 min. The 24-well plate was washed several times by PBS and imaged. Cell Imaging. One photon cell imaging was taken Olympus FV 1200 and Two photon cell imaging using a Zeiss LSM 710 confocal laser-scanning microscopy.

2 Synthesis and characterization

Synthesis and characterization of **Compound 1**

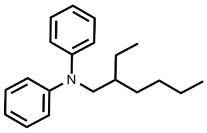

Diphenylamine (6.38 g, 37.5 mmol), sodium hydroxide (15.0 g, 375 mmol) and dimethyl sulfoxide (25.0 ml) were mixed together in a 50 ml flask, then stirred for 0.5 h, 2-Ethylhexylbromide (7.70 ml, 41.25 mmol) was added dropwise into the reaction mixture, stirring overnight at room temperature. Reaction was stopped, then we removed the excess dimethyl sulfoxide under high vacuum, and poured it into a mixture of ethyl acetate and water in equal volumes, the organic layer was washed by water 3 times, evaporated and crude product was purified by column chromatography with petroleum ether as eluent to give compound **1** (5.40 g, yield: 51%). ^{1}H NMR (400 MHz, $CDCl_3$, 25 °C): δ (ppm) = 7.27 (t, J = 7.6 Hz, 4 H), 7.03 (d, J = 7.6 Hz, 4 H), 6.95 (t, J = 8.00 Hz, 2 H), 3.61 (d, J = 8.00 Hz, 2 H), 1.79 (s, 1 H), 1.52-1.28 (m, 8 H), 0.88 (t, J = 8.00 Hz, 6 H); ^{13}C NMR (100.6 MHz, $CDCl_3$, 25 °C): δ (ppm) = 149.1, 128.9

, 121.2, 121.0, 56.6, 37.6, 30.7, 28.6, 24.0, 23.2, 14.1, 10.7. HR-MS (ESI): m/z = 282.2214 $[M+H]^+$, calcd. for 282.2216.

Synthesis and characterization of **Compound 2**

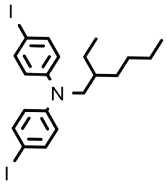

(2-ethylhexyl)-phenylaniline (1.41 g, 5 mmol) was dissolved in THF (20 ml) and pyridine (20 ml) at 70 °C, then iodine was added (6.30 g, 50 mmol) and the solution was stirred for one hour at 70 °C. A saturated solution of sodium thiosulfate was then added until the brown color disappeared. The mixture was extracted with dichloromethane and washed with water for many times, solution was dried on sodium sulfate and rotary evaporated. The crude product was purified by filtration through a short column chromatography with petroleum as eluent to give compound **2** (1.95 g, yield: 73%). ^{1}H NMR (400 MHz, $CDCl_3$, 25 °C) δ (ppm) = 7.53 (d, *J* = 12 Hz, 4 H), 6.77 (m, 4 H), 3.54 (d, *J* = 9.6 Hz, 2 H), 1.71 (s, 1 H), 1.50-1.27 (m, 8 H), 0.87 (m, 6 H), ^{13}C NMR (100.6 MHz, $CDCl_3$) δ 149.0, 129.4, 121.2, 84.0, 56.6, 37.4, 30.5, 28.7, 23.8, 23.0, 13.9, 10.3. HR-MS (ESI): m/z = 534.0144, $[M+H]^+$, calcd. for 534.0149.

Synthesis and characterization of **Compound 3**

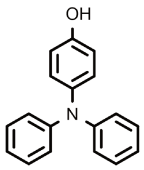

To a solution of 4-methoxy-N-diphenylaniline (1.95 g, 7.09 mmol) in dry dichloromethane (70 ml) was added boron tribromide (10.64 ml, 10.64 mmol, 1.0 mol/L solution in dichloromethane) at 0 °C and the resulting solution was stirred for 30 min. The reaction

mixture was allowed to warm up to room temperature and further stirred for 4 h, then poured into water and extracted with DCM, dried by Na_2SO_4 and rotary evaporated. The residue was chromatographed on silica gel with petroleum and ethyl acetate (petroleum:ethyl acetate = 40 :1) as eluent to get compound **3** (1.64 g, yield: 89%). ^{1}H NMR (400 MHz, $CDCl_3$, 25 °C) δ (ppm) = 9.40 (s, 1 H), 7.23 (m, 4 H), 6.93 (m, 8 H), 6.77 (m, 2 H), ^{13}C NMR (100.6 MHz, $CDCl_3$) δ (ppm) = 151.9, 148.2, 140.9, 132.1, 129.1, 127.4, 122.9, 121.8. HR-MS (ESI): m/z = 261.1154, $[M+H]^+$, calcd. for 261.1184.

Synthesis and characterization of **Compound 4**

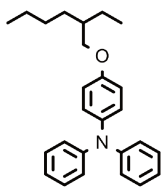

Compound 3 (0.52 g, 2 mmol), 2-(bromo-methyl)heptane (0.97 g, 5 mmol) and K_2CO_3 (1.10 g, 8 mmol) were dissolved in DMF (8 ml). After being stirred overnight at 90 °C under argon atmosphere, the mixture was poured into ice water while stirring and then extracted by DCM for 3 times. The organic layers were combined and the solvent was removed under reduced pressure, the residue was purified by chromatography on a silica gel column with petroleum as eluent to get compound **4 (**0.35 g, yield: 47%). ^{1}H NMR (400 MHz, $CDCl_3$, 25 °C) δ (ppm) = 7.23 (m, 4 H), 6.97 (m, 10 H), 3.84 (d, *J* = 8 Hz, 2 H), 1.71 (m, 1 H), 1.50-1.27 (m, 8 H), 0.87 (m, 6 H). ^{13}C NMR (100.6 MHz, $CDCl_3$) δ (ppm) = 153.8, 145.3, 137.5, 131.8, 129.6, 126.8, 125.7, 115.4, 74.9, 40.3, 30.4, 29.6, 23.8, 23.0, 14.1, 11.9. HR-MS (ESI): m/z = 373.2406, $[M+H]^+$, calcd. for 373.2439.

Synthesis and characterization of **Compound 5**

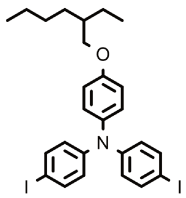

Compound **4** (0.397 g, 1.06 mmol) was dissolved in THF (5 ml) and pyridine (2.5 ml) at 70 °C, iodine (1.53 g, 12 mmol) was added in one portion, the solution progressively took a dark brown colour. After 2 h, saturated solution of sodium thiosulfate was then added until the brown color disappeared, the mixture was extracted by DCM and washed with water for many times. After evaporation of residual solvents, the crude product was purified by chromatography on a silica gel column with petroleum to get compound **5** (0.51 g, yield: 76 %). ^{1}H NMR (300 MHz, $CDCl_3$, 25 °C) δ (ppm) = 7.49 (d, *J* = 7.2 Hz, 4 H), 7.03 (d, *J* = 7.2 Hz, 2 H), 6.83 (m, 6 H), 3.83 (d, *J* = 8 Hz, 2 H), 1.71 (m, 1 H), 1.50-1.27 (m, 8 H), 0.90 (m, 6 H). ^{13}C NMR (100.6 MHz, $CDCl_3$) δ (ppm) = 156.8, 147.4, 139.1, 138.1, 127.6, 124.6, 115.0, 84.3, 70.2, 39.5, 30.2, 29.0, 24.2, 23.0, 14.0, 10.9. HR-MS (ESI): m/z = 625.0339, $[M+H]^+$, calcd. for 625.0372.

Synthesis and characterization of **Compound 6**

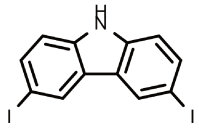

Carbazole (6.00 g, 36 mmol) and KI (7.80 g, 47 mmol) were dissolved in acetic acid (50 ml) at room temperature, Then after slowly adding K_2CO_3 (10.00 g, 47 mmol) by portions, the reaction mixture was heated to 80 °C for 6 h, then cooled to room temperature, filtered and washed with water. After removal of the solvent by rotary evaporation, the crude product was

recrystalized from ethanol to give compound **6** (10.05 g, yield: 71%). Spectral data were in accordance with literature 3. CAS number 57103-02-3.

Synthesis and characterization of **Compound 7**

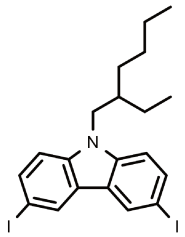

Compound 6 (0.84 g, 2.0 mmol) , 2-(bromo-methyl)heptane (0.42 g, 2.2 mmol) and NaOH (0.80 g, 20 mmol) were dissolved in DMSO (10 ml). After being stirred overnight at 50 °C in argon atmosphere, the mixture was poured into ice water while stirring and then extracted by DCM for 3 times. The organic layers were combined and the solvent was removed under reduced pressure, then the residue was purified by chromatography on a silica gel column with petroleum as eluent to get compound **7** (0.67 g, yield: 63%). Spectral data were in accordance with literature 3. CAS number 350474-29-2.

Synthesis and characterization of **Compound 8**

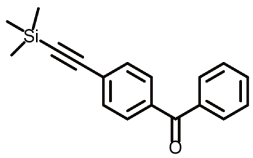

Into a septum sealed 100 mL two-necked round-bottom flask were successively added $Pd(PPh_3)_2Cl_2$ (70.1 mg, 0.1 mmol), CuI (19 mg, 0.1 mmol), PPh_3 (13 mg, 0.05 mmol), **4-bromobenzophenone** (1.3 g, 5 mmol) and a degased solvent mixture of THF/Et_3N (5 ml/50 ml) in an atmosphere of argon. After the catalysts were completely dissolved, (trimethylsiyl)acetylene (0.9 ml, 6.5 mmol) was injected into the flask and the mixture was stirred at 70 °C for 24 h. The formed solid (mostly triethylammonium bromide) was removed

by filtration and washed with diethyl ether. Filtrate was recovered, solvent was removed by rotary evaporation and the crude product was purified on a silica-gel column using pentane as eluent to get a pale brown solid (1.26 g, yield: 91%). ^{1}HNMR (400 MHz, $CDCl_3$, 25 °C) δ (ppm) = 7.77 (d, *J* = 7.20 Hz, 2 H), 7.75 (d, *J* = 8.4 Hz, 2 H), 7.57 (m, 3 H), 7.48 (m, 2 H), 0.27 (s, 9 H). ^{13}C NMR (100.6 MHz, $CDCl_3$, 25 °C) δ (ppm) = 195.9, 137.3, 136.9, 132.5, 131.7, 129.9, 129.8, 128.3, 127.3, 104.0, 97.8, 0.18.

Synthesis and characterization of **Compound 9**

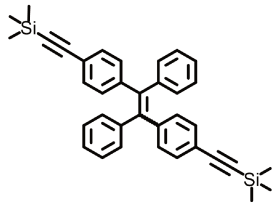

Into a 100 mL schlenk tube equipped with a reflux condenser were added zinc dust (12.1 g, 18 mmol) and THF (50 ml) . The tube was bubbled with argonfor 1 h. The mixture was cooled to 0 °C and $TiCl_4$ (1.0 ml, 9 mmol) was slowly added. The mixture was slowly warmed to room temperature, stirred for 2.0 h. **Compound 8** (4.18 g, 15 mmol,) in THF was added, then the resulting mixture was refluxed overnight. The reaction was quenched with 10% aqueous K_2CO_3 solution and large amount of water was added until the solid turned to gray. The mixture was extracted with DCM for three times. The organic layers were combined and washed with brine twice. After solvent rotary evaporation, the crude product was purified by column chromatography (silica gel) using pentane as eluent to get a yellow solid (0.14 g, yield:18%). Spectral data were in accordance with literature 4.

Synthesis and characterization of **Compound 10**

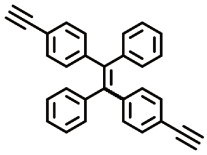

Into a 100 mL round bottom flask was added 30 mL of THF solution of **compound 9** (0.53 g, 1 mmol), followed by addition of K_2CO_3 (0.83 g, 6 mmol) (dissolved in THF: MeOH/5:1), After stirring for 3 h, 30 mL of water was added and the mixture was extracted with DCM three times. The DCM solution was washed with brine twice. The mixture was dried over anhydrous sodium sulfate. After solvent rotary evaporation, the crude product was purified by column chromatography (silica gel) using hexane as eluent to obtain a light yellow solid （0.31 g, yield: 82%). Spectral data were in accordance with literature 4.

Synthesis and characterization of **Compound 11 (polymer-1)**

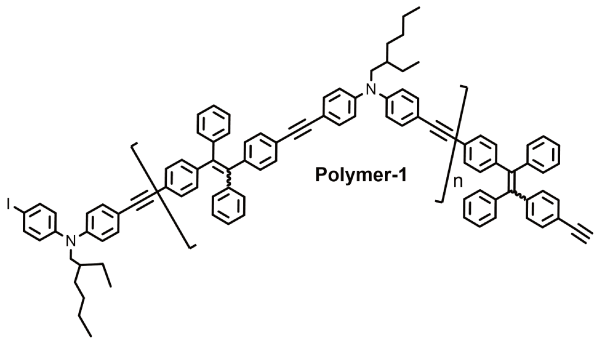

To an argon degassed mixture of compound **2** (monomer 2) (171 mg, 0.32 mmol), compound **10** (monomer 1) (121 mg, 0.32 mmol), bis(triphenylphosphine)palladium(II) chloride (22.5 mg, 0.032 mmol) and copper (I) iodide (12.2 mg, 0.064 mmol) were added into schlenk tube, the tube was purged under vacuum and flushed with argon three times. Then dry THF (10 mL) and triethylamine (10 mL) were injected into it, and the reaction mixture was stirred at reflux until TLC indicated complete conversion. After cooling to room temperature, pouring the

mixed reaction into 500 ml water and extracting organic layer by dichloromethane, the organic layer was dried under sodium sulfate and rotary evaporated. The crude product was washed through with large amounts of methanol and a little diethyl ether. Finally, a light dark yellowish solid (0.11 g, yield: 38%) was obtained. (400 MHz, $CDCl_3$, 25 °C) δ (ppm) = 7.56 (m, 42 H), 6.91 (m, 198 H), 3.60 (m, 20 H), 1.74 (m, 10 H), 1.30 (m, 94 H), 0.86 (m, 60 H). ^{13}C NMR (101 MHz, $CDCl_3$, 25 °C) δ (ppm) = 146.9, 142.2, 139.9, 137.2, 131.4, 130.3, 129.9, 129.7, 126.8, 126.7, 125.8, 123.6, 120.7, 120.5, 119.9, 118.8, 114.6, 89.1, 87.7, 55.3, 36.9, 29.7, 27.4, 23.1, 22.0, 13.3, 9.9. GPC: M_w = 7181, M_n = 4165, M_z = 11306, M_w/M_n = 1.72.

Synthesis and characterization of **Compound 12 (polymer-2)**

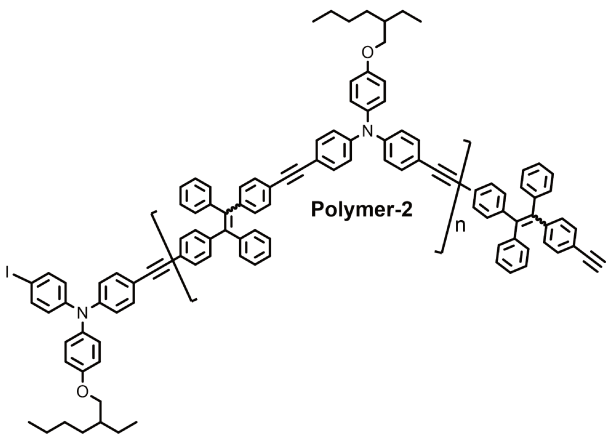

Compound **5** (monomer 3) (125 mg, 0.20 mmol), compound **10** (monomer 1) (76 mg, 0.20 mmol), bis(triphenylphosphine)palladium(II) chloride (14.5 mg, 0.02 mmol) and copper (I) iodide (7.6 mg, 0.04 mmol) were added into schlenk tube. The tube was purged under vacuum and flushed with argon three times. Then dry THF (15 mL) and triethylamine (10 mL) were injected into it, and the reaction mixture was stirred at reflux temperture until TLC indicated complete conversion. After cooling to room temperature, pouring the mixed reaction into 500 ml water and extracting by dichloromethane. the organic layer was dried with sodium sulfate

and rotary evaporated. The crude product was then washed thoroughly with large volumes of methanol and a little diethyl ether. Finally, a brownish yellow solid (70 mg, yield: 35%) was obtained. (400 MHz, $CDCl_3$, 25 °C) δ (ppm) = 7.61 (m, 62 H), 7.01 (m, 334 H), 3.84 (m, 28 H), 1.73 (m, 14 H), 1.27 (m, 112 H), 0.92 (m, 84 H). ^{13}C NMR (101 MHz, $CDCl_3$, 25 °C) δ (ppm) = δ 155.9, 146.1, 142.6, 139.7, 131.7, 130.5, 129.7, 126.8, 125.7, 121.1, 115.3, 114.7, 98.4, 87.8, 69.6, 38.4, 29.5, 28.0, 22.8, 21.7, 12.8, 9.9. GPC: M_w = 10748, M_n = 3959, M_n = 19772, M_w/M_n = 2.71.

Synthesis and characterization of **Compound 13 (polymer-3)**

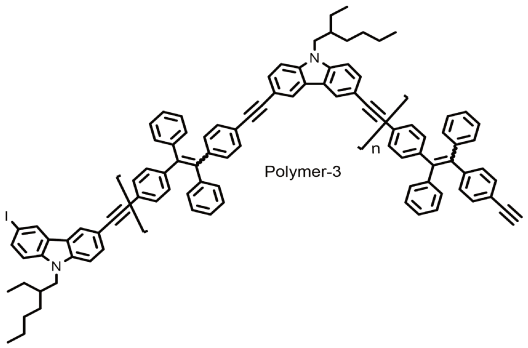

Compound **7** (monomer 4) (85 mg, 0.16 mmol), compound **10** (monomer 1) (61 mg, 0.16 mmol), bis(triphenylphosphine)palladium(II) chloride (18.4 mg, 0.016 mmol) and copper (I) iodide (6.1 mg, 32 mmol) were added into schlenk tube. The tube was purged under vacuum and flushed with argon three times. Then dry THF (10 mL) and triethylamine (10 mL) were injected into it, and the reaction mixture was stirred at reflux temperature until TLC indicated complete conversion. After cooling to room temperature, pouring the mixed reaction into 500 ml water and extracting by dichloromethane. the organic layer was dried with sodium sulfate and rotary evaporated. The crude product was then washed thoroughly with large volumes of methanol and a little diethyl ether. Finally, a brownish yellow solid (58 mg, yield: 40%) was

obtained. (400 MHz, $CDCl_3$, 25 °C) δ (ppm) = 8.3 (m, 22 H), 7.50 (m, 94 H), 7.15 (m, 182 H), 4.17 (m, 24 H), 2.04 (m, 12 H), 1.27 (m, 104 H), 0.90 (m, 84 H). ^{13}C NMR (101 MHz, $CDCl_3$, 25 °C) δ (ppm) 142.2, 139.9, 139.1, 138.6, 133.2, 130.3, 129.9, 129.8, 128.8, 128.3, 126.9, 126.7, 125.7, 123.8, 123.0, 121.4, 120.7, 112.8, 110.2, 108.2, 89.9, 86.7, 80.7, 46.3, 37.9, 29.9, 27.7, 23.3, 21.9, 12.9, 9.8. GPC: M_w = 7547, M_n = 4359, M_n = 11972, M_w/M_n = 1.73.

Synthesis and characterization of **Compound 14**

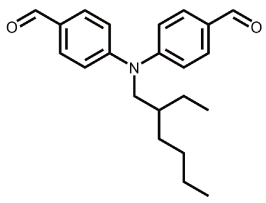

Phosphorus oxychloride (1.67 ml, 0.018 mol) was added dropwise to dimethylformamide (1.24 ml, 0.018 mol) at 0 °C, then compound **1** (0.50 g, 1.8 mmol) was added to the above solution and stirred at 90 °C for 20 h. After reaction, saturated sodium carbonate solution was added until PH is 6-8. Organic layer was extracted with dichloromethane and then dried with sodium sulfate and rotary evaporated. Purification with column chromatography by petroleum ether and ethyl acetate (20 : 1), compound **14** (0.24 g, yield: 40%) was obtained. ^1H NMR (300 MHz, $CDCl_3$, 25 °C) δ (ppm) = 9.89 (s, 2 H), 7.82 (d, *J* = 8.7 Hz, 4 H), 7.18 (d, *J* = 8.6 Hz, 4 H), 3.79 (d, *J* = 7.4 Hz, 4 H), 1.78 (s, 2 H), 1.51-1.28 (m, 16 H), 0.87 (m, 12 H). ^{13}C NMR (75 MHz, $CDCl_3$, 25 °C): δ (ppm) = 190.4, 152.6, 131.4, 130.6, 121.0, 56.4, 37.7, 30.6, 28.5, 24.0, 22.9, 13.9, 10.6. HR-MS (ESI): m/z = 338.2124, $[M+H]^+$, calcd. for 338.2115.

Synthesis and characterization of **Compound 15**

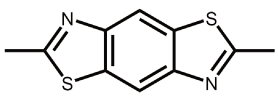

2,5-diaminobenzene-1,4-dithiol-dihydrochloride (0.74 g, 3.0 mmol) was suspended in

dimethylformamide (6.0 ml), and then pyridine (0.5 ml, 6.25 mmol) was added dropwise. A mixture of triethylorthoacetate (1.49 g, 9.0 mmol) and $Sc(OTf)_3$ (73.5 mg, 0.15 mmol) was added into the reaction solution and stirred at 50 °C for 2 h, then cooled to room temperature and diluted with water, finally extracted with dichloromethane. Organic layer was dried on sodium sulfate then rotary evaoprated. The crude product was purified by column chromatography with petroleum ether and ethyl acetate (8 : 1). Compound **15** (0.43 g, yield: 65%) was obtained. Spectral data were in accordance with literature 5. CAS number 13399-12-7.

Synthesis and characterization of **Compound 16 (DAD)**

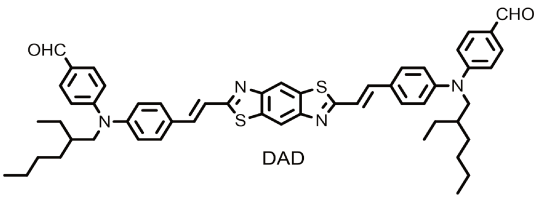

Compound **15** (10.0 mg, 0.045 mmol) and compound **14** (45.9 mg, 0.135 mmol) were added into sodium hydroxide solution (2.0 ml, 2.5 M). Then tetrabutylammonium hydrogen sulfate as catalyst (10 mg), the solution was stirred at 50 °C for 1.0 h. Reaction was stopped, the solid precipitate was filtered and washed thoroughly by diethyl ether. Compound **16** (24 mg, yield: 62%) was obtained. ^{1}H NMR (400 MHz, $CDCl_3$, 25 °C) δ (ppm) = 9.83 (s, 2 H), 8.45 (s, 2 H), 7.74 (d, J = 8.0 Hz, 4 H), 7.66 (d, J = 7.6 Hz 4 H), 7.55 (d, J = 16.0 Hz, 2 H), 7.43 (d, J = 16.0 Hz, 2 H), 7.26 (s, 4 H), 6.97 (d, J = 8.0 Hz, 4 H), 3.77 (d, J = 6.4 Hz, 4 H), 1.84 (s, 2 H), 1.51-1.28 (m, 16 H), 0.90 (m, 12 H). ^{13}C NMR (101 MHz, $CDCl_3$, 25 °C) δ (ppm) = 190.3, 167.9, 153.5, 152.1, 147.8, 137.4, 133.8, 131.7, 131.5, 129.0, 127.9, 125.7, 121.5, 116.3, 114.9, 56.4, 37.7, 30.6, 28.5, 24.0, 23.0, 14.0, 10.7. HR-MS (ESI): m/z = 859.4066, $[M+H]^+$,

calcd. for 859.4074.

Synthesis and characterization of **Compound 17 $(DA)_2D$**

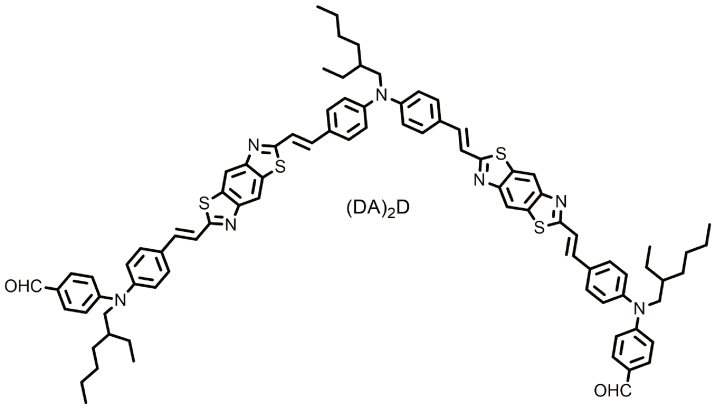

Compound **15** (0.061 g, 0.28 mmol) and compound **14** (0.14 g, 0.42 mmol) were added into sodium hydroxide solution (15 ml, 5 M). Then tetrabutylammonium hydrogen sulfate as catalyst (0.05 g), and solution was stirred at 50 °C for 1.5 h. Reaction was stopped, the solid precipitate was filtered and washed thoroughly by diethyl ether. Compound **17** (0.31 g, yield: 52%) was obtained. ^{1}H NMR (400 MHz, $CDCl_3$, 25 °C): δ (ppm) = 9.78 (s, 2 H), 8.43 (m, 4 H), 7.75 (d, *J* = 8.8 Hz, 4 H), 7.65 (d, *J* = 8.4 Hz, 4 H), 7.60-7.30 (m, 14 H), 7.26 (s, 4 H), 7.12 (d, *J* = 6.8 Hz, 4 H), 6.96 (d, *J* = 8.8 Hz, 4 H), 3.77 (d, *J* = 7.2 Hz, 6 H), 1.84 (s, 3 H), 1.44-1.21 (m, 24 H), 0.90 (m, 18 H). ^{13}C NMR (100.6 MHz, $CDCl_3$, 25 °C) δ (ppm) = 190.2, 168.2, 153.5, 152.3, 150.8, 147.8, 137.8, 133.9, 131.5, 128.8, 127.6, 125.8, 121.3, 116.5, 114.7, 56.6, 38.0, 30.8, 28.7, 24.2, 23.0, 14.2, 10.7. HR-MS (ESI): m/z = 690.8038, $[M+2H]^{2+}$, calcd. for 690.8053.

Synthesis and characterization of **Compound 18 ((D-A)$_5$-D)**

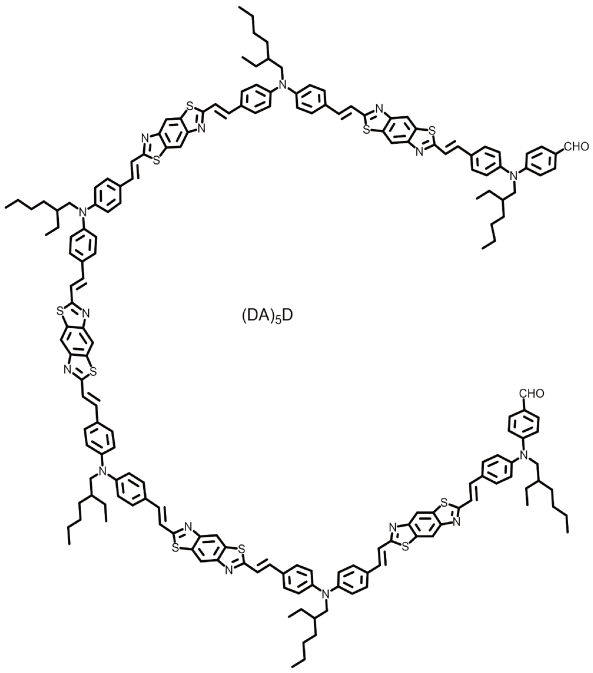

Dissolving compound **15** (0.13 g, 6 mmol) and compound **14** (0.21 g, 6 mmol) in dichloromethane (1.0 mL), then adding sodium hydroxide solution (15 ml, 5 M) which was added tetrabutylammonium hydrogen sulfate as catalyst, first stirring at room temperature for 0.5 h and then 45 °C for 2.5 h, Reaction was stopped, the solid precipitate was filtered and washed thoroughly by diethyl ether, (in fact an oligomeric mixtures of compounds with an average n value of 5). Compound **18** 0.21 g (yield: 61%) was obtained. ^{1}H NMR (400 MHz, $CDCl_3$, 25 °C) δ (ppm) = 9.75 (s, 2 H), 8.50-8.24 (m, 10 H), 7.74 (d, *J* = 8.8 Hz, 4 H), 7.64 (d, *J* = 8.4 Hz, 4 H), 7.59-7.29 (m, 36 H), 7.26 (d, *J* = 8.4 Hz, 4 H), 7.10 (d, *J* = 8.0 Hz, 14 H), 6.96 (d, *J* = 8.8 Hz, 6 H), 3.76 (m, 12 H), 1.83 (s, 6 H), 1.51-1.27 (m, 48 H), 0.91 (m, 36 H). ^{13}C NMR (101 MHz, $CDCl_3$, 25 °C) δ (ppm) = 190.5, 168.2, 153.8, 152.0, 149.3, 147.8, 137.8, 133.3, 131.5, 128.6, 125.8, 121.3, 119.8, 116.2, 114.4, 56.3, 38.0, 30.5, 28.3, 24.2, 23.3, 13.7, 10.9.

Synthesis and characterization of **Compound 19**

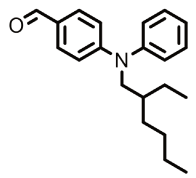

Phosphorus oxychloride (1.67 ml, 0.018 mol) was added dropwise to dimethylformamide (1.24 ml, 0.018 mol) at 0 °C, then compound **1** was added to the above solution and stirred at 30 °C overnight. After reaction, saturated sodium carbonate solution was added until pH is 6-8. Mixture was extracted with dichloromethane, organic layer was dried on sodium sulfate and solvents were removed by rotary evaporation. Raw material was purified on column chromatography using petroleum ether and ethyl acetate as eluent (100 : 1). Compound **19** (3.01 g, yield: 54%). ^{1}H NMR (300 MHz, $CDCl_3$, 25 °C) δ (ppm) = 9.76 (s, 1H), 7.67 (d, *J* = 9.0 Hz, 2 H), 7.45 (t, *J* = 7.8 Hz, 2 H), 7.31-7.19 (m, 6 H), 6.76 (d, *J* = 8.7 Hz, 2 H), 3.69 (d, *J* = 7.2 Hz, 2 H), 1.80 (m, 1 H), 1.51-1.18 (m, 8 H), 0.94 (m, 6 H). ^{13}C NMR (75 MHz, $CDCl_3$, 25 °C) δ (ppm) = 190.1, 154.3, 146.2, 131.6, 130.0, 127.4, 126.5, 126.1, 113.8, 56.5, 37.8, 30.5, 28.5, 23.9, 23.0, 14.0, 10.6.

Synthesis and characterization of **Compound 20 (D'AD')**

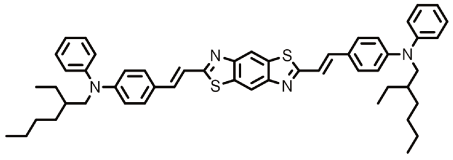

Compound **15** (40 mg, 0.18 mmol) and compound **19** (0.14 g, 0.45 mmol) were dissolved in dichloromethane (5 ml), then sodium hydroxide solution (15 ml, 5 M) which was added tetrabutylammonium hydrogen sulfate as catalyst, stirring at 50 ℃ overnight. Stop reaction, extracted with dichloromethane and evaporated the organic layer, then got the crude product,

washed with diethyl ether to give compound **20** (75 mg, yield: 52%). ^{1}H NMR (400 MHz, $CDCl_3$, 25 °C): δ (ppm) = 8.25 (s, 2 H), 7.38-7.34 (m, 6 H), 7.29 (m, 4 H), 7.18 (d, *J* = 5.2 Hz, 2 H), 7.13-7.05 (m, 6 H), 6.76 (d, *J* = 8.8, 4 H), 3.57 (d, *J* = 7.2, 4 H), 1.71 (m, 2 H), 1.41-1.18 (m, 16 H), 0.79 (t, *J* = 14.8 Hz, 12 H). ^{13}C NMR (101 MHz, $CDCl_3$, 25 °C) δ (ppm) = 168.7, 152.0, 150.4, 147.4, 138.2, 133.5, 129.6, 128.7, 125.6, 125.5, 124.3, 118.0, 116.7, 114.4, 56.7, 37.7, 30.6, 28.5, 23.9, 23.2, 13.9, 10.6. HR-MS (ESI): m/z = 803.4175, $[M+H]^+$, calcd. for 803.4176.

Synthesis and characterization of **Compound 21 (DA'D)**

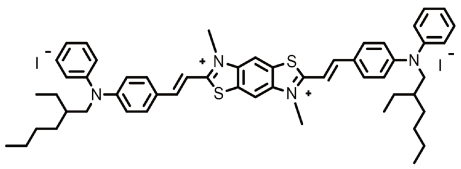

Compound **20** (80 mg, 1.0 mmol) in 1,2-dichlorobenzene (2 mL) and an excess of dimethyl sulfate (2.0 mL, 21.1 mmol) were exposed to microwave irradiation for 1 hour at 120 °C. Evaporated the rest of the dimethyl sulfate after cooling down the reaction to room temperature. Dissolving the residue in 10% NaI (6 ml), stirred for 30 min. The precipitate was filtered and dried, crude product was purified by recrystallization from water to obtain compound **21** (65 mg, yield is 60%). ^{1}H NMR (300 MHz, DMSO, 25 °C) δ (ppm) = 8.97 (s, 2 H), 8.23 (d, *J* = 15.3 Hz, 2 H), 7.93 (d, *J* = 9.0 Hz, 4 H), 7.71 (d, *J* = 15.3 Hz, 4 H), 7.54 (t, *J* = 7.5 Hz, 4 H), 7.37 (m, 6 H), 6.83 (d, *J* = 9.0 Hz, 4 H), 4.26 (s, 6 H), 3.81 (d, *J* = 7.8 Hz, 4H), 1.65 (s, 2 H), 1.41-1.19 (m, 16 H), 0.82 (m, 12 H). ^{13}C NMR (75 MHz, DMSO, 25 °C) δ (ppm) = δ 173.0, 154.0, 152.1, 145.1, 141.3, 133.7,130.6, 127.7, 127.5, 127.1, 123.6, 114.3, 111.1, 107.7, 57.7, 38.0, 36.6, 30.2, 28.3, 23.7, 22.8, 14.3, 10.9. HR-MS (ESI): m/z = 416.2281,

$[M]^{2+}$, calcd. for 416.2274.

Synthesis and characterization of **Compound 22**

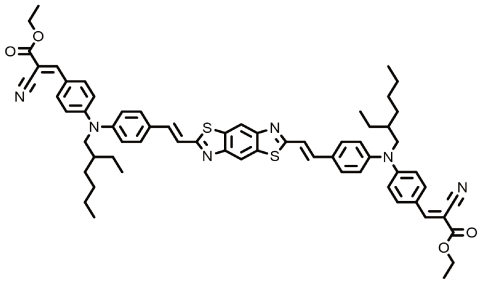

Ethyl cyanoacetate (32 mg, 0.291 mmol) and **DAD** (50 mg, 0.0582 mmol) were dissolved in a mixture of ethanol (8 ml) and chloroform (2 ml), then two drops of piperidine was added, after stirring at 70 °C for one night, then cooling to room temperature, the precipitated product was collected by filtration, washed with a small amount of ether and dried to give bright yellow compound **22** (48 mg, yield: 80%). ^{1}H NMR (300 MHz, $CDCl_3$, 25 °C): δ (ppm) = 8.34 (s, 2 H), 7.61 (d, *J* = 5.1 Hz, 4 H), 7.56(s, 2 H) , 7.45 (d, *J* = 6 Hz, 4 H), 7.42 (s, 2H), 7.28 (s, 1 H), 7.22 (s, 1H), 7.14 (d, *J* = 8.7 Hz, 4 H), 6.94 (d, *J* = 8.7 Hz, 4 H), 3.92 (t, *J* = 9.3 Hz, 8 H), 3.68 (d, *J* = 6.9 Hz, 4 H), 3.18 (t, *J* = 9.3 Hz, 8 H), 1.78 (s, 2 H), 1.42 (m, 16H), 0.86 (m, 12H). ^{13}C NMR (75 MHz, $CDCl_3$) δ 167.9, 163.9, 154.2, 152.8, 152.2, 147.3, 137.4, 134.0, 133.4, 132.6, 126.4, 122.0, 121.9, 117.1, 115.8, 115.0, 96.3, 77.1, 62.2, 56.3, 37.7, 30.7, 28.5, 24.0, 23.1, 14.2, 13.9, 10.6. HR-MS (ESI): m/z =1049.4852, $[M+H]^+$, calcd. 1049.4816.

Synthesis and characterization of **Compound 23**

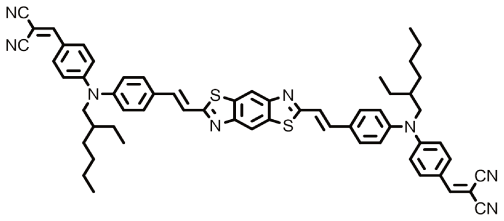

Malononitrile (38 mg, 0.5820 mmol) and **DAD** (50 mg, 0.0582 mmol) were mixed with 2 ml dimethyl sulfoxide and heated at 115 °C for 3 h under microwave activation. Mixture was cooled to room temperature, solution was filtered to afford a dark precipitate, which was purified by column chromatography using petroleum ether and ethyl acetate (5 : 1) as eluent to obtain the compound **23** (23 mg, yield 42.0 %). ^{1}H NMR (400 MHz, DMSO, 25 °C): δ (ppm) = 8.69 (s, 2 H), 8.15 (s, 2 H), 7.92 (d, *J* = 9.2 Hz, 4 H), 7.87 (m, 8 H), 7.75 (d, *J* = 16 Hz, 2 H), 7.66 (d, *J* = 16 Hz, 2 H), 7.38 (d, *J* = 8 Hz, 4 H), 6.94 (d, *J* = 8 Hz, 4 H), 3.82 (d, *J* = 8 Hz, 4 H), 1.67 (m, 2 H), 1.32 (m, 16 H), 0.89 (t, *J* = 7.2 Hz, 12H). ^{13}C NMR (101 MHz, DMSO, 25 °C): δ (ppm) 167.9, 159.5, 153.9, 152.1, 146.1, 137.6, 134.1, 133.8, 133.4, 129.9, 127.3, 122.4, 121.5, 116.2, 115.8, 115.3, 72.1, 55.6, 37.9, 30.1, 28.3, 23.5, 22.9, 14.3, 10.9. HR-MS (ESI): m/z =955.4282, $[M+H]^{+}$, calcd. 955.4295.

Synthesis and characterization of **Compound 24**

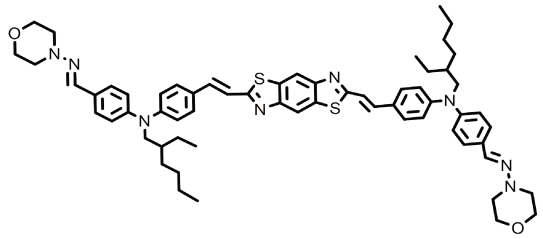

4-**amino-morpholine** (36 mg, 0.291 mmol) and **DAD** (50 mg, 0.0582 mmol) were dissolved in a mixture of methanol (8 ml) and chloroform (2 ml), then three drops of acetic acid were added. After stirring at 70 °C for one night, then cooling to room temperature, the precipitated product was collected by filtration, washed with a small amount of ether and dried to give compound **24** as a fluffy orange powder (26 mg, yield: 43%). ^{1}H NMR (300 MHz, $CDCl_3$, 25 °C): δ (ppm) = 8.34 (s, 2 H), 7.61(d, *J* = 5.1 Hz, 4 H), 7.56 (s, 2 H) , 7.45 (d, *J* = 6 Hz, 4 H), 7.42 (s, 2H), 7.28 (s, 1 H), 7.22 (s, 1H), 7.14 (d, *J* = 8.7 Hz, 4 H), 6.94 (d, *J* = 8.7 Hz, 4 H),

3.92 (t, J = 9.3 Hz, 8 H), 3.68 (d, J = 6.9 Hz, 4 H), 3.18 (t, J = 9.3 Hz, 8 H), 1.78 (s, 2 H), 1.42 (m, 16H), 0.86 (m, 12H); ^{13}C NMR (75 MHz, $CDCl_3$, 25 °C): δ (ppm) = 169.3, 152.2, 150.3, 147.7, 138.2, 136.3, 133.5, 131.17, 128.6, 127.7, 126.5, 124.1, 118.8, 118.3, 114.6, 66.4, 56.3, 52.3, 38.0, 30.7, 28.9, 24.1, 22.9, 14.1, 10.4; HR-MS (ESI): m/z =1027.5446, $[M+H]^+$, calcd. 1027.5449.

3 Preparing film DAD@PMMA and DAD@PS

PMMA as matrix preparing film: dissolving PMMA (143 mg, M_w = 120,000) in 5 ml of $CHCl_3$, 2 mg **DAD** were added to them and the resulting solution was poured into a petri dish (5 cm in diameter). The solution was left to evaporate over 2 h at room temperature to obtain a green fluorescent film (~ 1 mm in thickness).

PS (polystyrene) as matrix preparing film: dissolving PS (150 mg, M_w= 350,000) in 5 ml of $CHCl_3$ with sonication, 2 mg **DAD** were added to them and the resulting solution was poured into a petri dish (5 cm in diameter). The solution was left to evaporate overnight at room temperature to obtain an green fluorescent film (~ 1 mm in thickness)

Reference of experiment part:

[1] L. Porres, A. Holland, Palsson, *et al*., Absolute measurements of photoluminescence quantum yields of solutions using an integrating sphere. *Journal of Fluorescence,* 2006, 16 (2), 267-273.

[2] H. F. Wittmann, R. H. Friend, *et al*., An improved experimental determination of external photoluminescence quantum efficiency. *Advanced Materials,* 1997, 9 (3), 230-232.

[3] G. Krucaite, D. Tavgeniene, *et al*., 3, 6-Diaryl substituted 9-alkylcarbazoles as hole transporting materials for various organic light emitting devices. *Dyes and Pigments*, 2014, 106, 1-6.

[4] W. Z. Yuan, Z. Q. Yu, *et al*., High solid-state efficiency fluorescent main chain liquid crystalline polytriazoles with aggregation-induced emission characteristics. *Macromolecules*, 2011, 44(24), 9618-9628.

[5] P. Hrobárik, V. Hrobáriková, et al., Quadrupolar benzobisthiazole-cored arylamines as highly efficient two-photon absorbing fluorophores. *Organic letters*, 2014, 16(24), 6358-6361.

Bibliography

[1] J. B. Birks, *Photophysics of Aromatic Molecules* [M], Wiley, London, 1970.

[2] K. R. J. Thomas, J. T. Lin, Y. T. Tao, C. H. Chuen, *et al*., Star-Shaped Thieno-[3,4-b]- pyrazines: a new class of red-emitting electroluminescent materials. *Advanced Materials*, 2002, 14 (11), 822-826.

[3] T. M. Figueira-Duarte, P. G. Del Rosso, R. Trattnig, S. Sax, E. J. List, K. Müllen, *et al*., Designed suppression of aggregation in polypyrene: toward high-performance blue-light-emitting diodes. *Advanced Materials*, 2010, 22(9), 990-993.

[4] S. Hecht, J. M. J. Frechet, *et al*., Dendritic encapsulation of function: applying nature's site isolation principle from biomimetrics to materials science. *Angewandte Chemie International Edition*, 2001, 40(1), 74-91.

[5] J. Luo, Z. Xie, J. W. Lam, L. Cheng, B. Z. Tang, *et al*., Aggregation-induced emission of 1-methyl-1, 2, 3, 4, 5-pentaphenylsilole, *Chemical communications*, 2001, (18), 1740-1741.

[6] G. G. Stokes, On the change of refrangibility of light. *Philosophical transactions of the Royal Society of London*, 1852, 142, 463-562.

[7] Z. Zhao, H. Zhang, J. W. Lam,, B. Z. Tang, *et al*., Aggregation-Induced Emission: New Vistas at the Aggregate Level. *Angewandte Chemie International Edition*, 2020, 59(25), 9888-9907.

[8] J. Mei, N. L. Leung, R. T. Kwok, J. W. Lam, B. Z. Tang, *et al*., Aggregation-induced emission: together we shine, united we soar! *Chemical reviews*, 2015,115 (21), 11718-11940.

[9] J. He, B. Xu, F. Chen, H. Xia, K. Li, L. Ye, *et al*., Aggregation-induced emission in the crystals of 9,10-distyrylanthracene derivatives: the essential role of restricted intramolecular torsion. *Journal of Physical Chemistry C*, 2009, 113(22), 9892-9899.

[10] C. J. Bhongale, C. W. Chang, C. S. Lee, *et al*. Relaxation Dynamics and Structural Characterization of Organic Nanoparticles with Enhanced Emission. *Journal of Physical Chemistry B*, 2005, 109(28),13472-13482.

[11] Y. X. Li, Z. Chen, Y. Cui, G. M. Xia, X. F. Yang, *et al*., Stbstitution position directing the molecular packing, electronic structure, and aggregate emission property of bis[2-(9-anthracenyl)vinyl]benzene system. *Journal of Physical Chemistry B,* 2012, 116 (10), 6401-6408.

[12] (a) Z. Zheng, Z. P. Yu, M. D. Yang, F. Jin, Q. Zhang, H. P. Zhou, J. Y. Wu, Y. P. Tian, *et al*., Substituent group variations directing the molecular packing, electronic structure, and aggregation-induced emission property of isophorone derivatives. *The Journal of Organic Chemistry*, 2013, 78(7), 3222-3234. (b) J. Massin, W. Dayoub, Y. Bretonniere,C. Andraud, Near-Infrared Solid-State Emitters Based on Isophorone: Synthesis, Crystal Structure and Spectroscopic Properties [J], *Chemistry of Materials*,2011, 23(3), 862-873.

[13] Ma X, Sun R, Cheng J, *et al*. Fluorescence aggregation-caused quenching versus aggregation-induced emission: A visual teaching technology for undergraduate chemistry students. *Journal of Chemical Education*, 2016, 93(2), 345-350.

[14] J. Z. Liu, J. W. Y. Lam, B. Z. Tang. *et al*., Acetylenic polymers: syntheses, structures, and functions. *Chemical reviews*, 2009, 109(11), 5799-5867.

[15] B. He, S. Ye, Y. Guo, B. Chen, X. Xu, H. Qiu, Z. Zhao, *et al*., Aggregation-Enhanced Emission and Efficient Electroluminescence of Conjugated Polymers Containing Tetraphenylethene Units. *Science China Chemistry*, 2013, 56(9), 1221-1227.

[16] R. Hu, J. W. Y. Lam, J. Liu, H. H. Y. Sung, I. D.Williams, B. Z. Tang, *et al*., Hyperbranched Conjugated Poly(tetraphenylethene): Synthesis, Aggregation-Induced Emission, Fluorescent Photopatterning, Optical Limiting and Explosive Detection. *Polymer Chemistry,* 2012, 3(6), 1481−1489.

[17] Z. Wang, S. Chen, J. W. Lam, W. Qin, R. T. Kwok, B. Z. Tang, *et al*., Long-term fluorescent cellular tracing by the aggregates of AIE bioconjugates. *Journal of the American Chemical Society*, 2013, 135(22), 8238-8245.

[18] M. Arseneault, N. L. C. Leung, L. T. Fung, R. Hu, J.F. Morin, B. Z. Tang, *et al*., Probing the Dendritic Architecture Through AIE: Challenges and Successes. *Polymer Chemistry*, 2014, 5(20), 6087-6096.

[19] J. Mei, Y. Hong, J. W. Lam, A. Qin, B. Z. Tang, *et al*., Aggregation‐induced emission: the whole is more brilliant than the parts. *Advanced materials*, 2014, 26(31), 5429-5479.

[20] Y. Hong, J. W. Lam, B. Z. Tang, Aggregation-induced emission. *Chemical Society Reviews*, 2011, 40(11), 5361-5388.

[21] G. G. Shan, D. X. Zhu, H. B. Li, P. Li, Z. M. Su, Y. Liao, *et al*., Creation of cationic iridium(Ⅲ) complexes with aggregation-induced phosphorescent emission (AIPE) properties by increasing rotation groups on carbazole peripheries. *Dalton Transactions,* 2011, 40(12), 2947-2953.

[22] D. G. Khandare, H. Joshi, M. Banerjee, M. S. Majikand, A. Chatterjee, *et al*., Fluorescence turn-on chemosensor for the detection of dissolved CO_2 based on ion-induced aggregation of tetraphenylethylene derivative, *Analytical chemistry*, 2015, 87(21), 10871-10877.

[23] D. Maurel, S. Banala, T. Laroche, K. Johnsson, *et al*., Photoactivatable and photoconvertible fluorescent probes for protein labeling. *ACS chemical biology*, 2010, 5(5), 507-516.

[24] Y. Hong, *et al*., Aggregation-induced emission-fluorophores and applications. *Methods and applications in fluorescence*, 2016, 4(2), 022003.

[25] M. Jiang, X. Gu, R. T. K. Kwok, *et al*., Multifunctional AIEgens: ready synthesis, tunable emission, mechanochromism, mitochondrial, and bacterial imaging. *Advanced Functional Materials*, 2018, 28(1), 1704589.

[26] I. M. Khan, S. Niazi, M. K. I. Khan, *et al*., Recent advances and perspectives of aggregation-induced emission as an emerging platform for detection and bio-imaging. *TrAC Trends in Analytical Chemistry*, 2019, 119, 115637.

[27] H. Wang , G. Liu, *et al*., Advances in luminescent materials with aggregation-induced emission (AIE) properties for biomedical applications[J]. *Journal of Materials Chemistry B*, 2018, 6(24), 4029-4042.

[28] D. Li, J. Liu, R. T. Kwok, Z. Liang, B. Z.Tang, J. Yu, *et al*., Supersensitive detection of explosives by recyclable AIE luminogen-functionalized mesoporous materials. *Chemical Communications*, 2012, 48(57), 7167-7169.

[29] Y. Li, L. Xu, B. Su, *et al*., Aggregation induced emission for the recognition of latent fingerprints. *Chemical Communications*, 2012, 48(34), 4109-4111.

[30] N. Zhao, M. Li, Y. Yan, J. W. Y. Lam, Y. L. Zhang, Y. S. Zhao, *et al*., A tetraphenylethene-substituted pyridinium salt with multiple functionalities: synthesis, stimuli-responsive emission, optical waveguide and specific mitochondrion imaging. *Journal of Materials Chemistry C*, 2013, 1(31), 4640.

[31] J. Huang, N. Sun, Y. Dong, R. Tang, P. Lu, P. Cai, *et al*., Similar or totally different: the control of conjugation degree through minor structural modifications, and deep-blue aggregation-induced emission luminogens for non-doped oleds. *Advanced Functional Materials*, 2013, 23(18), 2329-2337.

[32] H. Li , Z. Chi, X. Zhang, B. Xu, S. Liu, Y. Zhang, J. Xu, *et al*., New thermally stable aggregation-induced emission enhancement compounds for non-doped red organic light-emitting diodes. *Chemical Communications*, 2011, 47(40), 11273-11275.

[33] J. Wang, J. Mei, R. Hu, J. Z. Sun, A. Qin, B. Z. Tang, *et al*., Click synthesis, aggregation-induced emission, e / z isomerization, self-organization, and multiple chromisms of pure stereoisomers of a tetraphenylethene-cored luminogen. *Journal of the American Chemical Society*, 2012, 134(24), 9956-9966.

[34] J. Liu, H. Su, L. Meng, Y. Zhao, C. Deng, J. C. Y. Ng, *et al*., What makes efficient circularly polarised luminescence in the condensed phase: aggregation-induced circular dichroism and light emission. *Chemical Science*, 2012, 3(9), 2737.

[35a] T. P., Flaten, Aluminium as a risk factor in Alzheimer's disease, with emphasis on drinking water [J]. *Brain research bulletin*, 2001, 55(2), 187-196.

[35b] J. M. De Freitas, R. Meneghini, *et al.*, Iron and its sensitive balance in the cell [J]. *Mutation Research/Fundamental and Molecular Mechanisms of Mutagenesis*, 2001, 475(1-2), 153-159.

[35c] X. Chen, X. Y. Shen, E. Guan, Y. Liu, A. Qin, , J. Z. Sun, B. Z. Tang, *et al*., A pyridinyl-functionalized tetraphenylethylene fluorogen for specific sensing of trivalent cations. *Chemical Communications*, 2013, 49(15), 1503-1505.

[36] D. Ding, C. C. Goh, B. Liu, *et al.*, Ultrabright organic dots with aggregation‐induced emission characteristics for real‐time two‐photon intravital vasculature imaging. *Advanced Materials*, 2013, 25(42), 6083-6088.

[37] L. Shi, Y. H. Liu, K. Li, A. Sharma, K. K. Yu, M. S. Ji, X. Q. Yu, *et al*., An AIE‐Based Probe for Rapid and Ultrasensitive Imaging of Plasma Membranes in Biosystems. *Angewandte Chemie International Edition*, 2020, 59(25), 9962-9966.

[38] N. Zhao, M. Li, Y. Yan, J. W. Y. Lam, Y. L. Zhang, Y. S. Zhao, K. S. Wong, B. Z. Tang, *et al*., A tetraphenylethene-substituted pyridinium salt with multiple functionalities: synthesis, stimuli-responsive emission, optical waveguide and specific mitochondrion imaging. *Journal of Materials Chemistry C*, 2013, 1(31), 4640-4646.

[39] C. W. T. Leung, Y. Hong, S. Chen, E. Zhao, J. W. Y. Lam, B. Z. Tang, *et al*., A photostable AIE luminogen for specific mitochondrial imaging and tracking. *Journal of the American Chemical Society*, 2013, 135(1), 62-65.

[40] W. Zhang, R. T. K. Kwok, Y. Chen, S. Chen, E. Zhao, C. Y. Y. Yu, J. W. Y. Lam, Q. Zheng, B. Z. Tang, *et al*., Real-Time Monitoring of the Mitophagy Process by a Photostable Fluorescent Mitochondrion-Specific Bioprobe with AIE Characteristics. *Chemical Communications*, 2015, 51, 9022-9025.

[41] L. Zhang, W. Liu, X. Huang, G. Zhang, X. Wang, Z. Wang, D. Zhang, X. Jiang, *et al*., Old is new again: a chemical probe for targeting mitochondria and monitoring mitochondrial membrane potential in cells. *Analyst*, 2015, 140(17), 5849-5854.

[42] N. Zhao, S. Chen, Y. Hong, B. Z. Tang, *et al*., A red emitting mitochondria-targeted AIE probe as an indicator for membrane potential and mouse sperm activity. *Chemical Communications*, 2015, 51(71), 13599-13602.

[43] X. Gu, E. Zhao, T. Zhao, M. Kang, C. Gui, J. W. Y. Lam, S. Du, M. M. T. Loy, B. Z. Tang, *et al*., A Mitochondrion‐Specific Photoactivatable Fluorescence Turn‐On AIE‐Based Bioprobe for Localization Super‐Resolution Microscope. *Advanced Materials*, 2016, 28(25), 5064-5071.

[44] D. Li, X. Ni, X. Zhang, L. Liu, J. Qu, D. Ding, J. Qian, *et al*., Aggregation-induced emission luminogen-assisted stimulated emission depletion nanoscopy for super-resolution mitochondrial visualization in live cells. *Nano Research*, 2018, 11(11), 6023-6033.

[45] M. Gao, Q. Hu, G. Feng, B. Z. Tang, B. Liu, *et al*., A fluorescent light-up probe with "AIE+ ESIPT" characteristics for specific detection of lysosomal esterase. *Journal of materials chemistry B*, 2014, 2(22), 3438-3442.

[46] R. Hu, C. A. Gómez-Durán, J. W. Lam, J. L. Belmonte-Vázquez, C. Deng, S. Chen, R. Ye, E. Pea-Cabrera, Y. Zhong, K. S. Wong, *et al*., Synthesis, solvatochromism, aggregation-induced emission and cell imaging of tetraphenylethene-containing BODIPY derivatives with large Stokes shifts. *Chemical communications*, 2012, 48(81), 10099-10101.

[47] C. W. T. Leung, R. T. K. Kwok, A. C. S. Leung, R. Wen, B. Li, J. W. Y. Lam, B. Z. Tang, *et al*., An acidic pH independent piperazine–TPE AIEgen as a unique bioprobe for lysosome tracing. *Chemical science*, 2017, 8(11), 7593-7603.

[48] E. Wang, E. Zhao, Y. Hong, J. W. Y. Lam, B. Z. Tang, *et al*., A highly selective AIE fluorogen for lipid droplet imaging in live cells and green algae. *Journal of Materials Chemistry B*, 2014, 2(14), 2013-2019.

[49] T. K. Ryan, W. T. Chris, W. Y. Jacky, B. Z. Tang, *et al*., A near-infrared AIEgen for specific imaging of lipid droplets. *Chemical Communications*, 2016, 52(35), 5957-5960.

[50] Z. Wang, C. Gui, E. Zhao, J. Wang, X. Li, A. Qin, Z. Zhao, Z. Yu, B. Z. Tang, *et al*., Specific fluorescence probes for lipid droplets based on simple AIEgens. *ACS Applied Materials & Interfaces*, 2016, 8(16), 10193-10200.

[51] X. Xu, S. Yan, Y. Zhou, R. Huang, Y. Chen, J. Wang, X. Weng, X. Zhou, *et al*., A novel aggregation-induced emission fluorescent probe for nucleic acid detection and its applications in cell imaging. *Bioorganic & medicinal chemistry letters*, 2014, 24(7), 1654-1656.

[52] C. Y. Y. Yu, W. Zhang, R. T. K. Kwok, C. W. T. Leung, J. W. Y. Lam, B. Z. Tang, *et al*., A photostable AIEgen for nucleolus and mitochondria imaging with organelle-specific emission. *Journal of Materials Chemistry B*, 2016, 4(15), 2614-2619.

[53] H. Ma, M. Yang, C. Zhang, Y. Ma, Y. Qin, Z. Lei, L. Chang, L. Lei, T. Wang, Y. Yang, *et al*., Aggregation-induced emission (AIE)-active fluorescent probes with multiple binding sites toward ATP sensing and live cell imaging. *Journal of Materials Chemistry B*, 2017, 5(43), 8525-8531.

[54] Z. Zheng, H. Liu, S. Zhai, H. Zhang, G. Shan, R. T. Kwok, K. S. Wong, *et al*., Highly efficient singlet oxygen generation, two-photon photodynamic therapy and melanoma ablation by rationally designed mitochondria-specific near-infrared AIEgens. *Chemical Science*, 2020, 11(9), 2494-2503.

[55] E. Zhao, Y. Hong, S. Chen, C. W. Leung, R. T. Kwok, *et al*., Highly Fluorescent and Photostable Probe for Long-Term Bacterial Viability Assay Based on Aggregation-Induced Emission. *Advanced Healthcare Materials,* 2014, 3(1), 88-96.

[56] C. Zhou, W. Xu, P. Zhang, M. Jiang, Y. Chen, R. T. K. Kwok, *et al*., Engineering sensor arrays using aggregation-induced emission luminogens for pathogen identification. *Advanced Functional Materials*, 2018, 29(4), 1805986.

[57] B. Guo, M. Wu, Q. Shi, T. Dai, B. Liu, *et al*., All-in-One Molecular Aggregation-Induced Emission Theranostics: Fluorescence Image Guided and Mitochondria Targeted Chemo-and Photodynamic Cancer Cell Ablation. *Chemistry of Materials*, 2020, 32(11), 4681-4691.

[58] E. Bilgen, M. Forough, *et al*., A conjugated gold nanoparticle-azacyanine off-on-off fluorescence probe for sensitive and selective detection of G-quadruplexes. *Talanta*, 2020, 217.

[59] M. Riikka, W. Valtteri, T. P. Hiltunen, *et al*. Rapid Detection of Angiotensinogen M/T235 Polymorphism by Fluorescence Probe Melting Curves. *Clinical Chemistry*, 2000, 46(6), 880-881.

[60] (a) N. Andreas, S. Nina, S. C. Andreas, *et al*., Different Real-Time PCR Formats Compared for the Quantitative Detection of Human Cytomegalovirus DNA. *Clinical Chemistry,* 1999, 45(11), 1932-1937. (b) D. Ray, P. K. Bharadwaj, *et al*., A Coumarin-Derived Fluorescence Probe Selective for Magnesium. *Inorganic Chemistry*, 2008, 47(7), 2252-2254.

[61] (a) Y. Yang, Q. Zhao, W. Feng , *et al.,* Luminescent chemodosimeters for bioimaging [J]. *Chemical Reviews*, 2013, 113(1), 192-270. (b) K. Kaur, R. Saini, A. Kumar, *et al.,* Chemodosimeters: an approach for detection and estimation of biologically and medically relevant metal ions, anions and thiols [J]. *Coordination Chemistry Reviews*, 2012, 256(17-18), 1992-2028.

[62] (a) H. W. Liu , L. Chen , C. Xu , *et al.*, Recent progresses in small-molecule enzymatic fluorescent probes for cancer imaging [J]. *Chemical Society Reviews*, 2018, 47(18), 7140-7180. (b) V. Bernard, *et al*., Molecular Fluorescence: Principles and Applications, Second Edition, 2012, ISBN:9783527650002

[63] R. Y. Tsien, *et al*., New calcium indicators and buffers with high selectivity against magnesium and protons: design, synthesis, and properties of prototype structures. *Biochemistry*, 1980, 19, 2396-2404.

[64] K. P. Carter, A. M. Young, A. E. Palmer, *et al*., Fluorescent sensors for measuring metal ions in living systems. *Chemical reviews*, 2014, 114(8), 4564-4601.

[65] W. Sun, M. Li, J. Fan, *et al*., Activity-Based Sensing and Theranostic Probes Based on Photoinduced Electron Transfer. *Accounts of Chemical Research*, 2019, 52(10), 2818-2831.

[66] X. Jing, F. Yu, W. Lin, *et al*., A PET-based lysosome-targeted turn-on fluorescent probe for the detection of H_2S and its bio-imaging application in living cells and zebrafish. *New Journal of Chemistry*, 2019, 43(43), 16796-16800.

[67] X. Liang, L. Zhang, X. Xu, *et al*., An ICT-Based Mitochondria-Targeted Fluorescent Probe for Hydrogen Peroxide with a Large Turn-On Fluorescence Signal. *ChemistrySelect*, 2019, 4(4), 1330-1336.

[68] X. He, L. H. Xiong, Y. Huang, *et al*., AIE-based energy transfer systems for biosensing, imaging, and therapeutics [J]. *TrAC Trends in Analytical Chemistry*, 2020, 122: 115743.

[69] (a) A. Kunishita, H. Ishimaru, S. Nakashima, T. Ogura, S. Itoh, *et al*., Reactivity of mononuclear alkylperoxo copper(II) complex. O-O bond cleavage and C-H bond activation. *Journal of the American Chemical Society*, 2008, 130(13), 4244-4245. (b) M. Taki, S. Iyoshi, A. Ojida, I. Hamachi, Y. Yamamoto, *et al*., Development of highly sensitive fluorescent probes for detection of intracellular copper(I) in living systems. *Journal of the American Chemical Society*, 2010, 132, 5938–5939.

[70] Y. S. Chung, J. M. Posimo, S. Lee, *et al*. Activity-based ratiometric FRET probe reveals oncogene-driven changes in labile copper pools induced by altered glutathione metabolism. *Proceedings of the National Academy of ences*, 2019, 116(37), 201904610.

[71] K. Khownium, J. Romsaiyud, S. Borwornpinyo, *et al*., Turn-on fluorescent sensor for the detection of lipopolysaccharides based on a novel bispyrenyl terephtalaldehyde-bis-guanylhydrazone. *New Journal of Chemistry*, 2019, 43(18), 7051-7056.

[72] J. S. Wu, W. M. Liu, X. Q. Zhuang, *et al.*, Fluorescence turn on of coumarin derivatives by metal cations: a new signaling mechanism based on C=N isomerization. *Organic Letters*, 2007, 9(1), 33-36.

[73] T. Yu, P. Sun, Y. Hu, *et al*. A novel and simple fluorescence probe for detecting main group magnesium ion in HeLa cells and Arabidopsis. *Biosensors & Bioelectronics*, 2016, 86, 677-682.

[74] C.S. Lim, B.R. Cho, Two-photon probes for biomedical imaging [J], *Tetrahedron*, 2015, 71, 8219-8249.

[75] (a) M. Göppert‐Mayer, Über Elementarakte mit zwei Quantensprüngen. *Annalen Der Physik*, 1931, 401(3), 273-294. (b) W. Kaiser, C. G. B. Garrett, Two-photon excitation in CaF_2: Eu^{2+}. *Physical review letters,* 1961, 7(6), 229.

[76] J. D. Bhawalkar, G. S. He, P. N. Prasad, *et al*., Nonlinear multiphoton processes in organic and polymeric materials. *Reports on Progress in Physics*, 1996, 59(9), 1041-1045.

[77] M. Rumi, B. Barlow, J. Wang; J. W. Perry, S. R. Marder, *et al*., Two-photon absorbing materials and two-photon-induced chemistry [M]. *Advances. Polymer. Science*, 2008, 213, 1-95.

[78] A. R. Sarkar, D. E. Kang, H. M. Kim, B. R. Cho, *et al*., Two-photon fluorescent probes for metal ions in live tissues. *Inorganic Chemistry*, 2014, 53(4), 1794-1803.

[79] H. M. Kim; B. R. Cho, *et al*., Two-photon probes for intracellular free metal ions, acidic vesicles, and lipid rafts in live tissues. *Accounts of chemical research,* 2009, 42(7), 863-872.

[80] H. M. Kim; B. R. Cho, *et al*., Two-Photon Fluorescent Probes for Metal Ions. *Chemistry–An Asian Journal,* 2011, 6(1), 58-69.

[81] C. S. Lim, B. R. Cho, *et al*., Two-photon probes for biomedical applications. *BMB Reports*, 2013, 46(4), 188-194.

[82] M. Leslie, Do lipid rafts exist?. *Science*, 2011, 334(6059), 1046-1047.

[83] C. S. Lim, B. R. Cho, *et al*., Two-photon probes for biomedical imaging. *Tetrahedron*, 2015, 71(43), 8219-8249.

[84] J. Liu, X. Guo, R. Hu, *et al*., Molecular Engineering of Aqueous Soluble Triarylboron-Compound-Based Two-Photon Fluorescent Probe for Mitochondria H_2S with Analyte-Induced Finite Aggregation and Excellent Membrane Permeability. *Analytical Chemistry*, 2015, 88(1), 1052-1057.

[85] Y. T. Gao, Y. Qu, T. Jiang, H. Zhang, N. N He, B. Li, J. C Wu, J. L. Hua, *et al*., Alkyl-triphenylamine end-capped triazines with AIE and large two-photon absorption cross-sections for bio-imaging. *Journal of Materials Chemistry C*, 2014, 2(31), 6353-6361.

[86] G. S. He, L. S. Tan, Q. Zheng, P. N. Prasad, *et al*., Multiphoton absorbing materials: molecular designs, characterizations, and applications. *Chemical reviews,* 2008, 108(4), 1245-1330.

[87] M. Pawlicki, H. A.Collins, R. G. Denning; H. L. Anderson, *et al*., Two-Photon Absorption and the Design of Two-Photon Dyes. *Angewandte Chemie International Edition,* 2009, 48(18), 3244-3266.

[88] Lim X. The nanolight revolution is coming. *Nature,* 2016, 531, 26-28.

[89] G. Chen, I. Roy, C. Yang, *et al*., Nanochemistry and nanomedicine for nanoparticle-based diagnostics and therapy. *Chemical reviews,* 2016, 116(5), 2826-2885.

[90] R. Y. Tsien, The green fluorescent protein. *Annual review of biochemistry,* 1998, 67(1), 503-544.

[91] B. J. Bevis, B. S. Glick, Rapidly maturing variants of the discosoma red fluorescent protein (DsRed). *Nature biotechnology,* 2002, 20(1), 84-87.

[92] J. Zhang, R. E. Campbell, A. Y. Ting, *et al*., Creating new fluorescent probes for cell biology. *Nature reviews Molecular cell biology,* 2002, 3(12), 906-918.

[93] H. Kobayashi, M. Ogawa, R. Alford, *et al*., New strategies for fluorescent probe design in medical

diagnostic imaging. *Chemical reviews,* 2010, 110(5), 2620-2640.

[94] X. Michalet, F. Pinaud, L. Bentolila, *et al*., Quantum dots for live cells, in vivo imaging, and diagnostics. *Science*, 2005, 307(5709), 538-544.

[95] A. M. Derfus, W. C. W. Chan, *et al*., Probing the cytotoxicity of semiconductor quantum dots. *Nano Letters,* 2004, 4(1), 11-18.

[96] J. Zhou, Q. Liu, *et al*., Upconversion luminescent materials: advances and applications. *Chemical reviews,* 2015, 115(1), 395-465.

[97] Y. H. Chan, P. J. Wu, *et al*., Semiconducting polymer nanoparticles as fluorescent robes for biological imaging and sensing. *Particle & Particle Systems Characterization,* 2015, 32(1), 11-28.

[98] K.Y. Pu, B. Liu, *et al*., Fluorescent conjugated polyelectrolytes for bio-imaging,. *Advanced Functional Materials,* 2011, 21(18), 3408-3423.

[99] S. Y. Li, J. Chen, G. Chen, *et al*., Semiconductor polymer dots induce proliferation in human gastric mucosal and adenocarcinoma cells. *Macromolecular Bioscience,* 2015, 15(3), 318-327.

[100] S. W. Thomas, G. D. Joly, *et al*., Chemical sensors based on amplifying fluorescent conjugated polymers. *Chemical reviews*, 2007, 107(4), 1339-1386.

[101] S. Ito, K. Murata, *et al*., Simple synthesis of water-soluble conducting polyaniline. *Synthetic Metals,* 1998, 96(2), 161-163.

[102] Q. L. Fan, Y. Zhou, *et al*., Water-soluble cationic poly(p-phenyleneethynylene)s (PPEs): Effects of acidity and ionic strength on optical behaviour. *Macromolecules,* 2005, 38(7), 2927-2936.

[103] J. Pecher, S. Mecking, *et al*., Nanoparticles of conjugated polymers. *Chemical reviews,* 2010, 110(10), 6260-6279.

[104] Y. F. Li, G. F. He, *et al*., Effect of preparation conditions on the two doping structures of polypyrrole. *Synthetic Metals,* 1998, 94(1), 127-129.

[105] L. Feng, C. Zhu, H. Yuan, *et al*. Conjugated polymer nanoparticles: preparation, properties, functionalization and biological applications[J]. *Chemical Society Reviews,* 2013, 42(41), 6620-6633.

[106] Lee J.; Jun H.; Kim J. Polydiacetylene-liposome microarrays for selective and sensitive

mercury (II) detection. *Advanced Materials,* 2009, 21, 3673-3677.

[107] R. Osterbacka, C. P. An, X. M. Jiang, *et al*., Two-dimensional electronic excitations in self-assembled conjugated polymer nanocrystals. *Science* 2000, 287(5454), 833-842.

[108] H. KorriYoussoufi, F. Garnier, P. Srivastava, *et al*., Toward bioelectronics: Specific DNA recognition based on an oligonucleotide-functionalized polypyrrole. *Journal of the American Chemical Society,* 1997, 119(31), 7388-7389.

[109] F. K. Wang, G. C. Bazan, *et al*., Aggregation-mediated optical properties of pH-responsive anionic conjugated polyelectrolytes. *Journal of the American Chemical Society,* 2006, 128(49), 15786-15792.

[110] P. Brocorens, *et al*., Solid-state supramolecular organization of polythiophene chains containing thienothiophene units. *Advanced Materials,* 2009, 21, 1194-1198.

[111] K. Li, B. Liu, *et al*., Polymer encapsulated conjugated polymer nanoparticles for fluorescence bio-imaging. *Journal of Materials Chemistry*, 2012, 22(4), 1257-1264.

[112] C. Wu, D. T. Chiu, *et al*., Highly fluorescent semiconducting polymer dots for biology and medicine. *Angewandte Chemie International Edition*, 2013, 52(11), 3086-3109.

[113] Y. Wang, L. Feng, S. Wang, *et al*., Conjugated polymer nanoparticles for imaging, cell activity regulation, and therapy. *Advanced Functional Materials*, 2019, 29(5), 1806818.

[114] C. Szymanski, J. Hooper, *et al*., Single molecule nanoparticles of the conjugated polymer MEH-PPV, preparation and characterization by near-field scanning optical microscopy[J]. *Journal of Physical Chemistry B*, 2005, 109(18), 8543–8546.

[115] C. F. Wu, C. Szymanski, *et al*., Conjugated polymer dots for multiphoton fluorescence imaging[J]. *Journal of the American Chemical Society*, 2007, 129(43), 12904-12905.

[116] M. C. Baier, J. Huber, S. Mecking, *et al*., Fluorescent conjugated polymer nanoparticles by polymerization in miniemulsion. *Journal of the American Chemical Society*, 2009, 131(40), 14267-14273.

[117] L. Polavarapu, Q. H. Xu,Water-soluble conjugated polymer-induced self-assembly of gold nanoparticles and its application to SERS. *Langmuir*, 2008, 24(19), 10608-10611.

[118] J. Liang, B. Z. Tang, B. Liu, *et al*., Specific light-up bioprobes based on AIEgen conjugates. *Chemical Society Reviews*, 2015, 44(10), 2798-2811.

[119] L. Yan, Y. Zhang, W. Tian, Fluorescent nanoparticles based on AIE fluorogens for bio-imaging. *Nanoscale*, 2016, 8(5), 2471-2487.

[120] R. Hu, A. Qin, B. Z. Tang, AIE polymers: Synthesis and applications. *Progress in Polymer Science*, 2020, 100, 101176.

[121] T. Zhou, A. Qin, *et al*., AIE conjugated polymer with ultra-strong ROS generation ability and great biosafety for efficient therapy of bacterial infection. *Angewandte Chemie International Edition,* 2020.

[122] (a) W. Z. Yuan, Z. Q. Yu, *et al*., High solid-state efficiency fluorescent main chain liquid crystalline polytriazoles with aggregation-induced emission characteristics. *Macromolecules*, 2011, 44(24), 9618-9628. (b) J. U. Izunobi, C. L. Higginbotham, *et al*., Polymer molecular weight analysis by ^{1}H NMR spectroscopy. *Journal of Chemical Education*, 2011, 88(8), 1098-1104.

[123] (a) Y. Gao, Y. Qu, *et al.*, Alkyl-triphenylamine end-capped triazines with AIE and large two-photon absorption cross-sections for bioimaging [J]. *Journal of Materials Chemistry C*, 2014, 2(31), 6353-6361. (b) B. Z. Tang, Y. Geng, J. W. Y. Lam, *et al.*, Processible nanostructured materials with electrical conductivity and magnetic susceptibility: preparation and properties of maghemite/polyaniline nanocomposite films [J]. *Chemistry of materials*, 1999, 11(6), 1581-1589. (c) F. Würthner, T. E. Kaiser, C. R. Saha-Möller, *et al*., J-Aggregates: From Serendipitous Discovery to Supramolecular Engineering of Functional Dye Materials. *Angewandte Chemie International Edition*, 2011, 50(15), 3376–3410. (d) Y. Wang, D. Xu, *et al.*, Mechanofluorochromic properties of aggregation-induced emission-active tetraphenylethene-containing cruciform luminophores [J]. *Dyes and Pigments*, 2018, 156, 291-298. (e) H. Sun, Y. Jiang, *et al*., Multi-stimuli-responsive tetraphenylethene-based thiazole compound: Time-dependently enhanced blue-shift emission, reversible acidichromism and mechanochromism [J]. *Dyes and Pigments*, 2020, 173, 107938.

[124] M. Ferrari, M. C. Fornasiero, A. M. Isetta, MTT colorimetric assay for testing macrophage cytotoxic activity in vitro[J]. *Journal of immunological methods*, 1990, 131(2), 165-172.

[125] J. Adler, I. Parmryd, *et al*., Quantifying colocalization by correlation: the Pearson correlation coefficient is superior to the Mander's overlap coefficient. *Cytometry Part A*, 2010, 77(8), 733-742.

[126] J. Y. Kwon, Y. J. Jang, J. Yoon, *et al*., A highly selective fluorescent chemosensor for Pb^{2+}. *Journal of the American Chemical Society,* 2005, 127(28), 10107-10111.

[127] S. Saha, A. Ghosh, P. Mahato, A. Das, *et al*., Specific recognition and sensing of CN^{-} in sodium cyanide solution. *Organic. Letters*, 2010, 12(15), 3406-3409.

[128] S. Y. Kim, J. Park, J. I. Hong, *et al*., Fluorescent probe for detection of fluoride in water and bio-imaging in A549 human lung carcinoma cells. *Chemical communications*, 2009, (31), 4735-4737.

[129] X. Liu, Y. Su, J. W. Foley, *et al*., Ratiometric fluorescent probe for lysosomal pH measurement and imaging in living cells using single-wavelength excitation. *Analytical chemistry*, 2017, 89(13), 7038-7045.

[130] (a) Y. Yue, S. Lee, J. Yoon, *et al*., A review: the trend of progress about pH probes in cell application in recent years. 2017, *Analyst*, 142(1), 30-41. (b) J. Han, K. Burgess. Fluorescent indicators for intracellular pH [J]. *Chemical reviews*, 2010, 110(5), 2709-2728.

[131] C. X.Yin, J. C. Salamanca, R. M. Strongin, *et al*., Fluorescent probes with multiple binding sites for the discrimination of Cys, Hcy, and GSH. *Angewandte Chemie International Edition*, 2017, 56(43), 13188-13198.

[132] X.Wu, W. Shi, H. Ma, *et al*., Recognition moieties of small molecular fluorescent probes for bio-imaging of enzymes. *Accounts of chemical research*, 2019, 52(7), 1892-1904.

[133] T. Yu, X. Tian, H. Zhou, *et al*., A reversible and highly selective fluorescence “on-off-on” probe for detecting nickel ion in the mitochondria of living cells. *Biosensors and Bioelectronics*, 2016, 82, 93-98.

[134] L. Yuan, W. Lin,*et al*., A ratiometric fluorescent probe for specific detection of cysteine over homocysteine and glutathione based on the drastic distinction in the kinetic profiles. *Chemical Communications*, 2011, 47(22):6275-6277.

[135] Y. Wang, L. Zhang, *et al*. A ratiometric fluorescent probe for detecting the endogenous biological signaling molecule superoxide anion and bio-imaging during tumor treatment. *Journal of Materials Chemistry B*, 2020, 8.

[136] Y. Tang, X. Kong, W. Lin, *et al*., Lysosome-targeted turn-on fluorescent probe for endogenous formaldehyde in living cells. *Analytical Chemistry*, 2016, 88(19), 9359-9363.

[137] X. X. Zhang, D. O. Kiesewetter, X. Y. Chen, *et al*., pH-sensitive fluorescent dyes:are they really pH-sensitive in cells?. *Molecular Pharmaceutics*, 2013, 10(5), 1910-1917.

[138] W. Liu, R. Sun, M. Ihara, *et al*., Reversible near-infrared pH probes based on benzo[a]phenoxazine. *Analytical Chemistry*, 2013, 85(15), 7419-7425.

[139] X. Y. Li, , *et al*., A novel nanogel-based fluorescent probe for ratiometric detection of intracellular pH values. *Chemical Communications*, 2014, 50(63), 8787-8790.

[140] T. Myochin, K. Kiyose, T. Nagano, *et al*., Rational design of ratiometric near-infrared fluorescent pH probes with various pKa values, based on aminocyanine. *Journal of the American Chemical Society*, 2011, 133(10), 3401-3409.

[141] L. X. Cao, G. Q. Yang, *et al*., In vivo observation of the pH alternation in mitochondria for various external stimuli. *Chemical Communications*, 2015, 51(97), 17324-17327.

[142] A. R. Sarkar, C. H. Heo, H. M. Kim, *et al*., A ratiometric two-photon probe for quantitative imaging of mitochondrial pH values. *Chemical Science*, 2016, 7(1), 766-773.

[143] R. C. Gilson, R. Tang, A. Som, *et al.*, Protonation and trapping of a small pH-sensitive near-infrared fluorescent molecule in the acidic tumor environment delineate diverse tumors in vivo [J]. *Molecular pharmaceutics*, 2015, 12(12), 4237-4246.

[144] (a) W. Yang, F. Liu, R. Li, *et al.*, Multiple Stimuli-Responsive Fluorescent Sensor from Citric Acid and 1-(2-Aminoethyl) piperazine [J]. *ACS applied materials & interfaces*, 2018, 10(10), 9123-9128. (b) M. Villabona, M. Benet, S. Mena, *et al*., Multistimuli-responsive fluorescent switches based on spirocyclic meisenheimer compounds: Smart molecules for the design of optical probes and electrochromic materials [J]. *The Journal of organic chemistry*, 2018, 83(16), 9166-9177. (c) Q. Yu, X. Su, T. Zhang, *et al.,* Non-invasive fluorescence switch

in polymer films based on spiropyran-photoacid modified TPE [J]. *Journal of Materials Chemistry C*, 2018, 6(8), 2113-2122. (d) M. Li, J. Liu, C. Shang, *et al.*, Porous Particle‐Based Inkjet Printing of Flexible Fluorescent Films: Enhanced Sensing Performance and Advanced Encryption [J]. *Advanced Materials Technologies*, 2019, 4(8), 1900109. (e) R. Miao, J. Peng, Y. Fang, Recent advances in fluorescent film sensing from the perspective of both molecular design and film engineering [J]. *Molecular Systems Design & Engineering*, 2016, 1(3), 242-257.

[145] (a) H. Y. Wang, G. Chen, *et al*., Synthesis and characterization of triphenylamine-benzothiazole-based donor and acceptor materials. *Synthetic Methods*., 2010, 160(9), 1065-1072. (b) N. Zhao, Z. Yang, J I. D. Williams, K. S. Wong, B. Z. Tang, *et al*., Benzothiazolium-functionalized tetraphenylethene: an AIE luminogen with tunable solid-state emission. *Chemical Communications,* 2012, 48(69), 8637-8639.

[146] Hrobárik P, Hrobáriková V, Semak V, et al. Quadrupolar benzobisthiazole-cored arylamines as highly efficient two-photon absorbing fluorophores [J]. *Organic letters*, 2014, 16(24), 6358-6361.

[147] (a) C. Öğretir, S. Demirayak, *et al*., Determination and evaluation of acid dissociation constants of some substituted 2-aminobenzothiazole derivatives. *Journal of Chemical & Engineering Data*, 2008, 53(2), 422-426.

(b) W. J. Catallo, T. Junk, Transformation of benzothiazole in estuarine sediments. *Journal of environmental quality*, 2005, 34(5), 1746-1754.

[148] R. R. Naredla, S. O. Nilsson Lill, *et al*., Charge delocalization and enhanced acidity in tricationic superelectrophiles. *Journal of the American Chemical Society*, 2011, 133(33), 13169-13175.

[149] K. H. Khoo, Y. Chen, S. Li, *et al*., Length dependence of electron transport through molecular wires–a first principles perspective. *Physical Chemistry Chemical Physics*, 2015, 17(1), 77-96.

[150] D. L. Pearson, J. S. Schumm, *et al*., Molecular scale electronics. Syntheses and Testing. *Synthetic metals*, 1997, 84(1-3), 303-306.

[151] K. Li, Q. Feng, B. Z. Tang, *et al*., Benzothiazole-based AIEgen with tunable excited-state intramolecular proton transfer and restricted intramolecular rotation processes for highly sensitive physiological pH sensing. *ACS sensors*, 2018, 3(5), 920-928.

[152] V. Kachwal, L. Fageria, *et al*., Exploring the hidden potential of a benzothiazole-based Schiff-base exhibiting AIE and ESIPT and its activity in pH sensing, intracellular imaging and ultrasensitive & selective detection of aluminium (Al^{3+}). *Analyst*, 2018, 143(15), 3741-3748.

[153] B. S. Chang, R. R. Mahoney, Enzyme thermostabilization by bovineserum albumin and other proteins: evidence for hydrophobic interactions. B*iotechnology and applied biochemistry*, 1995, 22(2), 203-214.

[154] Y. L. Jeyachandran, E. Mielczarski, *et al*., Quantitative and qualitative evaluation of adsorption/desorption of bovine serum albumin onhydrophilic and hydrophobic surfaces. *Langmuir*, 2009, 25(19), 11614-11620.

[155] R. Li, Z. Wu, *et al*., Role of pH-induced structuralchange in protein aggregation in foam fractionation of bovine serum albumin. *Biotechnology Reports*, 2016, 9, 46-52.

[156] W. Qin, D. Ding, *et al*., Biocompatible nanoparticles with aggregation‐induced emission characteristics as far‐red/near‐infrared fluorescent bioprobes for in vitro and in vivo imaging applications. *Advanced Functional Materials*, 2012, 22(4), 771-779.

[157] S. A. Hilderbrand, R. Weissleder, *et al*., Near-infrared fluorescence: application to in vivo molecular imaging. *Current opinion in chemical biology*, 2010, 14(1), 71-79.

[158] Z. Guo, S. Park, J. Yoon, *et al*. Recent progress in the development of near-infrared fluorescent probes for bio-imaging applications. *Chemical Society Reviews*, 2014, 43(1), 16-29.

[159] E. A. Owens, M. Henary, H. S. Choi, *et al*., Tissue-specific near-infrared fluorescence imaging. *Accounts of chemical research*, 2016, 49(9), 1731-1740.

[160] J. B. Li, W. Tan, *et al*., Recent progress in small-molecule near-IR probes for bio-imaging. *Trends in Chemistry*, 2019, 1(2), 224-234.

[161] P. K. Upputuri, M. Pramanik, Photoacoustic imaging in the second near-infrared window: a review. *Journal of biomedical optics*, 2019, 24(4), 040901.

[162] A. Zampetti, A. Minotto, F. Cacialli, Near-Infrared (NIR) Organic Light-Emitting Diodes (OLEDs): Challenges and Opportunities. *Advanced Functional Materials*, 2019, 29(21), 1807623.

[163] L. Yuan, W.Y. Lin, K. B. Zheng, *et al*., Far-red to near infrared analyte-responsive fluorescent probes based on organic fluorophore platforms for fluorescence imaging. *Chemical Society Reviews*, 2013, 42(2), 622-661.

[164] S. Pascal, C. Monnereau, O. Maury, *et al*., Expanding the polymethine paradigm: Evidence for the contribution of a bis-dipolar electronic structure. *The Journal of Physical Chemistry A*, 2014, 118(23), 4038-4047.

[165] A. Mishra, R. K. Behera, P. K. Behera, *et al*., Cyanines during the 1990s: A review. *Chemical Reviews*, 2000, 100(6), 1973-2012.

[166] W. Pham, L. Cassell, *et al*., A near-infrared dye for multichannel imaging. *Chemical communications*, 2008 (16), 1895-1897.

[167] (a)A. Samanta, M. Vendrell, *et al*., Development of photostable near-infrared cyanine dyes. *Chemical communications*, 2010, 46(39), 7406-7408. (b) S. Pascal, C. Andraud, *et al*., Keto-polymethines: a versatile class of dyes with outstanding spectroscopic properties for in cellulo and in vivo two-photon microscopy imaging [J]. *Chemical science*, 2017, 8(1), 381-394.

[168] W. H. Mills, LIV–The cyanine dyes. Part IV. Cyanine dyes of the benzothiazole series. *Journal of the Chemical Society, Transactions*, 1922, 121, 455 – 466.

[169] M. Losytskyy, V. Kovalska, *et al*., Interactions of cyanine dyes with nucleic acids. XXIV. Aggregation of monomethine cyanine dyes in presence of DNA and its manifestation in absorption and fluorescence spectra. *Spectrochimica Acta Part A: Molecular and Biomolecular Spectroscopy*, 2001, 57(7), 1525-1532.

[170] T. Deligeorgiev, S. Kaloyanova, *et al*., Intercalating cyanine dyes for nucleic acid detection. *Recent Patents on Materials Science*, 2001, *2*(1), 1-26.

[171] T. Deligeorgiev, N. Gadjev, *et al*., Preparation of intercalating dye thiazole orange and derivatives. *Dyes Pigments,* 1995, 29(4), 315-322.

[172] Q. Q. Shi, J. M. Lu, *et al*., A comparative study of symmetrical and unsymmetrical trimethine cyanine dyes bearing benzoxazolyl and benzothiazolyl groups. *Dyes Pigments,* 2012, 93(1-3), 1506-1512.

[173] B. Renikuntla, H. Rose, *et al*., Improved photostability and fluorescence properties through polyfluorination of a cyanine dye. *Organic letters*, 2004, 6(6), 909-912.

[174] M. Matsui, Y. Hashimoto, *et al*., Application of near-infrared absorbing heptamethine cyanine dyes as sensitizers for zinc oxide solar cell. *Synthetic metals*, 2005, 148(2), 147-153.

[175] S. Pascal, S. Denis-Quanquin, *et al*., Keto-polymethines: a versatile class of dyes with outstanding spectroscopic properties for in cellulo and in vivo two-photon microscopy imaging. *Chemical science*, 2017, 8(1), 381-394.

[176] S. Dähne, Der ideale Polymethinzustand. *CHIMIA International Journal for Chemistry*, 1991, 45(10), 288-296.

[177] X. Y. Shen, Y. J. Wang, *et al*., Effects of substitution with donor–acceptor groups on the properties of tetraphenylethene trimer: aggregation-induced emission, solvatochromism, and mechanochromism. *The Journal of Physical Chemistry C*, 2013, 127(14), 7334-7347.

[178] F. Terenziani, A. Painelli, M. Blanchard-Desce, *et al*., Charge instability in quadrupolar chromophores: Symmetry breaking and solvatochromism. *Journal of the American Chemical Society*, 2006, 128(49), 15742-15755.

[179] D. Carmona-Gutierrez, F. Madeo, *et al*., The crucial impact of lysosomes in aging and longevity. Ageing research reviews, 2016, 32, 2-12.

[180] R. Lüllmann-Rauch, History and morphology of the lysosome[M]//Lysosomes. *Springer*, Boston, MA, 2005, 1-16.

[181] M. Gao, Q. Hu, *et al*., A fluorescent light-up probe with "AIE+ ESIPT" characteristics for specific detection of lysosomal esterase. *Journal of materials chemistry B*, 2014, 2(22), 3438-3442.

[182] T. Chen, S. Zheng, A NIR fluorescent probe for detection of viscosity and lysosome imaging in live cells. *Organic & biomolecular chemistry*, 2019, 17(26), 6398-6403.

[183] J. L. Zhu, Z. Xu, *et al*., Small-molecule fluorescent probes for specific detection and imaging of chemical species inside lysosomes. *Chemical Communications*, 2019, 55(47), 6629-6671.

[184] A. N. Bourque, S. Dufresne, W. G. Skene, *et al*., Thiophene-phenyl azomethines with varying rotational barriers-model compounds for examining imine fluorescence deactivation. *The Journal of Physical Chemistry C*, 2009, 113(45), 19677-19685.

[185] M. Jiang, J. W. Y. Lam, *et al*., Two-photon AIE bio-probe with large Stokes shift for specific imaging of lipid droplets. *Chemical science*, 2017, 8(8), 5440-5446.

[186] E. Abbe, Contributions to the theory of the microscope and microscopic detection (translated from German). *Arch Mikroskop Anat*, 1873, 9, 413-468.

[187] A. Neice, Methods and limitations of subwavelength imaging. *In Advances in imaging and electron physics,* 2010, 163, 117-140.

[188] M.J. Rust, M. Bates, X. Zhuang, Sub-diffraction-limit imaging by stochastic optical reconstruction microscopy (STORM). *Nature methods*, 2006, 3(10), 793-796.

[189] E. Betzig *et al*., Imaging intracellular fluorescent proteins at nanometer resolution. *Science,* 2006, 313(5793), 1642-1645.

[190] S. J. Sahl, S. W. Hell, S. Jakobs, Fluorescence nanoscopy in cell biology. *Nature reviews Molecular cell biology*, 2017, 18(11), 685.

[191] G. Patterson, M. Davidson, *et al*., Superresolution imaging using single-molecule localization. *Annual review of physical chemistry*, 2010, 61, 345-367.

[192] A. Jimenez, K. Friedl, C. Leterrier, About samples, giving examples: optimized single molecule localization microscopy. *Methods*, 2020, 174, 100-114.

[193] H. Li, J. C. Vaughan, Switchable fluorophores for single-molecule localization microscopy. *Chemical reviews*, 2018, 118(18), 9412-9454.

[194] R. M. Dickson, A. B. Cubitt, *et al*., On/ off Blinking and Switching Behaviour of Single Molecules of Green Fluorescent Protein. *Nature* 1997, 388, 355-358.

[195] G. T. Dempsey, J. C. Vaughan, X. Zhuang, *et al*., *Natural Methods,* 2011, 8 (12), 1027-1036.

[196] L. Nahidiazar, A. V Agronskaia, J. Broertjes, B. van den Broek, K. Jalink, *PLoS One* 2016, 11(7),

e0158884.

[197] R. M. Dickson, A. B. Cubitt, R. Y. Tsien, W. E. Moerner, *et al*., On/off blinking and switching behaviour of single molecules of green fluorescent protein. *Nature,* 1997, 388(6648), 355-358.

[198] J. Lippincott-Schwartz, G. H. Patterson, *et al*., Photoactivatable fluorescent proteins for diffraction-limited and super-resolution imaging,. *Trends Cell Biology,* 2009, 19(11), 555–565.

[199] P. Hoyer, T. Staudt, J. Engelhardt, S. W. Hell, *et al*., Quantum dot blueing and blinking enables fluorescence nanoscopy. Nano letters, 2011, 11(1), 245-250.

[200] K. A. Lidke, B. Rieger, T. M. Jovin, R. Heintzmann, *et al*., Superresolution by localization of quantum dots using blinking statistics. *Optics express*, 2005, 13(18), 7052-7062.

[201] N. C. Verma, S. Khan, C. K. Nandi, *et al*., Single-molecule analysis of fluorescent carbon dots towards localization-based super-resolution microscopy. *Methods and applications in fluorescence*, 2016, 4(4), 044006.

[202] B. Zhi, Y. Cui, S. Wang, B. P. Frank, D. N. Williams, R. P. Brown, E. S. Melby, R. J. Hamers, Z. Rosenzweig, D. H. Fairbrother, *et al*., Malic acid carbon dots: from super-resolution live-cell imaging to highly efficient separation. *ACS nano,* 2018, 12(6), 5741-5752.

[203] M. Heilemann , S. Van De Linde , M. Schüttpelz, *et al*., Subdiffraction‐resolution fluorescence imaging with conventional fluorescent probes. *Angewandte Chemie International Edition*, 2008, 47(33), 6172-6176.

[204] S. H. Shim, C. Xia, G. Zhong, *et al*., Super-resolution fluorescence imaging of organelles in live cells with photoswitchable membrane probes. *Proceedings of the National Academy of Sciences*, 2012, 109(35), 13978-13983.

[205] D. Berdnikova, O. Fedorova, *et al*., Photoinduced in situ generation of a DNA-binding benzothiazoloquinolinium derivative. *Chemical Communications*, 2012, 48(38), 4603-4605.